UNIVERSITY OF SOUTHAMPTON

FACULTY OF PHYSICAL SCIENCES AND ENGINEERING

School of Physics and Astronomy

Supergiant fast X-ray transients and their place within the high mass X-ray binary population

by

Sebastian Peter Kenneth Drave

Presented for the degree of

Doctor of Philosophy

June 2013

UNIVERSITY OF SOUTHAMPTON

ABSTRACT

FACULTY OF PHYSICAL SCIENCES AND ENGINEERING
School of Physics and Astronomy

DOCTOR OF PHILOSOPHY

SUPERGIANT FAST X-RAY TRANSIENTS AND THEIR PLACE WITHIN THE HIGH MASS X-RAY BINARY POPULATION

by Sebastian Peter Kenneth Drave

Supergiant Fast X-ray Transients (SFXT) are a class of HMXB that have only recently been unveiled by the wide field, high sensitivity monitoring of the Galactic Plane performed by the *INTEGRAL* observatory. Characterised by rapid X-ray flaring behaviour, on the order of hours, these extreme transients display X-ray dynamic ranges of $10^4 - 10^5$ with peak outburst luminosities of $\sim 10^{36}\,\mathrm{erg\,s^{-1}}$. In this work, detailed studies of four of the twelve confirmed SFXTs are presented. Soft and hard X-ray observations are used to probe the nature of these individual sources and the accretion processes occurring within them. In each case the orbital period and hard X-ray outburst history is determined from *INTEGRAL* data. An *RXTE* study also discovered the likely neutron star spin period of IGR J17544−42619 and showed that a centrifugal barrier to the accretion flow may generate the deep X-ray quiescent states observed in this source. Orbital phase targeted *INTEGRAL* and *XMM-Newton* observations of IGR J16418−4532 allowed the detailed characterisation of this system. The detection of an X-ray intensity dip suggests that IGR J16418−4532 may undergo accretion regime transitions and implies the presence of a highly magnetised neutron star ($\mathrm{B} \sim 10^{14}\,\mathrm{G}$). Through considerations of the orbital configurations of these systems it is concluded that the accretion processes occurring in SFXTs are heavily influenced by both the variable stellar wind environment and the action of higher order accretion processes, such as impeded accretion regimes and/or magnetic and centrifugal barriers. An assessment is made as to how the SFXTs may be reconciled with the classical, persistent supergiant X-ray binary population. Beyond the persistent versus transient segregation of the whole SgXRB population, a more physically meaningful divide may be drawn between systems that spend the majority of the time in an impeded or un-impeded accretion regime. Additionally, some members of the SFXT class may show a direct evolutionary link between HMXB systems with a main sequence and post main sequence companion for the first time.

Contents

List of Figures

List of Tables

Declaration of Authorship

I declare that the thesis entitled *'Supergiant fast X-ray transients and their place within the high mass X-ray binary population'* and the work presented in the thesis are both my own and have been generated by me as a result of my own original research. I confirm that this work was done wholly while in candidature for a research degree at this University. I also confirm that where I have consulted the published work of others this is always clearly attributed, where I have quoted from the works of others the source is always given and where the thesis is based on work done jointly with others I have made clear what was done by others and what I have contributed myself.

In particular I wish to highlight the following sections in which the presented material is not wholly of my own work:

- Chapter 1 is a broad introduction to the field of X-ray binaries for which I found the works 'Compact Stellar X-ray Sources', Lewin & van der Klis 2006 and 'X-ray Binaries', Lewin, van Paradijs, & van den Heuvel 1997 to be useful sources of reference;
- For the study in Chapter 4 the *RXTE*/PCA science event mode data extraction, reduction and processing was performed by L. J. Townsend, a fellow graduate student at the University;
- Parts of the discussion on the nature of IGR J17354−3255 presented in Chapter 5 were written by V. Sguera, a colleague at IASF-INAF, Bologna, Italy. V. Sguera also performed all liaisons with the *AGILE* team with regards to the analysis of the MeV source AGL J1734−3310.

This thesis contains work which has previously been published in the following works:

- S. P. Drave, et al. 2013, MNRAS, in press, 'An in-depth study of the Supergiant Fast X-ray Transient IGR J16418−4532 using *INTEGRAL* and *XMM-Newton*'
- S. P. Drave, et al. 2012, A&A, 539, A21, 'X-ray pulsations from the region of the supergiant fast X-ray transient IGR J17544−2619'

- S. P. Drave, et al. 2010, MNRAS, 409, 1220, 'Discovery of the 51.47-d orbital period in the supergiant fast X-ray transient XTE J1739−302 with *INTEGRAL*'
- V. Sguera, S. P. Drave, et al. 2011, 'IGR J17354−3255 as a candidate intermediate supergiant fast X-ray transient possibly associated with the transient MeV source AGL J1734−3310'

In addition I have also contributed to the following works, that do not feature in this thesis, during the course of my Ph.D.:

- S. P. Drave, et al. 2010, Proceedings of Science '8^{th} *INTEGRAL* Workshop: The Restless Gamma-ray Universe', 117, 'Temporal Studies of Supergiant Fast X-ray Transients'
- D. J. Clark, et al. 2010, MNRAS, 406, L75, 'The orbital period in the supergiant fast X-ray transient IGR J16465−4507'
- L. J. Townsend, et al. 2011, MNRAS, 410, 1813, 'The orbital solution and spectral classification of the high-mass X-ray binary IGR J01054-7253 in the Small Magellanic Cloud'
- L. J. Townsend, S. P. Drave, et al. 2013, MNRAS, in press, 'Contrasting behaviour from two Be/X-ray binary pulsars: insights into differing neutron star accretion modes'
- V. Sguera, S. P. Drave, et al. 2013, A&A, in press, 'X-ray, optical and infrared investigation of the candidate supergiant fast X-ray transient IGR J18462−0223'
- M. Fiocchi, et al. 2013, ApJ 762, 19, 'The *INTEGRAL* source IGR J16328−4726: A High-mass X-ray Binary from the *BeppoSAX* Era'
- M. E. Goossens et al. 2013, MNRAS, in submission, 'Discovering a 5.72 day orbital period in AX J1845.0−0433'
- S. P. Drave, et al. 2012, ATel, 4218, '*INTEGRAL* detects the BeXRB GS 0834−43 returning to an active state'
- S. P. Drave, et al. 2011, ATel, 3396, '*INTEGRAL* Galactic Plane Scanning shows 4U 0115+63 appearing to enter a new type-II outburst'

Signed: .....
Date: .....

Acknowledgements

I would like to acknowledge and thank the following people for their support, guidance and encouragement over the past three and half years. First and foremost I would like to thank my supervisor, Tony Bird, for all of the support and direction he has given me throughout my studies as well as the knowledge I have gained through working alongside him. In particular the responsibility for writing and leading observing proposals given to me has been one of the most informative aspects of my studies, allowing me to help direct the research we have undertaken and develop many skills that will serve me well in the future. Beyond the direct scientific supervision I would also like to thank Tony for the many other things he has taught me, such as cluster computer management and the principles of computer programming (although I never quite broke my IDL habit), the great experiences we had at conferences and allowing me to travel to South Africa to undertake an observing run at SAAO which has formed one of the most valuable experiences I have had during my studies. I would also like to thank all of my collaborators for their insightful advice and suggestions, which has enhanced the quality of our published works together, and their willingness to provide hasty comments for rapidly approaching telescope proposal deadlines. In particular I would like to thank Adam Hill for his ever present enthusiasm and willingness to discuss and explain both computational methods and theoretical topics. I also wish to thank Lara Sidoli and Vito Sguera for both their help as collaborators and their wonderful hospitality during my recent visit to their institutions in Italy.

In Southampton I would like to thank all of the staff members, postdocs and graduate students in the Astronomy Group for providing a fantastic environment in which to work. Specifically I would like to thank the staff and postdocs for always being willing to discuss queries and issues and providing tough but fair questions during group seminars that drove me to investigate new avenues within my research and helped in preparing for giving presentations in a conference environment. I would also like to thank the students as a whole for the great environment they create in which it has been a pleasure to work. In particular I would like to thank Liz Bartlett, Lee Townsend, Grace Thomson, Tana Joseph and Sadie Jones for all of the fun we've had over the last few years. I would like thank Grace for organising some great trips to the cricket at the Rose Bowl and Sadie and Tana for getting me

into circuit training at the Jubilee (with all of the hours of complaining about it afterwards included) along with all the cracking rugby watching we've done together. Academically I would like to thank Lee for all of the conceptual discussions we've had as well as his assistance and knowledge of the *RXTE* telescope and data analysis. Out of the office I thank Lee for all of the great evenings spent in the pub, whilst he beat me at pool, and all of the squash matches, which are thankfully a bit more even! Finally I thank Liz for the great camaraderie we have shared throughout our undergraduate days, year in Boston and Ph.D. studies. Never has this been as important as in the last 6 months where writing up at the same time, whilst also sharing a flat, has lead to such a level of hilarity and banter about the process that it has acted as a great source of support and has hugely aided in getting to this point, for which I again thank you.

I would not have been able to get to this point without the constant love and support of my family also. I cannot thank my parents enough for their continual encouragement down the years along their unswerving dedication to myself and my siblings for which I again express my deepest thanks. Having now learnt to drive myself I also thank my dad for the countless number of times he drove back and forth along the M4 to take me to and from Southampton during my undergraduate years, all without a single word of complaint. The degree to which both my mum and dad went out of their way to support me through both my undergraduate and postgraduate studies is greatly appreciated and will never be forgotten. To my wider family and friends who were also a constant source of love, support, encouragement and assistance I also express my deepest gratitude.

My last and deepest thanks go to Elaine. You have been the most integral part of my life since we met on the first day of my Ph.D. studies. I am truly grateful for the continual love you show me along with the unfaltering support and encouragement you have provided over the last three and half years which has helped me get to where I am today.

Chapter 1

Introduction

X-ray binaries kick started the field of X-ray astronomy more than 50 years ago through the detection of Sco X-1, the first extra-solar source of X-ray radiation, in 1962 (Giacconi et al., 1962). Ever since, X-ray binaries have remained at the forefront of X-ray astronomy, consistently showing themselves to be some of the most dynamic and intriguing sources in the high energy sky. Being a rare endpoint of stellar evolution in binary star systems, X-ray binaries are comprised of a compact, degenerate stellar remnant in a gravitationally bound system with any one of a variety of stellar companions. The X-rays observed from these systems are generated through the accretion of matter transferred from the stellar companion in the binary. The intrinsically turbulent and unstable nature of mass transfer and accretion in X-ray binary systems is the major driving force in generating the extremely variable, and often transient, behaviour observed from these systems.

Whilst in principle all gravitationally bound systems comprised of a main sequence (MS) or post main sequence star transferring mass to a degenerate stellar object are X-ray binaries, in this thesis only systems with neutron stars (NS) or black holes (BH) as the degenerate object are discussed. The remaining systems possessing a white dwarf (WD) as the degenerate object generally fall into the Cataclysmic Variable (CV) class of objects. CVs are a varied class of objects comprised of several sub-groups determined by the nature of the binary components, such as the magnetic field strength of the WD, and also the properties of the Nova explosions that characterise this class of objects. These Nova explosions manifest as an extreme increase in the optical brightness of systems, by over 10 magnitudes in the most luminous cases, resulting from runaway thermonuclear burning on the surface of the WD once a critical surface density is exceeded as a result of mass transfer from the companion. A detailed discussion of varied demography of CVs and the Nova outburst mechanism is beyond the scope of this thesis, however. Additionally double degenerate binaries, often WD-NS or NS-NS systems, are not discussed further other than to note that these systems are the next evolutionary phase after

the traditional stellar-degenerate X-ray binary phase and are likely sources of gravitational wave emission.

The observational properties of any particular X-ray binary are strongly dependent on the nature of both the stellar and compact objects in the system. Additionally the method through which mass transfer occurs in a system is also heavily dependant on the nature of the companion star. Generally X-ray binaries fall into one of two categories. The Low Mass X-ray Binaries (LMXB) are comprised of a compact object in an orbital system with a stellar companion with a mass of less than $\sim 1\,M_\odot$ whereas High Mass X-ray Binaries (HMXB) possess companion stars that are significantly more massive, having masses of greater than $\sim 10\,M_\odot$. NSs and BHs have been identified as the compact objects in both LMXBs and HMXBs. Additionally there are a small number of examples of Intermediate Mass X-ray Binaries (IMXB) whose companions occupy the $1 - 10\,M_\odot$ mass range between the LMXBs and HMXBs. The specific properties of each of these classes of system are outlined in the following sections.

The observed Galactic distribution of both LMXBs and HMXBs is shown in Fig. 1.1 (Grimm, Gilfanov, & Sunyaev, 2002). The HMXBs are located in a narrow band along the Galactic Plane whilst the LMXBs are spread throughout the Galaxy with concentrations in regions of older stellar populations such as the Galactic Bulge and Globular Clusters. These varied distributions result from the different evolutionary timescales over which these types of system exist. The lifespans of HMXBs are determined by the evolution of the massive companion (Myr) such that HMXBs cannot travel large distances from their birth location before the cessation of the X-ray phase. These sources are therefore tracers of the recent star formation occurring in the disc and spiral arms of the Milky Way. The lifespans of LMXBs on the other hand are determined by the length of time required for the X-ray binary phase to be initiated and the much slower evolution of the low mass companion (Gyr). LMXBs are therefore concentrated in regions of older stellar populations such that the binary evolution was initiated sufficiently far in the past for the systems to have reached the X-ray binary phase at the current epoch. Further details of the evolutionary processes undergone by LMXBs and HMXBs are given in Sections 1.1 and 1.2 below.

1.1 Low Mass X-ray Binaries - LMXB

LMXBs are some of the brightest and most numerous sources observed in the X-ray sky. The compact object in a LMXB can be either a NS or a BH which, in both cases, dominate the orbital dynamics of the system as they are the more massive component of the binary. As low mass, main sequence (MS) stars do not suffer significant mass loss through strong stellar winds, the mass transfer occurring in

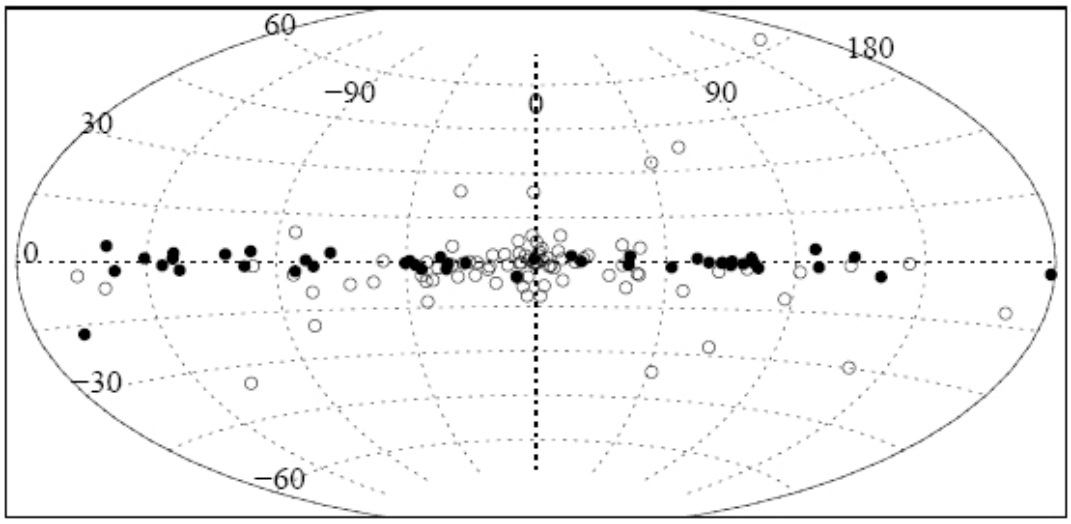

Figure 1.1: The galactic distribution of LMXBs (open circles) and HMXBs (filled circles) in the Milky Way using Galactic co-ordinates (Grimm, Gilfanov, & Sunyaev, 2002).

LMXBs must be driven by Roche-Lobe Overflow (RLO). This therefore requires LMXBs to possess short orbital periods, on the order of $\sim 1 - 100$ hours, such that the stellar companion overfills its Roche-lobe and an accretion stream is generated as stellar material is forced through the L1 point toward the compact object. As a result of this RLO the orbits of LMXBs circularise very early on in the lifetime of the X-ray binary due to tidal and frictional forces. The evolutionary mechanism through which LMXBs form is not straight forward, however. Given that the compact object in these systems is either a NS or a BH this requires that the progenitor star was massive ($> 8\,M_{\odot}$). However, the compact orbits of LMXBs are often smaller than the size of the progenitor during the pre compact object supergiant stage, requiring a significant shrinking of the orbit through the course of the binary evolution. The contraction in the orbit is ascribed to a 'Common Envelope' (CE) phase whereby the low mass companion star enters the atmosphere of the supergiant primary and, due to frictional forces, descends towards the core of the star. This action has the effect of expelling the envelope of the primary and shrinking the orbit due to the large amount of mass loss generated, leaving the low mass companion in orbit around the stripped, Helium core of the progenitor. The LMXB phase is then initiated after the He star has undergone a supernova, creating the NS or BH, and the orbit shrinks to allow the initiation of RLO either through the mass loss from the companion as a result of its own evolution of the MS or the energy loss through gravitational wave radiation. The mass transfer in the LMXB phase continues over timescales of $10^8 - 10^9$ yr eventually resulting in a double degenerate NS-WD binary or, in extreme cases, the complete dissociation of the companion star. Figure 1.2 illustrates an example pathway for the creation of an LMXB that eventually creates a binary millisecond pulsar (Tauris & van den Heuvel, 2006). It should be noted however, that the detailed physics of CE

evolution is only poorly understood, resulting in large uncertainties in the stellar and orbital parameters of the progenitor systems of LMXBs. Additionally many systems that enter a CE phase are unable to expel the primary's envelope before the low mass secondary mergers with the core of the primary resulting in a single, rejuvenated star, and others that do survive the CE phase may be unbound by the He star SN. Hence the successful completion of the evolutionary track to form a LMXB is a rare occurrence. In the densest stellar environments the requirement for the two components of the LMXB to have evolved as a bound system is removed as the successful capture of a stellar companion by an isolated compact object become statistically likely. Such captures are believed to be the origins of the populations of LMXBs found within Globular Clusters such as Terzan 5 (Heinke et al., 2006).

The material transferred through the L1 point in a LMXB retains a large amount of angular momentum and hence cannot fall directly onto the compact object. Instead an accretion disc forms around the compact object to conserve the angular momentum of the in-falling material, creating a reservoir of matter that orbits close to the compact object. The angular momentum of the material is then shed through viscous processes as the transferred material moves inward through the disc towards the compact object. When the material that has been drawn through the L1 point enters the outer regions of the accretion disc, it does not know about the nature of the compact object at the centre of the disc and it is therefore expected that accretion discs in LMXBs will be described by the same physical processes over the majority of their radial extent. In their innermost regions the different environments encountered at a BH event horizon and a NS magnetosphere/solid surface drive different physical behaviours that are observed in BH and NS LMXBs, a summary of which is given below.

Due to the temperature of the circling matter the accretion disc emits strongly in the blue region of the optical spectrum, often being several orders of magnitude more luminous than the intrinsic emission of the low mass stellar companion. However, the optical luminosity of the disc is dependent upon its size and radial extent which does not remain constant, hence in the optical band LMXBs are often detected as variable, intrinsically blue stars whilst the intrinsic emission of the companion star often remains undetected apart from during periods of X-ray quiescence (see below). The low mass companion star is often heavily distorted on the L1 point facing side as a result of the gravitational force of the compact object. This distortion, combined with X-ray illumination from the compact object can result in a hot spot on the surface of the companion that rotates with the binary orbit. The impact point of the accretion flow entering the outer regions of the accretion disc can also cause a hot spot and inflation in outer regions of the accretion disc. Finally absorption lines in the optical spectra of the low mass companions display radial velocity (RV) induced variations in the central wavelength of the line as a result of the binary motion. All of these effects may

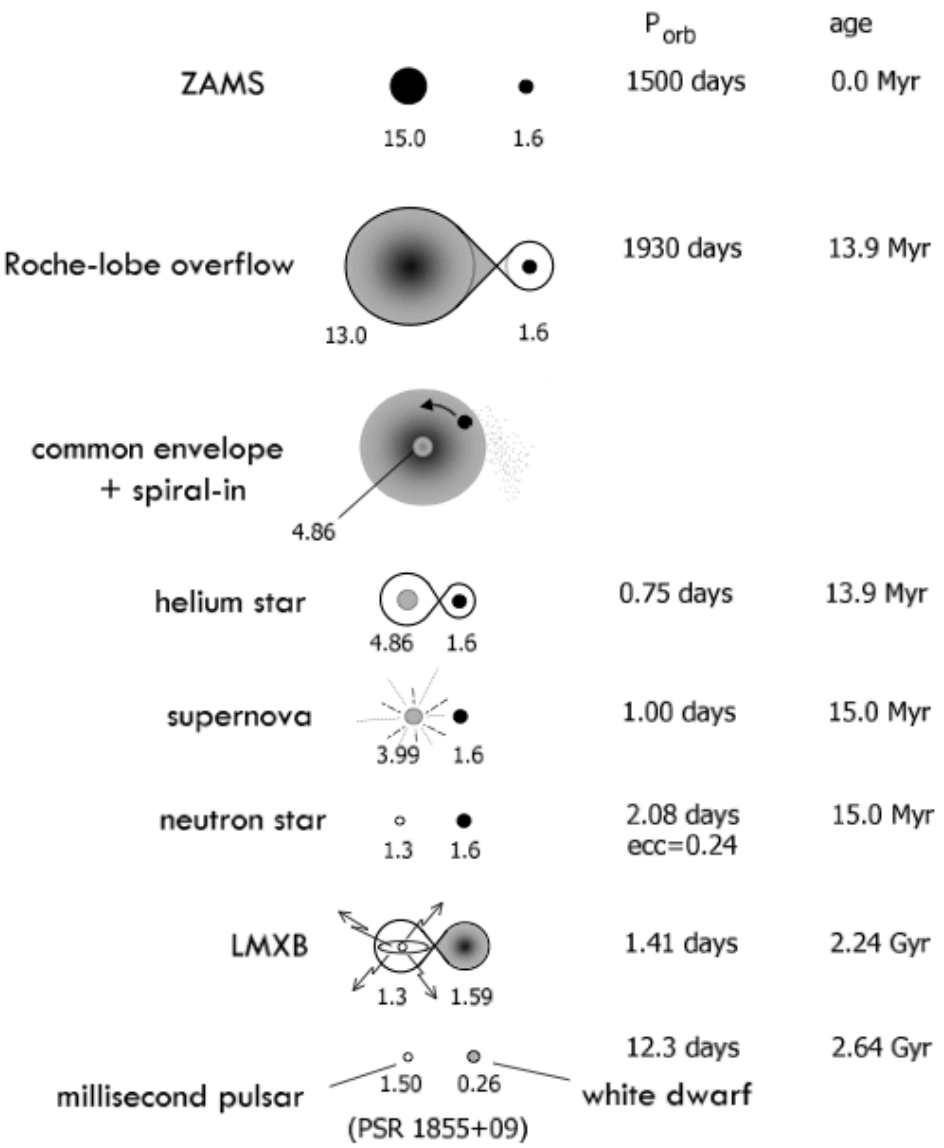

Figure 1.2: An example evolutionary path for a LMXB systems that end its life as a NS-WD double generate binary (Tauris & van den Heuvel, 2006)

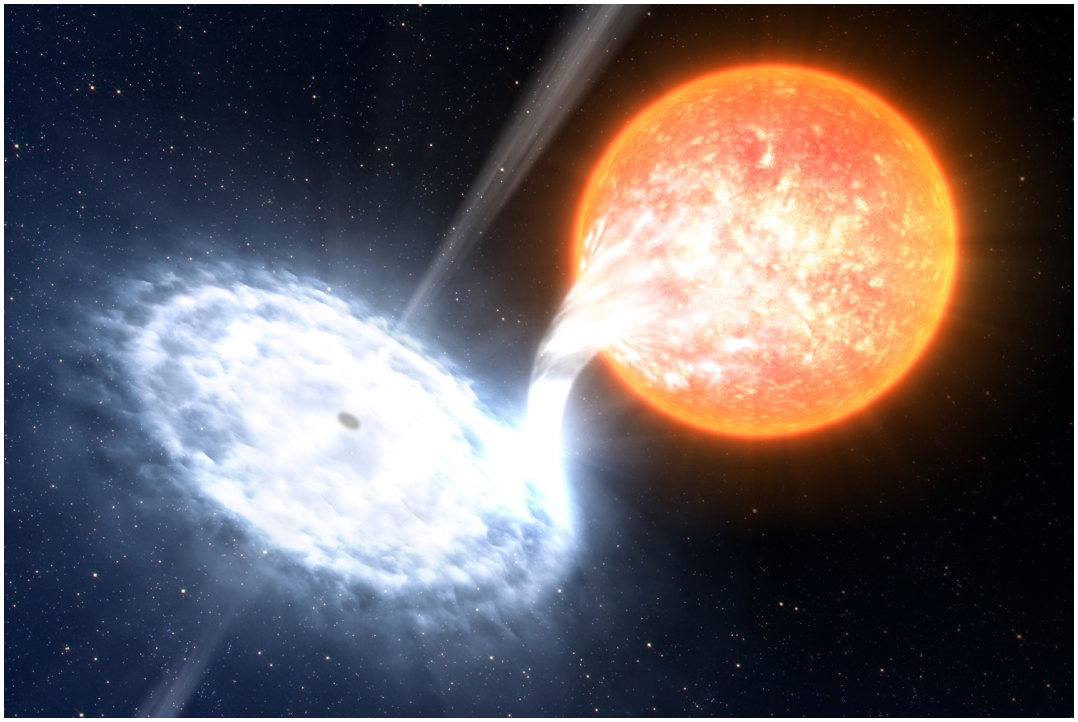

Figure 1.3: An artist's impression of a Low Mass X-ray Binary showing the main components of the system, including an accretion stream extending from the low mass, red companion to the outer edge of a hot, blue accretion disc. Image Credit: ESO/L. Calcada

cause a detectable, periodic modulation of the optical flux and spectra allowing the binary orbital period, and in the case of RV studies the mass ratio, of the system to be determined, as was demonstrated by Wagner et al. (2001) for the 4.1 hr binary XTE J1118+480 using RV measurements of the secondary during an X-ray quiescent state.

Figure 1.3 shows an artist's impression of a LMXB system. An accretion stream is shown being drawn off the cool, red low mass companion and focused through the L1 point in to a hot, blue accretion disc around the compact object. In this example a jet is also seen being launched from the central regions of the accretion disc and the compact object. LMXBs that produce jets can also be bright radio sources whilst the jet is active and are collectively known as 'micro-quasars', being the stellar mass equivalents of their galactic scale cousins, Active Galactic Nuclei (AGN). It should be noted, however, that in the case of LMXBs, NSs can also produce jets and fall into the micro-quasar category (e.g. Sco X-1, Bradshaw, Fomalont, & Geldzahler 1999). Whilst there is a reasonably constant flow of material into the outer regions of the accretion disc from the companion star, the X-ray emission observed from LMXBs is very variable, with both BH and NS systems able to display long periods of quiescence, interspersed with bright outbursts of varying duration and luminosity. The mechanisms that generate outbursts vary depending on the nature of the compact object in the systems. A

brief overview of the most common observational features and the physical interpretations of the behaviour of each source type is given here; however, this does not represent a full and comprehensive overview of this varied and detailed subject.

Thanks to the sensitive, wide field monitoring capability in the X-ray band that was provided by instruments such as the 'All Sy Monitor' aboard the *Rossi X-ray Timing Explorer* (*RXTE*/ASM, (Swank, 2006)) all LMXBs containing a BH (BHXRB) are now known to be transient X-ray sources over a certain time frame. The observed nature of the transient activity varies from source to source with some systems, such as 4U 1630−47 (Tomsick et al., 2005), undergoing outbursts on timescales of weeks to months which are separated by long periods of lower activity or a deep quiescence. Some sources display X-ray outbursts for much longer periods, however, such as GRS 1915+105 which has been continually active since it entered an outburst in 1992 (Castro-Tirado, Brandt, & Lund, 1992). Despite the varied outburst durations and recurrence rates observed in different sources, the monitoring data showed that BHXRBs follow a characteristic flux evolution over the course of their outbursts (Fender, Belloni, & Gallo, 2004). Figure 1.4 is a schematic representation of this characteristic evolution with the upper central panel showing the Hardness - Intensity diagram (HID) of a typical outburst of a BHXRB (Fender, Belloni, & Gallo, 2004).

The canonical interpretation of the evolution observed in the HID is through the varying influence of the two main sources of X-ray photons in a BHXRB as the accretion rate onto the BH changes, namely: a thin, optically thick accretion disc that extends from large radii toward the BH and a hot, optically thin corona that surrounds the BH at smaller radii. At low accretion rates (a few % of the Eddington accretion rate) BHXRBs occupy the 'Hard State' and display unbroken powerlaw spectra up to energies of at least 100 keV that are consistent with the Comptonization of soft photons by the hot, optically thin corona. There is only a small or undetectable contribution to the X-ray spectra from the accretion disc in this state and steady jets are also detected in the radio band (which may also contribute to the detected hard X-ray flux). This behaviour is interpreted as evidence of the accretion disc being truncated at a large distance from the BH at low accretion rates (Narayan, McClintock, & Yi, 1996). A BHXRB will enter an outburst when the accretion rate begins to increase, most likely as the result of a disk instability that releases matter toward the central BH (Dubus, Hameury, & Lasota, 2001). When this happens, the source luminosity increases, initially maintaining a hard spectrum before softening as the accretion disk becomes the dominant spectral component at the highest luminosities. As the X-ray spectrum reaches its softest state the outflow velocity of the jet is observed to increase rapidly, causing a shock induced radio flare as the faster material leaving the base of the jet collides with slower material further along the outflow, before the production of jets ceases and the soft disc component dominates the X-ray spectrum.

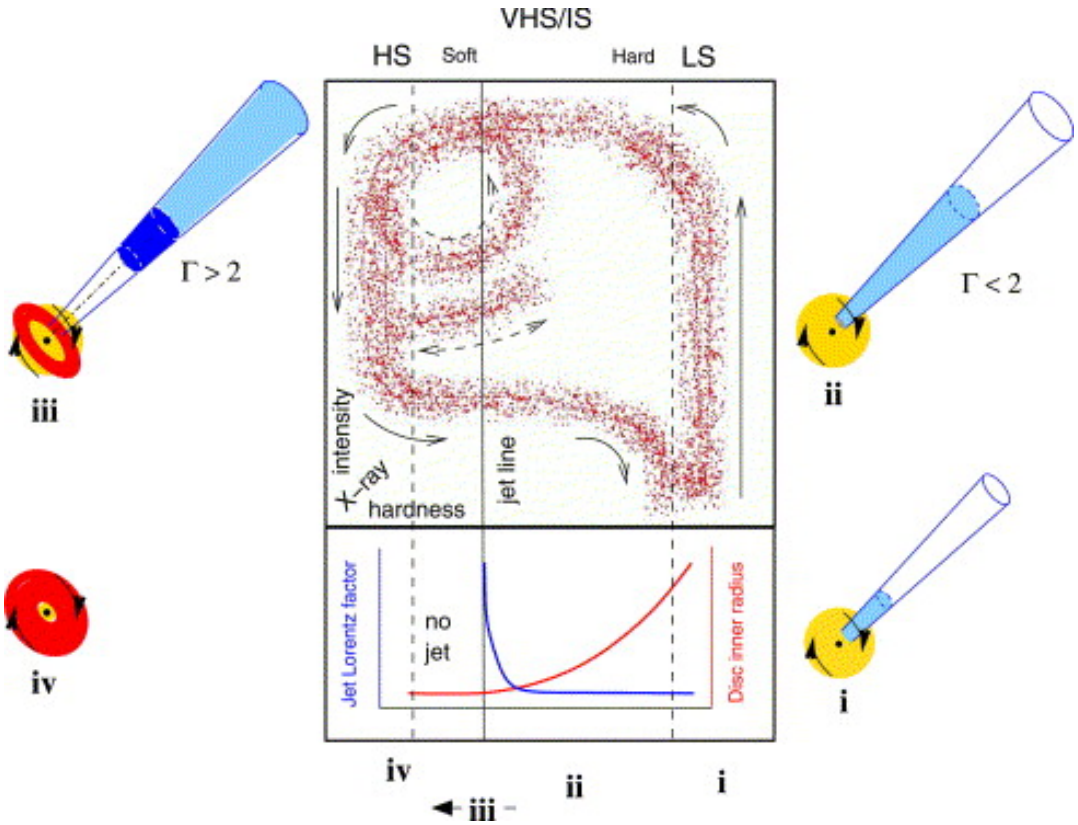

Figure 1.4: A schematic of the BHXRB outburst Hardness - Intensity diagram showing the typical evolution of the X-ray flux during an outburst event (Fender, Belloni, & Gallo, 2004)

This 'disk-jet coupling', uncovered by simultaneous radio and X-ray observations, suggests that as the accretion rate increases, the inner edge of the accretion disc moves towards the Innermost Stable Circular Orbit (ISCO) around the BH, increasing the size and temperature of the soft X-ray production region, whilst, simultaneously compressing the hot coronal material until it is almost entirely ejected along the jet. This process is illustrated by the 'jet line' in Fig. 1.4 which defines the hardness at which the jet's production is 'quenched'. Observationally this is indicated by the cessation of radio emission and the transition to the most disc-dominated X-ray spectral state. The BHXRB remains in this state whilst the accretion rate remains high with jet production inhibited. As the reservoir of material in the outer regions of the accretion disc is depleted, the accretion rate begins to decrease and the inner edge of the accretion disc retreats from the ISCO, reducing the contribution of the soft component to the total spectrum. Finally the source returns to quiescence via the hard state, with its associated steady state jets showing the repopulation of the coronal region, and completes the outburst cycle.

The presence of jets only during the harder X-ray spectral states is suggestive that they are of a coronal origin and are often interpreted under the Magneto Hydrodynamic (MHD) model of jet formation. Under this model the jet is launched from the wound up magnetic field lines that are frozen into the rotating coronal material comprising the inner regions of the accretion flow in the hard state. The jet production is suppressed during the softer X-ray states as the accretion flow is dominated by the thin accretion disc (Meier, Koide, & Uchida, 2001). This interpretation of BHXRB outbursts as the draining of material from an accretion disc after an instability is triggered can also help in understanding the different outburst durations and recurrence frequencies observed in different BHXRBs. The varied orbital dynamics, with orbital periods in the range between 4.1 and 804.0 hr (XTE J1118+480 (McClintock et al. 2001,Wagner et al. 2001) and GRS 1915+105 (Greiner, Cuby, & McCaughrean, 2001a) respectively), and companion stars of spectral types K and M (e.g. Greiner et al. 2001b, Wagner et al. 2001) observed in the confirmed BHXRBs will likely cause significant variation in the mass transfer rate achieved from source to source. Consequently the characteristic timescales required to accumulate enough mass in the accretion disc to trigger an instability, and the amount of time required to drain the accumulated mass from the disc, will also vary from source to source helping to create the distribution of outburst duty cycles observed.

The LMXB population with BH primaries described above are dynamic systems that provide some of the best astrophysical laboratories for testing General Relativity under strong gravity. However, the LMXB population with NS primaries also offer fascinating insights into the physics of matter under extreme physical conditions. Similar to the BHXRBs some NS LMXBs display characteristic X-ray emission states (the so-called 'Z-sources', Hasinger & van der Klis 1989) and also

generate collimated jets that are detectable in the radio band and correlated with the X-ray flux (e.g. GX 17+2, Penninx et al. 1988). Despite the fact that NS LMXB jets are comparatively radio quiet for the observed X-ray luminosities compared to their BH counterparts, their presence alone provides further evidence that the launching mechanism behind jets originates in the accretion flow and is not intrinsic to the compact object. The lack of an event horizon around a NS prevents NS LMXBs from displaying the deep X-ray quiescent states observed in BHXRBs as the accretion flow is observable over its full radial extent, as opposed to the inner regions being lost behind the event horizon as in BHXRBs, and there is an additional emission component from the hot NS surface. In addition to these common behaviours NS LMXBs also display many observational features that are unique to these systems and result from the presence of the solid surface and magnetic field of the NS.

Two observational features that can be observed in NS LMXBs but not in the BHXRBs are Type-I X-ray bursts and coherent X-ray pulsations. Type-I X-ray bursts are mainly observed from NS LMXBs with X-ray luminosities of $> 10^{36}\,\mathrm{erg\,s^{-1}}$, such as GS 1826−238 (Kong et al., 2000), as a direct result of the matter transferred through RLO encountering the solid surface of the NS. As material accretes it accumulates in a layer on the surface of the NS until a critical density is reached and thermonuclear burning is ignited on the surface. The result is a short, intense burst of X-ray radiation that displays a sharp rise ($< 10\,\mathrm{s}$) associated with the thermonuclear burning followed by a longer decay, up to a few minutes, that is consistent with the cooling of the NS surface. Type-I bursts are recurrent on the time scale of hours, the specific value of which is dependent on the specific chemical make up of the accreted material and the rate at which it accumulates on the NS surface in a particular system.

Coherent X-ray pulsations can also be detected in some NS LMXBs resulting from the channeling of incoming material from the accretion disc to the magnetic poles of the NS along magnetic field lines. A more in depth discussion of X-ray pulsars is given in Section 1.2, here it is sufficient to say that the detection of pulsations from an LMXB provides definitive proof that the compact object is a NS as there is no physical mechanism able to produce this type of signal in a BHXRB. The lack of coherent pulsations, however, does not rule out NSs as the compact objects in LMXBs as the prolonged periods of accretion implied by their inhabitation of regions of old stellar populations are likely to have suppressed the magnetic fields of the NS. This suppression is likely the result of either the erosion of the natal magnetic field through the interaction of the magnetic field and plasma in the accretion process or the disruption of the magnetic field carrying fluid within the core of the NS as a result of the spin period evolution experienced by accreting NSs (Bhattacharya & van den Heuvel, 1991). When a NS magnetic field is suppressed below a critical threshold of $\simeq 10^9\,\mathrm{G}$ it is unable to disrupt the accretion flow and

focus it towards the magnetic poles and thus generate the coherent, pulsed X-ray emission (Alpar et al., 1982). Simultaneously the prolonged period of accretion will have transferred large amounts of angular momentum from the companion resulting in the 'spin-up' of the NS to short spin periods. Above a certain threshold spin frequency, matter is prevented from reaching the NS surface and magnetic poles because of a centrifugal barrier. Once a pulsating NS in an LMXB reaches this so-called 'propellor' state (Illarionov & Sunyaev, 1975) the generation of X-ray pulsations will be prevented and the source will switch off as an X-ray source. It is this process of 'spinning up' a neutron star that is believed to generate the population of 'milli-second pulsars' detected within binaries in the radio band (e.g. Thorsett & Chakrabarty 1999). These are the 'recycled' pulsars and are characterised by low magnetic fields $\leq 10^8$ G as a result of the long periods of accretion required to generate the large spin-up of the NS. These pulsars are distinct from the population of young, rotation-powered pulsars which possess high magnetic field strengths ($\geq 10^{12}$ G) and a high spin frequency imparted during the core collapse SN events that lead to their creation, e.g. the Crab pulsar. Confirmation of the recycled pulsar evolutionary mechanism for the generation of the binary milli-second pulsar population was provided with the detection of the first 'accreting milli-second pulsars' which illustrated the action of accretion on to rapidly rotating NSs (e.g. SAX J1808.4−3658, Wijnands & van der Klis (1998); XTE J0929−3314, Galloway et al. (2002)).

The study of LMXBs has helped drive and focus the field of X-ray binary research since the first detection of Sco X-1. However, equally as influential and dynamic are the HMXBs and it is members of this class that are focused on throughout the remainder of this thesis.

1.2 High Mass X-ray Binaries - HMXB

High mass X-ray binaries are some of the most intriguing systems in the Galaxy, combining the most dynamic, massive stars ($M_* > 10\,M_\odot$) with the degenerate remnant of an even more massive companion progenitor. Due to the high mass nature of the companion stars in HMXBs these objects trace out regions of recent star formation in the Galaxy, as the systems should not have been able to move a large distance from their birth locations during the ∼Myr lifespan of the high mass companion. Bodaghee et al. (2012b) recently provided the first statistically significant ($> 7\sigma$ for distances of < 1 kpc) observational evidence of such an association between the locations of HMXBs and OB star forming complexes within the Galaxy and derived an average natal super nova (SN) kick of $100 \pm 50\,\mathrm{km\,s^{-1}}$ for the Galactic HMXB population.

As in the case of LMXBs the evolutionary processes followed by massive binary star

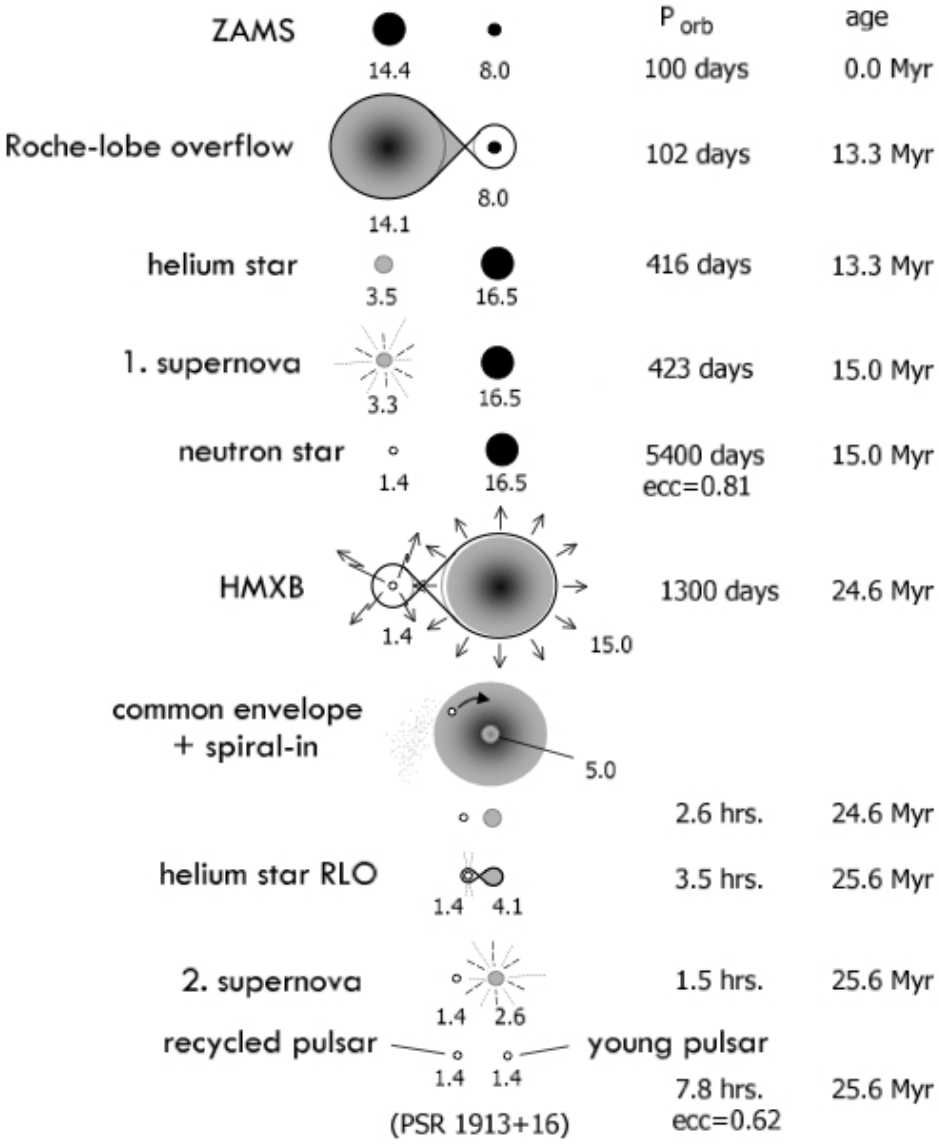

Figure 1.5: An example evolutionary path for a HMXB system that ends its life as a double NS binary (Tauris & van den Heuvel, 2006)

systems to create HMXBs are complex and not fully understood. An example of a possible evolutionary pathway is shown in Fig. 1.5 (Tauris & van den Heuvel, 2006). In this case the massive binary begins its evolution in a wide orbit with the primary approximately twice the mass of the secondary. As the more massive primary evolves off the MS it expands and fills its Roche-lobe, leading to significant mass transfer to the secondary. This process inverts the mass ratio of the binary, leaving the stripped, helium core of the primary in orbit about the more massive companion. Eventually the helium core undergoes a SN explosion, becoming either a NS or BH, and the HMXB phase is initiated when mass transfer from the companion to the compact object begins. The exact nature of the mass transfer in the HMXB phase depends on the initial orbital parameters and stellar masses with some systems accreting from the dense, slow equatorial wind of a MS Be (or Oe) star (BeXRB) and some accreting from the fast, radial wind of an evolved giant or supergiant star (SgXRB, see Sections 1.2.1 and 1.2.2 for further details). Figure 1.5 proceeds to show the evolutionary stages occurring after the HMXB phase as the system undergoes common envelope evolution due to the continued evolution of the companion and finally undergoes a second SN event leaving a double NS binary.

As stated above the exact evolution followed by any particular binary is heavily dependent upon the masses and orbital separation of the components of the original binary. While stellar population synthesis studies increasingly show that the vast majority of high mass stars in the Galaxy are born and evolve as binary systems ($\sim$70%, Sana et al. 2012), there are currently only $\sim$110 HMXBs known in the Galaxy (Liu, van Paradijs, & van den Heuvel, 2006). This therefore illustrates the rarity of progenitor binaries that are able to survive the evolution and SN of the initially more massive component and initiate the HMXB phase. Rarer still are the binaries that also survive a second SN event to evolve into double NS binaries.

Whilst the evolution of each HMXB is different, the overall picture of the evolutionary process can help to understand the observed distribution of compact objects within the HMXB population. 66 of the 114 HMXBs reported by Liu, van Paradijs, & van den Heuvel (2006) are known X-ray pulsars showing that at least 58% of HMXBs contain a NS, a proportion that is likely higher when taking into account undetectable pulsars and non-pulsating NSs, suggesting that a NS is the most common stellar remnant produced in binaries that become HMXBs. The large amount of mass lost by the primary during its evolution (Maeder & Meynet, 2008) and the initial RLO phase may, in many cases, reduce the mass of the primary below the point where a BH can form out of the subsequent SN explosion resulting in the low number of HMXBs with BHs as the compact object. However, as an overlap has been observed in the masses of NSs and BHs determined by dynamical measurements it is likely that the pre-SN core mass is not the only factor in determining the nature of the stellar remnant that is created, with other factors such as the magnetic field and spin of the core possibly playing a major role (Ergma

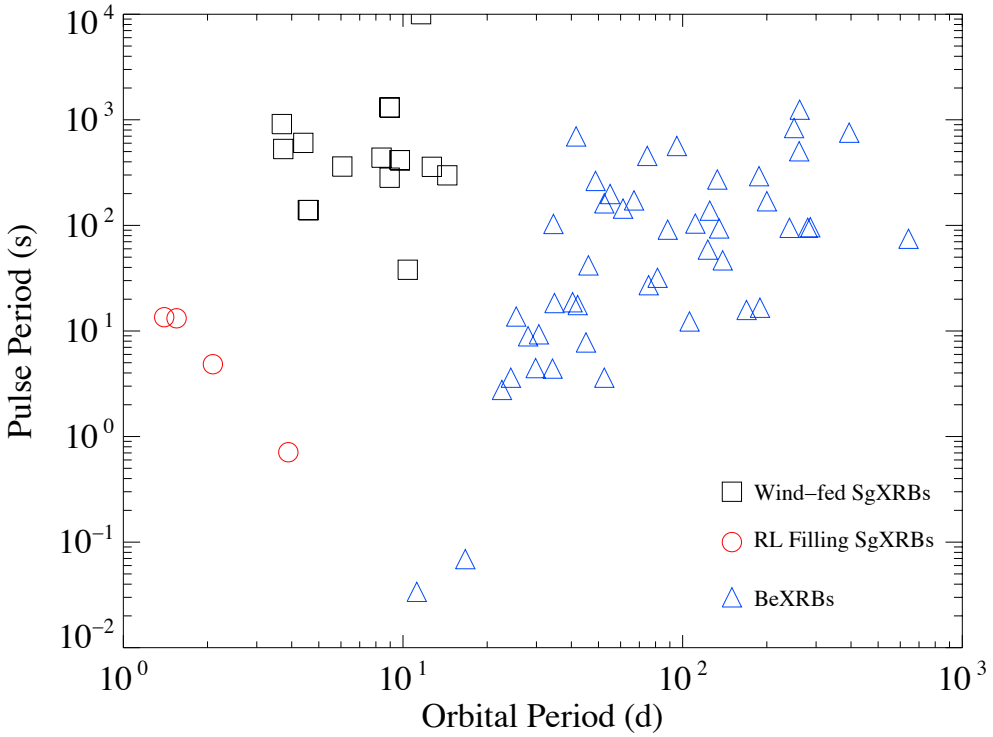

Figure 1.6: The Corbet diagram illustrating the distribution of the different types of HMXB within the $P_{orb} - P_{spin}$ parameter space (Corbet 1986, period data from Liu, van Paradijs, & van den Heuvel 2006 and Bodaghee et al. 2007)

& van den Heuvel, 1998). Belczynski & Ziolkowski (2009) considered the apparent lack of BHs in the BeXRBs specifically (none of the 64 Galactic BeXRBs have a confirmed BH) and concluded from evolutionary scenarios that the expected number of Galactic BeXRBs with a BH as the compact object is only of the order of $0-2$ which is entirely consistent with the Galactic sample. While the predicted number of BHs in BeXRBs is $\sim$30 times less than the number of NS, the number of WD-BeXRBs is predicted to be $\sim$10 times greater than the number of NSs (Waters et al., 1989). However, the predicted X-ray luminosities of these systems are in the range $10^{29} - 10^{33}\,\mathrm{erg\,s^{-1}}$ which, combined with the soft X-ray spectrum produced by WDs and extinction by the interstellar medium, has limited the detection of WD BeXRBs to only a small number of systems to date (e.g. XMMU J010147.5−715550, (Sturm et al., 2012)). In Sg-XRBs, however, the larger mass of the initial primary results in more massive He stars after the primary has undergone mass loss, preventing the creation of WDs in these systems.

The individual types of HMXB can be summarised in terms of their location within the $P_{orb} - P_{spin}$ parameter space, otherwise known as the Corbet diagram (Corbet, 1986). Figure 1.6 shows the Corbet diagram for the Galactic HMXBs that have known orbital and pulse periods (data taken from Liu, van Paradijs, & van den Heuvel 2006 and Bodaghee et al. 2007) and illustrates how the three sub-types of

HMXB are distinct in this space. The BeXRBs are illustrated by the blue triangles and occupy the longer orbital period region of the diagram ($P_{orb} > 10$ days) with pulse periods on the order of $\sim 1 - 1000$s that are correlated with the orbital period of the binary. The Roche-lobe filling SgXRBs occupy the lower left hand region of the diagram with short orbital and pulse periods. Finally the wind-fed SgXRBs occupy the upper region with orbital periods in the region of a few to ~ 10 days and uncorrelated pulse periods. The observational properties of each of these types of HMXB are discussed below along with the physical mechanisms behind the observed $P_{orb} - P_{spin}$ distribution.

1.2.1 Be X-ray Binaries - BeXRB

BeXRBs are HMXBs comprised of a massive B-type emission line star (Be) of luminosity class $III - V$ and a NS in a long (> 10 days) orbit of significant eccentricity. The MS nature of the Be star combined with the long orbits results in the Be star sitting deep within its Roche Lobe, preventing accretion through RLO of the stellar surface. Instead the X-ray emission observed from BeXRBs is generated through accretion from the dense, circumstellar outflow (or decretion disc) produced by the Be star. This feature of Be stars was identified through optical and IR studies which revealed strong, structured Hα emission lines and an IR excess resulting from free-free emission within the decretion disc.

The mechanism, or mechanisms, that produces the circumstellar disc is not totally understood. However, as isolated Be stars are also seen in the Galaxy, the mechanism must be intrinsic to the Be star as opposed to being driven solely through binarity. It is known that the Be stars rotate at speeds that approach their break-up velocities, likely as a result of the mass transfer that occurred during an earlier phase of evolution in the binary case, making the stellar surface unstable. Additionally non-radial pulsations (NRPs) have also been detected in these stars (e.g. Penrod 1986). It is possible that the decretion disc is generated by NRPs providing an added velocity kick to material in the equatorial regions of the star such that this material locally exceeds the break-up velocity and flows off the star into the decretion disc (e.g. Osaki 1999). Optical studies, in particular the structure of the Hα emission line, allow the structure of the decretion disc to be probed and it is observed that the X-ray emission produced at any particular time is inextricably linked to the state of the decretion disc.

In the X-ray band BeXRBs are extremely variable sources showing quiescent emission at the $10^{33}\,\mathrm{erg\,s^{-1}}$ level and rising to approximately Eddington-limited luminosities of $10^{38}\,\mathrm{erg\,s^{-1}}$ during the brightest outbursts. Typically BeXRBs display two types of X-ray outburst, referred to as Type-I (not to be confused with the Type-I X-ray bursts of NS LMXBs) and Type-II, which are related to the state

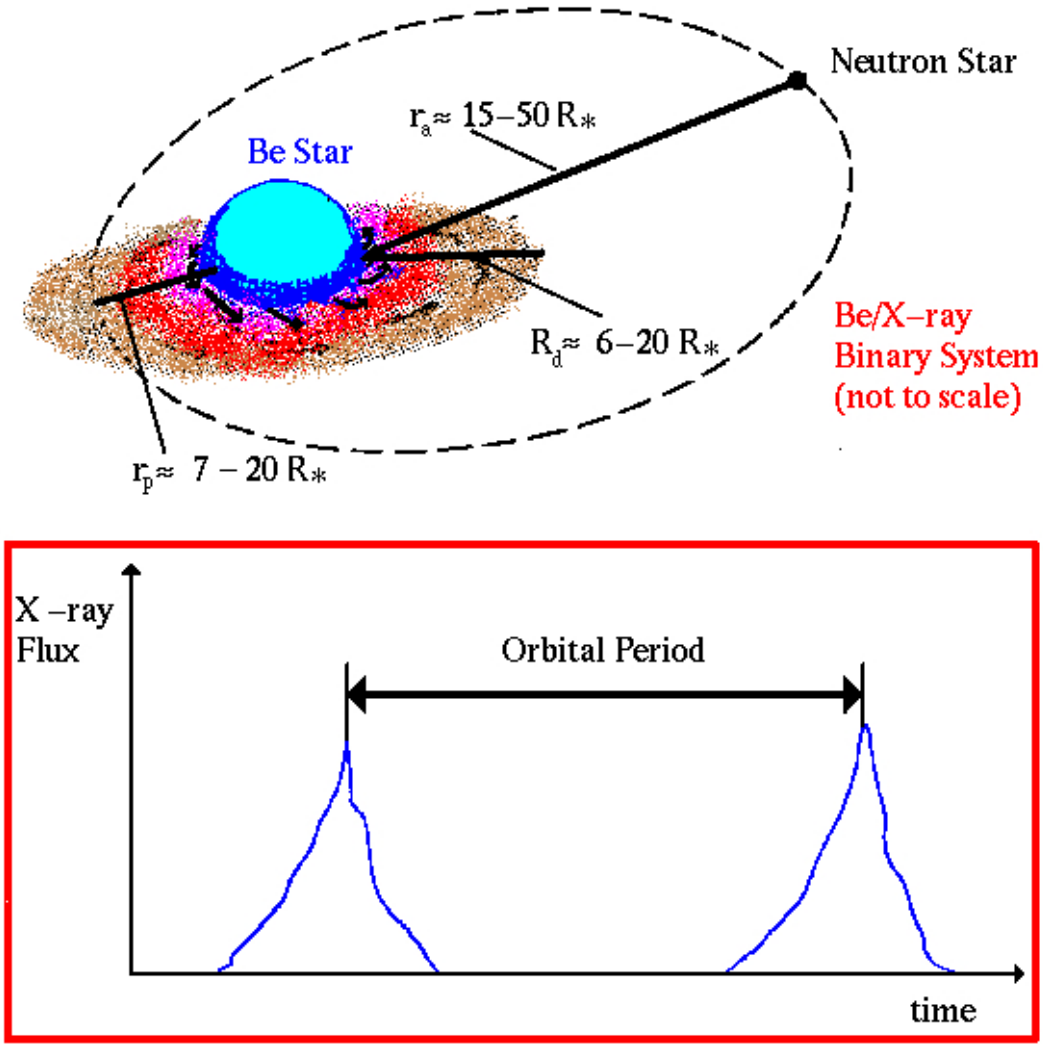

Figure 1.7: Schematic representation of a BeXRB. The NS travels on a long, eccentric orbit and accretes from the decretion disc of the Be star during its periastron passage, producing the Type-I outbursts observed (Image Credit: I. Negueruela, http://www.disc.ua.es/∼ignacio/bex.html).

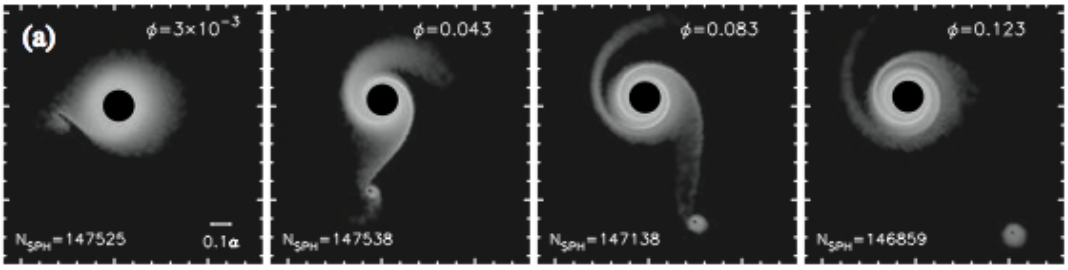

Figure 1.8: SPH simulation of the NS periastron passage in a model BeXRB. The greyscale is the logarithmic density of stellar wind material showing the development of rotating structures in the decretion disc and at the formation of an accretion disc about the NS from the captured wind material (Okazaki & Hayasaki, 2007).

of the decretion disc. Figure 1.7 illustrates the nominal model of a BeXRB and the mechanism behind the Type-I outbursts. Type-I outbursts are detected on an orbital timescale and are generated as the NS interacts with, and accretes from, the decretion disc during its closest approach, generating an increase in the X-ray luminosity to the $\sim 10^{36-37}\,\mathrm{erg\,s^{-1}}$ level. Traditionally this interaction was viewed as the NS 'plunging' through the decretion disc at periastron passage. More recently, however, it has been shown through modelling and simulation that in their nominal states decretion discs do not extend out from the Be star to very large radii but are in fact truncated, through viscous and tidal processes, at certain resonance points between the circular Keplerian orbits within the decretion disc and the binary orbit (Okazaki & Negueruela, 2001). Type-I outbursts are then observed when the L1 point passes through the decretion disc during the NS periastron passage, capturing material with high amounts of angular momentum that forms an accretion disc around the NS and fuels the outburst. A simulation of this process in a model BeXRB, generated using 'Smoothed Particle Hydrodynamics' (SPH) code, is shown in Fig. 1.8 (Okazaki & Hayasaki, 2007). It shows the generation of density structures within the decretion disc due to the NS passage and also the formation of an accretion disc from captured stellar wind material around the NS. The truncation point of the decretion disc extends further out from the companion as the eccentricity of the binary orbit increases, generating regular Type-I events in more eccentric systems whilst prohibiting them in the most circular systems.

In reality, however, only one BeXRB system displays Type-I outbursts during almost every orbit (EXO 2030+375 displayed a Type-I outburst on 87% of periastron passages observed between April 1991 and August 2001, Wilson et al. 2002) whereas most are less regularly recurrent. Okazaki & Negueruela (2001) explain the varying levels of regularity within the BeXRB class as a result of the geometry of the decretion disc. The size of the decretion disc is intrinsically variable and it is also likely to be non-symmetric leading to precessing structures within the outflow ('warped discs'). It is only during periastron passages where the

denser, more extended regions of the disc coincide with the L1 point that a Type-I outburst can be observed, hence reducing the regularity of observed outbursts. This picture is supported by studies of the Hα emission line profile which can show varying strengths in the red and blue wing of the line, indicating structures moving toward and away from the observer in the decretion disc (e.g. Clark et al. (2001)).

Occasionally BeXRBs display bright X-ray emission on time scales significantly longer than the orbital period of the binary, the so-called Type-II outbursts. These events appear to have no correlation with the orbital phase of the binary and the X-ray flux is not modulated on the binary orbit during these states. The outbursts can reach Eddington limited luminosities of several $10^{38}\,\mathrm{erg\,s^{-1}}$ in the brightest cases. Type-II outbursts are correlated with the optical maxima of the systems indicating that the decretion disc is at its most enhanced during these periods. Again the traditional view of these events was that, through a major mass loss event from the Be star, the decretion disc expands to fill the entire binary orbit, hence generating the optical maxima as a result of the larger surface area of the disc, and the NS constantly accretes matter over the course of the outburst. Whilst this model could explain co-planar systems, where the NS orbital and companion star equatorial planes are roughly aligned, it is more difficult to account for inclined systems. Given that Type-II outbursts appear to be a feature of all BeXRBs, whose formation involves complicated mass transfer mechanisms and SN explosions, it is unlikely that every resulting BeXRB is co-aligned, hence a different Type-II mechanism is required to explain all BeXRB systems. Okazaki, Hayasaki, & Moritani (2012) proposed that the Type-II outbursts could be generated as the result of the capture of large amounts of material from a decretion disc that is enhanced in both its spatial extent and density, again producing the optical maxima. The resulting accretion disc that forms around the NS contains more mass and has a longer viscous timescale, fueling the longer, more luminous Type-II outbursts. In the cases of the highest decretion disc densities super-Eddington luminosities can result as supercritical accretion flows are generated by the transit of the enhanced decretion disc.

Okazaki, Hayasaki, & Moritani (2012) point out that the specific observational properties of the Type-I and II outbursts of each BeXRB are heavily dependent on the individual system parameters with the orbital period, eccentricity, tilt angle between the orbital and equatorial planes and structure of the decretion disc being particularly influential. Whilst for most HMXBs the characterisation of their orbits to such high precision is challenging, the Type-II outbursts of pulsating BeXRBs provide an excellent physical laboratory to constrain the physical nature of these systems. As the systems remain bright in X-rays across several orbital cycles the spin period of the NS is detectable across all orbital phases. The frequency of the pulsar is then modulated by the Doppler shift induced by the binary orbit, the modelling of which allows the orbital parameters of the system to be derived.

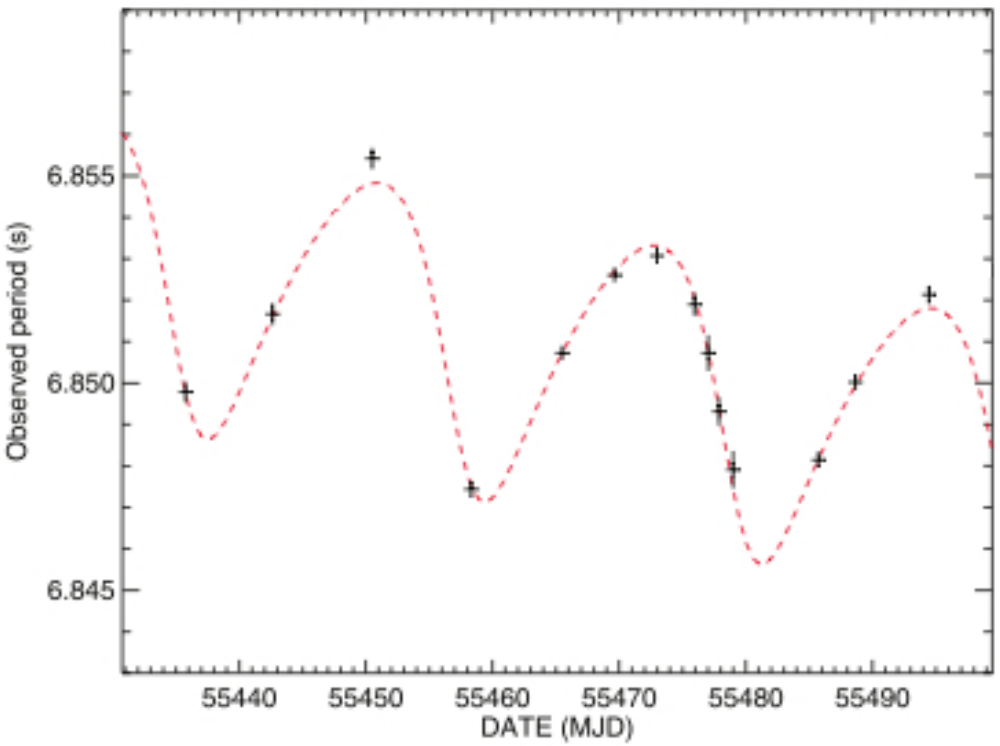

Figure 1.9: The spin period evolution and best fit orbital solution of the SMC BeXRB SXP 6.85 achieved during a Type-II outburst that occurred in August 2010 (Townsend et al., 2011). The Doppler induced variations in the detected spin period and the accretion driven 'spin-up' of the NS are clearly observed.

Additionally over long outbursts and/or the consideration of multiple outbursts the rate of change of the spin period can be measured ($\dot{P}_{spin}$). Well determined $\dot{P}_{spin}$ values provide observational evidence of an accretion disc forming during the outbursts of BeXRBs, as a coherent increase in the frequency of a pulsar can only be achieved by the effective transfer of angular momentum from captured stellar wind material to the NS through an accretion disc. Figure 1.9 illustrates the orbital solution derived for the SMC BeXRB SXP 6.85 achieved during a Type-II outburst observed by *RXTE* during August 2010 where the accretion driven 'spin-up' of the NS is clearly observed (Townsend et al., 2011).

As BeXRBs are the most numerous class of HMXB they can also be considered as a population as well as individual sources. Currently there are $\sim$70 Galactic BeXRB systems (Liu, van Paradijs, & van den Heuvel, 2006) along with $\sim$90 and $\sim$35 BeXRBs in the Small and Large Magellanic Clouds respectively (SMC, LMC, Liu, van Paradijs, & van den Heuvel 2005). It is worth noting that the BeXRB population of the SMC is strongly in excess of that expected from the relative mass ratio of the Milky Way to the SMC (100:1). Under this ratio only $\sim$1-2 HMXBs would be expected in the SMC, and even taking into account the low metallicity environment present there, this number would not be expected to exceed $\sim$10 (Dray, 2006). The widely accepted origin of this anomalously large population of HMXBs is a burst of star formation initiated by the last closest approach of the SMC to the LMC $\sim$100 Myr ago (Gardiner & Noguchi, 1996). The LMC HMXB population on the other hand is in line with what would be expected given its mass ratio in relation to the Milky Way (10:1) suggesting that the more massive LMC was relatively unperturbed by the interaction.

The distribution of BeXRBs on the Corbet diagram (Fig. 1.6, Corbet 1986) shows a correlation between the orbital and spin periods of the systems where both of these parameters have been identified. No such correlation is observed for the wind-fed SgXRB population. The origin of this correlation is believed to result from the magnetic fields of the NSs. A fuller description of the accretion regimes achieved in HMXBs is given in Section 1.2.2 below. Here it is sufficient to point out that transferred material can only be accreted onto the NS in a HMXB if the edge of the magnetosphere, the point at which the magnetic and plasma energy densities are equal, does not extend beyond the co-rotation radius, the radius at which the local Keplerian orbital velocity is equal to that of the rotating magnetosphere. The ambient gas pressure experienced by the NS will likely be lower in longer orbits which allows the magnetosphere to expand to larger radii. Hence for accretion to occur and X-rays to be generated in longer orbital period systems the NS must possess a longer spin period such that the co-rotation radius also extends further from the NS. Conversely it can be viewed that NSs with shorter spin periods will have smaller co-rotation radii and hence a higher ambient gas pressure is required to compress the magnetosphere sufficiently to allow accretion to occur, a situation

that is only satisfied in systems with shorter orbital periods.

Finally Knigge, Coe, & Podsiadlowski (2011) have utilised the BeXRB pulsar population to identify two separate distributions of X-ray pulsar within this population. Statistically significant signatures of these sub-populations were observed in the combined Galactic and LMC sample, SMC sample and total BeXRB pulsar sample as is shown in Fig. 1.10. The authors suggest the separate populations as a signature of different NS production channels with electron capture SN events creating systems with short orbits, spins and lower eccentricities whereas iron core collapse SN events create systems with longer, more eccentric orbits and longer spin periods. The suggested difference in the characteristic eccentricity of the two populations, which was shown to be marginally significant in the small sample of systems with an accurately determined eccentricity, can be explained by the different SN kicks that are expected in the two formation channels, with electron capture SN having lower and iron core collapse SN having higher kick velocities. Observational evidence of SN kicks aids in confirming the given explanation for the tight range of companion spectral types present in BeXRBs where there are no companions of spectral type later than B2 (Negueruela, 1998). This is possibly due to the fact that binaries comprised of a companion of spectral type B3 or later are likely to be disrupted by the first SN event even if only minimal velocity kicks are imparted on the binary (van Bever & Vanbeveren, 1997).

BeXRBs have shown themselves to be excellent probes of stellar physics and massive star evolution in high mass binaries through their large population and luminous X-ray behaviour. Beyond the BeXRBs, however, are the SgXRBs which constitute the highest and most extreme end of the mass distribution of X-ray binaries. It is on these enigmatic systems that this thesis now focuses.

1.2.2 Wind-fed Supergiant X-ray Binaries - SgXRB

X-ray binaries containing a supergiant star are the most extreme X-ray binary end point in the evolution of a massive binary system. The mass transfer in SgXRBs is driven, in the majority of cases, through accretion from the fast, radially outflowing stellar wind of the supergiant companion. It is these 'wind-fed' SgXRBs that are considered in detail here whereas Section 1.2.3 below highlights the small number of cases in which the mass transfer occurs instead through full RLO.

The wind-fed SgXRBs are detected as persistent X-ray sources at luminosities of $\sim 10^{36}\,\mathrm{erg\,s^{-1}}$ that display a moderate level of flux variability, nominally displaying an X-ray dynamic range of $\sim$10. Until recently SgXRBs appeared to be a minor sub-population of HMXBs in comparison to the BeXRBs with only 5 confirmed systems in the Galactic catalog of Liu, van Paradijs, & van den Heuvel (2000) (compared to the 54 confirmed BeXRBs). However, with the launch of the

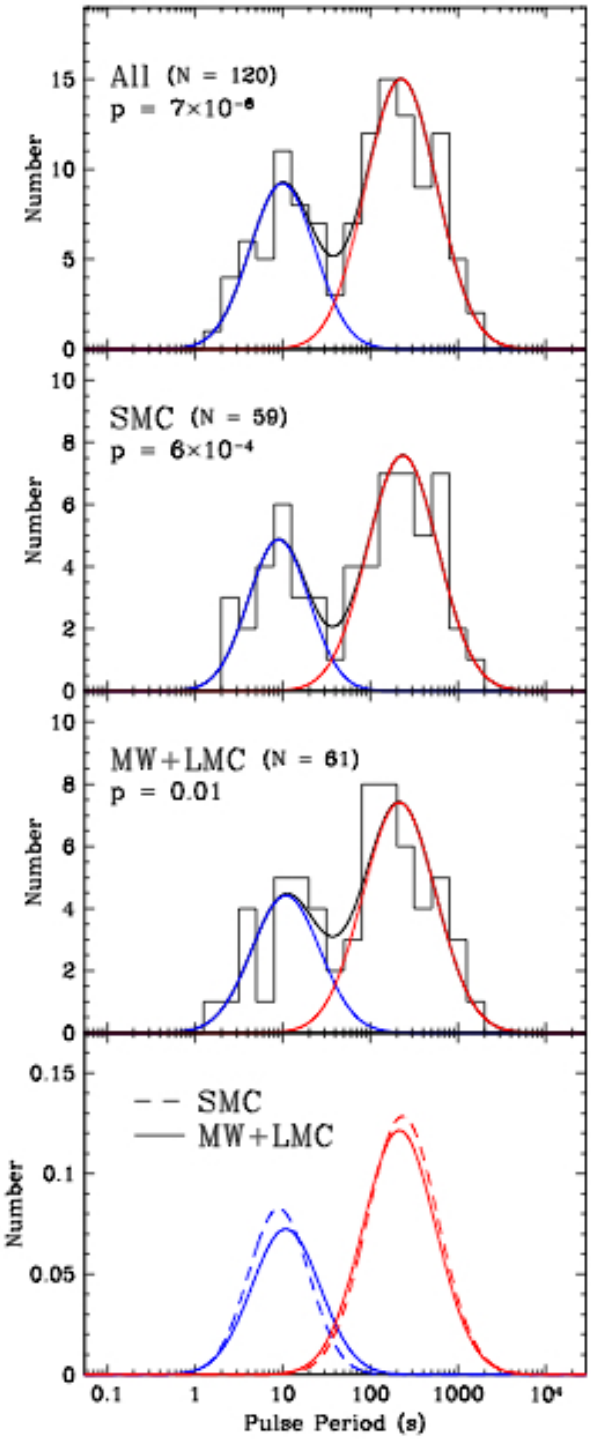

Figure 1.10: The distribution of NS spin periods in the different samples of BeXRBs (top: all BeXRB pulsars; second: SMC pulsars; third: Galactic and LMC pulsars; bottom: over plotted distributions) illustrating the two sub-populations of BeXRB pulsars possibly indicating formation through different SN channels (Knigge, Coe, & Podsiadlowski, 2011).

INTEGRAL satellite (Winkler et al., 2003) providing high sensitivity, wide field coverage of the Galactic Plane in the $15\,\mathrm{keV} - 10\,\mathrm{MeV}$ band with the IBIS instrument (Ubertini et al., 2003), the picture began to change. One of the major scientific achievements of the *INTEGRAL* mission has been the unveiling of two new populations of SgXRB thanks to the removal of the effects of absorption at higher energies and the regular wide field monitoring: the highly absorbed SgXRBs and the Supergiant Fast X-ray Transients (SFXT). The highly absorbed systems were previously hidden from the view of earlier soft X-ray telescopes through high levels of absorption intrinsic to the system, the most extreme case being IGR J16318−4848 which displays N_H column densities of at least $10^{24}\,\mathrm{cm}^{-2}$ (Matt & Guainazzi, 2003), but were easily detectable in the the IBIS band. The SFXTs, however, were detected thanks to the regular monitoring of the Galactic Plane which allowed the identification of the fast flaring behaviour that has come to characterise this class. As these sources are the main focus of this thesis a full history and description is given in Section 1.3. The impact of these discoveries was quickly felt with the number of SgXRBs increasing to 30 in the Galactic HMXB catalog of Liu, van Paradijs, & van den Heuvel (2006) (representing an increase from 4% to 26% of the total number of HMXBs) forming the basis of a SgXRB population as opposed to the small number of individual sources (i.e. Vela X-1, 4U 1700−377) that had been known previously.

The X-rays generated in SgXRBs come from the compact object accreting from the dense, supersonic wind of the supergiant companion star. The high level of mass loss from OB stars is driven by the radiation pressure exerted on the stellar atmosphere from the intense continuum produced by the star. In particular it is the force applied to the spectral lines of heavier elements such as Nitrogen and Oxygen at UV energies that acts to generate the outflow of material from the stellar surface (Lucy & Solomon, 1970). Castor, Abbott, & Klein (1975) developed this model by taking into account the influence of local velocity gradients on the generated force and concluded that the stellar wind in massive OB stars is supersonic, with terminal velocities in excess of $1000\,\mathrm{km\,s}^{-1}$, and drives significant mass loss rates of $\sim 10^{-6}\,\mathrm{M}_{\odot}\,\mathrm{yr}^{-1}$. Also known as the CAK model, this work predicted that mass loss through a stellar wind could significantly affect the evolution of massive stars, removing up to 25% of the stellar mass during the Hydrogen burning phase. In the SgXRB case this stellar wind driven mass loss provides the matter that is accreted by the orbiting NS creating the observed X-ray source, as illustrated in the artist's impression shown in Fig. 1.11.

The material accreted from the fast, radial wind of the supergiant stars in SgXRBs possesses little angular momentum removing the requirement for an accretion disc to form in these systems. Instead the stellar wind material is accreted through the 'Bondi-Hoyle' scenario (Bondi & Hoyle, 1944). Under this model the stellar wind material flows past the NS at supersonic speeds creating a bow shock that precedes

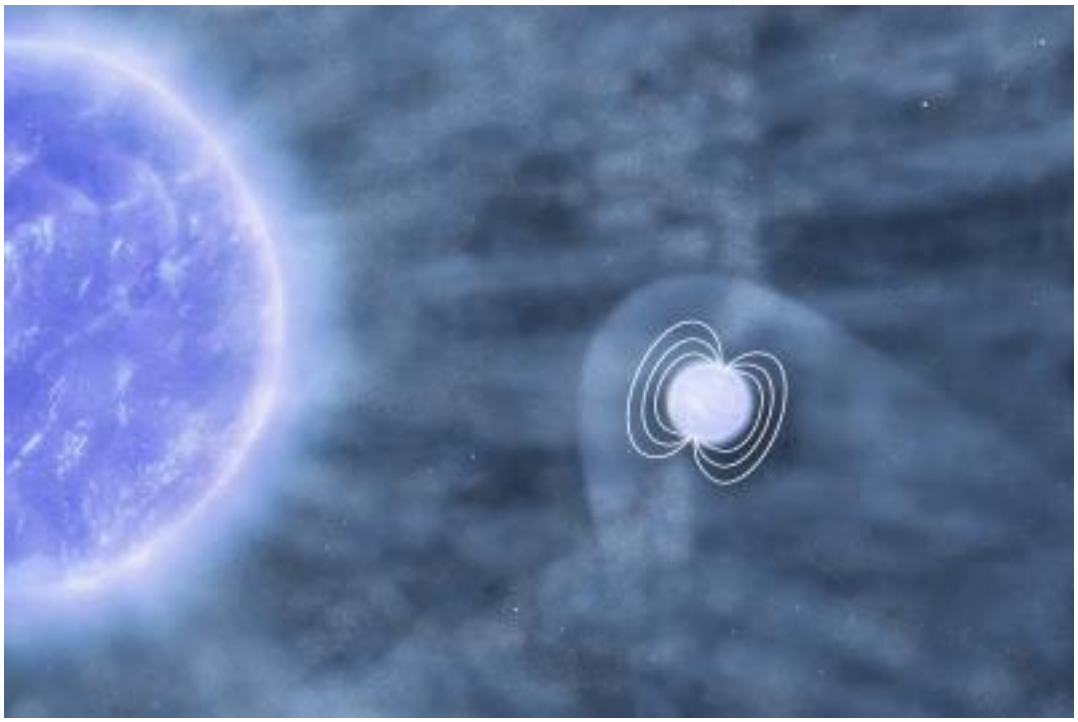

Figure 1.11: An artist's impression of a NS orbiting in the fast, radial stellar wind of its supergiant companion. Image credit: ESA/AOES Medialab.

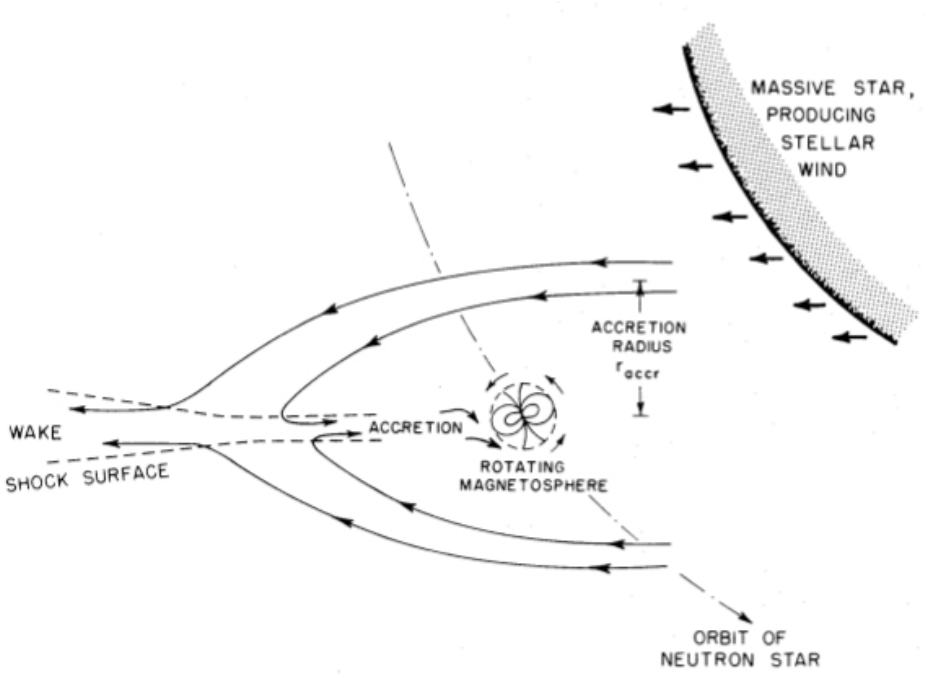

Figure 1.12: A schematic representation of a NS accreting from the dense, radial wind of a supergiant companion as presented in Davidson & Ostriker (1973).

the NS. Within a certain radius, however, the stellar wind material is deflected by the gravitational potential of the NS, colliding in a shocked tail region that trails the NS before descending in the gravitational potential. A schematic representation of this process is shown in Fig. 1.12 (Davidson & Ostriker, 1973) and a two dimensional 'gas dynamics' simulation of a NS orbiting in the equatorial plane of a supergiant companion is shown in Fig. 1.13, illustrating the shocked tail region trailing the NS that is generated in a variety of short, circular orbits (Blondin, Stevens, & Kallman, 1991). Interestingly these plots show the development of features related to a 'Transitional Roche Lobe Overflow' (TRLO) regime at the smallest orbital separations (see below for further details).

The radius about the NS within which the stellar wind material is gravitationally deflected and focused towards the NS is known as the 'accretion radius' and is defined as:

$$R_{acc} = 2GM_{NS}/v_{rel}^2 \tag{1.1}$$

where M_{NS} is the mass of the NS and v_{rel} is the relative velocity between the NS orbital and stellar wind radial velocities, which is calculated as $v_{rel} = \sqrt{v_{NS}^2 + v_w^2}$ for a circular system[1]. A first order approximation of the X-ray luminosity generated by wind accretion can then be made by assuming all the material captured by the accretion radius efficiently falls to the surface of the NS as $L_X = GM_{NS}\dot{M}_{capt}/R_{NS}$. However, the NSs in HMXBs have only been accreting for a relatively short period (∼Myr) and retain strong magnetic fields on the order of 10^{12} G. Hence the captured material will not be able to free-fall all the way to the NS surface but will first encounter the magnetosphere of the NS. If the plasma is able to enter the magnetosphere it latches on to magnetic field lines and is funnelled towards the magnetic poles of the NS, forming a hot 'accretion column' directly above the NS surface that generates the X-ray emission. If the NS rotational and magnetic axes are not aligned and the system is at an appropriate inclination to the observer, the X-ray source is detected as a pulsar as the accretion columns sweep through the line of sight. The exact nature of the interaction between the plasma and magnetosphere in an accreting NS and its influence on the observed X-ray radiation remains one of the most challenging areas of the study of HMXBs.

[1] formally the relative velocity is calculated as the vector product of the two velocities which reduces to the given expression in the case of circular orbits as the velocities are always perpendicular, whereas in an eccentric system the angle between the orbital and stellar wind velocities at all orbital phases must be considered

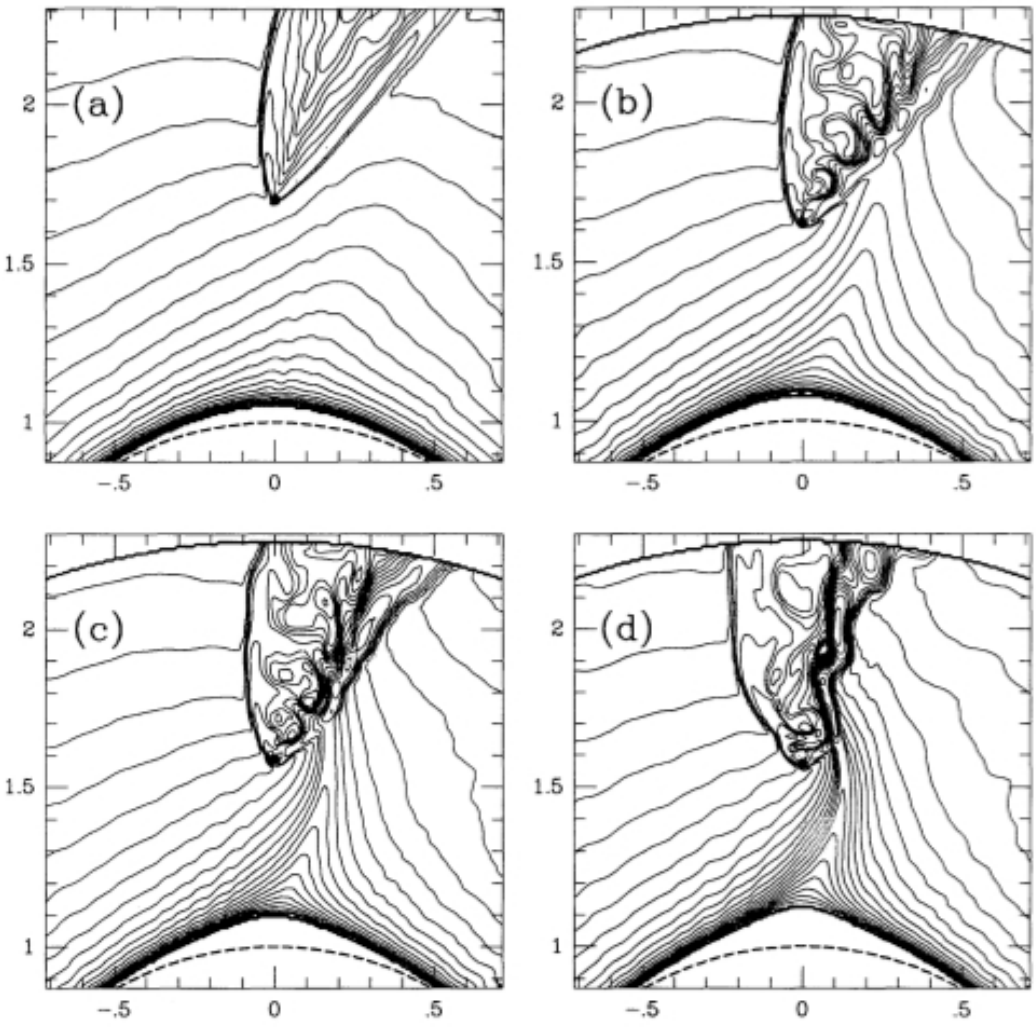

Figure 1.13: Density contour maps of the matter distribution about the NS in a wind-fed SgXRB showing the shocked region downstream of the NS (Blondin, Stevens, & Kallman, 1991). The four panels show the matter distribution as a function of decreasing orbital separation ($a/R_* = 1.57$ in panel (d)) and a tidal stream of material from the supergiant is seen to form with increasing strength at the shorter orbital separations. The development of such a stream is also known as accretion through 'Transitional Roche Lobe Overflow'.

Accretion Regimes

Stellar wind material deflected and focused towards the NS within the accretion radius descends within the gravitational potential until it encounters the NS magnetosphere. The captured material then enters the magnetosphere through dynamical instabilities occurring at the edge of the magnetosphere, the 'magnetic radius', the dominant method of which is dependant upon several factors such as the nature of the flow of the material, the NS spin period and the strength of the NS magnetic field. The two main instabilities believed to be at work in accreting X-ray pulsars are the Rayleigh-Taylor Instability (RTI, also known as the interchange instability, Arons & Lea 1976) whereby the accretion flow is the denser fluid atop the less dense fluid of the magnetosphere (as the magnetic field has a pressure and an associated density) and the Kelvin-Helmholtz Instability (KHI) generated by the shear velocity between the rotating magnetosphere and the captured wind material (Burnard, Arons, & Lea, 1983). The regimes where these different instabilities operate was recently considered by Bozzo, Falanga, & Stella (2008a) who postulated different accretion scenarios using the relative positions of the characteristic radii about a NS (Stella, White, & Rosner, 1986), namely: the accretion radius R_a, the magnetic radius R_M and the co-rotation radius R_{co}. Conversely Shakura et al. (2012) (further developed in Shakura et al. (2013)) propose that different accretion regimes could be realised as a result of different processes cooling the accretion flow and influencing the efficiency of matter penetration of the magnetosphere. A brief overview of these two models is given here but the reader is referred to the relevant works for a full description of the models.

The three characteristic radii defined in the model of Bozzo, Falanga, & Stella (2008a) are the accretion radius which defines the extent of the gravitational influence of a NS, the magnetic radius which determines the fullest extent of the magnetosphere and the co-rotation radius defining the point whereby the angular velocity of the rotating magnetosphere is equal to the local keplerian velocity of a circular orbit. R_{acc} is defined in Eq. 1.1, the relation for R_M is given by Davies & Pringle (1981), in the case of $R_M > R_{acc}$, as:

$$R_M = 3.3 \times 10^{10} \dot{M}_{-6}^{-1/6} v_8^{-1/6} a_{10d}^{1/3} \mu_{33}^{1/3} cm \tag{1.2}$$

where $\dot{M}$ is the mass loss rate of the supergiant, v is the relative wind velocity, a is the semi-major axis of the orbit and μ is the magnetic moment of the NS in the order of magnitude unit system of Bozzo, Falanga, & Stella (2008a), and R_{co} is given by:

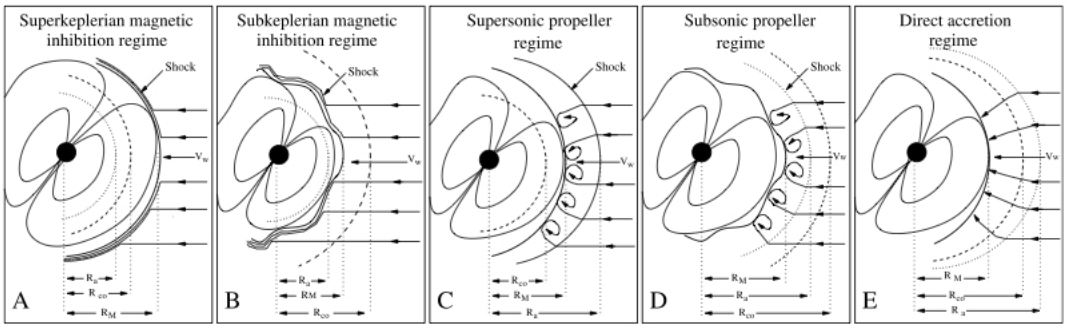

Figure 1.14: Schematic view of the different accretion regimes that can be generated by changing the relative positions of R_a, R_M and R_{co} (Bozzo, Falanga, & Stella, 2008a).

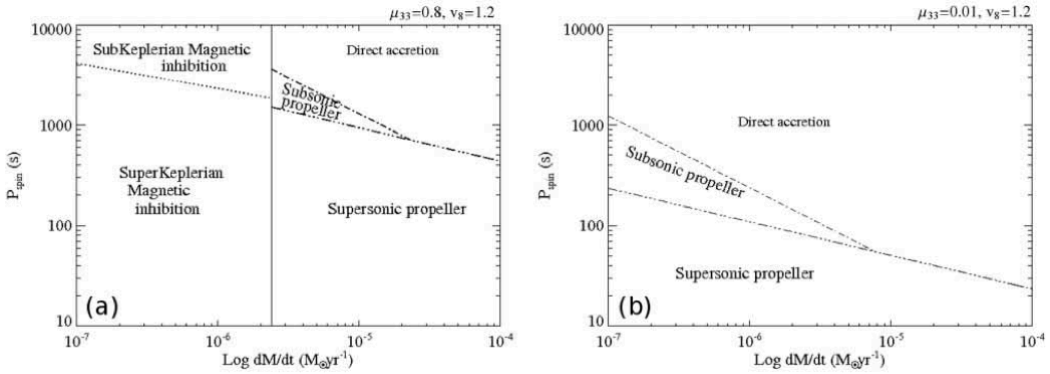

Figure 1.15: The accretion regimes of Fig. 1.14 occupied by NSs with magnetic fields of 2×10^{14} G (left) and 2×10^{12} G (right) orbiting a stellar wind with velocity 1200 km s^{-1} in the parameter space: $10 < P_{spin} < 10000$ s and $10^{-7} < \dot{M} < 10^{-4}$ $M_{\odot}yr^{-1}$ (Bozzo, Falanga, & Stella, 2008a).

$$R_{co} = 1.7 \times 10^{10} P_{s3}^{2/3} cm \tag{1.3}$$

where P is the spin period of the NS in the same order of magnitude units. Figure 1.14 illustrates the accretion regimes achieved by the five different possible configurations of these radii and Fig. 1.15 illustrates which regimes can be occupied by NSs with magnetic field strengths of 2×10^{14} G (left) and 2×10^{12} G (right) orbiting in a stellar wind of velocity 1200 km s^{-1} for NS spin periods in the range $10 < P_{spin} < 10{,}000$ s and supergiant mass loss rates of $10^{-7} < \dot{M} < 10^{-4}$ $M_{\odot}yr^{-1}$ (Bozzo, Falanga, & Stella, 2008a).

At the highest luminosities of $\sim10^{37}$ erg s^{-1} NSs occupy the 'direct accretion' regime (panel E of Fig. 1.14) where the shocked plasma outside of the magnetosphere cools efficiently (likely through Compton processes due to the intense photon field produced by the X-ray source (Shakura et al., 2013)) and the material is efficiently transported through the magnetosphere such that it is

essentially in free-fall and the X-ray luminosity directly traces the mass capture rate (otherwise known as Supersonic Bondi accretion). However, as can be seen from Fig. 1.15, the region of parameter space where direct accretion occurs is quite limited, especially for observationally justified supergiant mass loss rates of up a few $10^{-6}\,\mathrm{M}_{\odot}\,\mathrm{yr}^{-1}$, suggesting that most wind-fed SgXRBs accrete through an inhibited regime. Additionally the lack of multiple order of magnitude flux variations in wind-fed SgXRBs with short orbital periods is also indicative of the fact that the luminosity generated in these systems does not directly trace the gas density of the stellar wind (see below). Under this model the inhibited accretion regimes come in two forms, the magnetically inhibited regimes (panels A and B of Fig. 1.14) and the centrifugally inhibited regimes (panels C and D). Which of these types of inhibition are at work in any particular system depends on the relative positions of the magnetic and accretion radii.

In situations where $R_M > R_{acc}$ the stellar wind material impacts directly on the magnetosphere in a supersonic manner as there has been no gravitational focusing prior to the interaction with the magnetosphere. If R_M is also larger than R_{co} then the material cannot enter the magnetosphere and accretion is completely impeded (although a low X-ray luminosity is generated by the supersonic shock at the magnetopause). Whereas if R_M is smaller than R_{co} then the material can enter the magnetosphere through the KHI allowing the generation of X-rays. These 'magnetically gated' regimes are more likely to occur in systems with higher B-field NSs, which acts to expand the magnetosphere, and faster stellar winds, which reduce the radial extent of the gravitational influence of the NS. On the other hand, in systems where $R_M < R_{acc}$, the stellar wind material is first gravitationally focused and shocked at the accretion radius and descends towards the magnetosphere in a turbulent tail trailing the NS (e.g. Fig 1.13). When the X-ray luminosity is not high enough to allow direct accretion to occur, the in-falling stellar wind material is stopped at the NS magnetosphere and redistributes itself into a quasi-spherical layer that resembles an atmosphere around the NS (Davies & Pringle, 1981). If R_M is larger than R_{co} then matter cannot penetrate the magnetosphere and is expelled, through bulk motions in the atmosphere generated by the extraction of the NSs rotational energy and leading to the 'spin-down' of the pulsar. This is the 'propellor mechanism' described by Illarionov & Sunyaev (1975) during which no accretion occurs and a NS cannot be an X-ray source. Finally if R_M is smaller than R_{co} then the captured material still forms a convective atmosphere around the magnetosphere but the base of the atmosphere is susceptible to KHIs allowing plasma to enter the magnetosphere and generate X-rays. This is the 'Subsonic Propellor regime' and the luminosity generated by the KHI in this case was first evaluated by Bozzo, Falanga, & Stella (2008a). These centrifugally inhibited regimes are more likely to occur in systems where the NS B-field is lower and the stellar wind slower such that the magnetosphere has a reduced size and the

gravitational influence of the NS is experienced out to greater radii.

The model described above attempts to explain all possible accretion regimes over a wide parameter space using a well established theoretical framework (Illarionov & Sunyaev 1975, Davies & Pringle 1981, Stella, White, & Rosner 1986). However, this framework is based upon considerations of systems where an accretion disc forms from the captured matter (i.e. RLO SgXRBS and BeXRBs). Therefore whilst it is an informative model to consider a wide range of possible accretion regimes under, its applicability to wind-fed SgXRBs has to be considered. In particular the influence of the co-rotation radius in many SgXRBs is uncertain as the shocked, turbulent material of the accretion flow will not be following Keplerian orbits when interacting with the magnetosphere. Shakura et al. (2012) also noted that in the case of slowly rotating pulsars (i.e. the wind-fed SgXRBs) $R_{co} >> R_M$ such that the angular momentum transfer between the in-falling plasma and the magnetosphere always occurs a large distance from the co-rotation radius, preventing R_{co} from having a strong influence on the accretion regimes realised about these NSs.

Shakura et al. (2012) instead propose that in the case of slowly rotating pulsars undergoing quasi-spherical accretion it is the impact of different plasma cooling regimes that could define the different accretion scenarios. As in the case of Bozzo, Falanga, & Stella (2008a) a direct accretion regime is also realised in the model of Shakura et al. (2012) for systems at high X-ray luminosities as Compton processes rapidly cool the in-falling plasma, allowing it to travel at supersonic speeds and efficiently enter the magnetosphere via RTIs. At more commonly observed luminosities in wind-fed SgXRBs (a few $10^{36}\,\mathrm{erg\,s^{-1}}$) the plasma is not cooled rapidly enough by the photon field to initiate direct accretion and the plasma instead descends as a hot, subsonic flow that forms an atmosphere around the magnetosphere. Material is then able to enter the magnetosphere through RTIs in the magnetospheric equatorial plane of the NS through the cooling of the base of the atmosphere. This cooling proceeds via Compton processes at higher luminosities and radiative processes once the X-ray luminosity decreases below a critical value (L_{crit}) of $\sim 3\times10^{35}\,\mathrm{erg\,s^{-1}}$. The switch from Compton dominated to radiatively dominated cooling is argued to originate from a change in the beam pattern of the pulsar. At higher luminosities the accretion column is optically thick and the X-ray radiation is scattered in a 'fan-beam' with a wide opening angle, illuminating large areas of the magnetosphere and generating efficient Compton cooling in the magnetic equatorial region. Below L_{crit} the accretion column becomes optically thin and the majority of the X-ray photons produced escape in a narrow 'pencil-beam' that is unable to illuminate the magnetospheric equator, choking off the supply of seed photons for Compton Cooling to proceed. Instead the plasma cools less efficiently through radiative processes (bremsstrahlung). In this state the cooling process is insensitive to small variations in the X-ray luminosity and accretion occurs at a steady rate for a wider range of external conditions. A schematic

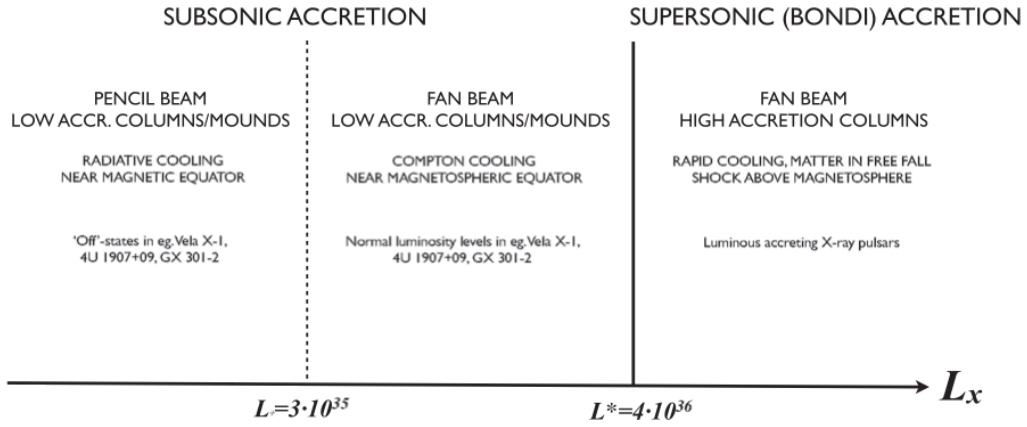

Figure 1.16: The accretion regimes possible for a slowly rotating NS under the 'Quasi-Spherical Accretion' model of Shakura et al. (2013).

representation of the X-ray producing regimes in this model is shown in Fig. 1.16.

If a NS was accreting from a homogeneous medium then it would only be able to switch accretion regimes on an evolutionary timescale as the spin-up/down of the NS slowly changed R_{co} and, in the case of an accreting regime, the magnetic field of the NS was slowly diminished, decreasing R_M. However, the stellar winds of supergiant stars occupied by the NSs in SgXRBs are highly inhomogeneous, as outlined in the next section, possibly allowing for the switching of accretion regimes on short timescales due to the intrinsic variability of the plasma interacting with the magnetosphere. The 'X-ray off-states' observed in the light curves of the wind-fed SgXRBs Vela X−1, GX 301−2 and 4U 1907+09 are believed to be generated by such accretion regime switches. During these states the X-ray flux rapidly drops by a factor of several tens from the nominal level but, crucially, X-ray pulsations are still detected (as observed by *Suzaku*) indicating that matter is still entering the magnetosphere at these times (Doroshenko, Santangelo, & Suleimanov 2011, Doroshenko et al. 2012). Doroshenko, Santangelo, & Suleimanov (2011) suggested that a switch from the 'Direct' to 'Subsonic Propellor' accretion regimes of the Bozzo, Falanga, & Stella (2008a) model is the source of the 'X-ray off-states' observed in these systems. Shakura et al. (2013), however, used the luminosities and variations in the pulse profile of Vela X-1 in the different emission states to argue that a switch from the Compton-cooled to radiatively-cooled accretion regimes under the Quasi-spherical accretion model is the cause of the off-states observed in these wind-fed SgXRBs. In both cases the earlier interpretation of Kreykenbohm et al. (2008), who, using less sensitive *INTEGRAL* data, concluded that Vela X−1 entered the propellor regime and accretion was completely impeded during the off-states, is ruled out.

The structure of supergiant stellar winds

That the stellar winds of massive stars are inhomogeneous has long been predicted by theory. The radiation pressure powered stellar winds of the CAK model were suggested to have unstable solutions by Lucy & Solomon (1970) which would result in shocks within the wind such that it developed into a population of dense clumps (Lucy & White, 1980). By performing simulations of the evolution of wind instabilities, Owocki, Castor, & Rybicki (1988) demonstrated that small variations in the velocity at the base of the wind creates a high level of structure at larger radii with dense, slow moving shells being interspersed with tenuous, high velocity regions with strong shocks being generated at the boundaries between these layers. Significant levels of structure are predicted to extend out to large, $\sim 1000 R_*$, radii (Runacres & Owocki, 2002). Observationally the existence of structures within the winds of massive stars has been identified in the shape of the absorption troughs of UV spectral lines displaying P-Cygni profiles (Lucy, 1982), the Hα emission line profile variability of Galactic O-type supergiants and the universal narrow subpeaks superimposed on the optical emission lines of O stars of different evolutionary stages (Lépine & Moffat, 2008). Additionally Nazé, Oskinova, & Gosset (2013) have recently shown direct evidence of a high level of fragmented structure within the wind of ζ Puppis in the X-ray band through the short term variability detected in sensitive *XMM-Newton*/RGS observations, concluding that at any one time the wind must be comprised of $> 10^5$ discrete packets (or clumps).

Oskinova, Feldmeier, & Kretschmar (2012) considered the effect of the stellar wind structure in the case of a wind-fed SgXRB. Using time-dependent hydrodynamical simulations it was shown that the stellar wind density and velocity were highly structured out to large radii. Crucially it was also shown that, whilst on average the velocity of the stellar wind followed the β-law of the CAK model, locally strong velocity gradients were present, resulting from the instability driven shells in the wind. This effect was observed to be at its greatest within a few stellar radii of the stellar surface and a snapshot of the velocity variations are illustrated, along with the density variations, in Fig. 1.17. Additionally the simulations were used to derive synthetic light curves for NSs orbiting in a variety of circular orbits and accreting under the supersonic Bondi scenario.

These synthetic light curves are shown in Fig. 1.18 and large amplitude variability is observed for all orbital separations which, at its most extreme, covers up to eight orders of magnitude. This is far in excess of the variability observed from any wind-fed SgXRB, including the SFXTs (see below). The origin of this variability comes from the v_{rel}^{-2} dependence of the accretion radius (where $v_{rel}^2 = v_{NS}^2 + v_w^2$ and v_{NS} is constant). These simulations therefore rule out Bondi-type 'Direct accretion' as the main accretion regime occupied by wind-fed SgXRBs and instead require a damping mechanism within the accretion flow to reduce the influence of the varying

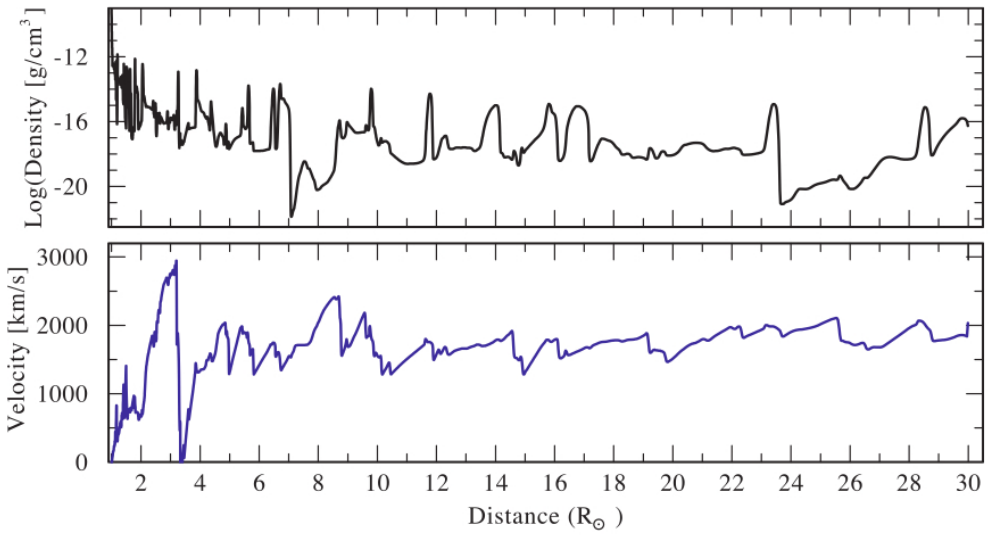

Figure 1.17: Snapshot of a time-dependent, hydrodynamically simulated model supergiant stellar wind showing the stellar wind density (top) and velocity (bottom) profiles as a function of separation from the supergiant. Both profiles show pronounced variability and sharp gradients superimposed on smooth decreasing (density) and increasing (velocity) trends (Oskinova, Feldmeier, & Kretschmar, 2012).

circumstellar environment on the accretion rate and observed X-ray luminosity. Such a damping is likely generated by the atmosphere about the NS in the 'Quasi-spherical accretion' model which predicts that wind-fed SgXRBs should inhabit a Compton cooling dominated subsonic accretion regime at their nominal luminosities (Shakura et al., 2013). The influence of the varying circumstellar environment will not be completely negated, however, leading to variability and possible accretion regime changes in these systems and may also be instrumental in generating the SFXT phenomenon.

1.2.3 Roche Lobe filling SgXRBs

In a small number of cases the supergiant companion in a SgXRB fills its Roche Lobe and mass transfer occurs via Roche Lobe Overflow with stellar material being forced through the L1 point and forming an accretion disc around the compact object. Unlike the wind-fed SgXRB and BeXRB populations, both NSs (e.g. SMC X−1) and BHs (e.g. Cyg X−1) have been identified as the compact objects in RLO SgXRBs. RLO SgXRBs are observed as bright, persistent X-ray sources with luminosities of $10^{37-38}\,\mathrm{erg\,s^{-1}}$ and also display behaviours more commonly associated with LMXBs such as ellipsoidal light variations from the deformed face of the supergiant in the optical band (e.g. Cyg X−1, Avni & Bahcall 1975), super orbital X-ray modulation due to a precessing warped accretion disc (SMC X−1, Trowbridge, Nowak, & Wilms 2007) and X-ray dipping behaviour due to

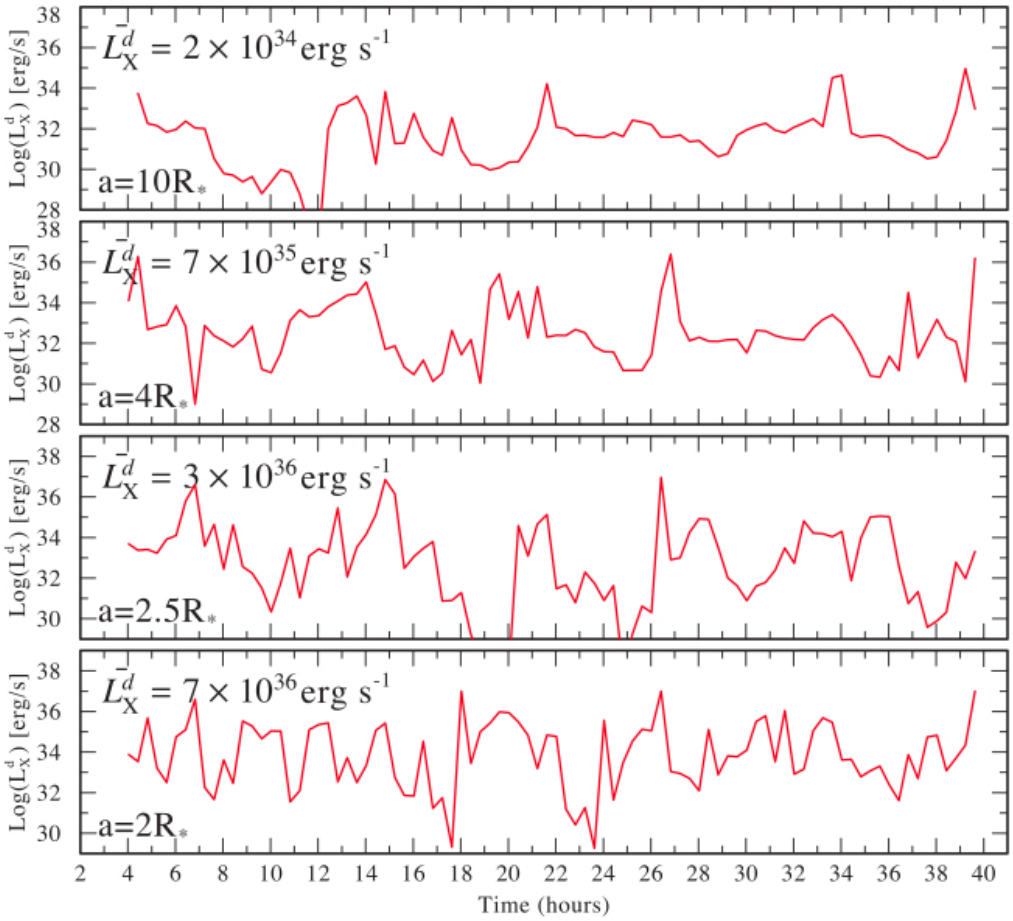

Figure 1.18: Synthetic X-ray light curves generated from time-dependent hydrodynamic simulations of a supergiant stellar wind for a variety of circular orbits. The X-ray luminosity is calculated under the Bondi-Hoyle approximation and at its most extreme displays variability over eight orders of magnitude on short time periods (Oskinova, Feldmeier, & Kretschmar, 2012).

obscuration by structures in the outer edge of the accretion disc (Cen X−3, Naik, Paul, & Ali 2011).

The fact that BHs are observed in RLO supergiant systems but (to date) not in wind-fed supergiant systems is likely attributed to the different methods of mass transfer occurring in these two cases. As stated previously an accretion disc forms in the RLO systems due to the effective transfer of angular momentum from the companion star, hence X-rays are produced through the standard processes attributed to BHXRBs, namely the hot accretion disc, non-thermal corona and jets (Cyg X−1 is also a 'micro-quasar'). However, in the case of wind accretion the transferred material has little angular momentum and in NS systems the X-ray radiation is predominantly generated in accretion columns close to the NS surface. In the case of BH systems there is no solid surface for gravitationally captured material to interact with and the inner regions of the accretion flow are lost beneath the event horizon. Hence there is no physical mechanism which can generate luminous X-ray behaviour in this configuration (emission produced at the accretion radius bow shock is only expected to reach luminosities of $\sim 10^{29}\,\mathrm{erg\,s^{-1}}$ (Bozzo, Falanga, & Stella, 2008a)) and systems with a BH in a wide binary orbit with a supergiant companion would not be detectable X-ray sources. The small number of BH HMXBs currently identified in both the Galactic and Magellanic Cloud samples (Cyg X−1, Cyg X−3 and LMC X−1) is likely a combination of the restricted orbital geometries in which these binaries can be X-ray sources, the likelihood of a progenitor binary system surviving the SN event to produce the BH and/or avoiding a common envelope merger (Belczynski & Ziolkowski, 2009) and the difficulty in retaining a massive enough He core to produce a BH after the extreme mass loss expected in the binary influenced evolution of the initial primary (Maeder & Meynet, 2008).

The exact nature of the RLO in a SgXRB is somewhat different to the case of LMXBs, however. As a result of the extreme mass ratio of SgXRBs ($M_{sg}/M_X > 1$) nominal RLO would be dynamically unstable leading to the shrinking of the binary orbit and the coalescence of the binary components. Due to the large mass loss rates of supergiant stars through their stellar winds, however, the surface of a supergiant star is not well defined, likely unstable at the base of the stellar wind as well as being distorted by the gravitational potential of the NS or BH. As such it is often considered that the supergiant companion just under-fills its Roche Lobe and mass transfer occurs as material from the base of the stellar wind is focused towards the compact object through the L1 point, forming an accretion stream toward an accretion disc around the compact object. The increasing distortion of the stellar surface and density of the accretion stream can be observed as a function of decreasing orbital separation as one moves clockwise through Fig. 1.13. In this case even at the smallest orbital separation (panel d) the tidal stream of material is deflected around the NS and enters the accretion wake, with the asymmetry of the

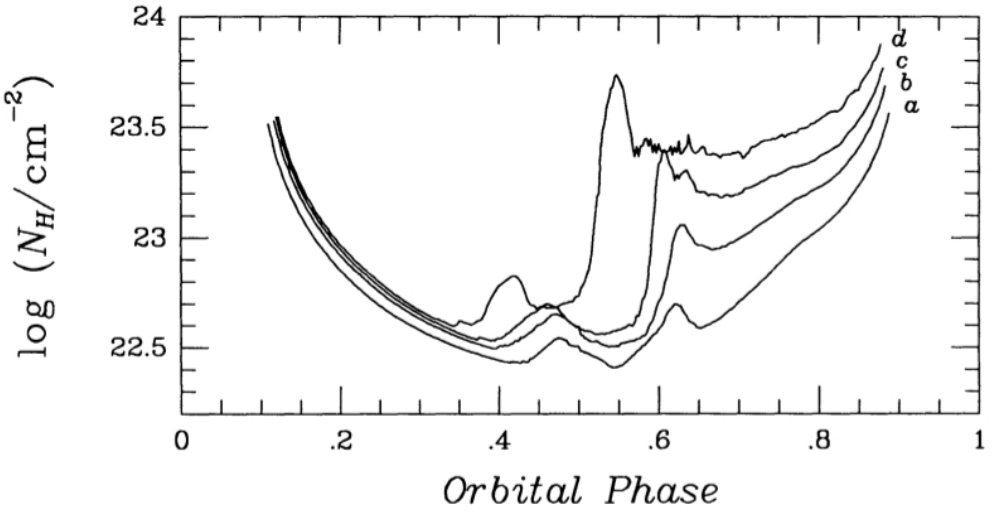

Figure 1.19: The predicted evolution of the absorbing column density across the orbital phase for the simulations of Fig. 1.13 observed from an edge-on inclination. The small features at $\phi \sim 0.4$ - 0.5 are from the leading edge of the bow shock and are roughly independent of the orbital separation whereas the features from $\phi \sim 0.5$ onwards are as a result of the influence of the tidal stream which is at its greatest at the smallest separations.

resulting accretion flow leading to the transfer of angular momentum of a constant sign (Blondin, Stevens, & Kallman, 1991). As the orbital separation were to decrease further, the tidal stream would continue to be enhanced, eventually leading to the direct formation of an accretion disc from the tidal stream. At larger orbital separations (panel a), however, a tidal stream does not form and the system undergoes pure wind accretion with inefficient, randomly orientated transfer of angular momentum. Hence there is a natural progression between the RLO and wind-fed SgXRBs as a function of the orbital separation (and mass ratio of the binary) with intermediate states often defined as 'Transitional Roche Lobe Overflow (TRLO)' (Blondin, Stevens, & Kallman, 1991).

As the physical features described by the Blondin, Stevens, & Kallman (1991) model are formed of varying gas densities they result in characteristic N_H evolutions across the orbital phase of systems viewed from an edge on inclination. The N_H evolutions derived from the simulations outlined in Fig. 1.13 are shown in Fig. 1.19. The influence of the bow shock is observed between orbital phases of $\phi \sim 0.4{-}0.5$ and can be seen to be independent of the orbital separation, whereas the features generated by the tidal stream, at phases of $\phi \sim 0.5$ and above, are greatly enhanced as the orbital separation decreases. Sensitive soft X-ray monitoring of suitably inclined systems over a long baseline could provide observational evidence of such features and allow constraints to be placed on orbital parameters and stellar wind properties of some SgXRBs.

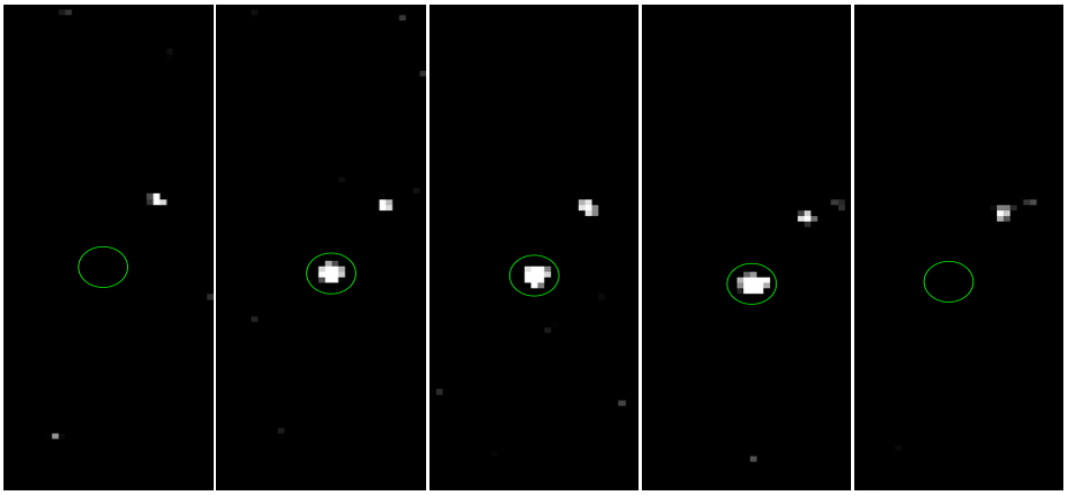

Figure 1.20: A sequence of *INTEGRAL*/IBIS 20−30 keV ScW images showing one of the first outbursts of XTE J1739−302 in March 2003 (Sguera et al., 2005). The source shows a rapid turn on and switch off and was only detectable for three consecutive ScWs (of nominal duration ∼2000 s).

1.3 Supergiant Fast X-ray Transients - SFXT

The discovery of Supergiant Fast X-ray Transients (SFXT) has been one of the major highlights of the *INTEGRAL* mission, unveiling an entirely unrecognised population of Galactic SgXRBs. Originally described as 'recurrent Fast X-ray Transients' by Sguera et al. (2005) these sources were only detected during short outbursts, with durations of hours, in the hard X-ray band which were interspersed with long periods of non-detection. A sequence of IBIS science window (ScW) 20−30 keV images illustrating one of the first outbursts, in March 2003, of XTE J1739−302 is shown in Fig. 1.20 with the source displaying a rapid rise to a luminous state for only 3 ScWs (of nominal duration ∼2000 s) before returning to an undetectable level (Sguera et al., 2005). The high instantaneous sensitivity and wide field of view of the hard X-ray imager IBIS (for a fuller description see Section 2.1 below) combined with the Galactic surveying/scanning pointing strategies of the *INTEGRAL* mission were fundamental in facilitating the repeated detection of the fast transient outbursts that have come to define these sources.

The arc minute scale uncertainties in the positions of the new transient sources provided by *INTEGRAL*/IBIS permitted straightforward follow-up using focusing soft X-ray instruments (e.g. *Swift* and *XMM-Newton*). These soft X-ray observations provided source positions to arc second accuracy and allowed the firm identification of optical/IR counterparts. Through photometric and spectroscopic studies the Optical/IR counterparts were individually characterised as confirmed, or likely, blue supergiant stars inhabiting a variety of environments. Some sources such as IGR J17544−2619 have showed optical reddening consistent with interstellar gas (Pellizza, Chaty, & Negueruela, 2006) whereas others, such as IGR J16465−4507,

Table 1.1: The spectroscopically confirmed SFXTs along with the optical counterpart, spectral type and best estimated distance.

Source	Counterpart	Spectral Type	Distance (kpc)
IGR J08408−4503	HD 74194	O8.5Ib	2.7
IGR J11215−5952	HD 306414	B0.7Ia	6.2
IGR J16418−4532	2MASS J16415078−4532253	BN0.5Ia	13
IGR J16465−4507	2MASS J16463526−4507045	O9.5Ia	9.4
IGR J16479−4514	2MASS J16480656−4512068	O9.5Iab	4.9
IGR J17354−3255	2MASS J17352760−3255544	O/BI	8.5
XTE J1739−302	2MASS J17391155−3020380	O8.5Iab(f)	2.7
IGR J17544−2619	2MASS J17542527−2619526	O9Ib	3.6
SAX J1818.6−1703	2MASS J18183790−1702479	O/BI	2.5
IGR J18410−0535	2MASS J18410043−0535465	B1Ib	3.2
IGR J18450−0435	2MASS J18450159−0433565	O9.5I	3.6
IGR J18483−0311	2MASS J18481720−0310168	B0.5Ia	2.8

Table 1.2: The candidate SFXTs based on their X-ray behaviour along with the optical counterpart and photometric spectral type constraints where available.

Source	Counterpart	Spectral Type
MAXI J1409−619	–	–
AX J161929−4945	2MASS J16193220−4944305	B1 supergiant
IGR J16328−4726	2MASS J16323791−4723409	OB supergiant
Swift J17435.5−285921	–	–
IGR J17541−2252	–	–
IGR J18159−3353	–	–
IGR J18219−1347	G017.324+00.1344	–
IGR J18462−0223	G030.2231+00.0791	OB supergiant
AX J1910.7+0917	2MASS J19104360+0916291	supergiant
IGR J20188+3647	–	–
IGR J21117+3427	–	–

display the influence of heavy local absorption (Nespoli, Fabregat, & Mennickent, 2008) similar to the absorbed SgXRBs also unveiled by *INTEGRAL*. The combined influence of these characterisations lead Negueruela et al. (2006a) to redefine the sources as the new SFXT class. Currently there are 12 spectroscopically confirmed SFXTs that are located along the Galactic Plane along with 12 candidate systems. The candidate systems are sources whose X-ray behaviour is similar to the confirmed SFXTs but for whom the nature of the optical counterpart, if one has been detected at all, has not been established. In a small number of cases the candidate system's optical counterpart has not been spectroscopically classified but the X-ray behaviour is reminiscent of both SFXT and BeXRB flaring behaviour leading to the current candidate status (e.g. IGR J19294+1816, Rodriguez et al. 2009). Tables 1.1 and 1.2 outline the current confirmed and candidate SFXTs along with their optical counterparts and spectral types where available.

Through analysis of the optical extinction, IR spectra and Optical/IR SED fitting of

the companion stars, the source distances have been derived and cover a range from $\sim$3 to 13 kpc (e.g. Nespoli, Fabregat, & Mennickent 2008, Chaty et al. 2008a and Rahoui et al. 2008a) allowing the luminosity of SFXT behaviour to be established. The peaks of outbursts detected by *INTEGRAL* correspond to luminosities of several times $10^{36}\,\mathrm{erg\,s^{-1}}$ (Ducci, Sidoli, & Paizis, 2010) whilst observations in the soft X-ray band show a variety of behaviours. At the most extreme end some SFXTs display quiescent states with luminosities of only a few $10^{32}\,\mathrm{erg\,s^{-1}}$ during observations with *XMM-Newton* (González-Riestra et al., 2004) and *Chandra* (in't Zand, 2005) which, when compared to the outburst states observed by *INTEGRAL*, illustrates an X-ray dynamic range of $10^4 - 10^5$ that can be realised over a period of only hours. Such behaviour marks a significant step away from the classical wind-fed SgXRBs which typically only display X-ray dynamic ranges on the order of $\sim 10 - 20$. Systems that display such a large dynamic range are known as the prototypical SFXTs, including IGR J17544−2619 and XTE J1739−302, and form the basis of the X-ray phenomenology of the SFXT class. In other cases, such as IGR J16465−4507 (Clark et al., 2010), the maximal dynamic range is not as large, being approximately $10^2 - 10^3$, but still represents a departure from the classical SgXRB picture. Collectively these sources are known as the intermediate SFXTs.

After the initial discoveries and characterisations in the hard and soft X-ray bands it seemed that, on average, SFXTs only occupied two states, namely a deep, spectrally soft quiescence for the majority of the time, that was occasionally interspersed with fast, luminous outbursts which constituted a few percent of the source duty cycle. However, long term monitoring in the soft X-ray band showed this characterisation to be driven by *INTEGRAL's* limiting sensitivity when compared to focusing X-ray instruments. Through *Swift*/XRT monitoring over several years, Romano et al. (2011) showed that SFXTs spend the majority of their time in an intermediate brightness state with luminosities of $10^{33-34}\,\mathrm{erg\,s^{-1}}$ with both the bright $10^{36}\,\mathrm{erg\,s^{-1}}$ level outburst and faint $10^{32}\,\mathrm{erg\,s^{-1}}$ level quiescent states being rare states in these systems that are only inhabited for a few percent of the system duty cycle. Spectrally SFXTs are consistent with other HMXBs hosting accreting NSs with both the intermediate and outburst states displaying hard powerlaw spectra, $\Gamma \sim 1-1.5$, in the soft X-ray band and steeper photon indexes in the hard X-ray band, $\Gamma \sim 2$, suggesting the presence of a high energy cut-off in the range 10−20 keV which has been confirmed by broadband observations (Sguera et al., 2007). In the quiescent state the spectra are softer and can often be described with blackbody models believed to originate from the hot surface of the NS (e.g. IGR J17544−2619, in't Zand 2005). Additionally the detection of X-ray pulsations ranging from $\sim$20 s (IGR J18483−0311, Sguera et al. 2007) to 1300 s (IGR J16418−4532, Walter et al. 2006) in several SFXTs has unambiguously confirmed that NSs are the compact objects in these systems. The presence of higher order spectral features such as iron (Fe) emissions and cyclotron lines has also been

suggested in some cases but have yet to be shown to be statistically required by the spectral modelling (e.g. IGR J18483−0311, Sguera et al. 2010).

Beyond the X-ray band, however, the behaviour of SFXTs is less well characterised. Single epoch optical and IR photometric and spectroscopic studies have been performed to identify and spectrally classify the companion stars as supergiants (e.g. Nespoli, Fabregat, & Mennickent 2008, Pellizza, Chaty, & Negueruela 2006). The characterisation of broadband SEDs and the presence, or lack of, MIR excesses also ruled out significant dust components about the supergiant stars in SFXTs and constrained the X-ray absorbing material to be local to the NS through the relative X-ray and optical extinctions (Chaty et al. 2008a, Rahoui et al. 2008a). Multi-epoch spectroscopic and photometric studies to identify the level of variability in the supergiant companions and any orbital modulations, including the deriving of Radial Velocity curves, have yet to be undertaken, however. No members of the SFXT class have been detected in the radio band, with only limited observational coverage, which is suggestive of the fact that jets are not produced in SFXTs. Similarly, in all but one case, see Section 5.2, SFXTs have not been detected at high energies (MeV, GeV) by the all-sky monitoring of *Fermi*/LAT and *AGILE*.

Observations in the soft X-ray band also facilitated the study of the absorption of the emitted X-rays to provide insights into the circumstellar environment being experienced by the compact object in SFXTs. As was found with studies of the optical extinction, some sources displayed X-ray absorption which was consistent with the Galactic value at their location whereas others displayed signatures of a large amount of absorbing material that is intrinsic to the binary system. Additionally some sources display significant variation in the absorption in different observations and luminosity levels (Romano et al., 2011) and also during continuous flux evolutions observed with *XMM-Newton*, an example of which was shown by Bozzo et al. (2011) for the SFXT IGR J18410−0535. The evolution of the spectral parameters during this outburst are shown in Fig. 1.21 and it can be seen that the N_H increases throughout the flare before rapidly decreasing back to the pre-flare level as the flux diminishes while the photon index stays relatively constant throughout this time (Bozzo et al., 2011).

An important implication of this result is that it provided some of the best observational evidence of a stellar wind clump interacting with a compact object during a flare in an SFXT system and provided strong support for the 'clumpy wind' model as a major driving process of the high level of variability observed in SFXTs. First proposed as an outburst generation mechanism in SFXTs by in't Zand (2005) and Walter & Zurita Heras (2007), the 'clumpy wind' theory proposed that SFXTs were observed in outburst during the short periods in which the NS interacted with dense clumps, containing a large fraction of the total mass loss, created by instabilities in the line driven stellar winds of the supergiant companion.

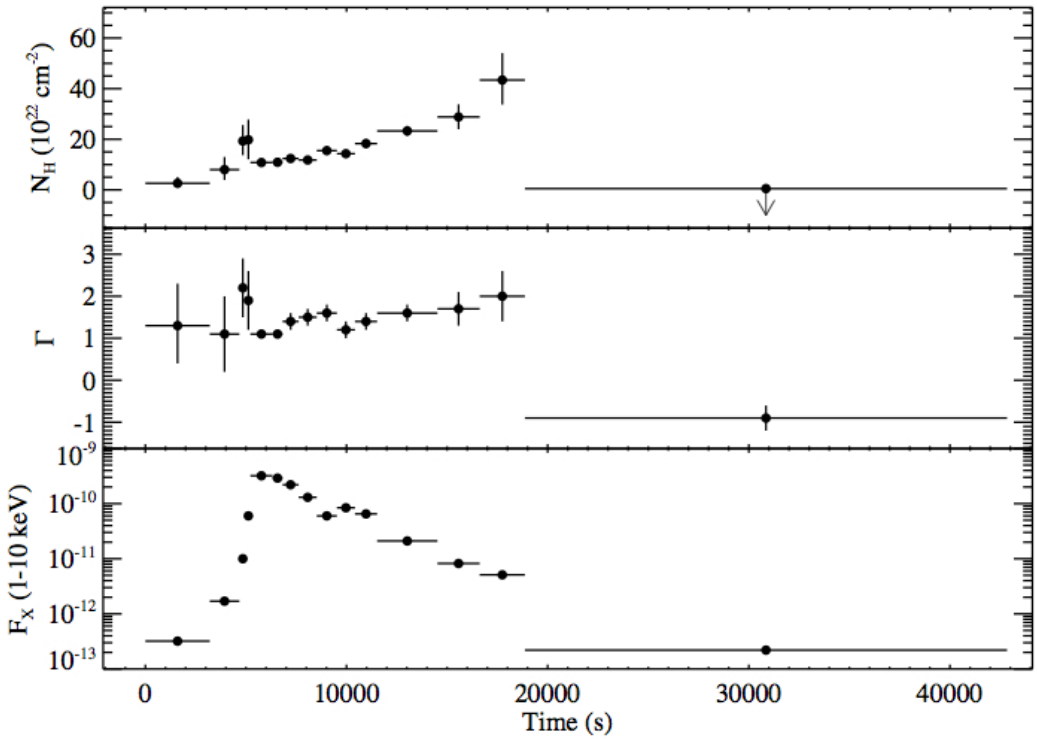

Figure 1.21: Evolution of the X-ray spectral parameters during a flare of IGR J18410−0535 observed by *XMM-Newton* showing the significant rise in N_H during the period of increased flux and a relatively constant photon index (Bozzo et al., 2011).

For the remainder of the time the SFXTs would be at low luminosities as they interacted with the tenuous, low density inter-clump gas. This model also predicted that SFXTs should have wider orbits than the classical SgXRBs, such that the intra-clump gas is of low enough density to produce the deep quiescence states sometimes observed. Extending this model Chaty (2008b) considered also the eccentricity of a system as a cause of the transient behaviour and proposed a unification mechanism whereby the classical and newly discovered heavily absorbed SgXRBs inhabited shorter, circular orbits that generate persistent emission through the accretion of a denser region of the supergiant stellar wind. The SFXTs on the other hand inhabit longer, more eccentric orbits such that they only sporadically encounter the denser region of the stellar wind during periastron passage and/or individual dense clumps further out in the stellar wind to produce the fast, transient flaring behaviour. Figure 1.22 illustrates this unification model of SgXRBs.

From early on, however, one system was clearly distinct from this model. IGR J11215−5952 is unique in the fact that it displays regular outbursts during every periastron passage of its long, 165 day orbit (Sidoli et al., 2007a). By modelling the duration and shape of the regular outbursts, as observed by *Swift*/XRT, Sidoli et al. (2007a) concluded that they were likely generated by the crossing of an 'enhanced equatorial density region' within the stellar wind of the supergiant. This enhanced equatorial density component takes the from of a preferential plane of outflow for the structured stellar wind and also has a lower terminal velocity than the symmetric 'polar wind' component. As such bright, long duration outbursts (~ 5 days) are observed during the crossing of the enhanced equatorial density region whilst outbursts typical of other SFXTs are observed during the majority of the orbital phase as the NS interacts with the fast polar wind component. The existence of such structures in the stellar winds of supergiant stars has been suggested observationally (e.g. Prinja, Massa, & Fullerton 2002) and as a consequence of magnetic confinement in the magnetohydrodynamic simulations of Ud-Doula, Owocki, & Townsend (2008). The identification of a distinct outburst generation mechanism in an SFXT is noteworthy as it suggests that the SFXT phenomenology may be generated by a variety of mechanisms.

Ducci et al. (2009) developed a wind-fed accretion model that took in to account the clumps in the stellar wind and the resulting effect on the observed X-ray emission in HMXBs. The model did not take into account radiative transfer effects and calculated the X-ray luminosity generated in a modified Bondi-Hoyle scenario where the accretion cross section was adapted depending on the relative size of the accretion and clump radii and the relative position of their centres during the interaction. Model light curves were produced for both persistent SgXRBs (Vela X−1 and 4U 1700−377) and the SFXT IGR J11215−5952 (including an enhanced equatorial density component) and the stellar wind clumps parameterised by comparing the model luminosity distributions to those observed. Ducci et al. (2009)

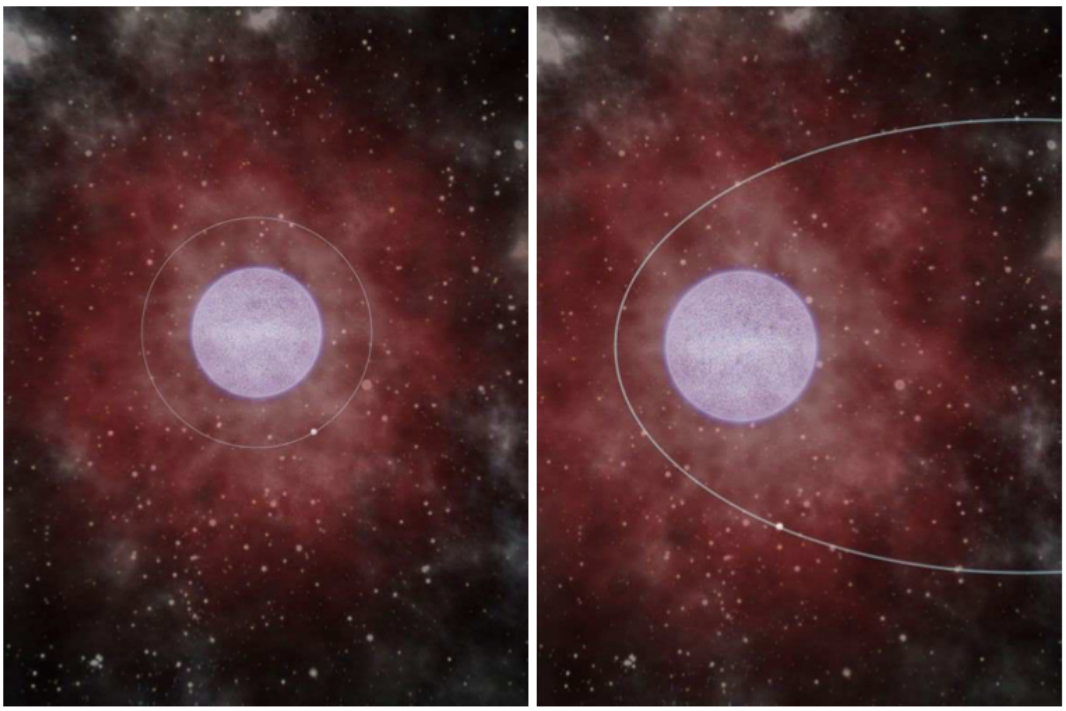

Figure 1.22: Illustration of the unification model of SgXRBs showing the classical case (left) defined by short, circular orbits in a dense region of the stellar wind and the SFXT case (right) in which the NS only sporadically interacts with the densest regions of the stellar wind during periastron passage (Chaty, 2008b).

concluded that the light curves of the three systems studied could not be produced by a consistent set of stellar wind parameters across all of the sources and that the different behaviour observed in the individual systems is a combination of varied stellar wind and orbital parameters. The stellar wind clumps were typically distributed with radii between 10^6 and 10^{11} cm and masses of 10^{16} to 10^{20} g with the best fit models having a high fraction of the mass loss of the wind contained within clumps ($\sim 75\%$) and a total mass loss rate a few times lower than that predicted by UV and Hα spectral line modelling. Smooth wind LTE models have also previously been predicted to overestimate the mass loss rates of O stars if the wind is in fact structured (e.g. Lépine & Moffat 2008). Observationally the duration and luminosity of X-ray flares in SFXTs have been used to place constraints on the mass and radius of stellar wind clumps using typical stellar wind and orbital velocities and have been shown to be consistent with the theoretical predictions. For example Fiocchi et al. (2013a) demonstrated that a flare of IGR J16328−4726 could be explained by the interaction with a clump of mass $\sim 4{\times}10^{22}$ g and radius $4.4{\times}10^{11}$ cm.

Contrary to the clumpy wind model, Bozzo, Falanga, & Stella (2008a) proposed a model to explain the large luminosity variations under the framework of barriers to the accretion flow via either centrifugal or magnetic inhibition as outlined in Section 1.2.2. Under this model the multiple order of magnitude swings in the

X-ray luminosity can be explained with more modest variations in the accretion rate when a pulsar is slowly rotating and has a magnetar strength magnetic field. In the absence of strong independent evidence of magnetars being present in SFXTs, the identifications of signatures of stellar wind clumps in the X-ray emission of SFXTs (as outlined above) and the more natural geometric progression from classical SgXRBs to SFXTs, it is the clumpy wind model that is more widely accepted as the main driving force behind the extreme X-ray variability of the SFXTs. With long base line coverage in the hard X-ray band, however, the orbital periods of several SFXTs systems have been identified, ranging from ~ 3 to 165 days, presenting challenges for the application of the nominal description of the SFXT phenomenon across the full period range and sample of sources. It is this question of whether the SFXTs can indeed be treated as a single class of objects with a self consistent emission mechanism across the entire population or whether there are sub-populations within the SFXTs that generate the observed variability through different mechanisms that is a central theme of this thesis.

1.4 Unusual classes of X-ray Binary

1.4.1 Intermediate Mass X-ray Binaries - IMXB

The preceding sections have focused on the two original classes of X-ray binary defined by the distinct high and low mass nature of the companion stars. However, as there is no dynamical or evolutionary process inhibiting the production of binaries with companions in the mass range $1 < M_*/M_\odot < 10$, this suggests there should be a population of binaries with such a companion, but only a small number of X-ray sources are known. Some examples of these so-called 'Intermediate Mass X-ray Binaries (IMXB)' are Her X$-$1, which has a NS primary and a $2.3 M_\odot$ companion (Reynolds et al., 1997), and LMC X$-$3 which is comprised of a $4.7 M_\odot$ subgiant companion in orbit around an $\sim 8 M_\odot$ BH (Soria et al., 2001). van den Heuvel (1975) explained the low number of observed IMXBs through a selection effect driven by the short X-ray producing lifetimes of such systems. The companion stars in IMXBs are not massive enough to produce strong stellar winds and so accretion is only initiated when the companion evolves off the main sequence and RLO is initiated. As a result of the large mass ratios in these systems, however, especially in NS systems, the initiated mass transfer is dynamically unstable and/or a system may enter a common envelope evolution phase, resulting in a short lived X-ray emitting phase on the order of a few thousand years. Therefore the number of X-ray active IMXBs at any time is small as reflected in the current population. Additionally the high mass transfer rate initiated during the X-ray phase may also create sufficient absorption to completely attenuate any X-ray radiation produced, further reducing the detectable sample of IMXBs.

1.4.2 γ-ray binaries

Beyond the soft and hard X-ray regimes, a small number of Galactic binary systems have also been detected at high (HE, GeV) and very high (VHE, TeV) energies showing that particles can be effectively accelerated to highly relativistic velocities in binary systems. All the γ-ray binaries have a high mass companion and the dominant method of HE and VHE production is believed to be the Inverse Compton scattering by highly relativistic electrons of UV photons from the dense photon field produced by the massive companion. HE emission has been detected from binaries with both a confirmed NS (PSR B1259−63, Aharonian et al. 2005) and a likely BH (Cyg X−3, (Fermi LAT Collaboration et al., 2009)) which has lead to the development of two theories of HE production within binary systems. As Cyg X−3 is a microquasar the HE emission is believed to originate from the relativistic jets as the γ-ray activity is correlated with changing radio states. In the case of NS systems the HE emission is believed to originate under the 'pulsar model' where the pulsar wind interacts with the decretion disc of the Be star companion during periastron passage. PSR B1259−63 is the only confirmed pulsar of the γ-ray binaries, however, LSI $+61^o$ 303 and LS 5039 also have similar orbital parameters and Be star companions as well as being detected in the VHE, as is PSR B1259−63, suggesting they are of a similar nature.

The link between the GeV and TeV emission is not fully understood, however, as the systems show variable emission states. For example LSI $+61^o$ 303 was first detected at VHEs (Albert et al., 2006) with emission being modulated on the orbital period, but peaking close to the apastron of the system. Early *Fermi* results detected the source at GeV energies and identified an orbital modulation in this flux for the first time (Abdo et al., 2009) but found that the GeV flux peaked at periastron in anti-correlation with the TeV emission. This anti-correlation was predicted theoretically by Dubus, Cerutti, & Henri (2008) (specifically for LS 5039 in this case) as at TeV energies photons interacting with the UV seed photons undergo electron positron pair production and are therefore heavily attenuated in regions of higher UV photon density (i.e. periastron). Whereas at lower energies this attenuation does not occur and the observed flux follows the underlying IC production profile which is proportional to the UV field density, hence the GeV flux peaks at periastron and generates the observed anti-correlation. In addition to the affect of pair production attenuation at TeV energies, the anisotropic nature of the IC interactions as a function of viewing angle (i.e. the relativistic effects generated by the varying relative velocities of the electrons and UV photons) results in shifts of the orbital phase positions of the GeV and TeV peaks. This effect is related to the line of sight through the UV photon fields resulting in a more complex orbital profile with the locations of the flux peaks influenced by the superior and inferior conjunctions, as discussed in Dubus, Cerutti, & Henri (2008) and others. However,

from early 2009 the γ-ray behaviour of LSI $+61^o$ 303 began to change, with the source displaying an increased flux in the GeV band whilst simultaneously the orbital modulation became undetectable at these energies (Hadasch et al., 2012). Concurrently with the increased GeV flux the source became undetectable in the TeV band apart from a single periastron flare, which is in contradiction with earlier behaviour (Acciari et al., 2011). Such variable behaviour is yet to be fully explained with some authors suggesting that it may be related to the changing state of the Be star decretion disc in LSI +61 303 (Zamanov et al., 1999) and others invoking the presence of a magnetar to explain the behaviour (Torres et al., 2012).

A final common feature of the pulsar driven γ-ray binaries is that they are all X-ray quiet in comparison to the non-HE emitting BeXRBs. Understanding how the γ-ray binaries accelerate particles to such high energies in small spatial regions and identifying how they fit in with the wider X-ray binary population are the biggest challenges currently facing this area of study.

1.5 Thesis Outline

The primary aim of this thesis is to consider the nature of the SFXT class of SgXRBs, the extent to which they can indeed be considered a single class and their place within the HMXB hierarchy. As the detection in large numbers of SFXTs and some of their key characteristics, such as orbital periods, outburst durations and X-ray dynamic range, were provided by *INTEGRAL*, Chapter 2 provides an overview of the observatory and the data analysis methods utilised for the hard X-ray characterisation of SFXTs using IGR J17544−2619 as an example. Chapters 3, 4 and 5 then undertake in-depth analysis of three individual SFXTs using a variety of observatories. Chapter 3 provides an analysis of IGR J16418−4532 using archival *INTEGRAL*/IBIS data along with recent co-ordinated, orbital phase constrained *INTEGRAL* and *XMM-Newton* observations. Chapter 4 describes a temporal and spectral study of IGR J17544−2619 using *RXTE*. Chapter 5 then describes predominantly *INTEGRAL* studies of XTE J1739−302 and IGR J17354−3255 to identify the orbital periods of the systems and discusses their implications on the nature of these binaries. Finally the results of all the studies presented are combined, along with other recent works, to consider the current understanding of SFXTs and conclude on their nature in Chapter 6. The future direction of this field of study is also considered, including the short term, approved observational programmes and longer term scientific goals.

Chapter 2

INTEGRAL data analysis methods and techniques

The impact of the *INTEGRAL* observatory on the SFXT field cannot be understated, with the telescope providing not only the first detections of the recurrent, fast transient sources that revealed the SFXT class, but also characterising many aspects of the nature of these extreme X-ray sources. Of greatest importance perhaps is the determination of orbital periods in SFXTs allowing the outbursts detected in the hard X-ray band and the targeted follow-up by focusing soft X-ray telescopes to be placed in a dynamical context. Given the importance of such determinations in developing an understanding of the physical processes acting to generate the X-ray behaviour observed in SFXTs, this Chapter is devoted to detailing the analyses used to extract periodicities and outbursts from long baseline *INTEGRAL* datasets.

Initially the *INTEGRAL* mission is outlined with specific reference being made to the 'Coded Aperture' nature of the imaging utilised in the hard X-ray band and the challenges this presents for the detection of transient sources. The techniques employed to detect orbital periodicities in long baseline *INTEGRAL*/IBIS light curves and identify outbursts in the dataset are then discussed along with the statistical significance testing performed in each case. Examples of these techniques and the results they yield are presented using, predominantly, the case of the prototypical SFXT IGR J17544−2619.

2.1 The *INTEGRAL* observatory

The 'International Gamma-ray Astrophysics Laboratory' *INTEGRAL* (Winkler et al., 2003) was the most sensitive hard X-ray/soft γ-ray observatory ever built at the time of its launch, being only recently surpassed by NuStar (Harrison et al., 2010).

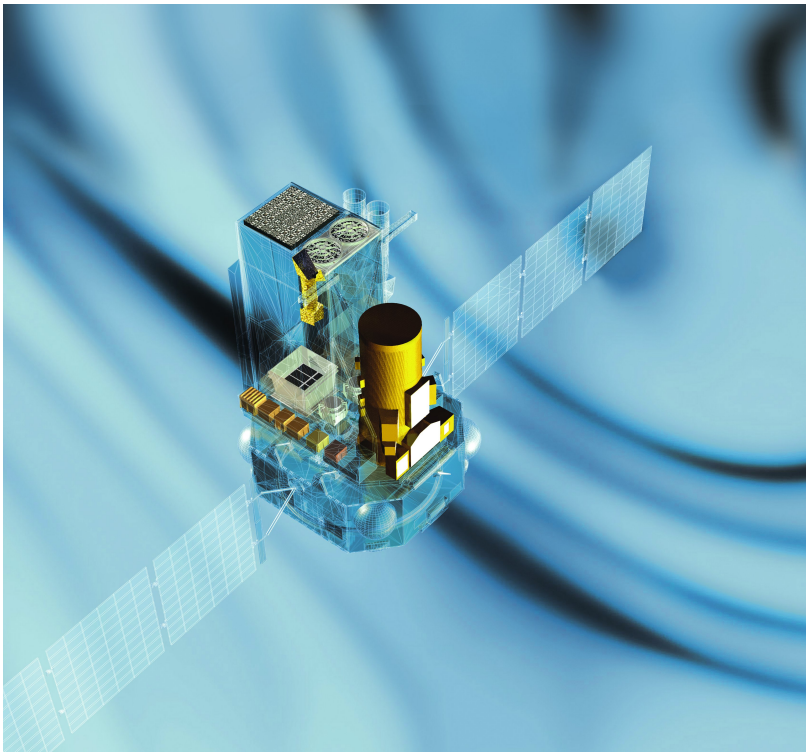

Figure 2.1: Schematic diagram showing the scientific instruments aboard the *INTEGRAL* observatory. The three main science instruments, IBIS, JEM-X and SPI, are the highlighted sections in a diagonal line from the top left to bottom right of the schematic. All three instruments are co-aligned and the coded aperture mask of IBIS can be seen on the top left. Image Credit: ESA.

The telescope was launched on a Proton rocket into a 72 hour elliptical orbit which allows long, uninterrupted observations of celestial high energy sources. The observatory utilises 'Coded Aperture' techniques to perform fine high energy imaging and spectroscopy over a range of 3 keV to 10 MeV across three separate co-aligned telescopes. The 'Joint European X-ray Monitor' JEM-X (Lund et al., 2003) is the soft X-ray telescope and provides arc minute imaging in the 3−35 keV band for a field of view (FOV) of diameter 13.2^o (7.5^o) at zero (half) response. The 'Imager on Board the INTEGRAL satellite' IBIS (Ubertini et al., 2003) provides fine hard X-ray imaging (PSF FWHM 12'), timing and coarse spectroscopy between 15 keV and 10 MeV across a FOV of 29.1^o by 29.4^o (at zero response) allowing the serendipitous detection of large numbers of hard X-ray sources in each observation and facilitating the accumulation of deep survey data. Finally the 'Spectrometer on INTEGRAL' SPI (Vedrenne et al., 2003) performs coarse imaging (PSF FWHM 2.5^o) and fine γ-ray spectroscopy of point and extended sources in the 18 keV to 8 MeV energy range. Figure 2.1 shows a schematic of the *INTEGRAL* observatory in which the three main science instruments are highlighted.

Due to the Galactic Plane location, fast transient behaviour and relatively low fluxes of SFXTs the IBIS instrument has been the main source of SFXT discoveries.

The coarse imaging capabilities, small effective area and optimisation for spectral analysis of SPI prevents the unambiguous detection of fainter sources in the Galactic Plane with this instrument. The smaller FOV and lower effective area of JEM-X compared to IBIS (500 and 2600 cm^2 respectively, although this is somewhat offset by the soft X-ray spectra of SFXTs) results in a coarser sampling of the Galactic Plane at lower sensitivity with this instrument which restricts the rate of increase of exposure, and therefore the number of outbursts detected (see Section 2.4.3), compared to IBIS. Hence JEM-X does not contribute greatly to the knowledge of the global properties of SFXTs and from this point only methods for the analysis of IBIS data are discussed. It should be noted, however, that JEM-X has made some specific, significant contributions to the study of SFXTs such as the identification of IGR J18483−0311 as a 21 s pulsar (Sguera et al., 2007).

The coded aperture instruments aboard *INTEGRAL* facilitated the effective production of hard X-ray/soft γ-ray images at a time when γ-ray focusing optics were not technically feasible. Instead a 'mask' is placed above the detector plane with a characteristic pattern of opaque and transparent 'cells' such that a γ-ray source illuminating the mask casts a shadow of the pattern on to the detector plane. The mask used in IBIS is a 16 mm thick tungsten mask with $\sim$50% transparency (i.e. half of the cells are tungsten and opaque to γ-ray photons up to energies of several MeV and the other half are transparent). Figure 2.2 illustrates the effect of two sources illuminating the IBIS coded mask and generating a superimposed pattern on the detector plane, the exact form of which is dependant upon the relative position and intensities of the two sources. To convert these 'shadowgrams' in to sky maps the detector plane image is 'de-convolved' by correlating the known mask pattern with the detector plane image at all positions. The resulting 'correlation map' outlines the relative positions and intensities of sources in the FOV during the observation. The correlation map can then be 'back projected' to form an image of the sky by combining the known position, orientation and pointing of the satellite with a preliminary source list (nominally the *INTEGRAL* 'General reference catalog', Ebisawa et al. 2003) to model the detector plane image and reconstruct the source content of the IBIS FOV during the observation. The production of sky images is performed by the *INTEGRAL* 'Offline Science Analysis (OSA)' software described by Goldwurm et al. (2003), to which the reader is referred for a full and detailed discussion of this complex process of image reconstruction. Here the implications of this method of X-ray imaging on the subsequent data analysis are briefly outlined and the methods of overcoming them are discussed in detail in the following sections.

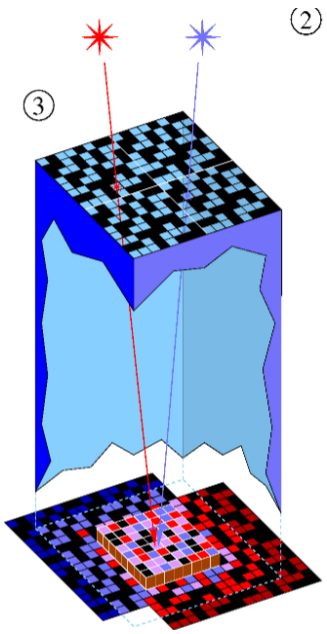

Figure 2.2: Illustration of a coded aperture telescope being illuminated by two sources. A superimposed mask pattern is accumulated on the detector plane, the exact form of which depends on the relative positions and intensities of the two sources. Image Credit: ISDC/M. Türler.

2.2 IBIS images and light curve extraction

INTEGRAL observations are performed in individual pointings called Science Windows (ScW) that have a typical duration of ∼2000 s. Each ScW is de-convolved by the OSA software and a sky image produced in a specified energy band. The nominal energy band used in the analysis of SFXTs here is 18−60 keV unless stated otherwise. A ScW resolution light curve is produced by extracting the count rate and uncertainty at the best known position of a source from each IBIS image where the source is within the FOV. It is IBIS ScW light curves produced in this manner that underpin much of the *INTEGRAL* analysis of SFXTs presented in this work.

The main effect of the coded aperture imaging used by IBIS is that imperfect reconstructions of the sky images results in a higher level of positionally dependant systematic uncertainty and a deviation from the typical Poissonian statistics encountered in conventional focusing optics systems. Additionally as the flux from each source in the FOV is spread across the whole detector plane every source acts as a source of background for every other source. This enhanced background contribution fundamentally limits the sensitivity of coded aperture instruments compared to focusing optics where the flux from each source is concentrated on a specific region of the detector plane. Figure 2.3 shows an example de-convolved sky significance map from a single ScW of the region around the SFXT IGR J17544−2619. IGR J17544−2619 is clearly detected during an outburst in the image along with several other bright point sources. The logarithmic colour scale

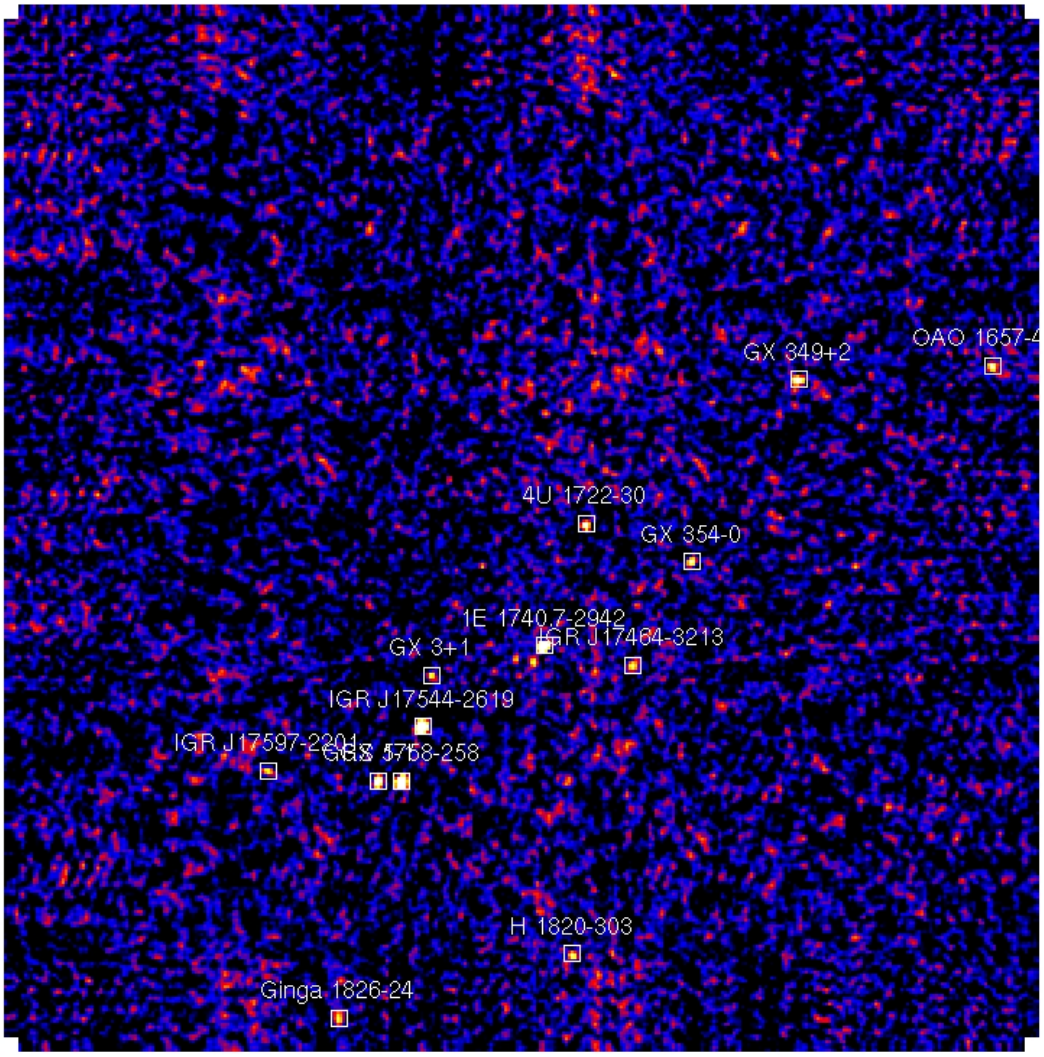

Figure 2.3: A significance map of the region around the SFXT IGR J17544−2619 from a single ScW in the 18−60 keV band using a logarithmic colour scale. Several bright sources, indicated by the white squares, are detected at $> 5\sigma$ along with lower significance artefacts seen across the whole image and systematic noise in the outer regions resulting from the imperfect de-convolution of the shadowgram accumulated on the detector plane.

also illustrates the large number of artefacts present in this single image as well as systematic noise structures present in the outer regions of the image. These artefacts and structures, which are of particular concern when they stack on top of each other in successive ScWs, present difficulties that have to be overcome when analysing source light curves derived from such images.

In the case of detected sources the magnitude of the uncertainty on the count rates extracted from each image increases as a source moves to larger off-axis angles as the source projects an incomplete section of the mask pattern onto the detector, thus accumulating an incomplete shadowgram on which to perform deconvolution. Sources at off-axis angles of less than 4.5^o project a full mask pattern on to the detector plane and are in the 'Fully Coded Field of View (FCFOV)' where the uncertainties in the flux detected in each pixel approximate to being purely statistical. At larger off-axis angles, however, sources are in the 'Partially Coded Field of View (PCFOV)' where there is an increasing systematic contribution to the uncertainties in each pixel. The origin of this uncertainty is two fold. The first effect is a result of sources at larger off-axis angles projecting an in-complete mask pattern on to the detector plane such that the deconvolution is intrinsically less well defined, resulting in an increased count rate uncertainty. The second effect is a result of the imperfectly modelled energy response of IBIS for sources at large off-axis angles resulting from the effect of photons interacting with different surfaces of multiple pixels in the detector plane. Due to computational limitations these effects cannot be modelled for the production of each image resulting in an additional source of systematic uncertainty in the derived count rates at the level of $\sim$2%. At sky positions where a source is not detected, however, the image is dominated by artefacts that result from random fluctuations in the correlation of the mask pattern to regions of noise in the detector plane. For a sky position free of X-ray sources these random correlations are equally as likely to be negative as positive and hence the light curve of an empty region of sky will consist of a distribution of positive and negative count rates centred on, and with an average of, zero. When studying persistent sources these random correlations are of little concern as the count rates at the source position are dominated by the detected flux. In the case of transient sources, however, extracted light curves contain epochs where the count rates are extracted from both flux-dominated and random artefact-dominated images. Hence caution must be taken in the analysis of these light curves to avoid the identification of false positive outbursts resulting from the random fluctuation of artefacts at the source position whilst the source is in a dormant state. In all cases short exposures ($\sim$ a few hundred seconds) also result in count rates with large uncertainties as insufficient detail can be accumulated in the detector plane shadowgram to allow effective deconvolution and the production of a well modelled sky image during such short observations.

To illustrate the impact of these effects Fig. 2.4 shows the $18-60$ keV light curve of

IGR J17544−2619 extracted from each ScW in which the source was in the IBIS FOV between MJD 52698.174 and MJD 55698.030. The ScWs with a short exposure and/or where IGR J17544−2619 was at a large off-axis angle can be easily identified by the data points with the large uncertainties. Large negative points are also observed, indicating the anti-correlations that can occur during the de-convolution process. Additionally the distribution of count rate uncertainties (in logarithmic space) as a function of the off-axis angle of the observations are illustrated in Fig. 2.5, where the red points illustrate observations with an exposure of greater than 200 s and where IGR J17544−2619 was at an off-axis angle of less than 12^o (see Section 2.3) and the black points are the observations of lower exposure length and/or larger off-axis angle. The systematic increase in the magnitude of the uncertainty as a function of the off-axis angle is clearly observed with the increasing curvature of the distribution at the higher end of the angle range indicating the increasing influence of the poorly modelled IBIS response for sources at the edge of the FOV. The distribution of points in the vertical direction for any given off-axis angle is a combination of two factors. The first, and more dominant factor is the exposure length of the individual ScWs where longer exposures provide better constrained uncertainties due to the higher photon statistics achieved. Conversely the black points at lower off-axis angles illustrate the shortest exposures where the de-convolution could not be performed effectively even for sources in the FCFOV. The second factor is the influence of the varying photon statistics of a transient source detected at different intensity levels with detections of the source in a brighter state having a larger $\sqrt{N}$ uncertainty, despite being detected at higher significance, than when the source is in a fainter state. The following section discusses how these effects are accounted for in subsequent analyses of the IBIS light curves of SFXTs.

2.3 Timing analysis

Periodicities in the IBIS light curves of SFXTs are identified using the Lomb-Scargle (LS) periodogram (Lomb 1976, Scargle 1982) which performs least squared fitting of sinusoids over a range of frequencies to identify periodic modulation in an unevenly sampled dataset. However, the application of this method to a raw light curve, as shown in Fig. 2.4, will often suppress true periodic signals as they are disrupted by observations of short exposure length and in which the source of interest is located at a large off-axis angle due to the large count rate uncertainties this generates, as discussed in Section 2.2. The Lomb-Scargle analysis does not consider the significance of each data point, instead it only takes the central count rate value so that unreliable data points, such as the observations in excess of $100\,\mathrm{counts\,s^{-1}}$ (or less than $-100\,\mathrm{counts\,s^{-1}}$) in Fig. 2.4, are considered equally to the true count rates determined from times when the source was firmly

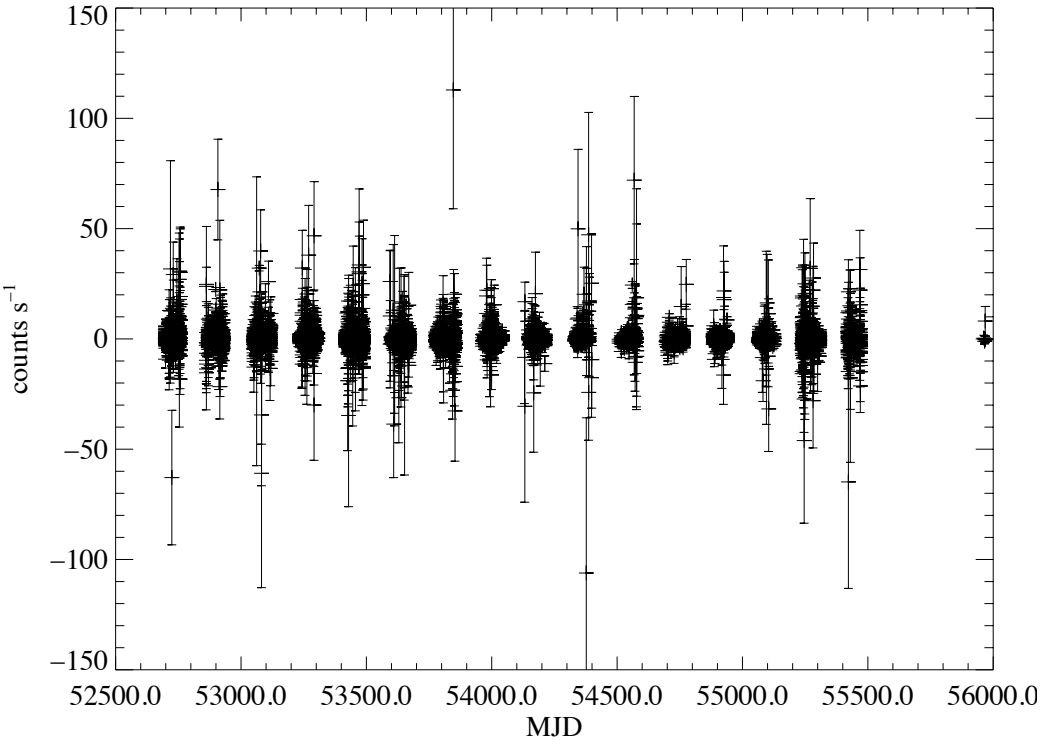

Figure 2.4: The 18−60 keV IBIS light curve of IGR J17544−2619 extracted from all observations of the source between MJD 52698.174 and MJD 55698.030.

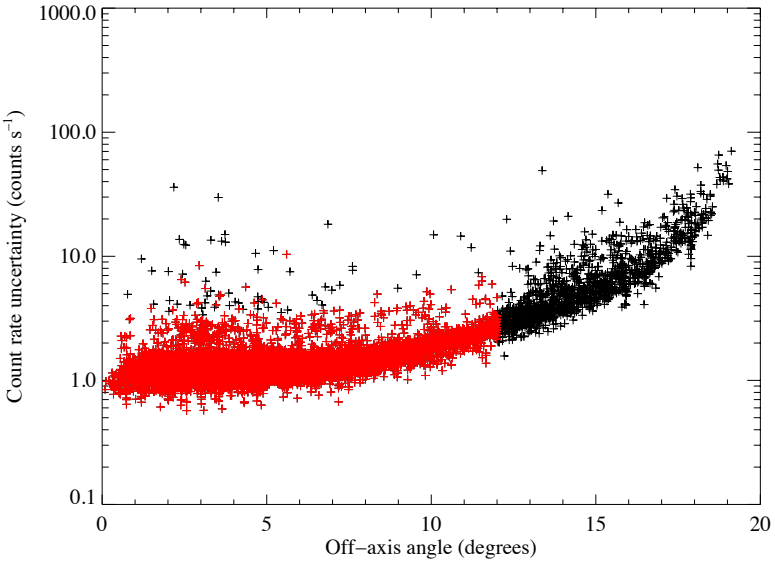

Figure 2.5: The count rate uncertainty as a function of off-axis angle in the 18−60 keV light curve of IGR J17544−2619. The red points highlight the data remaining after the optimal light curve filtering described in Section 2.3 has been applied.

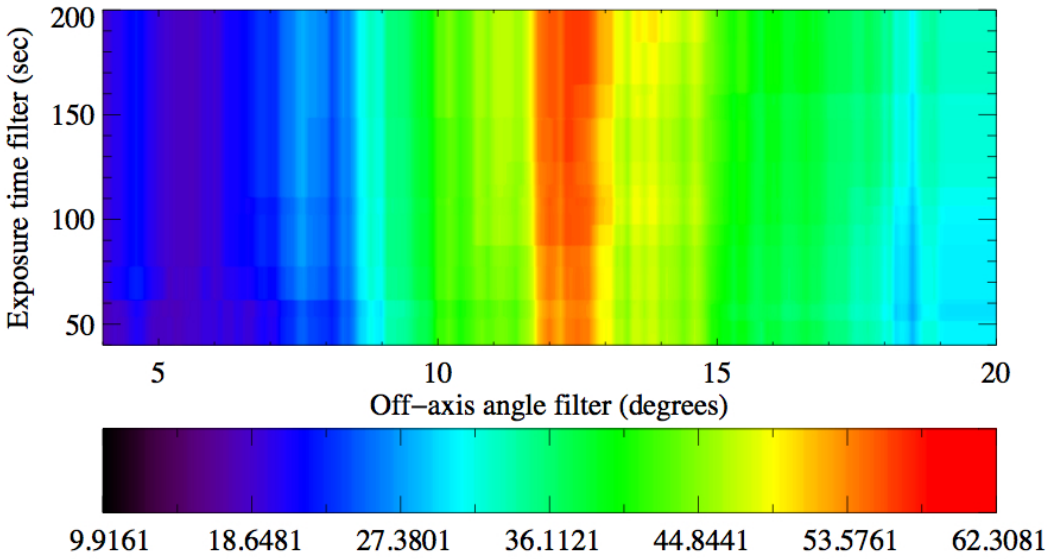

Figure 2.6: A colour scale diagram showing the peak Lomb-Scargle periodogram power detected from the IBIS light curve of SAX J1818.6−1703 across a wide variety of filtering constraints. The lower colour bar shows the linear scale of the plot. A filter with parameters of off-axis angle $< 12 - 13^o$ and exposure time $\geq 200s$ is shown to provide the strongest detection of the known 30 day orbital period.

detected. This has the effect of blurring out true periodic signals and masking their detection with the LS periodogram.

To overcome this effect the IBIS light curves are filtered for data taken at large off-axis angles and also short exposure times. The exact thresholds used for filtering are a matter of optimisation, however, as too lenient a filter will include a sufficient amount of poor quality data to mask periodic signals, whereas too strict a filter will remove a large enough proportion of data to limit the sampling of the periodic modulation which again inhibits detection. For example the ScW light curve of IGR J17544−2619 shown in Fig. 2.4 is derived from 10,576 observations for a total exposure of ∼16.9 Ms. If it were to be filtered for data taken only when the source was in the FCFOV the light curve would only contain 4051 data points, 40% of the original dataset. Intuitively it is clear that removing 60% of a dataset will dramatically reduce the amount of diagnostic information it is possible to extract from it. To derive the optimum filtering an empirical method is used whereby the light curve of a source with a known orbital period is subjected to a wide range of off-axis angle and exposure time filter constraints. A LS analysis is performed on each separate light curve and the peak power generated in each periodogram is recorded allowing for an assessment of the optimal filtering constraints.

The example used here is that of the SFXT SAX J1818.6−1703 which has a well defined 30 day orbital period (Bird et al., 2009). The SAX J1818.6−1703 IBIS light curve was filtered for maximal off-axis angles in the range 4^o to 20^o and minimum exposure times of 0 to 200 s. The distribution of peak powers detected is shown in

Fig. 2.6 where the colour scale indicates the peak power detected in the periodogram analysis for each set of filtering parameters. It is observed that a filter with parameters of off-axis angle $\sim 12 - 13^o$ and exposure time $\geq 200s$ produces the strongest detection of the known orbital period with a LS periodogram power of $\sim$60. Either side of this central belt of the strongest detections the peak power detected in the periodogram analyses decreases towards the level of noise detected in each periodogram. To the left of the central belt this is due to the effect of the large amounts of data loss incurred by the strict off-axis constraints, whereas the power loss to the right of the central belt is a result of the influence of poor quality data points with large uncertainties disrupting the periodic signal in the light curve. The influence of the exposure time filter is observed in the vertical direction and it can be seen to be the less dominant factor compared to the off-axis angle constraints, but the detected power diminishes when the shortest exposures are included in the analysis. From this analysis the standard filtering selected for the analysis of IBIS light curves of SFXTs is an off-axis angle $< 12^o$ and an exposure time $> 200\,s$. Applying the optimum filtering to the IBIS light curve of IGR J17544−2619 results in a light curve with 9121 data points (86% of the full dataset) and a total exposure of $\sim$14.9 Ms that is shown in Fig. 2.7. The reduced count rate axis range in this figure compared to Fig. 2.4 and the subset of red points in Fig. 2.5 both illustrate the removal of the poor quality data points under these optimal filtering conditions.

A LS analysis is performed on the optimally filtered dataset to detect and define any periodic signatures within the light curve. The LS periodogram of the light curve of IGR J17544−2619 is shown in Fig. 2.8 which indicates the detection of a strong periodicity at $\sim$4.9 days in the dataset. The methods used to define the significance of detected peaks and the uncertainty on the central period are now described in the following sections.

2.3.1 Detection confidence determination

Due to the systematic noise generated in the IBIS images power can be generated in the LS periodogram of source light curves at periods which are not physically related to the source. Some sources of noise occur on timescales related to the nature of the *INTEGRAL* observing strategy, such as long term cyclic observing programmes like the weekly scanning of the Galactic Plane (Bazzano et al., 2011), annual *INTEGRAL* visibility constraints and the sequential dither patterns followed during nominal observing strategies, the signals from which, if present, can be identified through their characteristic, discrete periods. However, additional random variations in the light curves also generate power in the periodogram across a wide range of frequencies. To test for the presence of such 'white noise' and estimate its statistical signature within a light curve, a Monte-Carlo based 'randomisation test' is used. To assess the maximum power that the random

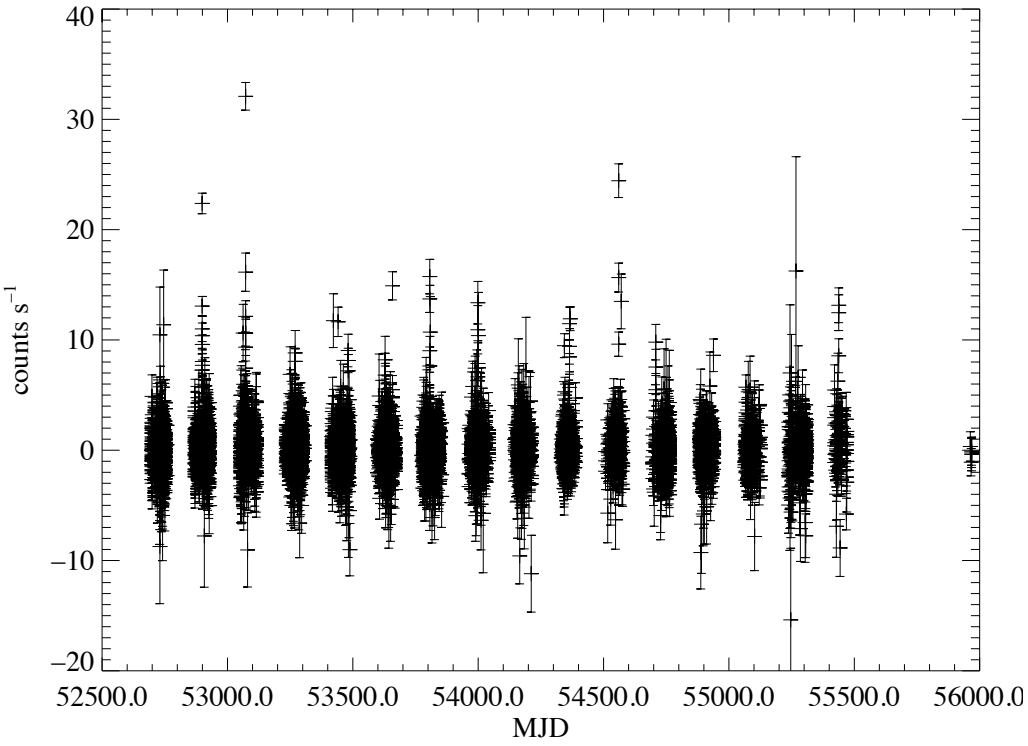

Figure 2.7: The 18−60 keV IBIS light curve of IGR J17544−2619 after the optimal filtering constraints of off-axis angle $< 12^o$ and exposure time $> 200\,s$ have been applied.

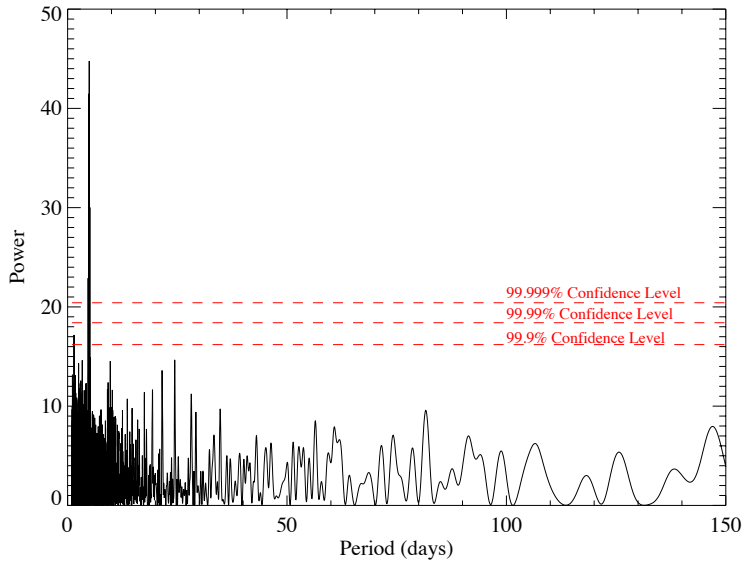

Figure 2.8: Lomb-Scargle periodogram of the optimally filtered IGR J17544−2619 IBIS light curve showing a strong peak at ∼4.9 days. The 99.999% confidence level is also drawn at a power of 20.42 as derived by the method outlined in Section. 2.3.1.

fluctuations in the light curve could generate, the count rates in the filtered IBIS light curve are randomly re-ordered, a LS periodogram produced and the peak power generated recorded. This process is repeated a large number of times with a different randomisation used in each iteration to develop a distribution of the power that can be randomly produced in the light curve. The minimum number of randomisations required is dependent upon the confidence level to which a light curve is to be tested. In the context presented here the 99.999% confidence level provides the LS power above which there is a 1 in 100,000 chance that a signal was generated by random noise, equivalent to a significance of 4.42σ. Hence, to draw the 99.999% confidence level at least 200,000 simulations must be performed.

A major advantage of this method of significance testing is that the statistical properties of the true light curve are retained exactly in each randomisation, as are the discrete frequencies used by the LS analysis on each light curve as the sampling also remains consistent across the simulation. This would not necessarily be the case if simulated light curves were not generated from the data itself. It should be noted, however, that randomisation tests only evaluate the effects of random 'white noise', whereas signatures of low frequency 'red noise' will be destroyed by this process. Hence this method should be used with caution on datasets that contain signatures of red noise. Inspection of the LS periodogram in Fig. 2.8 illustrates that the light curve of IGR J17544−2619 is not affected by red noise, however, as there are no signatures of systematically increasing power at the longer period end of the spectrum. The absence of a red noise tail is a feature that is universal across the sample of SFXT IBIS light curves analysed.

The distribution of 200,000 randomly generated LS powers in the filtered light curve of IGR J17544−2619 is shown in Fig. 2.9. By calculating the LS powers below which 99.9, 99.99 and 99.999% of the distribution resides, the corresponding confidence levels are extracted at powers of 16.20, 18.41 and 20.42 respectively. The 99.999% confidence level is also over plotted on the LS periodogram of the true light curve in Fig. 2.8 and the 4.9 day period can be identified as a real signal to far in excess of 99.999% confidence. When a signal has been confirmed as being significant within a periodogram, the exact value and uncertainty of the detected periodicity must then be determined.

2.3.2 Period uncertainty calculation

A fundamental property of all methods of testing for periodicities (e.g. Fourier Transforms, Epoch-folding, LS periodograms) is that the evaluation is performed on a discrete set of frequencies and not a continuum of infinitesimally spaced frequencies. As a result there is a fundamental limit on the accuracy to which a periodic signal can be defined, being the separation of the test frequencies in its

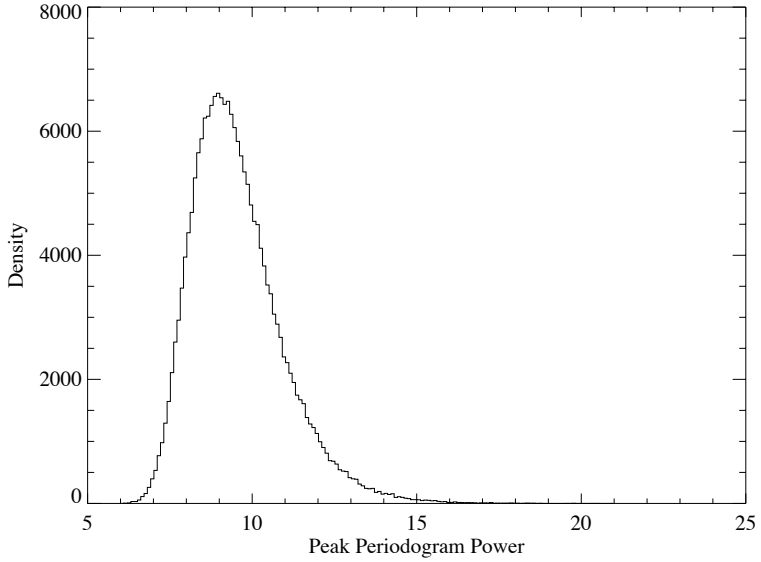

Figure 2.9: The distribution of LS periodogram peak powers generated in a 200,000 simulation randomisation test of the IBIS light curve of IGR J17544−2619. The 99.9, 99.99 and 99.999% confidence levels are drawn from this distribution at LS powers of 16.20, 18.41 and 20.42 respectively.

simplest interpretation. In the case of the analysis of observational data there are additional sources of noise that prevent the optimal characterisation of the signal, such as statistical uncertainty on the measurements and imperfect sampling of the light curve. To assess the stability of, and derive the uncertainty on, signals detected in IBIS light curves, a variant of the randomisation test is used which assesses the spread of the distribution of the particular period that is detected in a dataset as the count rates in the true light curve are 'blurred' within their 1σ error bars. Each blurred light curve is generated by deriving a random deviation from the central count rate value, drawn from a Gaussian distribution, for each point in the light curve. A LS periodogram of the blurred light curve is generated and the period at which the peak power is generated is recorded. Crucially, as the new data points retain the same temporal distribution as the true data, the exact same set of discrete frequencies is tested for in each iteration of the simulation.

This random blurring process is repeated until a well defined distribution of detected periods is developed. To characterise the shape of the distribution it is fit with a standard one dimensional Gaussian function of the form:

$$f(P) = A \exp(\frac{P - P_{cen}}{2\sigma_P^2}) \tag{2.1}$$

where A is the normalisation factor, P_{cen} is the central period and σ_P is the width (standard deviation) of the Gaussian function. Hence the fitted value of σ_P

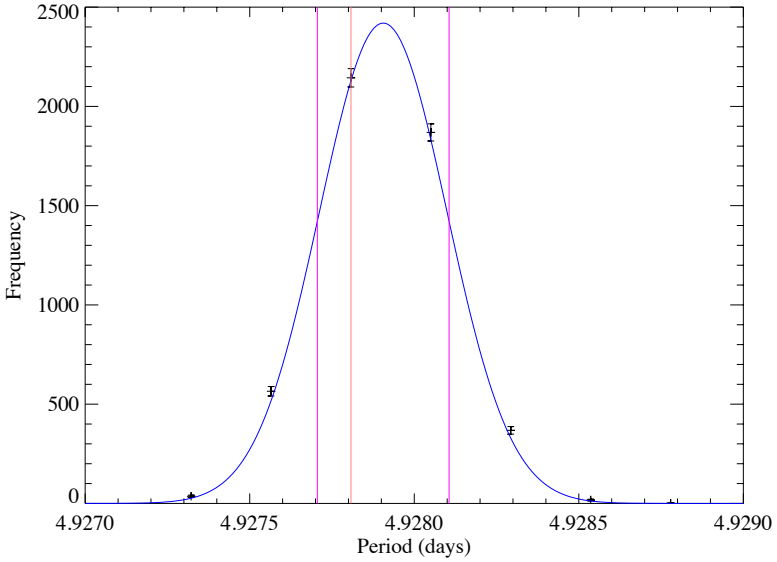

Figure 2.10: The distribution of peak periods detected through a 5000 simulation 'blurred count rate' randomisation test of the IGR J17544−2619 IBIS light curve. The number of detections of each period (black points), model Gaussian function (blue line) and 1σ width of the fitted Gaussian profile (magenta lines) are shown along with the period detected in the true data (orange line).

provides the 1σ uncertainty on the detected periodicity and the value of P_{cen} allows the discrete frequency spacing of the LS periodogram to be overcome.

The period distribution and fitted Gaussian function derived from 5000 blurring simulations of the filtered IGR J17544−2619 light curve is shown in Fig. 2.10. The black points are the distribution of detected periods from the simulations (with $\sqrt{N}$ uncertainties), the blue line is the fitted Gaussian curve, the vertical magenta lines illustrate the 1σ width of the Gaussian profile and the orange vertical line illustrates the period detected in the un-blurred light curve. The centroid of the fitted Gaussian curve in Fig. 2.10 is at a period of 4.9279 days and the width of the profile is 0.0002 days. The orbital period detected in the *INTEGRAL*/IBIS 18−60 keV light curve of IGR J17544−2619 is therefore defined as $4.9279 \pm 0.0002\,(1\sigma)$ days.

2.3.3 Orbital phase-folded light curves

Orbital phase-folded light curves can be generated once a suitably well defined period has been identified in an IBIS light curve. The orbital phase of each point is calculated using the orbital period and a zero phase ephemeris. Nominally the zero phase ephemeris used in the folding of IBIS light curves is the time of the first observation in the filtered dataset, however, in some cases a different zero phase will be defined, such as the time of the brightest outburst of a source. These different conventions are used as to date there are no dynamical solutions for the orbit of an SFXT to provide a definitive physical reference point. In this work the convention

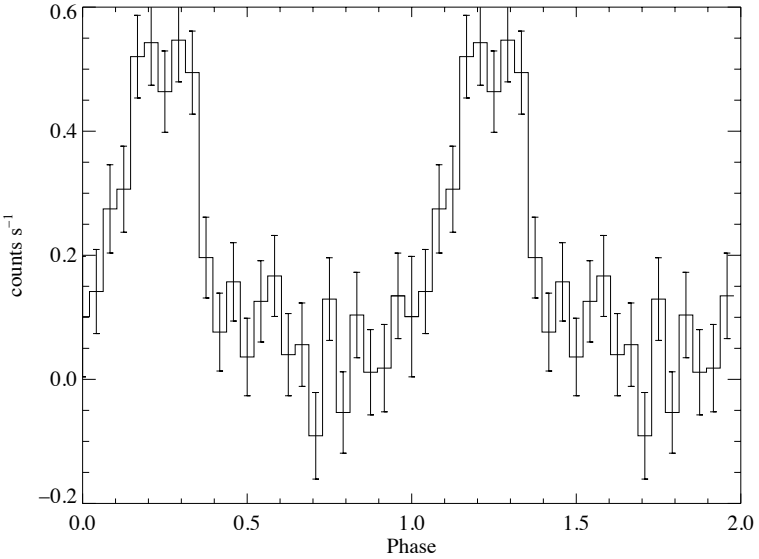

Figure 2.11: The orbital phase-folded light curve of IGR J17544−2619 using the best determined orbital period of 4.7929 days and a zero phase ephemeris of MJD 55924.271.

of the first IBIS data point is used to define the zero phase ephemeris unless stated otherwise. Using the determined orbital phase of each data point an average orbital profile of the detected emission is generated by grouping observations in to phase bins of a set width (a sample of 20 bins is typical) and taking the weighted mean and uncertainty on the weighted mean of each bin using expressions of the form:

$$\bar{x} = \frac{\sum_{i=1}^{n}(x_i/\sigma_i^2)}{\sum_{i=1}^{n}(1/\sigma_i^2)} \tag{2.2}$$

$$\sigma_{\bar{x}} = \sqrt{\frac{1}{\sum_{i=1}^{n}(1/\sigma_i^2)}} \tag{2.3}$$

where $\bar{x}$ and $\sigma_{\bar{x}}$ are the weighted mean and its uncertainty respectively and x_i and σ_i are the count rate and uncertainty of each observation collected into a phase bin.

The phase-folded light curve of IGR J17544−2619 derived by this method is shown in Fig. 2.11 and shows a peaked flux modulation that is at a maximum between an orbital phase of $\phi \sim 0.15 - 0.35$ and becomes consistent with zero between $\phi \sim 0.5 - 0.9$. The shape of this modulation is believed to arise from the orbital motion of a NS in an eccentric orbit with ϕ of 0.25 and 0.75 relating to the passage of periastron and apastron respectively. The shape of this profile is discussed further in Section 2.4.3.

Finally it should be noted that while the timing techniques and examples outlined here are focused on the LS analysis of *INTEGRAL*/IBIS data they are equally valid for the analysis of any data with well defined, non-zero count rate errors and for use with any method of periodicity testing such as Fourier Transforms, Epoch Folding or Phase Dispersion Minimisation techniques.

2.4 Outburst detection

Whilst the timing techniques described above are applicable to most light curves, the outburst detection techniques described in the following sections are designed specifically for the identification of outbursts from transient sources in long baseline light curves derived from coded aperture telescopes (i.e. *INTEGRAL*/IBIS, *Swift*/BAT). The example used in the following sections is that of the prototypical SFXT IGR J17544−2619. The transient *INTEGRAL* catalog source IGR J18136−2739 (Bird et al., 2010) is also used, for the sake of simplicity, in the detection significance considerations described in Section 2.4.2 as there is only a single detected outburst of this source to consider.

2.4.1 Outburst identification

As can be seen from Fig. 2.4 *INTEGRAL*/IBIS SFXT datasets have exceeded, by far, the length where manually searching for outbursts is a viable method of detection. For example the light curve of IGR J17544−2619 that was investigated for outbursts is drawn from 10,576 observations for a total exposure of ∼16.9 Ms. Instead an automated method of outburst detection has been developed to identify the small percentage of the time for which systems are active in the *INTEGRAL* band. The method used to locate the outburst activity searches the light curve for localised regions of high significance. This process is achieved by using a sliding window of varying size to calculate the local significance of each region of the light curve. The size of the window is defined in the time domain and ranges from 30 minutes (the approximate duration of an *INTEGRAL* ScW) to the lesser of 2 days or half of the binary orbit in the case of SFXTs. The window is stepped through the light curve at a resolution of one tenth of the window length and the combined significance of all the data points contained within it is calculated as $\bar{x}/\sigma_{\bar{x}}$ where $\bar{x}$ and $\sigma_{\bar{x}}$ are given by Eqs. 2.2 and 2.3 above. The length of the window is then increased by 30 minutes and the process repeated until all window lengths up to the maximum have been moved through the light curve. This process allows the light curve to be sampled at high resolution for each window length whilst reducing the computation time to manageable levels compared with using the finest resolution for all window lengths. Once this process is completed, the window with the highest

significance in the shortest time is identified as an outburst, the corresponding ScWs removed from the light curve and the identification procedure repeated to identify the next most significant section of the light curve. The identification procedure is iterated until all regions down to a minimum significance cutoff, nominally 4σ, have been identified.

As the uncertainties on each count rate are taken into account through the calculation of weighted means under this method, the IBIS light curves are not filtered for large off-axis angles and small exposure length when identifying outbursts as was the case for the timing techniques in Section 2.3. When applying the outburst identification algorithm described above to the IGR J17544−2619 light curve, 33 events were found with a significance of $\geq 4\sigma$. These events represent a preliminary outburst list, however, as the appropriate significance cut-off to be applied must be estimated from the statistical tests outlined in the next sections.

2.4.2 Significance limits

In the context of outburst identification, the sources of systematic uncertainty and random variations in the noise of the IBIS images, generated by the deconvolution-based image reconstruction described in Section 2.1, require a deeper consideration of the local significances calculated from the raw analysis of the light curve detailed above. In essence the problem lies in the fact that a '3σ source' in an IBIS image is not detected at the same significance as a '3σ source' in an image produced by focusing optics due to the higher variability of the background in images generated through coded aperture techniques. Additionally the large number of trials incurred during the outburst identification process samples the extreme end of the distribution of significances that can be generated randomly by the noise in the data at the position of a transient source when it is not active. Two methods of assessing both of these effects and placing an accurate cut-off on the minimum significance of an outburst to ensure it is of a physical origin are outlined in the following sections.

Inversion test

The first minimum significance test utilises the fact that noise in the light curve of a transient source during periods of non-detection will be equally distributed about zero due to the positive and negative correlations occurring in the shadowgram deconvolution. Therefore by running the burst-finding algorithm down to low significances (e.g 2σ) on both the true light curve and the true light curve inverted about zero, two separate distributions of the signature of the random noise in the light curve can be developed. For the light curve of a real transient source the low significance distribution should be the same for both the true and inverted light

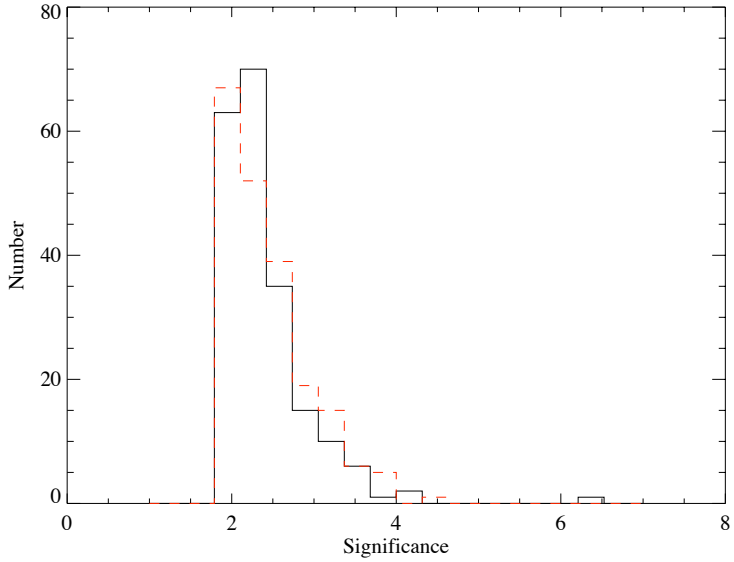

Figure 2.12: The distribution of the significance of events detected by the burst finding algorithm in the true (black) and inverted (dashed red) 20−40 keV IBIS ScW light curves of the transient catalog source IGR J18136−2739 (Bird et al., 2010).

curves, but an excess generated by the physical outbursts of the source would be observed at higher significances in the distribution of the true light curve. The maximum significance detected in the inverted light curve can therefore be used as a hard minimum on the significance of real outbursts as the events detected in the negative data points are not, by definition, of a physical origin.

Figure 2.12 shows the distribution of the significance of 'events' detected in the true (black) and inverted (dashed red) 20−40 keV light curve of IGR J18136−2739 (Bird et al., 2010). It is seen that both light curves produce a similar distribution extending out to $\sim 4.5\sigma$, illustrating that events detected in the true light curves at or below this significance are likely generated by random fluctuations within the noise. The event at 6.6σ identified in the true light curve appears to be an outlier of the distribution produced by the random noise in the light curve, however, and is therefore concluded to be of a real physical origin. By considering the total number of events detected in the noise distributions, the likelihood of the 6.6σ event being generated by a random event can be coarsely estimated as less than 1 in 200. This value should be considered a conservative lower limit on the true likelihood, however, as a fit to the noise distribution, assuming a Gaussian profile, would indicate that the separation of the 6.6σ event from the centroid of the distribution is of high significance. Such a method of estimating the likelihood of the 6.6σ event being generated through random noise is demonstrated in the following section using an independent method of deriving the noise distribution in the calculation.

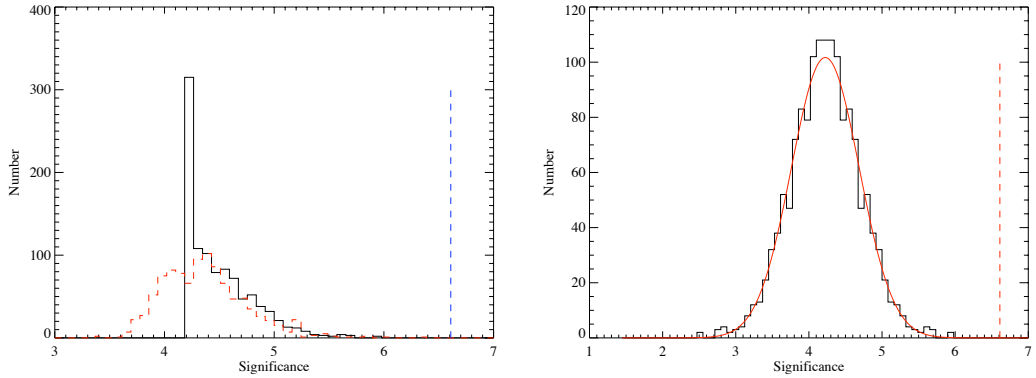

Figure 2.13: Left: The distributions of the events of maximum significance identified in 1000 randomised 20−40 keV light curves of IGR J18136−2739 in the case of searching down to a minimum test window of a single (black) and three (dashed red) ScWs. The vertical blue line shows the 6.6σ event detected in the true light curves as an outlier to these distributions. Right: Mirrored single ScW distribution (with the $\sim 4.2\sigma$ hard limit bin removed) fitted with a Gaussian curve.

Randomisation test

An independent test for the reality of identified events in a light curve is performed by building on the concept of the randomisation test used to define the confidence levels for periodic signals described in Section 2.3.1. In this case the data points in the light curve are randomised to test for the most significant event that can be generated as a result of random, unphysical combinations of data points within the dataset. The burst-finding algorithm was used to identify the most significant event in 1000 randomised light curve and distributions accumulated. The black line in the left panel of Fig. 2.13 illustrates the distribution accumulated from the randomised light curves of IGR J18136−2739 in the case where they were searched down to a minimum window of a length consistent with a single ScW. The distribution displays a large spike at $\sim 4.2\sigma$ followed by a smooth, approximately Gaussian, decline at higher significances. The origin of the large spike is the ScW in the light curve that has the highest individual significance of $\sim 4.2\sigma$. This ScW acts as a hard limit on the significance as it is detected as the most significant event in every simulation where multiple ScWs do not randomly align to generate a higher significance. The dashed red line illustrates the removal of this hard limit when a simulation is performed that only searches to a minimum window length equivalent to three ScWs such that it is always a combination of ScWs that produces the maximal event and the influence of the single, most significant ScW is reduced. The distributions generated at significances greater than the hard limit in both simulations are seen to be consistent.

The 6.6σ event identified in the true source light curve of IGR J18136−2739 is again observed as an outlier of the distributions generated by the randomised simulations.

The profile of the randomised distributions can be used to estimate the confidence level to which it can be concluded that the 6.6σ event is a real outburst. The right panel of Fig. 2.13 shows the single ScW derived distribution mirrored about the location of the hard limit (with the large peak removed) which allows the fitting of a Gaussian curve to the simulated profile generated above the hard limit when searching down to single ScW timescales. The Gaussian profile has a width (σ_g) of 0.464 and the 6.6σ event is separated from the centre of the profile by $5.14\sigma_g$. Hence it can be concluded that the 6.6σ event detected in the true IGR J18136−2739 20−40 keV light curve is a real outburst of the source, and not generated by a random statistical fluctuation, to a confidence level of greater than 99.999%.

By performing the tests described above, the preliminary set of outbursts defined by the burst finding algorithm can be filtered for events that are likely caused by random statistical fluctuations in the data which are identified as a result of the large number of trials incurred by the automated outburst procedure. The final set of confirmed physical outbursts of a source can then be utilised to investigate the nature of the transient system in which they are produced.

2.4.3 Outburst history of IGR J17544−2619

Applying the outburst significance limits derived with the above methods to the events identified in the light curve of the SFXT IGR J17544−2619 results in a final set of 31 outbursts detected at significances in the range of 27.9σ to 4.5σ between MJD 52698.174 and MJD 55968.030. The basic properties of these outbursts are outlined in Table 2.1 where the peak fluxes have been calculated assuming a thermal Bremsstrahlung spectral model with a plasma temperature of 10.4 keV as defined by the best fit to the spectrum extracted from the most significant outburst detected in the IGR J17544−2619 dataset ($\hat{\chi}^2 = 0.78\,(4\ d.o.f.)$). IGR J17544−2619 is detected in outburst for ∼225 ks of the ∼16.9 Ms dataset, corresponding to an outburst duty cycle of 1.3%. The 31 detected outbursts are shown over-plotted on the full 18−60 keV light curve in Fig. 2.14. In this figure the uncertainties of the non-outburst data points have been removed in order to view the identified outbursts with greater clarity. The need to weight count rates when calculating the significance of each data window in the burst finding algorithm is also emphasised in this figure by the large number of points that have a higher count rate than the brightest outbursts but are not detected as significant events when their uncertainties are taken into account.

At a cursory glance the outbursts highlighted in Fig. 2.14 appear as though they may be grouped into regions of greater and lesser frequency, suggesting a level of variability in the activity of the source. However, this effect can be seen to be a result of the overlapping data points in the plot preventing an accurate by eye

Table 2.1: Complete outburst history of IGR J17544−2619 identified in the archival *INTEGRAL*/IBIS dataset. The orbital phase given relates to the ScW with the maximal count rate in each event. The peak flux is that of the same ScW in the 18 - 60 keV band, calculated assuming a thermal Bremsstrahlung model with a temperature of 10.4 keV as measured from the spectrum of the most significant outburst detected.

Significance	Start MJD	End MJD	Duration (hours)	Orbital Phase ϕ	Peak Flux erg cm^{-2} s^{-1}
6.0	52732.35	52732.39	0.9	0.26	2.8×10^{-10}
29.7	52899.05	52899.58	12.6	0.09	9.7×10^{-10}
5.0	52904.01	52904.58	13.6	0.21	2.3×10^{-10}
5.3	53062.34	53062.21	20.9	0.24	4.6×10^{-10}
6.0	53067.28	53067.49	5.1	0.24	2.3×10^{-10}
26.0	53072.36	53072.50	3.5	0.28	1.4×10^{-9}
11.6	53072.54	53072.70	4.1	0.30	4.6×10^{-10}
9.9	53269.89	53270.08	4.5	0.38	3.8×10^{-10}
5.1	53422.34	53422.36	0.6	0.28	5.1×10^{-10}
8.7	53441.23	53441.25	0.4	0.12	5.1×10^{-10}
5.1	53451.41	53451.50	2.0	0.20	2.5×10^{-10}
10.7	53481.26	53481.33	1.6	0.24	3.9×10^{-10}
5.9	53628.73	53628.87	3.3	0.18	3.6×10^{-10}
11.7	53658.35	53658.36	0.3	0.18	6.5×10^{-10}
5.8	53658.37	53658.41	0.9	0.19	2.4×10^{-10}
16.0	53806.87	53807.04	4.1	0.32	6.8×10^{-10}
5.6	53850.87	53851.11	2.7	0.29	4.5×10^{-10}
8.0	53987.52	53987.59	1.6	0.99	3.2×10^{-10}
11.3	53998.42	53998.60	4.3	0.19	9.9×10^{-10}
9.6	54343.56	54343.63	1.6	0.24	4.1×10^{-10}
11.4	54364.25	54364.32	1.9	0.43	5.0×10^{-10}
11.1	54367.23	54367.25	0.6	0.03	5.2×10^{-10}
4.8	54545.89	54545.95	1.5	0.29	2.0×10^{-10}
20.3	54560.24	54560.36	2.7	0.20	1.1×10^{-9}
4.5	54560.37	54560.63	6.1	0.22	1.9×10^{-10}
5.4	54570.44	54570.45	0.2	0.27	5.6×10^{-10}
8.8	54708.09	54708.17	1.9	0.21	4.3×10^{-10}
5.2	54886.35	54886.42	1.6	0.39	1.9×10^{-10}
5.8	54938.38	54938.39	0.3	0.93	3.7×10^{-10}
6.8	55067.64	55067.96	7.6	0.17	2.5×10^{-10}
12.4	55437.96	55438.02	1.4	0.31	5.7×10^{-10}

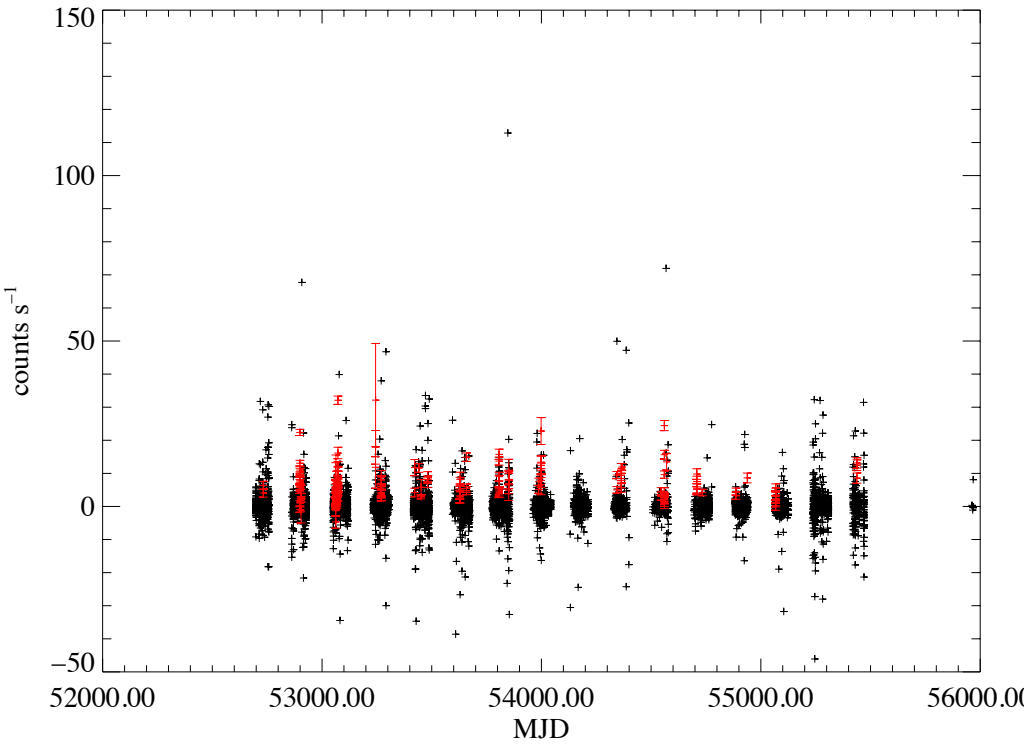

Figure 2.14: IBIS 18−60 keV light curve of IGR J17544−2619 with the 31 confirmed outbursts identified by the red points. The data points that do not originate from times of outburst have had their error bars removed for the sake of clarity. The notable outliers within the black points are ScWs with large uncertainties resulting from short exposures or IGR J17544−2619 being located at a large off-axis angle.

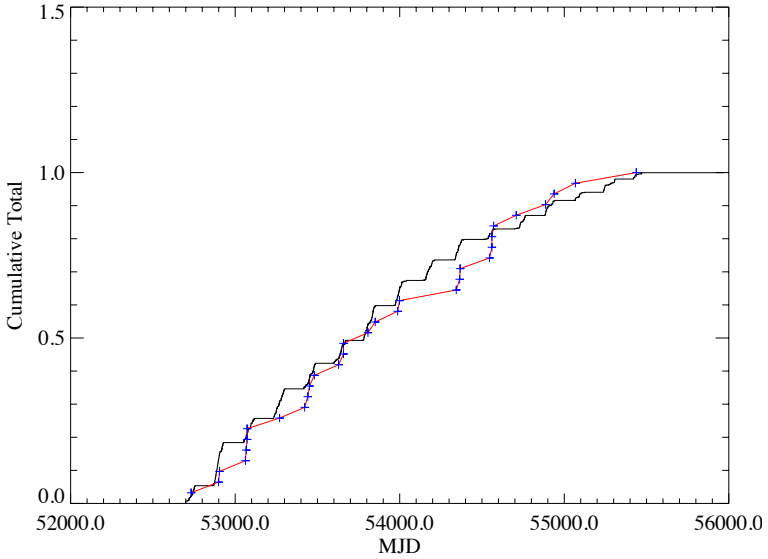

Figure 2.15: The cumulative distributions of the exposure time (black curve) and number of outbursts (red curve with times of the individual outbursts indicated by blue points) detected in the *INTEGRAL*/IBIS dataset of IGR J17544−2619. The rate of outburst detection is observed to follow closely the rate of increase of exposure in the dataset removing the need for any intrinsic variability in the activity of the source.

estimation of the exposure in each region of the light curve. Figure 2.15 illustrates the normalised cumulative distributions of exposure (black) and detected outbursts (red line, blue points illustrate the times of each outburst) across the IBIS light curve and it is seen that the number of outbursts detected scales directly with the on-source exposure achieved by *INTEGRAL*, ruling out the need for an intrinsic long term variability in the source activity. It is also of note that the rate of increase of exposure, and therefore outburst detection, decreases from approximately MJD 54300 (July 2007) onwards. This date is consistent with the cessation of the original *INTEGRAL* key programme within which Galactic Plane scanning observations were a key component. In subsequent years the increase in exposure of many SFXTs decreased, resulting in lower outburst detection rates. As of May 2011, however, a Galactic Plane scanning programme was reinitialised (Bazzano et al., 2011) which should yield an increase in the rate of SFXT outburst detection in the coming years.

Clark et al. (2009) identified the orbital period of the IGR J17544−2619 system as 4.926±0.001 days using an *INTEGRAL*/IBIS dataset of ∼8 Ms. Using the timing analysis techniques described above the orbital period determination was improved to 4.9279±0.0002 days when applied to the optimally filtered light curve of a 14.9 Ms dataset. This temporal information can be combined with the times of the detected outbursts to identify their distribution in orbital phase. Figure 2.16 shows the IBIS phase-folded light curve (left) and the orbital phase distribution of

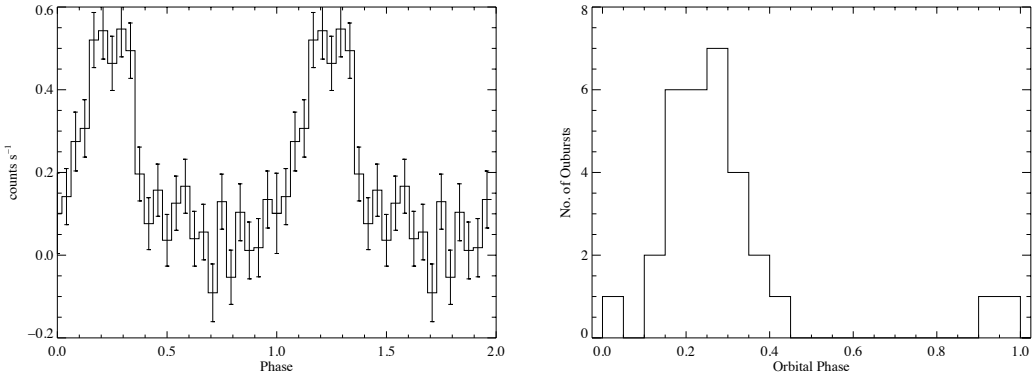

Figure 2.16: Left: The orbital phase-folded 18−60 keV IBIS light curve of IGR J17544−2619 using the orbital period and zero phase ephemeris of 4.9279 days and MJD 55924.271 respectively. Right: The orbital phase distribution of the 31 outbursts detected by IBIS using the same orbital parameters. The peaked profiles observed over a consistent orbital phase range in both plots is highly indicative of the NS occupying an orbit with significant eccentricity in IGR J17544−2619.

outbursts (right) folded on the 4.9279 day orbital period with a zero phase ephemeris of MJD 55924.271 (the date of the first IBIS observation of the source brought forward to January 2012). Both the phase-folded light curve and the outburst distribution are peaked between $\phi \sim 0$ and 0.4, with no outbursts detected between ϕ of 0.45 and 0.9, at which time the phase-folded light curve is also consistent with zero. These profiles suggest that IGR J17544−2619 is comprised of a NS in an eccentric orbit about the supergiant that produces X-ray emission during periastron passage. Therefore the 'prototypical' SFXT IGR J17544−2619 appears to fit into the SgXRB unification model presented by Chaty (2008b). It is worth noting, however, that as a dynamical orbital solution has not yet been achieved for any member of the SFXT class, the nomenclature of 'periastron' generally refers to the orbital phase of peak detected emission from a source with 'apastron' being separated by a phase interval of 0.5. It is this convention that is used throughout this thesis. It will not be possible to assess the relationship between the phase of peak flux and physical closest approach in SFXT systems until dynamical orbital solutions have been achieved. Further detailed discussions on the nature of IGR J17544−2619 are provided in Chapter 4.

2.5 Summary

The techniques described in this chapter allow the detailed characterisation of the properties of SFXTs in the hard X-ray band. To further understand this sub-population of SgXRBs, however, requires not only the continued coverage of these sources in the hard X-ray band, but also in-depth study at other wavelengths, particularly the soft X-ray band. The following chapters present studies of

individual SFXT systems utilising *INTEGRAL* data to, not only characterise their hard X-ray behaviour using the methods described above, but to also provide the temporal basis for in-depth orbital phase targeted follow-up observations with *RXTE* and *XMM-Newton*. The results of these observations and their impact on the knowledge of the individual systems are discussed in each chapter along with wider considerations of the current understanding of the nature of the SFXT class as a whole in Chapter 6.

Chapter 3

INTEGRAL and *XMM-Newton* observations of IGR J16418−4532: evidence of accretion regime transitions in a supergiant fast X-ray transient

3.1 Introduction

IGR J16418−4532 was first detected by *INTEGRAL* during observations of the transient black hole system 4U 1630−47 between 2003 Februrary 1−5 with an average flux of 3×10^{-11} erg cm^{-2} s^{-1} 20−40 keV (Tomsick et al., 2004). IGR J16418−4532 was proposed as a member of the SFXT class by Sguera et al. (2006a) after the identification of a second short duration outburst from the system detected in two consecutive ScWs on 2004 February 26 that displayed variability on a timescale of hundreds of seconds. *XMM-Newton* observations reported by Walter et al. (2006) identified a neutron star pulse period of 1246 ± 100 s (later refined to 1212 ± 6 s by Sidoli et al. 2012) along with a high ($\sim 10^{23}$ cm^{-2}) X-ray absorption intrinsic to the system. The source was also localised to arcsecond accuracy and the IR counterpart proposed as 2MASS J16415078−4532253, which was later confirmed by Romano et al. (2012) through a *Swift*/XRT source localisation of RA,Dec (J2000) = 16^h 41^m $50^s.65$, -45^o 32$'$ 27$''.3$ with an uncertainty of $1''.9$ (90% confidence). Corbet et al. (2006) identified a short, eclipsing orbit of 3.7389±0.0004 days and 3.753±0.004 days in the system using *RXTE*/ASM and *Swift*/BAT datasets respectively (the statistical discrepancy in these two values is likely due to an underestimate of either one or both uncertainties). Levine et al.

(2011) recently improved these determinations to 3.73886 ± 0.00028 days using *RXTE*/ASM data over an ~ 14 year baseline and an enhanced periodicity searching technique using weighted ASM measurements and de-trended light curves. Combining the orbital and pulse periods places IGR J16418−4532 in the wind-fed Sg-XRB region of the Corbet diagram (Fig. 1.6, Corbet 1986). Chaty et al. (2008a) performed optical and IR photometry on the IR counterpart of IGR J16418−4532 and produced a broadband Spectral Energy Distribution (SED). By fitting an absorbed black body component, representing the companion star emission, to the optical through MIR photometric data within the SED, a stellar temperature of 32,800 K was determined for the companion suggesting it is of spectral type OB. Along with the location of IGR J16418−4532 in the Corbet diagram, the SED results confirmed the HMXB nature of this system and implied a minimum distance of ~ 13 kpc when assuming a supergiant companion. The supergiant nature of the companion was recently confirmed by Coleiro et al. (2013, private communication) who classified the companion as a BN0.5Ia nitrogen rich supergiant, thus confirming IGR J16418−4532 as a intermediate SFXT.

The maximal X-ray dynamic range observed in IGR J16418−4532, greater than 10^2 in the soft X-ray regime (Romano et al. 2012, Sidoli et al. 2012), is in excess of that observed from classical, wind-fed Sg-XRBs with comparable orbital parameters. Through modelling the flare - luminosity distribution observed during an intensive *Swift*/XRT monitoring campaign of IGR J16418−4532, Romano et al. (2012) concluded that the enhanced level of variability in this system could be described by the NS accreting stellar wind clumps in the mass range 10^{16} - 10^{21} g embedded in a highly structured wind with a terminal velocity between 800 and 1300 km s^{-1} (using the Ducci et al. (2009) formulation of the 'clumpy wind' scenario of SFXT outbursts (in't Zand 2005, Walter & Zurita Heras 2007)). However, using a 40 ks *XMM-Newton* observation in 2011, Sidoli et al. (2012) argue that the observed X-ray variability, orbital dynamics and quasi-periodic flaring activity is indicative of the NS accreting in a regime that is transitional between pure wind accretion and full Roche lobe overflow (RLO). It is argued that such a 'Transitional Roche Lobe Overflow (TRLO)' regime could be the dominant source of the observed X-ray variability in SFXTs with short orbital periods.

In this chapter new quasi-simultaneous, orbital phase targeted *INTEGRAL* and *XMM-Newton* observations of IGR J16418−4532 are presented, along with a study using archival *INTEGRAL* data. In Section 3.2 the datasets, analysis and results from both the archival and new *INTEGRAL* observations are outlined. Section 3.3 presents the analysis of, and results from, the new *XMM-Newton* dataset. These results are then discussed in Section 3.4 and final conclusions drawn in Section 3.5.

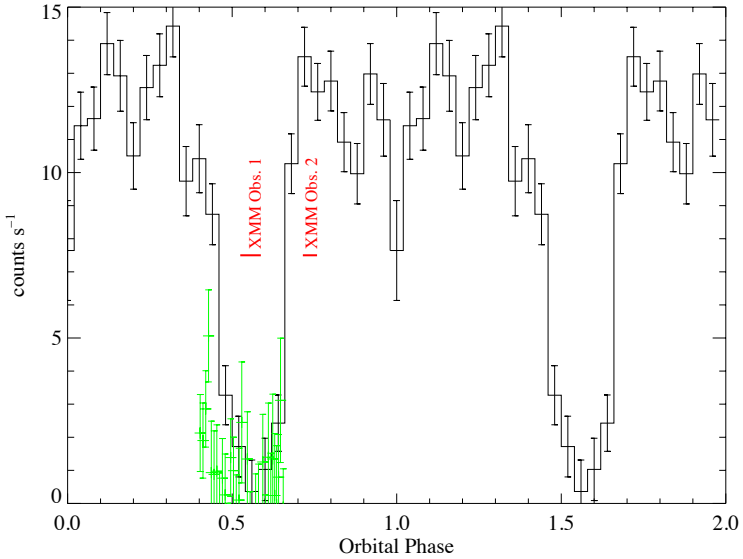

Figure 3.1: Archival *INTEGRAL*/IBIS 18 − 60 keV light curve of IGR J16418−4532 (scaled by a factor of 10) folded on P_{orb} = 3.73886 days with the zero phase ephemeris MJD 53560.20. The new IBIS observations are shown by the green points and the phase locations of the *XMM-Newton* observations are shown in red.

3.2 *INTEGRAL* data analysis and results

The archival *INTEGRAL*/IBIS dataset consisted of all observations of IGR J16418−4532 spanning 2003 January 11 through 2010 September 30, providing a total exposure of ∼10 Ms. ScW images were generated in the 18−60 keV band using version 9 of the OSA software and an archival light curve extracted following the methods outlined in Section 2.2. The new *INTEGRAL* observations were performed between UTC 09:57:33 2012-09-01 and 09:00:29 2012-09-02 for a total exposure of ∼78 ks. Images were again generated in the 18−60 keV band and a light curve extracted following the standard procedure.

Applying the timing analysis techniques outlined in Section 2.3 identified a significant periodicity of 3.7399 ± 0.0003 days in the archival dataset. This value is consistent, within 2σ, with the orbital period of 3.73886 ± 0.00028 days reported by Levine et al. (2011), which was identified in an *RXTE*/ASM dataset spanning 14 years. As the Levine et al. (2011) determination has a slightly better constraint and originates from a longer dataset it is this value of the orbital period that will be used for the remainder of this work. Additionally, to maintain consistency with previous work on the IGR J16418−4532 system, the zero phase ephemeris of MJD 53560.200 (Corbet et al., 2006) will be used throughout.

Figure 3.1 shows the archival 18 − 60 keV IBIS light curve folded on the 3.73886 day orbital period and scaled here by a factor of 10 for illustrative purposes.

Additionally the 18 - 60 keV ScW light curve of the new *INTEGRAL* observations is superimposed in green and the orbital phase locations of the *XMM-Newton* observations are shown in red (see below for further details). The orbital profile is dominated by the deep eclipse that spans ∼0.2 of the phase space between $\phi = 0.45$ and 0.65, corresponding to a duration of ∼0.75 days, and is consistent with the neutron star being fully eclipsed at its centre. Outside of the eclipse, the orbital profile is consistent with a constant flux at an unscaled IBIS count rate of ∼1.2 counts per second, corresponding to a flux of 7 mCrab in the $18 - 60$ keV band, showing that the eclipse is the driving factor in generating the observed periodicity.

The archival $18 - 60$ keV light curve was also searched for outbursts of duration 0.02 to 3 days using the techniques described in Section 2.4. The minimum real outburst significance defined by the inversion test was determined as 3.7σ. Applying this cut-off to the original set of excesses produced 35 distinct outburst events within the archival light curve down to a minimal significance of 4.48σ and with durations in the range ∼0.02 to 1.3 days. 16 of the 35 detected outbursts have already been reported in previous works (see Sguera et al. 2006a, Ducci, Sidoli, & Paizis 2010) while the remaining 19 are new detections, the main properties of which are reported in Table 3.1.

The total duration of these outbursts places the active duty cycle of IGR J16418−4532 at 6.14%. This figure is somewhat higher than that derived from the results of Ducci, Sidoli, & Paizis (2010) who give a duty cycle of ∼1.3%. Whilst the analyses were performed on data from different energy bands ($18 - 60$ keV here and $20 - 40$ keV in Ducci, Sidoli, & Paizis 2010) and on datasets of different total exposure, it is likely the difference in the methods used to identify outbursts in each work is the main cause of this disparity. Ducci, Sidoli, & Paizis (2010) consider only the ScWs in which IGR J16418−4532 was detected at a significance of $> 5\sigma$ from which to define outbursts whereas here we consider all ScWs in our searches and model the outburst significance cutoff to apply as described in Section 2.4.2. Under this method an outburst search becomes sensitive to a population of longer, fainter outbursts which are below the formal detection threshold for a known source in a single ScW (i.e. 5σ) but sum to a significant detection when the multiple ScWs of an outburst are combined. The extent to which the size of the increase in the active duty cycle observed for IGR J16418−4532 is specific to this source or represents a more global phenomenon, however, requires further investigation. Figure 3.2 shows the distribution, in orbital phase, of the peak emission from each identified outburst. It can be seen that, apart from the eclipse region where no outbursts are detected, there is no coherent structure in the outburst distribution, which is consistent with the unstructured phase-folded light curve (Fig. 3.1). This implies that outbursts are equally likely to occur at any point in the orbital phase.

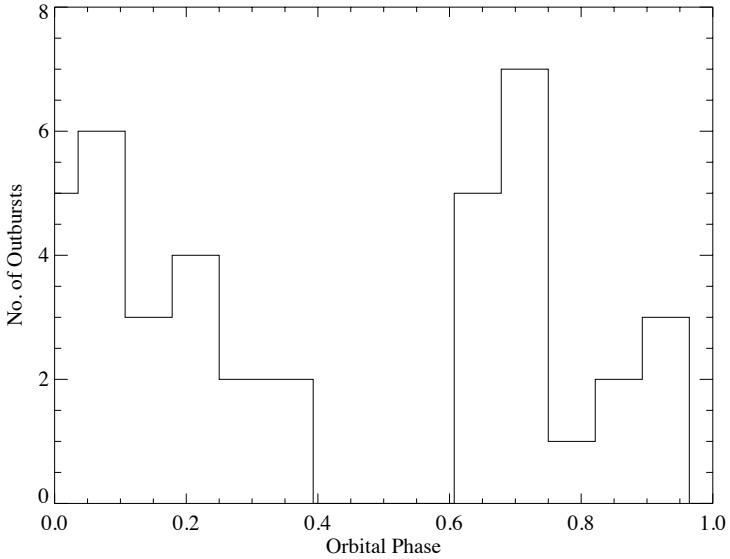

Figure 3.2: Orbital Phase Distribution of the archival IGR J16418−4532 outbursts using the ephemeris $P_{orb} = 3.73886$ days and a zero phase of MJD 53560.20.

The new *INTEGRAL* observations were constrained in orbital phase to cover the eclipse region of IGR J16418−4532's orbit, covering $\phi = 0.403$ through 0.655 using the above ephemeris. The light curve is shown by the green points in Fig. 3.1 and it can be seen to cover the eclipse ingress and fully eclipsed region but ends just before the egress. IGR J16418−4532 shows a low, but rising level of activity in the first 4 ScWs before the eclipse which is then cutoff sharply in the fifth ScW at an orbital phase consistent with the eclipse ingress. The source is not detected during the subsequent ScWs performed during the eclipse. A mosaic image of the first 5 ScWs was produced in which IGR J16418−4532 was detected at a significance of 6.1σ. A spectrum was extracted from these ScWs and fit with a powerlaw in XSPEC version 12.7.1 (Arnaud, 1996) with $\Gamma = 2.2^{+1.1}_{-0.7}$ and $\hat{\chi}^2 = 1.08(6\ dof)$. The corresponding $18 - 60$ keV flux was 1.4×10^{-10} erg cm^{-2} s^{-1}. A higher time resolution light curve with 1000 s bins was also extracted from these ScWs. This light curve is shown in Fig. 3.3 and it again displays a low level of activity, followed by an increase in flux at MJD 56171.53 which then rapidly drops again. The peak emission occurs at MJD 56171.537±0.0058, relating to an orbital phase of $\phi = 0.431$. Whilst it is possible that the flux variation could be due to X-ray flaring, the decrease in flux could also be resulting from eclipse ingress which would place a limit on the ingress duration of ~ 2000 s ($\Delta\phi = 0.006$) and provides an accurate eclipse ingress ephemeride. Unfortunately the signal-to-noise was insufficient to probe this emission at higher time resolutions.

IGR J16418−4532 was not detected in the soft $3 - 10$ keV X-ray band by the JEM-X instrument aboard *INTEGRAL* during these recent observations. The 3σ upper limit derived from the combined JEM-X1 and JEM-X2 mosaic image of all

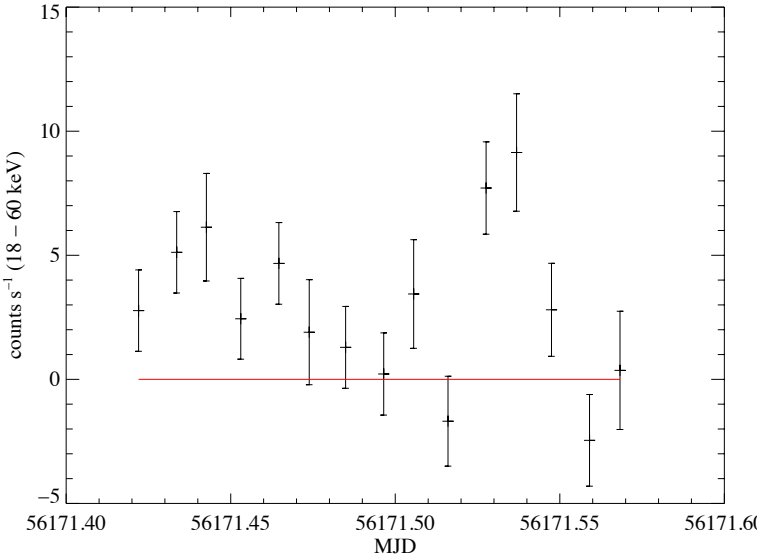

Figure 3.3: 1000 s binned 18 − 60 keV light curve of the low level activity observed during the first 5 ScWs of the recent *INTEGRAL*/IBIS observations of IGR J16418−4532.

ScWs where IGR J16418−4532 was in the FOV, giving a total exposure time of 14.5 ks the majority of which occurred whilst IGR J16418−4532 was in eclipse, is 3.4 mCrab (3 − 10 keV).

3.3 *XMM-Newton* data analysis and results

Two separate *XMM-Newton*/EPIC (Jansen et al. 2001, Turner et al. 2001, Strüder et al. 2001) observations were performed quasi-simultaneously with *INTEGRAL* to achieve sensitive soft X-ray coverage over a wider region of orbital phase. The first observation was performed between UTC 21:12:25 2012-09-01 and 02:53:22 2012-09-02 for an exposure of ∼20 ks. This observation covered the orbital phase range $\phi = 0.525 - 0.587$ and occurred whilst the NS was fully eclipsed by the supergiant. The second observation was performed after the NS had exited the eclipse, between UTC 14:16:33 and 19:12:03 2012-09-02, for an exposure of ∼14 ks and covered the orbital phase range $\phi = 0.715 - 0.758$. The phase location of these observations is shown in Fig. 3.1.

Data from both the EPIC-MOS and EPIC-pn detectors were analysed from each observation using SAS v12.0.1 (Gabriel et al., 2004) and the most recent instrument calibration files. The datasets were filtered for regions of high particle background following the method outlined in the *XMM-Newton* SAS data analysis threads[1]. The EREGIONANALYSE tool was used to define the optimal extraction region for

[1] http://xmm.esac.esa.int/sas/current/documentation/threads/

Table 3.1: Newly discovered outbursts of IGR J16418−4532 identified in the archival *INTEGRAL*/IBIS dataset. The orbital phase given relates to the ScW with the maximal count rate in each event. The peak flux is that of the same ScW in the 18 - 60 keV band, calculated assuming a powerlaw spectrum with $\Gamma = 2.2$ as observed in the activity at the start of the new *INTEGRAL*/IBIS dataset. Note: Fluxes denoted by a * are likely overestimates of the source flux due to large statistical uncertainties in the detected count rate.

Significance	Start MJD	End MJD	Duration (hours)	Orbital Phase ϕ	Peak Flux $\mathrm{erg\,cm^{-2}\,s^{-1}}$
6.3	52651.96	52652.21	5.8	0.14	2.3×10^{-9}*
11.8	52702.81	52703.61	19.4	0.71	2.2×10^{-10}
7.0	52711.66	52712.08	10.3	0.12	2.8×10^{-10}
7.3	52723.58	52724.23	15.6	0.37	1.7×10^{-9}*
7.3	52914.12	52914.59	11.3	0.29	4.8×10^{-10}
4.6	53107.99	53108.54	13.2	0.05	2.1×10^{-9}*
7.1	53430.09	53430.16	1.7	0.21	2.5×10^{-10}
6.6	53430.35	53430.38	0.7	0.27	2.7×10^{-10}
5.2	53455.90	53455.91	0.2	0.10	3.1×10^{-10}
8.3	54861.75	54861.81	1.7	0.13	4.6×10^{-10}
7.2	54868.76	54868.83	1.7	0.99	5.4×10^{-10}
5.7	55104.88	55104.92	1.2	0.15	3.2×10^{-10}
4.5	55239.69	55239.72	0.5	0.20	5.8×10^{-10}
6.6	55245.33	55245.71	9.1	0.72	2.5×10^{-10}
5.6	55257.83	55257.91	1.9	0.07	2.8×10^{-10}
8.6	55260.43	55261.11	16.3	0.77	2.2×10^{-10}
6.2	55287.64	55287.66	0.5	0.03	5.1×10^{-10}
5.9	55301.46	55301.60	3.1	0.73	2.7×10^{-10}
5.9	55429.87	55430.02	3.6	0.07	2.1×10^{-10}

all light curve and spectral generation procedures (note: all subsequent references to optimal extraction regions were defined using this method). The datasets were evaluated for the presence of photon pile-up using the EPATPLOT tool. The observations were found to be unaffected by pile-up apart from the final few ks of the second dataset, in which the pile-up effects were removed in the standard manner using annular extraction regions. The specific extraction regions used for both datasets are outlined in Sections 3.3.1 and 3.3.2. All spectra reported in this work were extracted following the standard procedures and the SAS tools RMFGEN and ARFGEN were used to extract the necessary response files for each spectrum. Spectra were again fitted using XSPEC version 12.7.1 with uncertainties quoted at the 90% confidence level throughout and the elemental abundances set to those of Wilms, Allen, & McCray (2000). Due to the very different nature of the detected emission in the two observations, the detailed analysis of each is reported separately in Sections 3.3.1 and 3.3.2 below.

3.3.1 Mid-eclipse Observation

Emission from IGR J16418−4532 was detected at a low level in the mid-eclipse observation (MEO) which, given its location in orbital phase, is assumed to originate from reprocessing of the NS X-ray flux by the stellar wind of the supergiant. There was insufficient signal to produce meaningful light curves and spectra in the MOS detectors so they are not considered further. Similarly in the pn detector only a low signal-to-noise light curve could be extracted in a broad (0.2 − 10 keV) energy band, but did not provide any detailed temporal information. It was possible to extract a meaningful spectrum from the full exposure of the pn detector, however. The spectrum was accumulated from an optimally defined circular extraction region of radius 14″. The background subtracted pn spectrum of the MEO, binned to a minimum of 25 counts per bin, is shown in the top panel of Fig. 3.4. It can be seen that the spectrum has a flat shape with a large emission feature consistent with the 6.4 keV iron-Kα line.

To further characterise the spectral shape of the pn spectrum it was first fit with a simple absorbed powerlaw continuum with an additional Gaussian component (PHABS(POWERLAW + GAUSSIAN) in XSPEC). The absorption was fixed to the Galactic value in the direction of IGR J16418−4532, 1.88×10^{22} cm^{-2} (Dickey & Lockman, 1990), as in this observation the powerlaw is simply parameterising a more complicated reprocessing mechanism and is unlikely to be describing the intrinsic, locally absorbed continuum emission. The power law index, Gaussian line energy and line width were left as free parameters. The spectrum was well fit by this model with $\hat{\chi}^2 = 1.02$ (8 *dof*), however, the Gaussian line width $\sigma_E = 0.15$ keV (EW =3.1 keV) corresponds to an electron plasma temperature of $\sim3\times10^6$ K which is well in excess of that expected for a supergiant atmosphere. This unphysical fit is

Table 3.2: IGR J16418−4532 MEO best fit EPIC-pn spectral parameters and uncertainties. The spectrum was fit using the model PHABS(POWERLAW + GAUSS + GAUSS) with N_H fixed and $\hat{\chi}^2 = 0.72$ (7 *dof*). The flux is quoted in the 0.5−10 keV band

Parameter	Value	Unit
N_H	1.88×10^{22}	cm^{-2}
Γ	$0.29\,^{+0.3}_{-0.3}$	
E_1 centroid	$6.40\,^{+0.03}_{-0.04}$	keV
E_1 EW	$0.63\,^{+0.28}_{-0.16}$	keV
E_1 intensity	4.9×10^{-6}	$\mathrm{ph\,cm^{-2}\,s^{-1}}$
E_2 centroid	$6.65\,^{+0.06}_{-0.05}$	keV
E_2 EW	$0.33\,^{+0.17}_{-0.15}$	keV
E_2 intensity	3.3×10^{-6}	$\mathrm{ph\,cm^{-2}\,s^{-1}}$
flux	$(2.80\,^{+0.34}_{-0.42})\times10^{-13}$	$\mathrm{erg\,cm^{-2}\,s^{-1}}$

likely resulting from the low signal-to-noise and coarsely sampled spectrum combined with the possible influence of the 7.1 keV iron absorption edge located within the emission line region of the spectrum.

To obtain a more physical characterisation of the iron line profile, the width of the Gaussian line was fixed at zero such that the line is intrinsically narrow and broadened only by the EPIC-pn response. Using a single Gaussian with the centroid energy as a free parameter provided a poor fit to the data ($\hat{\chi}^2 = 2.04$ (9 *dof*)) with large residuals in the region of the emission line. A second intrinsically narrow Gaussian was added at higher energy to account for emission from ionised iron and the spectrum fit with both line centroid energies left as free parameters. The resulting fit was of good quality with $\hat{\chi}^2 = 0.72$ (7 *dof*) and the line centroid energies $E_1 = 6.40\,^{+0.03}_{-0.04}$ and $E_2 = 6.65\,^{+0.06}_{-0.05}$ keV, consistent with both neutral 6.4 keV and ionised 6.67 keV Fe-Kα emission. The equivalent widths of the 6.40 and 6.65 keV lines were 0.63 and 0.33 keV respectively showing that the neutral emission is approximately twice the strength of the ionised emission. The $0.5 - 10$ keV detected flux was $(2.80\,^{+0.34}_{-0.42})\times10^{-13}$ erg cm^{-2} s^{-1}. The best fit parameters resulting from this model are outlined in full in Table 3.2 with the best fit model and residuals shown in Fig. 3.4, where the lower panels illustrate the improvement in the residuals as the Gaussian lines are added to the model.

3.3.2 Post-eclipse Observation

During the post-eclipse observation (PEO) IGR J16418−4532 was detected with good signal-to-noise. Figure 3.5 shows the $0.2 - 10$ keV EPIC-MOS1 (black) and MOS2 (red) light curves, extracted from optimally defined circular regions of radius $97''$ and $98''$ respectively, with time binning of 100 s. T_{zero} is defined as the first

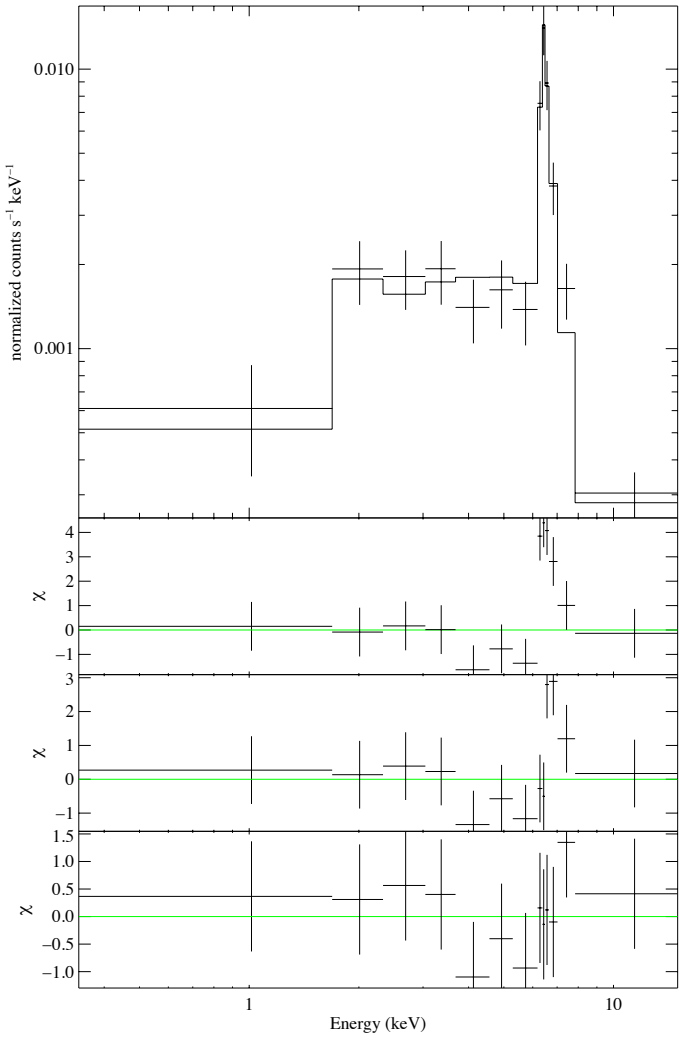

Figure 3.4: Top panel: EPIC-pn best fit spectrum of IGR J16418−4532 during the MEO. The spectrum is best fit with an absorbed powerlaw with two intrinsically narrow Gaussian emission lines at energies of $6.40\,^{+0.03}_{-0.04}$ and $6.65\,^{+0.06}_{-0.05}$ keV respectively. Lower panels: The three lower panels show the residuals of the fit when using an absorbed powerlaw, an absorbed powerlaw with one intrinsically narrow Gaussian and the best fit absorbed powerlaw with two intrinsically narrow Gaussians.

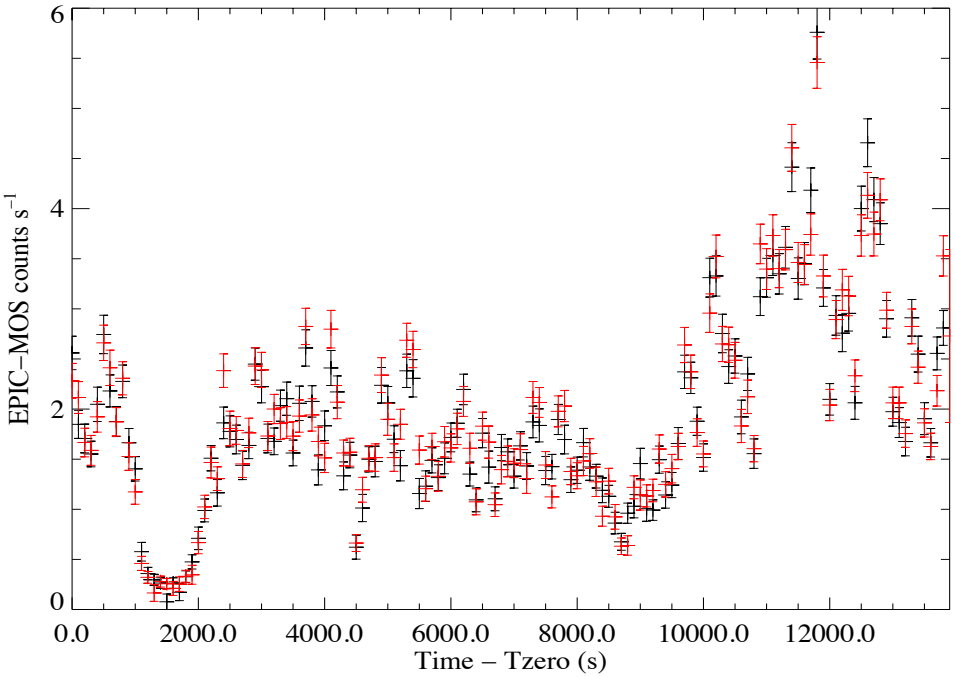

Figure 3.5: EPIC-MOS1 (black) and MOS2 (red) 100 s binned light curve of IGR J16418−4514 in the 0.2 − 10 keV band

time stamp in the MOS1 light curve and takes the value T_{zero} = MJD 56172.596. The light curves reveal a range of activities, including a steady emission at $\sim$ 2 counts s^{-1}, a rapid 'dipping' feature between t $\sim$ 800 and 2500 s and flaring behaviour at times of t > 10,000 s. There is also activity on short, hundreds of seconds timescales throughout the exposure, some of which may be due to the $\sim$1200 s pulse period. This activity was also observed in the EPIC-pn detector, the 100 s binned light curve of which is shown in the top panel of Fig. 3.6. The pn light curve was extracted from an optimal circular region of radius 68″. Due to additional observational overheads the pn detector did not start exposing until t = 1700 s, resulting in a lack of coverage during the majority of the 'dip' region observed by the MOS detectors. To account for the effects of pile-up at times greater than t = 10,000 s, annular extraction regions with inner radii of 7.5″ and 10″ for the MOS and pn detectors respectively were used to extract all data products.

The maximal dynamic range inferred from the 100 s binned broad band 0.2−10 keV light curves is 75 (MOS1) indicating a large variation in the flux detected during the relatively short exposure. 100 s binned light curves were also extracted in restricted 0.2−4 and 4−10 keV energy bands and the 0.2−4 / 4−10 keV hardness ratio (HR) calculated for each detector. The EPIC-pn HR is shown in the lower panel of Fig. 3.6 and it is seen to be composed of features on varying time scales. The most striking feature is the systematic hardening of the detected emission between t = 6000 and 10,000 s and the strong correlation between the HR and

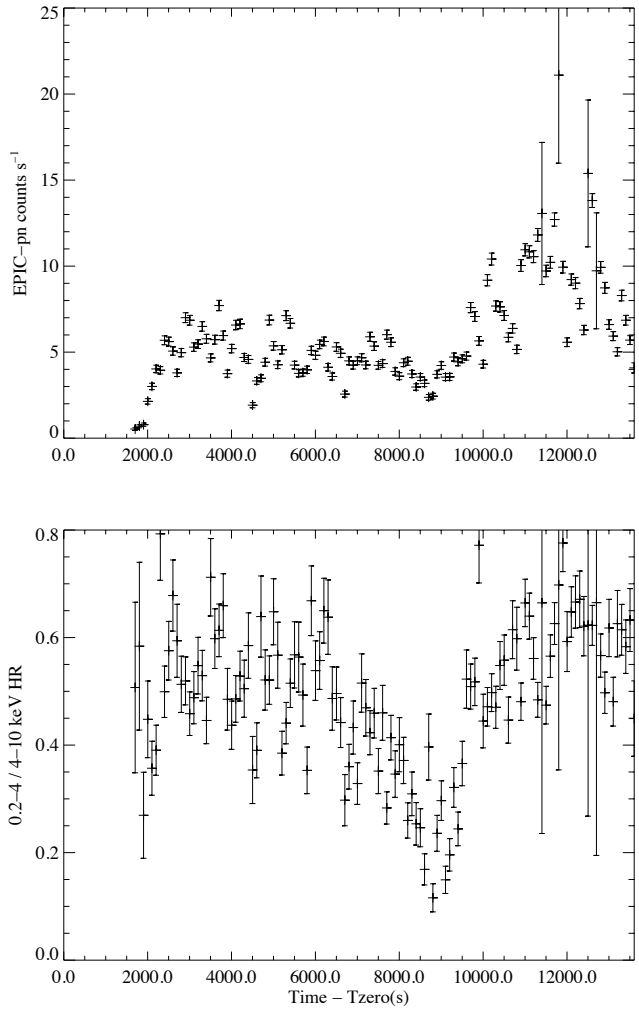

Figure 3.6: Top: EPIC-pn 100 s binned light curve of IGR J16418−4532 in the 0.2−10 keV band. Bottom: EPIC-pn 0.2−4 / 4−10 keV hardness ratio light curve at the same resolution where lower values indicate a hardening of the detected flux

detected source flux minima. The end of this hardening is also temporally coincident with the onset of the flaring behaviour observed from t = 10,000 s onwards. Variation is also observed on timescales of a few 100 s throughout the observation, regardless of flux level, and there is evidence of systematic softening of the detected emission as the source exits the 'dip' region of the light curve. HR light curves were also generated for the MOS detectors that showed the same evolution through the observation, albeit with less clarity due to the larger count rate errors, but could not provide additional diagnostics during the 'dip' region as a result of the limited photon statistics at this time.

Spectral Analysis

The lower panel of Fig. 3.6 illustrates the level and speed of variation in the emission of IGR J16418−4532 during the PEO through the evolution of the hardness ratio, implying fast variations in the detected source spectrum. In order to track these variations we extracted spectra accumulated from bins of length 400 s in steps of 200 s across the length of the exposure. An image was extracted for each time bin and the optimal extraction region for that region defined by the combination of EREGIONANALYSE and the circle/annulus shape constraints described above. Spectra were extracted, and binned to a minimum of 15 counts per bin, from both the MOS and pn detectors at times greater than t = 1700 s and the MOS detectors only prior to this. Such a systematic approach was adopted to remove possible biases introduced by the subjective selection of 'similar' regions while the extraction bin size of 400 s was chosen as a compromise between generating spectra of sufficient signal-to-noise to perform accurate fitting and reducing the amount of HR variation within each bin. The spectra were binned at 15 counts per bin to ensure a sufficient number of spectral bins to allow model fitting were present even in the spectra accumulated from the epochs of lowest flux. Step sizes of 200 s were chosen so that the evolution of spectral parameters could be followed at sufficient resolution but the data would only be over sampled by a factor of 2.

Inspection of the spectra showed no evidence of Fe emission lines so the spectra were fit with simple absorbed models to characterise their shapes. Absorbed powerlaws (PHABS(POWERLAW) in XSPEC) were simultaneously fit to the spectra from all available detectors in each time bin in the $0.5 - 15$ keV energy range with the absorption, powerlaw index and normalisation left as free parameters. The evolution of the spectral parameters, uncertainties and derived fluxes across the PEO are shown in Fig. 3.7. The plots inset in the second row of panels in Fig. 3.7 shows the $\hat{\chi}^2$ value of the fit to each bin throughout the observation. For the majority of the exposure time the $\hat{\chi}^2$ values are distributed about 1.0 showing a good fit to the spectra. However, bins falling within the 'dip'

region of the observation, in particular those occurring during the deepest part of the 'dip', gave unacceptable $\hat{\chi}^2$ values, indicating that an absorbed powerlaw is a poor description of the emission at these times. The spectra of this region are considered separately and in more detail below. For the rest of the observation it can be seen that when both N_H and Γ are left as free parameters (left column of Fig. 3.7) there is a level of variation in both parameters. However, a Chi-Squared test to the mean value of each parameter, where both the mean and Chi-squared statistic have been calculated with the poorly fitted bins omitted, gave a $\hat{\chi}^2$ value of 0.65 (67 *dof*) and 3.52 (67 *dof*) for Γ and N_H respectively. Hence the Γ parameter is consistent with being constant throughout the observation, whilst the absorption shows excess variation. The average Γ value is 1.195 and is over plotted as the red line in the second row of Fig. 3.7 (left).

A second set of fits was then performed with Γ fixed at the value of 1.195, whilst the normalisation and N_H were left as free parameters. The evolution of the spectral parameters and the goodness-of-fit in this case are shown in the right hand column of Fig. 3.7. A similar, better constrained N_H evolution as that seen in the left hand column of Fig. 3.7 is again observed when fitting a powerlaw of fixed Γ, with this model providing an acceptable fit for all bins apart from those occurring during the 'dip' feature. The N_H evolution shows that there is a constant, high level of absorption, $N_H \sim 7{\times}10^{22}\,\mathrm{cm}^{-2}$, that is intrinsic to the IGR J16418−4514 system (the Galactic value in the direction of the source is $1.88{\times}10^{22}$ cm^{-2}). The most striking feature of the evolution is the large, structured increase in N_H between t = 6500 and 9500 s which is co-incident with the 'Pre-flare hardening' feature observed in the HR. In particular the peak N_H is again temporally coincident with the HR and detected flux minima. Figure 3.8 shows an expanded view of the N_H evolution overlaid with the unabsorbed flux from each bin, calculated assuming the fixed powerlaw of $\Gamma = 1.195$. It is seen that removing the effects of absorption brings the flux back up to the level seen before the N_H increase, but it is not until after the N_H has returned to its base level that the large increase in flux starts to occur. Consideration of the physical interpretation of this behaviour is given in Section 3.4. Outside of the large increase the N_H also shows some level of variation that occurs on the same time scale as the NS pulsation ($\sim$1200 s). This variation is more pronounced in the spectral fits performed with a fixed Γ, adding to the justification for fixing the photon index as this produces spectral variations that may be linked to a physical origin whereas fixing the N_H and allowing Γ to vary only produces fits with very poor $\hat{\chi}^2$ values.

The time resolved spectra were also fit with the more complicated 'Partial Covering' absorption model (PCFABS in XSPEC) in an attempt to better understand the evolution of the absorbing material during the PEO. However, it was seen that the fits were insensitive to the additional parameters, with the covering fraction tending towards 100% for all spectra while the total N_H (the combination of a component

fixed to the galactic value and a free varying, partial covering component) was consistent with the best fit value for the simple absorbed powerlaw model. Hence no additional information could be drawn from this model. The time resolved spectral analysis was performed with different bin durations, step sizes and over sampling factors and the evolution was observed to follow a consistent path regardless of the extraction used. As a final test a blackbody continuum was used in place of the powerlaw model. A consistent N_H and flux evolution, with a similar distribution of $\hat{\chi^2}$ values, was observed throughout the observation producing further evidence that the evolution is explained by a relatively constant continuum modified by a varying photoelectric absorption. For the remainder of this work we refer only to the simple absorbed powerlaw fits when discussing the spectral evolution.

To characterise the emission during the dip region of the light curve a separate EPIC-pn spectrum was accumulated encompassing all available EPIC-pn data of the region, namely between $t = 1678$ s and $t = 2000$ s for a total exposure of 322 s. The spectrum showed no indication of Fe emission lines and was fit with a simple absorbed powerlaw where Γ was fixed to 1.195 (as above) and the best fit $N_H = (11.1^{+2.8}_{-2.1}) \times 10^{22}\,\mathrm{cm}^{-2}$. The $\hat{\chi^2} = 0.72(15\ dof)$ and the corresponding $0.5-10$ keV unabsorbed flux was $2.0\times10^{-11}\,\mathrm{erg\,cm^{-2}\,s^{-1}}$. When compared to the maximum, unabsorbed flux detected later in the observation ($27.2\times10^{-11}\,\mathrm{erg\,cm^{-2}\,s^{-1}}$ $(0.5-10\,\mathrm{keV})$) a soft X-ray dynamic range of 14 is observed during the PEO.

Timing Analysis

To test for signatures of the known 1212 ± 6 s NS spin period (Sidoli et al., 2012) the $0.2-10$ keV light curves from each instrument were re-extracted with a variety of bin sizes. Here we report on the results from light curves with a binning of 10 s but point out that the results were consistent in the analysis of each different binning. For the purposes of temporal analysis the 'dip' region of each light curve was removed as it occurs over a similar timescale to the known pulsation and could therefore generate significant power at frequencies similar to that of the NS pulse period, despite it not necessarily being of a rotational nature. The Lomb-Scargle technique was again applied to the light curves and strong signals detected at $\sim$403 s in all detectors. From here we consider only the MOS2 light curve as it has a longer baseline than that of the pn and the results are consistent with those from MOS1. The uncertainty on the peak was calculated using the method outlined in Section 2.3 and the peak period found to be 403.04 ± 0.14 s. This is consistent with being the third harmonic of the known pulse period, with the fundamental frequency relating to a period of 1209.12 ± 0.42 s. This spin period is consistent with the previously reported values, summarised in Sidoli et al. (2012), and with the addition of this detection there is still no significant detection of spin period

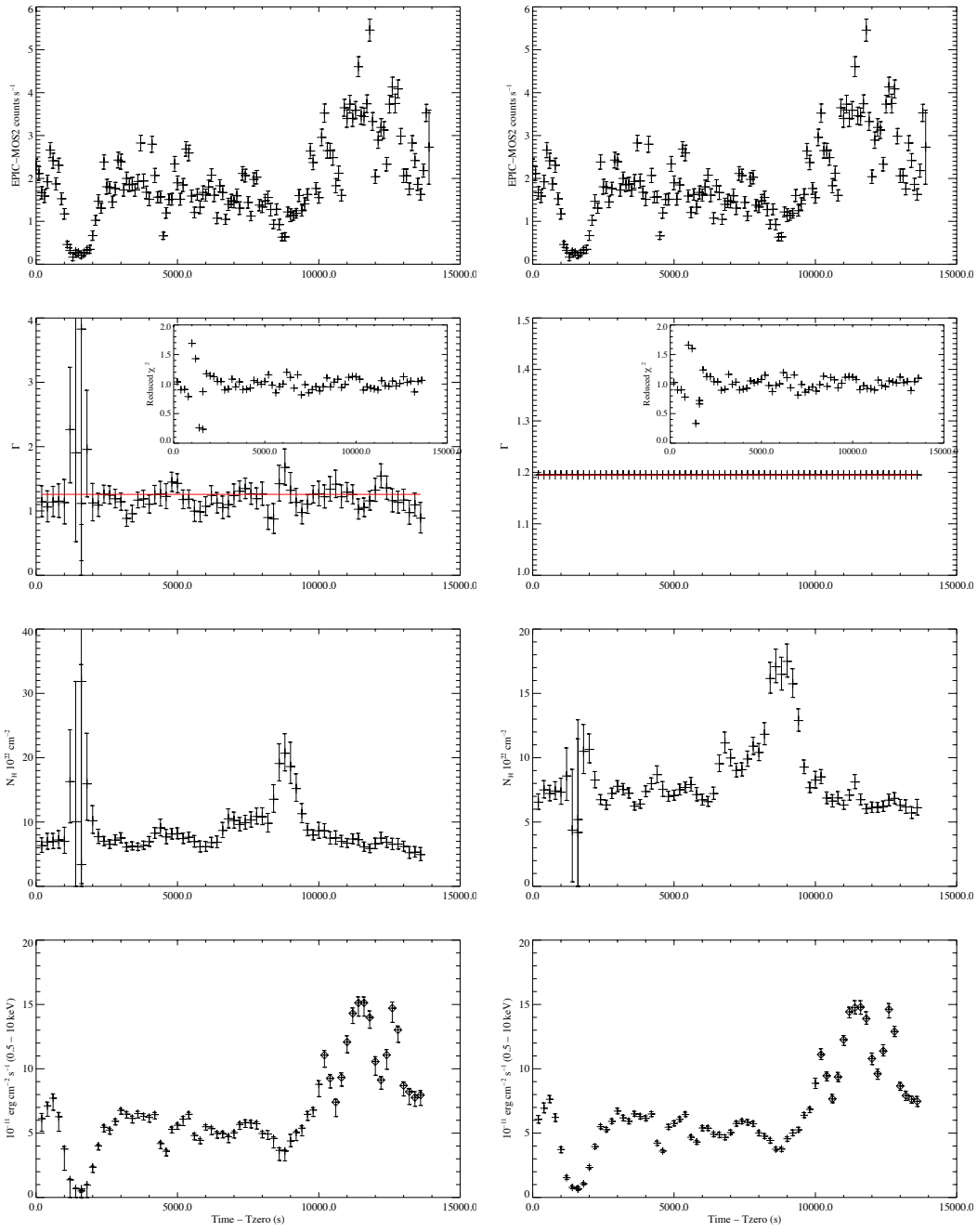

Figure 3.7: Temporal evolution of the best fit spectral parameters of an absorbed powerlaw to the 400 s binned spectra of IGR J16418−4532 with Γ as a free parameter (left) and with a fixed value of 1.195 (right). Top to bottom in both cases: EPIC-MOS2 $0.2-10$ keV light curve; Powerlaw index evolution; N_H evolution; inferred $0.5-10$ keV absorbed flux where the diamond points represent fluxes derived from the spectra accumulated from annular extraction regions. Inset: Reduced χ^2 values for the fit to each spectrum.

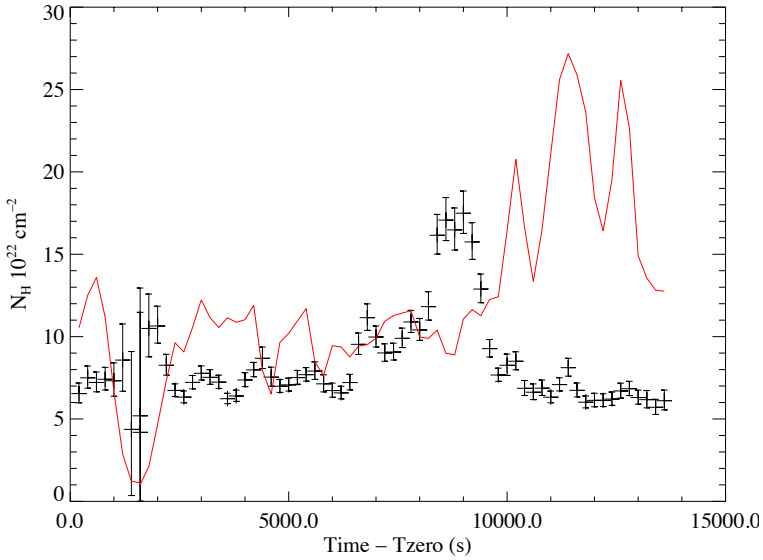

Figure 3.8: N_H evolution through the PEO of IGR J16418−4532 for an absorbed powerlaw with a fixed $\Gamma = 1.195$ overlaid with the calculated unabsorbed 0.5−10 keV flux in units of 10^{-11} erg cm^{-2} s^{-1}

evolution in IGR J16418−4532.

The upper and middle panels of Fig. 3.9 shows the MOS2 light curve folded on the fundamental period of 1209.12 s in the 0.2−4 keV and 4−10 keV bands respectively. A similar pulse profile, with one sharp narrow peak and one equally high but broader peak, is detected in both energy bands with the 0.2−4 keV displaying a pulse fraction of 25.0±3.6% and the 4−10 keV band 37.2±2.7%. The pulse fraction of the folded profile in the broad 0.2−10 keV band was 31.2±2.1%. A double peaked profile is consistent with the 2011 *XMM-Newton* observations of Sidoli et al. (2012) and shows a continued departure from the 2004 *XMM-Newton* observations of Walter et al. (2006) which displayed a pulse profile with a single, broad peak (Sidoli et al., 2012). The double peaked profile with uneven pulse widths could be the driving factor behind the detection of the third harmonic, as opposed to the fundamental frequency in these observations. The lower panel of Fig. 3.9 shows the hardness ratio as a function of pulse phase and it is seen that there is no systematic variation of the hardness with the progression of the pulsation.

3.4 Discussion

3.4.1 Stellar and Orbital Parameters

IGR J16418−4532 is an intermediate SFXT that has shown some peculiarities in its emission history. New combined *INTEGRAL* and *XMM-Newton* observations of the source that targeted the eclipse region of IGR J16418−4532's orbit have been

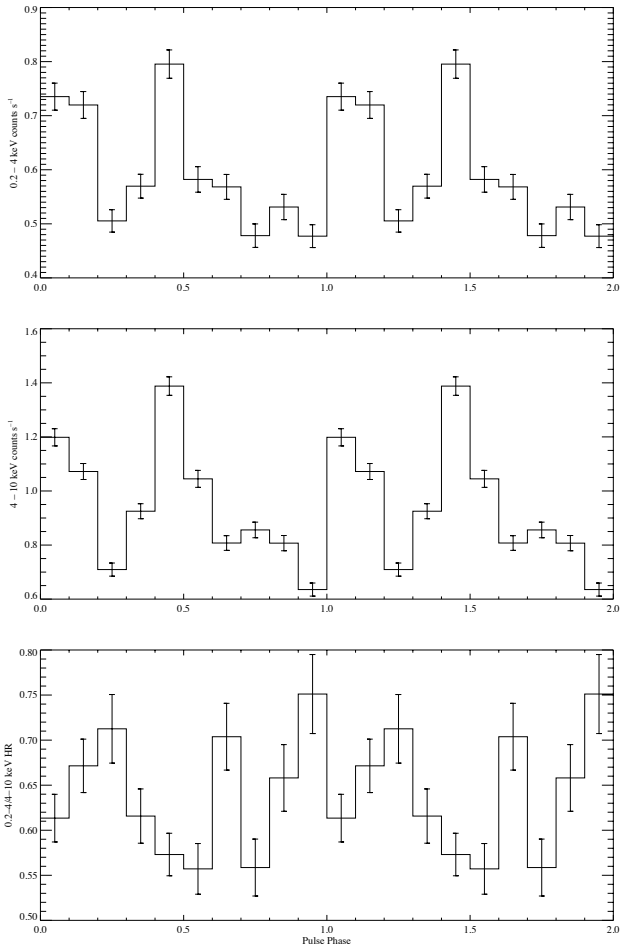

Figure 3.9: Pulse phase-folded profiles of IGR J16418−4532 using the pulse period of 1209.12 s where the zero phase is arbitrary. Top: 0.2−4 keV folded profile. Middle: 4−10 keV folded profile. Bottom: HR of folded profile.

presented here. The well determined orbital period of 3.73886±0.00028 days (Levine et al., 2011) allows constraints to be placed on the orbital geometry and nature of the companion star. The flat, unstructured phase-folded light curve and orbital phase distribution of outbursts (outside of the X-ray eclipse) detected by *INTEGRAL*, as shown in Fig. 3.1 and 3.2 respectively, indicate that the orbit is likely circular ($e \sim 0$) due to the lack of coherent modulation of the hard X-ray flux across the orbital phase. A similar flat orbital profile is also seen in IGR J16479−4514 which has a short 3.32 day eclipsing orbit (Jain, Paul, & Dutta, 2009). Conversely coherent orbital phase modulation has been observed in other SFXT systems which show evidence of a significant eccentricity in their orbit, such as a strongly peaked orbital emission profile with outbursts clustered around times of presumed periastron, i.e. IGR J17354−3255 (Sguera et al. 2011, Section 5.3). Additional dynamical considerations also suggest IGR J16418−4532 should possess a circular geometry, as with such a short orbital period the system would be expected to circularise relatively early in the lifetime of the X-ray binary (Zahn, 1977).

The stellar parameters of the supergiant companion in IGR J16418−4532 have very few dynamic or spectroscopic constraints, however. By combining the spectral classification (Coleiro et al. 2013, private communication), the IR SED fit parameters (Chaty et al., 2008a), the well determined orbital period (Levine et al., 2011) and the the L1 point separation equation of Eggleton (1983) an attempt can be made to place some constraints on the orbital parameters through the condition that full RLO does not occur in IGR J16418−4532. The Eggleton equation defines the size of the Roche Lobe about a mass as:

$$\frac{r_1}{a} = \frac{0.49q^{2/3}}{0.6q^{2/3} + ln(1 + q^{1/3})} \tag{3.1}$$

where $q = M_1/M_2$ is the mass ratio of the binary, a is the orbital separation and r_1 is the radius of the Roche Lobe about M_1. The condition that RLO does not occur in IGR J16418−4532 is based on the lower luminosity of the emission observed from this system compared to RLO systems ($\sim 10^{36}$ as opposed to $\sim 10^{38}\,\mathrm{erg\,s^{-1}}$) and the long 1212 s period of the pulsar in IGR J16418−4532 which would not be expected in RLO system as the effective transfer of angular momentum would likely 'spin-up' the NS to a faster spin period. Throughout these considerations a neutron star in a circular orbit with a mass of $1.4\,\mathrm{M_\odot}$, a radius of 10 km and a source distance of 13 kpc (Chaty et al., 2008a) is assumed. The R_{Sg}/D_{Sg} SED parameter of Chaty et al. (2008a) is utilised to calculate the range of possible stellar radii of the companion star, the central value of which (3.77×10^{-11}) gives a stellar radius of $21.7\,\mathrm{R_\odot}$. However, calculations of the L1 point separation for a range of companion

star masses indicate that RLO would be occurring for all companion masses of less than $50\,M_\odot$. Alternatively the lower limit of the R_{Sg}/D_{Sg} parameter (2.64×10^{-11}, 90% confidence) gives a stellar radius of $15.2\,R_\odot$ and RLO is only initiated up to a stellar mass of $20\,M_\odot$. For the remainder of this discussion a stellar mass of $30\,M_\odot$, the L1 point separation of which is $17.8\,R_\odot$, and a stellar radius of $17\,R_\odot$ such that the supergiant almost fills its Roche Lobe is assumed. Under these parameters the orbit of IGR J16418−4532 is characterised as circular, at an approximately edge-on inclination with a radius of $31.9\,R_\odot$ and a NS orbital velocity of $432\,\mathrm{km\,s^{-1}}$.

While the choice of these parameters may seen somewhat overly arbitrary it should be noted that the defining parameter in the remaining considerations, due to its strong influence on the size of the accretion radius, is the velocity of the stellar wind at the orbital separation of the neutron star. Following previous works on the properties of the stellar wind in IGR J16418−4532 (i.e. Romano et al. (2012), Ducci, Sidoli, & Paizis (2010)) the velocity law of Castor, Abbott, & Klein (1975) is adopted to describe the stellar wind velocity for both the smooth and clumped wind components, namely

$$v(r) = v_\infty(1 - 0.9983\frac{R_{Sg}}{r})^\beta \tag{3.2}$$

The stellar mass influences this relationship through the derived value of the orbital separation r, and the stellar radius influences through the value of R_{OB}. However, equally influential are the values of the terminal wind velocity v_∞ and the powerlaw index β. Through modelling of the flare luminosity distribution as observed by *Swift*/XRT, Romano et al. (2012) place v_∞ in the range 800 to $1300\,\mathrm{km\,s^{-1}}$ and β between 0.8 and 1.3. The value of the stellar wind velocity at the orbital separation calculated with the above stellar parameters and $v_\infty = 1000\,\mathrm{km\,s^{-1}}$, $\beta = 1$ is $470\,\mathrm{km\,s^{-1}}$. However, by varying the v_∞ and β parameters within their limits the stellar wind velocity occupies the range ∼370 to $610\,\mathrm{km\,s^{-1}}$. Similarly if a different set of allowed stellar parameters is selected ($M_{Sg} = 40M_\odot$, $R_{Sg} = 20R_\odot$) and the stellar wind velocity for the same range of allowed v_∞ and β values is calculated, the wind velocity at the orbital separation is in the range ∼340 to $560\,\mathrm{km\,s^{-1}}$. Hence the largest source of uncertainty in the stellar wind velocity comes from the poorly constrained wind parameters and not the unknown stellar parameters. For the remainder of this discussion the stellar parameters outlined above are adopted and the relative velocity of the NS orbital and stellar wind radial velocities calculated as $v_{rel} = (v_{NS}^2 + v_w^2)^{\frac{1}{2}}$. Uncertainties in derived physical values are then discussed in terms of the range of possible stellar wind parameters.

3.4.2 Eclipse Emission

Assuming that the cut-off in flux observed by *INTEGRAL*/IBIS was due to the eclipse ingress this provides an accurate ephemeris of MJD 56171.537±0.0058 for the start of the X-ray eclipse. Combining this with the first *XMM-Newton* observations (MEO) allows a firm lower limit, of 0.583 days ($\Delta\phi = 0.156$), to be placed on the duration of the X-ray eclipse in IGR J16418−4532.

The detection of X-ray flux from HMXB systems whilst the X-ray source is eclipsed by the supergiant companion is a common phenomenon amongst such sources, being detected in both classical Sg-XRBs (e.g. Cen X-3, Naik, Paul, & Ali 2011) and SFXTs (e.g. IGR J16479−4514, Bozzo et al. 2008b). The detected 0.5−10 keV flux of 2.8×10^{-13} erg cm^{-2} s^{-1} observed during the MEO corresponds to a luminosity of 6.3×10^{33} erg s^{-1} at the assumed source distance, ruling out direct emission from the companion star as the source of the detected emission. Instead the detections during eclipse are usually interpreted as resulting from the reprocessing of the intrinsic flux from the NS through the dense wind of the supergiant. In the MEO emission lines at energies consistent with atomic transitions from both neutral (6.4 keV) and ionised (6.67 keV) Fe were detected. The lack of Fe line features in the PEO indicate that the iron emission does not originate from close to the NS, but in extended regions throughout the supergiant atmosphere, with the relative equivalent widths of the lines (0.63 and 0.33 keV for the 6.4 and 6.67 keV lines respectively) suggesting that neutral Fe is the more abundant state.

3.4.3 Out of Eclipse Emission

Following the method of Sidoli et al. (2013), it is possible to use both *XMM-Newton* observations (MEO and PEO) to probe the supergiant total mass loss rate and the stellar wind density at the orbital separation. Using the system parameters discussed above gives an orbital separation of 2.2×10^{12} cm. Additionally the average flux detected whilst the NS was eclipsed in the MEO (2.8×10^{-13} erg cm^{-2} s^{-1}) is ∼0.56% of the average PEO flux detected outside of the X-ray dip and flare regions ($\sim 5.0\times10^{-11}$ erg cm^{-2} s^{-1}). This allows the wind density to be estimated, assuming that the X–ray emission detected during the eclipse is produced by X–ray scattering, as $n_{\rm w}(a) = 0.0056/(a\sigma_{\rm T})$, where $\sigma_{\rm T}$ is the Thomson scattering cross section and a is the orbital separation (Lewis et al., 1992).

The wind density at the orbital separation, $\rho_{\rm w}(a)$, is calculated as 6.3×10^{-15} g cm^{-3}. Assuming that the wind has a spherical geometry, and β=1 (Castor, Abbott, & Klein, 1975), the ratio between the wind mass-loss rate and the terminal velocity can be calculated as $\dot{M}_w/v_\infty = 4\,\pi\,a\,(a - R_{opt})\,\rho_{\rm w}(a)$, giving $\dot{M}_w/v_\infty = 9.3\times10^{-18}$ M$_\odot$ km^{-1}. If the wind terminal velocity is in the range 800−1300 km s^{-1} (Romano et al., 2012), the mass loss rate via the stellar wind lies

in the range $\dot{M}_w = (2.3{-}3.8){\times}10^{-7}\,\mathrm{M}_\odot\,\mathrm{yr}^{-1}$. Assuming direct accretion from the wind, the accretion rate onto the NS can be estimated as $\dot{M}_{acc} = ((\pi R_{acc}^2/4\pi a^2)\dot{M}_w)$, where R_{acc} is the accretion radius (Eq. 1.1). This implies an accretion rate at the orbital separation of between $\dot{M}_{\mathrm{acc}} \sim (9.7$ - $5.4){\times}10^{15}\,\mathrm{g\,s}^{-1}$, corresponding to X-ray luminosities in the range, $\mathrm{L_X} = (1.8{-}1.0){\times}10^{36}\,\mathrm{erg\,s}^{-1}$.

The average, unabsorbed flux detected during the PEO, outside of the X-ray dip and flare, corresponds to a luminosity of $2.0{\times}10^{36}\,\mathrm{erg\,s}^{-1}$ at a distance of 13 kpc, implying that the estimated wind density at the orbital separation, for the range of parameters assumed here, is able to generate the accretion luminosity observed outside of the eclipse in IGR J16418−4532. This is in contrast to the case of IGR J16479−4514 where the calculated stellar wind densities produced an X-ray luminosity two orders of magnitude greater than that observed, suggesting the need for a damping mechanism to reduce the effective mass accretion rate in this system (Sidoli et al., 2013). Such a mechanism would appear to not be required at nominal luminosities in the case of IGR J16418−4532.

N_H variations

The evolution of the spectral parameters and source flux observed during the PEO (Fig. 3.7) is intriguing, with evidence of a very variable accretion environment being experienced by the NS in IGR J16418−4532. Two striking features are observed during the course of the observation, the first being the deep dip observed in the detected flux that occurs between $\sim$t = 800 and 2500 s which is discussed separately below. The second is the pronounced increase and evolution in absorption observed between t $\sim$ 7000 s and t $\sim$ 10,000 s. The absorption first shows a sharp rise to $\sim 10^{23}\,\mathrm{cm}^{-2}$ from the base level of $\sim 7 \times 10^{22}\,\mathrm{cm}^{-2}$ followed by a second rapid step up to $1.7 \times 10^{23}\,\mathrm{cm}^{-2}$ approximately 1500 s later. After an additional 1500 s the absorption then rapidly decreases back to the base level observed in the earlier parts of the observation whilst, almost simultaneous, the flux begins to rise into the flaring activity observed at the end of the observation.

To understand this evolution consideration is given to the variation in N_H observed as the NS moves through its orbit. Sidoli et al. (2012) proposed that the NS in IGR 16418−4532 could be accreting through Transitional Roche Lobe Overflow (TRLO) due to the systems narrow orbit and the flux variations observed in *XMM-Newton* data taken in 2011. Such a transitional scenario was investigated by Blondin, Stevens, & Kallman (1991) where model orbital N_H profiles were produced for wind accretion powered binaries with narrow, circular orbits (Fig. 1.13). The overall shape of the profile is dominated by the line of sight through the bow shock about the NS with an additional, prominent component being generated by the tidal gas stream extending from the L1 point. The PEO was separated from the middle of

the eclipse by an orbital phase interval of ~ 0.2 which should, according to Blondin, Stevens, & Kallman (1991), result in a smooth decline in N_H. This suggests that the increase in N_H observed is not generated by a coherent structure in the NS environment (i.e. a tidal stream) but is instead more likely to be generated by an individual dense clump of material travelling through the line of sight to the NS at this time. Significant variation in the photon index of the powerlaw was not observed during the period of enhanced N_H and the unabsorbed flux remained at a constant level during this time (Fig. 3.8, red line). This is likely a signature of absorption of a constant intrinsic flux by optically thin material, as opposed to an optically thick/ionised absorber which might be expected in the case of obscuration by a coherent structure such as a tidal stream. It is noteworthy that sensitive, soft X-ray observations at a later orbital phase would be required to further test for the presence of a tidal stream arising from TRLO in IGR J16418−4532.

A dynamical estimate of the extent of the overdense region required to generate the excess N_H observed can be made by utilising the calculated relative velocity between the NS orbital motion and the radial stellar wind (see above). The increase in N_H is observed for $\sim 2500\,\mathrm{s}$ which relates to the passage of a wind clump of radius $\sim 8 \times 10^{10}\,\mathrm{cm}$ travelling at a velocity of $470\,\mathrm{km\,s^{-1}}$. This radius is consistent with the range of clump radii derived from the theoretical considerations of Ducci et al. (2009) and also similar to the observational results of Bozzo et al. (2011) who explained an outburst of IGR J18410−0535 as resulting from the accretion of a clump of approximate radius $8 \times 10^{11}\,\mathrm{cm}$. Therefore it is concluded that this absorption feature likely results from an optically thin clump of stellar wind material obscuring the intrinsic emission from the neutron star.

Absorption and flaring link?

The temporal relationship between the N_H increase and the onset of the flaring activity at the end of the PEO is of interest. Figure 3.8 shows the N_H evolution together with the unabsorbed $0.5 - 10\,\mathrm{keV}$ flux derived from the fixed Γ fit to each spectrum. It can be seen that the unabsorbed flux only begins to rise above the base level in the observation as the N_H returns to its pre-enhancement level. The lack of an overlap in the evolution of these parameters requires the consideration of the existence of a causal link between these features as this appears to be in contradiction to the best example of clump accretion as presented in Bozzo et al. (2011). In that work an outburst of the SFXT IGR J18410−0535 was described through the accretion of a dense clump of wind material. The N_H was observed to rise throughout the entire flux evolution, only returning to its pre-flare level when the flux also returned to pre-flare level, suggesting that there was excess material in the immediate vicinity of, and line of sight to, the NS throughout the duration of the flare.

However, in IGR J16418−4532 it appears that if the denser clump material is responsible for generating the subsequent flare, then the clump was only in our line of sight to the neutron star prior to the flux increase. This discrepancy seems somewhat unintuitive but can start to be understood from the more detailed knowledge of the orbital geometry of the IGR J16418−4532 system as a result of the X-ray eclipse. Using Fig. 3.1 the eclipse can be centred at an orbital phase of approximately $\phi = 0.55$ meaning that in the orbital phase range $\phi = 0.3$ to 0.8 the neutron star is more distant than the supergiant companion. Hence in this phase range, which the PEO inhabits, stellar wind clumps that are accreted will only be in our line of sight to the neutron star as they are approaching and interacting with it. As the clump moves beyond the X-ray emitting region the absorption detected along our line of sight would then drop rapidly, as is observed in Fig. 3.8, as the clump moves away behind the neutron star and its presence can no longer be detected.

To further consider whether this geometrical effect could be behind the observed evolution, the free fall time of stellar wind material from the accretion radius is estimated. The accretion radius is again assumed to be given by $\mathrm{R}_a = 2\mathrm{GM}_{NS}/v_{rel}^2$, and the free fall time by $\mathrm{t}_{ff} = (\mathrm{R}_a^3/2\mathrm{GM}_{NS})^{\frac{1}{2}}$. Under these assumptions and using the previously derived system parameters, the accretion radius is calculated as $\sim 9\times10^{10}$ cm and the estimated free fall time is ∼1500 s. This value should be considered a lower limit on the true infall time, however, as the descending material does not fall through the gravitational potential unimpeded, likely becoming a turbulent flow at some point which will increase the infall time. Given that the calculated free fall time is comparable to the observed delay between the onsets (and peaks) of the N_H and unabsorbed flux evolutions, Fig. 3.8, and the X-ray generation region is close to the neutron star, it is possible that, in this case, the dense wind clump passed through the accretion sphere before the additional accreted material had reached the X-ray generation region, hence creating the delay observed in Fig. 3.8.

Through considerations of the orbital geometry of IGR J16418−4532, the temporal coincidence (of the order of the free fall time from R_a) and approximately similar durations of the N_H and flux evolutions, a clump of over dense, optically thin wind material approaching the neutron star at a distance comparable to the accretion radius is suggested to be driving both features. In this case IGR J16418−4532 is showing signatures of accretion through the 'clumpy wind' model (in't Zand, 2005; Walter & Zurita Heras, 2007) viewed at an approximately edge-on inclination. However, at the current time it cannot definitely be concluded that these two features are causally related and they may instead be caused by two separate events. Long term monitoring of IGR J16418−4532 across all orbital phases would allow firmer conclusions to be drawn through the detection, or otherwise, of additional N_H - flux delays and their distribution in orbital phase. Currently it is

also not possible to conclude if the difference in the spectral evolution observed compared to the example of IGR J18410−0535 (Bozzo et al., 2011) is down to the same geometrical effects as the orbital configuration of IGR J18410−0535 is currently unknown.

Finally there is some evidence of a slow decrease in the base N_H level at times greater than t = 10,000 s. Such a decrease could be the result of increased X-ray photoionisation of the absorbing material by the enhanced X-ray flux produced during the flare (Hatchett & McCray, 1977), however, the observation ended before this effect could be more firmly identified.

The nature of the 'dip'

The observational properties of, and physical mechanisms behind, the X-ray dip observed towards the start of the PEO are now considered. Due to the unfortunate lack of EPIC-pn coverage of the majority of the dip region it was not possible to perform a detailed spectral analysis of the ingress and mid-dip regions, as shown by the large error bars on the spectral parameters and $\hat{\chi}^2$ values that indicate a poor fit to the data in the left and right hand columns of Fig. 3.7. However, more sensitive coverage was achieved during the dip egress. The main observable features of the X-ray dip are:

- a total duration of ~ 1500 s between t =800 and 2300 s that is comparable to the spin period of the neutron star
- a sharp drop in flux lasting less than 300 s at the start of the feature
- a steady, low level flux lasting for ~ 900 s with an unabsorbed flux of 2.0×10^{-11} erg cm^{-2} s^{-1} (0.5 − 10 keV) corresponding to a luminosity of 4.1×10^{35} erg s^{-1} at a distance of 13 kpc
- a slightly less sharp return to the pre-dip flux level over ∼300 s with some evidence of the N_H decreasing back to the pre-dip level as the flux recovers (see Fig. 3.8)
- a decrease in flux observed across the full 0.2−10 keV energy range during which spectral changes could not be identified
- a smooth spectrum with no evidence of Fe emission lines.

The presence of X-ray intensity dips, also referred to as 'off-states', in the light curves of wind-fed HMXB pulsars is a rare phenomenon, having only been observed in the classical Sg-XRBs Vela X-1 (Kreykenbohm et al., 2008), Centaurus X-3 (Naik, Paul, & Ali, 2011), 4U 1907+09 (in 't Zand, Baykal, & Strohmayer, 1998) and GX 301−2 (Göğüş, Kreykenbohm, & Belloni, 2011). Bozzo et al. (2012) also reported a similar feature in the non-pulsating, candidate SFXT IGR J16328−4726

but a detailed analysis and characterisation was prevented due to statistical constraints. Different mechanisms have been proposed to explain the observed behaviours, which are considered in turn here, with regards to IGR J16418−4514.

The Roche-Lobe filling Sg-XRB system Cen X-3 displayed several X-ray dips during the course of a long *Suzaku* observation that covered almost an entire binary orbit (Naik, Paul, & Ali, 2011). The dips were observed up to energies of 40 keV and the spectra characterised by a typical accreting HMXB pulsar continuum with multiple Fe emission lines that were detected throughout the observation. The equivalent widths (EW) of the Fe lines showed significant enhancement during both the dip and eclipse regions of the exposure. By following the evolution of the Fe line EWs and the amount of absorbing material in the line of sight (N_H values increased by a factor of 100 during these times), the authors concluded that the dips were most likely caused by the obscuration of the neutron star by dense structures in the outer edge of the accretion disc in the system. In this way Cen X-3 is a HMXB analogy of the 'dipper' class of LMXBs. Obscuration due to dense structures in the vicinity of the neutron star is unlikely in the case of IGR J16418−4532, however. Observationally the detection of prominent Fe emission during the MEO but not during the dip suggests that obscuration by dense, compton thick material is not the cause of the intensity dip observed in these observations. Additionally it is not clear how such dense material could inhabit the IGR J16418−4532 system as the supergiant is not believed to overfill its Roche-Lobe and therefore an accretion disc would not be present. In the TRLO regime such dense material could be found as a result of either the gravitationally focused 'tidal stream' coming from the L1 point or as a result of a transient accretion disc that may form. However, as discussed above, the orbital phase location of the dip is inconsistent with what would be expected if it were to originate from a tidal stream (Blondin, Stevens, & Kallman, 1991). Sidoli et al. (2012) suggested the presence of a transient accretion disc to explain the quasi-periodic flares observed in a previous observation of IGR J16418−4532, however, as no such features are present in these observations it is unlikely that a transient accretion disc was present to obscure the NS at this time. It is noted, however, that these observations cover an insufficient fraction of orbital phase to consider fully whether TRLO is occurring in IGR J16418−4532.

The signature of a typical stellar wind clump obscuring the neutron star in IGR J16418−4532 is believed to have been observed later in the PEO, as discussed above, and displayed a very different evolution to that observed during the dip feature. Hence it is also unlikely that the passage of a single stellar wind clump through the line of sight is responsible for the observed dip. Finally the passage of ionised material through the line of sight to the neutron star could cause a strong absorbing effect across a wide energy range as observed. Again, however, there was insufficient signal to test for this effect spectrally and the lack of Fe emission lines in the X-ray spectrum of the dip suggests this is an unlikely cause of the observed

feature.

The alternative explanation given for the presence of X-ray intensity dips or 'off-states' is the action of a barrier to the accretion flow. Kreykenbohm et al. (2008) invoked centrifugal barriers to explain the off-states observed in Vela X-1, where the source fell below the detection threshold in *INTEGRAL*/IBIS data, via the onset of the supersonic propellor mechanism (Illarionov & Sunyaev, 1975) to inhibit accretion during these times. More recently, however, Doroshenko, Santangelo, & Suleimanov (2011) used sensitive, broadband *Suzaku* observations to argue that the dips in Vela X-1 were instead the result of a magnetic barrier that reduces the emitted X-ray flux as direct accretion is impeded by the neutron star magnetosphere. However, accretion continues at a lower level through the Kelvin-Helmholtz Instability (KHI) which generates the lower flux detected. Additionally X-ray pulsations are still produced in the case of accretion through the KHI, as are detected in the *Suzaku* data, which would not be expected in the centrifugally inhibited case. Doroshenko, Santangelo, & Suleimanov (2011) used the detailed accretion scenario model of Bozzo et al. (2008b) to infer that a neutron star with a magnetic field strength in the range of a few 10^{13} to $\sim 1 \times 10^{14}$ G is required to produce the X-ray luminosity observed under the magnetically gated scenario (subsonic propellor regime, see Bozzo et al. 2008b and Chapter 1). Hence they argue that X-ray intensity dips in wind-fed HMXBs are evidence of a highly magnetised neutron star being present in the system. The same authors also found similar results for the HMXB 4U 1907+09 (Doroshenko et al., 2012).

Shakura et al. (2013), however, proposed that the X-ray dips observed in Vela X-1, GX 301−2 and 4U 1907+09 were instead caused by a switch in the neutron star polar X-ray beam configuration due to a variation in the optical depth of the accretion column. In this model both states occur within a 'quasi-spherical' subsonic accretion regime (Shakura et al., 2012). The Compton cooling regime occurs when the source luminosity is in excess of $\sim 5 \times 10^{35}\,\mathrm{erg\,s^{-1}}$ and the optical depth of the accretion column is high, creating a fan beam due to high levels of lateral scattering. The fan beam effectively cools plasma in the equatorial regions of the magnetosphere through Compton processes, allowing material to enter the magnetosphere through Rayleigh-Taylor instabilities. It is this state that generates the 'normal' luminosity level of the lower luminosity, persistent wind-fed HMXBs (i.e. Vela X-1). The radiative cooling regime occurs when the luminosity is less than $\sim 5 \times 10^{35}\,\mathrm{erg\,s^{-1}}$, causing a drop in the optical depth of the accretion column and the onset of pencil beam emission. In this configuration the equatorial region of the magnetosphere is not illuminated and plasma can only thread onto field lines at a lower rate through radiative plasma cooling, which is independent of the level of illumination from the central source. The authors argue it is the transition into this radiatively cooled accretion state from the Compton cooled state that generates the observed X-ray dips. Sources would only move into the direct accretion scenario

(supersonic Bondi accretion) when the source luminosity increased to greater than several $10^{36}\,\mathrm{erg\,s^{-1}}$ and in-falling material is rapidly cooled by Compton processes before reaching the magnetosphere (for a full description of the quasi-spherical accretion model see Shakura et al. (2012) and Shakura et al. (2013)).

Given the similarities in the observable features and luminosities of the X-ray dips observed in Vela X-1 and 4U 1907+09 to the dip observed here, the applicability of the Doroshenko, Santangelo, & Suleimanov (2011) and Shakura et al. (2013) interpretations of the origins of X-ray dips to IGR J16418−4532 are considered. The method of Doroshenko, Santangelo, & Suleimanov (2011), using the theoretical framework of Bozzo et al. (2008b), is followed to calculate the magnetic field strength required to produce the observed dip luminosity ($4.1\times10^{35}\,\mathrm{erg\,s^{-1}}$) for the range of stellar wind parameters considered in Section 3.4.1. Equation 21 of Bozzo et al. (2008b) and the conventions therein are used for the calculation, namely:

$$\begin{aligned} L_{KH} =& 1.8\times10^{35}\eta_{KH}P_{s3}^{-1}R_{M10}^{3}\dot{M}_{-6}a_{10d}^{-2}v_{8}^{-1} \\ & [1+16R_{a10}/(5R_{M10})]^{3/2}\frac{\sqrt{\rho_i/\rho_e}}{(1+\rho_i/\rho_e)}\mathrm{erg\,s^{-1}} \end{aligned} \tag{3.3}$$

Here the ρ_i/ρ_e term is the ratio of the plasma densities inside and outside of the magnetosphere and R_{M10} is the magnetic radius in units of $10^{10}\,\mathrm{cm}$ and defined as:

$$R_M = 2\times10^{10}a_{10d}^{4/7}\dot{M}_{-6}^{-2/7}v_8^{8/7}\mu_{33}^{4/7}\mathrm{cm} \tag{3.4}$$

where μ_{33} is the magnetic moment in units of $10^{33}\,\mathrm{G\,cm^3}$. The magnetic field required to produce the dip luminosity is calculated for the cases of $\rho_i/\rho_e = 1.0$, 0.5 and 0.1 where a ρ_i/ρ_e value of 1 gives an upper limit on the mass flow generated through the Kelvin-Helmholtz instability.

Using the calculated magnetic field strengths the critical accretion rate defining the transition between the subsonic propellor and direct accretion regimes is estimated. According to Bozzo et al. (2008b) this critical accretion rate is given by:

$$\dot{M}_{lim_{-6}} = 2.8\times10^{2}P_{s3}^{-3}a_{10d}^{2}v_8R_{M10}^{5/2}[1+16R_{a10}/(5R_{M10})]^{-3/2}\mathrm{g\,s^{-1}} \tag{3.5}$$

These critical values are compared to the accretion rate required to generate the observed dip luminosity of $4.1\times10^{35}\,\mathrm{erg\,s^{-1}}$ and the pre/post-dip luminosity of $\sim2\times10^{36}\,\mathrm{erg\,s^{-1}}$ to evaluate if a transition between accretion regimes could have occurred. Using the relation $L_X = GM_{NS}\dot{M}_{capt}/R_{NS}$ requires accretion rates of

Table 3.3: Calculated magnetic fields required to generate the observed dip luminosity of IGR J16418−4532 in the 'Subsonic Propellor' accretion mode according to Bozzo et al. (2008b). The wind condition parameter space is drawn from the limits on the terminal wind velocity range of Romano et al. (2012) and the total stellar wind mass loss rate calculated using the $\dot{M}_w/v_\infty$=$9.3\times10^{-18}\,\mathrm{M_\odot\,km^{-1}}$ parameter for each terminal wind velocity (see Sect. 3.4.3). The 'Transition?' columns indicate whether a transition from the subsonic propellor regime to the direct accretion regime is likely to have occurred for the X-ray dip and flare observed. The accretion rates required to produce the dip, pre/post-dip and peak flare luminosities are $2.2\times10^{15}\,\mathrm{g\,s^{-1}}$, $1.1\times10^{16}\,\mathrm{g\,s^{-1}}$ and $2.8\times10^{16}\,\mathrm{g\,s^{-1}}$ respectively.

ρ_i/ρ_e	B(G)	$\dot{M}_{lim}$ ($\mathrm{g\,s^{-1}}$)	Dip Transition?	Flare Transition?
$v_\infty = 800\,\mathrm{km\,s^{-1}}$, $\dot{M}_w$=2.3×10^{-7} $\mathrm{M_\odot\,yr^{-1}}$, $v_{rel} = 571\,\mathrm{km\,s^{-1}}$				
1.0	2.8×10^{13}	1.2×10^{17}	N	N
0.5	3.0×10^{13}	1.4×10^{17}	N	N
0.1	5.3×10^{13}	5.2×10^{17}	N	N
$v_\infty = 1000\,\mathrm{km\,s^{-1}}$, $\dot{M}_w$=2.9×10^{-7} $\mathrm{M_\odot\,yr^{-1}}$, $v_{rel} = 637\,\mathrm{km\,s^{-1}}$				
1.0	3.2×10^{13}	3.2×10^{17}	N	N
0.5	3.4×10^{13}	3.8×10^{17}	N	N
0.1	6.1×10^{13}	1.4×10^{18}	N	N
$v_\infty = 1300\,\mathrm{km\,s^{-1}}$, $\dot{M}_w$=3.8×10^{-7} $\mathrm{M_\odot\,yr^{-1}}$, $v_{rel} = 746\,\mathrm{km\,s^{-1}}$				
1.0	4.1×10^{13}	1.5×10^{18}	N	N
0.5	4.3×10^{13}	1.8×10^{18}	N	N
0.1	7.6×10^{13}	6.4×10^{18}	N	N

$2.2\times10^{15}\,\mathrm{g\,s^{-1}}$ and $1.1\times10^{16}\,\mathrm{g\,s^{-1}}$ to generate the observed dip and pre/post-dip luminosities respectively. Table 3.3 outlines the results of these calculations for the range of possible stellar wind velocities considered in Section 3.4.1.

It is seen from Table 3.3 that the critical accretion rate where the system would switch from the direct accretion regime to the subsonic propellor regime is in excess of the accretion rate required to generate the observed dip luminosity across the whole parameter space investigated. The calculations also require a highly magnetised NS with B of $\sim$ a few 10^{13} G to produce the observed luminosity. However, the critical accretion rate between the regimes is also in excess of the accretion rate required to generate the pre/post-dip luminosity ($1.1\times10^{16}\,\mathrm{g\,s^{-1}}$) across the whole parameter space, suggesting that the system should not undergo a transition. Furthermore, the luminosity at the peak of the flare observed in the PEO ($\sim5\times10^{36}\,\mathrm{erg\,s^{-1}}$) only requires an accretion rate of $2.8\times10^{16}\,\mathrm{g\,s^{-1}}$ which is still insufficient to cause a transition under this model. Hence this suggests that a transition between the 'subsonic propellor' and direct accretion regimes is not causing the X-ray dip observed in IGR J16418−4532.

Given the earlier arguments against obscuration as the source of the dip and the incompatibility of the required accretion rates for a subsonic propellor to direct accretion transition, a state change within the 'quasi-spherical' accretion model (Shakura et al., 2013) is favoured as the likely cause of the X-ray dip in IGR J16418−4532. As IGR J16418−4532 appears to stay in a subsonic quasi-spherical

accretion regime throughout the observation, this suggests the X-ray dip may be generated through a transition between the higher luminosity fan beam and lower luminosity pencil beam dominated states of the model. Under this scenario the magnetic field strength of the NS can be estimated through the luminosity detected during the dip using Equation 22 of Shakura et al. (2013), namely:

$$L_{X,rad} \approx 10^{35} \mu_{30}^{7/33} \mathrm{erg\,s^{-1}} \tag{3.6}$$

where μ_{30} is the magnetic moment in units of 10^{30} G cm^3. The dip luminosity of 4.1×10^{35} erg s^{-1} corresponds to a NS B-field of $\sim2\times10^{14}$ G, providing evidence of the presence of a highly magnetised NS in a SFXT. Additionally the shell of material that would be surrounding the NS under this model could be providing a significant contribution to the high base level of absorption observed in the PEO ($\sim7\times10^{22}$ cm^{-2}). As the derived B-field value is determined by the luminosity of the source during the X-ray dip the effect of the unknown source distance on this result must be taken into account. The confirmation of the companion as a supergiant requires the source to be at a large distance for all possible stellar radii (Chaty et al., 2008a), however, a distance of 13 kpc is still somewhat arbitrary and is used here to maintain consistency with previous works in the literature. If IGR J16418−4532 is located at a distance of 10 kpc (with a corresponding stellar radius of $16.7R_\odot$ for example) then the dip luminosity would be 2.4×10^{35} erg s^{-1} and the implied NS B-field would have a value of 1.6×10^{13} G. Whilst in this case the B-field does not reach magnetar field strengths it is nevertheless in the highly magnetised regime, being in excess of the nominal $\sim10^{12}$ G value observed in many HMXB pulsars. Additional constraints on the distance and/or radius of the supergiant will allow the implied B-field strength to be determined with a higher degree of certainty.

To date no cyclotron absorption line has been detected from IGR J16418−4532 to provide an independent estimate of the B-field in the system. The $\sim10^{14}$ G B-field implied by the quasi-spherical accretion interpretation of the X-ray dip would be expected to generate a cyclotron line at an energy of ∼2000 keV which helps to explain the lack of detections due to the lack of instruments with high sensitivity in the MeV energy range. This should be considered an upper limit on the cyclotron line energy, however, as the intrinsic B-field strength may be lower if the source is less distant and, for any intrinsic B-field, the detectable line energy may be reduced during bright outbursts as the accretion column extends further from the NS surface (Doroshenko et al., 2010). High sensitivity coverage in the hard X-ray band (i.e. *INTEGRAL*/IBIS and *NuStar*) during the brightest events may therefore provide the detection of a cyclotron line and allow a more thorough consideration of the quasi-spherical accretion model. A B-field of $\sim10^{14}$ G would also generate a proton

cyclotron line at 0.5 keV (Zane et al., 2001) which is accessible to instruments aboard *Swift* and *Chandra*. However, the high intrinsic absorption of the IGR J16418−4532 system makes the detailed spectral analysis of this low energy band challenging. Additional confirmation of the quasi-spherical transition could also come from the detection of a longer duration dip to investigate if pulsations remain active during the dip and if there are characteristic variations in the pulse profile of IGR J16418−4532 between the states, as is the case for Vela X-1 and 4U 1907+09.

The applicability of the quasi-spherical accretion model (Shakura et al., 2012) to these observations directly suggests that the neutron star in this system is highly magnetised and is impeding direct (supersonic Bondi) accretion via a magnetic barrier, the first time such strong evidence of this has been observed in an SFXT. Stricter, independent constraints on the orbital, stellar and stellar wind parameters of IGR J16418−4532 are nevertheless required to allow the testing of the applicability of both the quasi-spherical and subsonic propellor accretion regimes to IGR J16418−4532 under more stringent physical conditions.

Due to the lack of EPIC-pn coverage during the early regions of the dip it is difficult to evaluate what may have caused the on-set of the accretion regime transition for the duration of the dip. However, the hydrodynamical simulations of Oskinova, Feldmeier, & Kretschmar (2012) showed that, whilst on average the velocity of the stellar wind follows the velocity law stated above (Eq. 3.2), strong velocity jumps over small radial extents are also present. These jumps, which can have negative gradients, result from unstable growth in the line-driven wind and are at their most prominent at separations within a few stellar radii of the supergiant surface. As a result of its short orbital period the NS in IGR J16418−4532 is therefore occupying the most turbulent region of the supergiant wind and the accretion regime transition may also have been triggered by a strong, localised variation in the stellar wind environment interacting with the magnetosphere.

3.4.4 The nature of IGR J16418−4532

The strongly variable stellar wind environment being experienced by the NS in IGR J16418−4532 may also explain the origin of the enhanced dynamic range ($> 10^2$) observed in this system compared to classical Sg-XRBs. Many Sg-XRBs have longer orbits and should therefore occupy less turbulent regions of their supergiants atmosphere resulting in a lower level of variability. The sharp velocity and density variations near to the surface of the supergiant in IGR J16418−4532, however, may be helping to generate the observed SFXT level of variability in the system through their influence on the size of the accretion radius long with the achieved mass capture rate.

The transient nature of IGR J16418−4532 is defined more by the large source

distance of ∼13 kpc, however. Figure 3.1 shows that, outside of the eclipse, IGR J16418−4532 is detected as a weak persistent source in the *INTEGRAL*/IBIS 18−60 keV band (where most SFXTs were discovered) at a count rate of 1.2 counts per second (∼7 mCrab). If IGR J16418−4532 was located at a distance of 2 kpc (comparable with Vela X-1, Nagase 1989), however, it would be detected as a bright persistent Sg-XRB source with an unusually high dynamic range and an average flux of ∼300 mCrab in the *INTEGRAL* band. Hence it would not be viewed as a transient source. Therefore one may take the view that IGR J16418−4532 is a classical Sg-XRB with an enhanced X-ray dynamic range resulting from the turbulent stellar wind environment being experienced by the NS as a result of the short orbital period of the system. Its transient nature is then being generated as a result of its large distance making the persistent emission undetectable in single *INTEGRAL*/IBIS or *Swift*/BAT observations, but where the flares are instead detected as transient outbursts. This is at odds with many other SFXTs where the driver of the extreme level of flux variation is the large scale variation in stellar wind environment experienced by a NS over a longer, more eccentric orbit (e.g. SAX J1818.6−1703, Bird et al. 2009). Shakura et al. (2012) also suggest that the difference between SFXTs and classical wind-fed Sg-XRBs could be understood through the proportion of time spent in the fan beam dominated (higher luminosity) and pencil beam dominated (lower luminosity) regimes within the subsonic, quasi-spherical accretion mode. Classical Sg-XRBs (e.g. Vela X-1) spend the majority of the time in the fan beam dominated regime and occasionally enter the pencil beam regime during X-ray dips. Whereas SFXTs spend the majority of their time in the pencil beam dominated regimes and occasionally enter the fan beam regime during short periods of increased accretion, i.e. outbursts. Given IGR J16418−4532's emission history and the observations presented here this further suggests that, fundamentally, IGR J16418−4532 is a classical wind-fed Sg-XRB displaying an enhanced dynamic range and is observed as a transient source only due to its large distance. This difference in the fundamental cause of the variability observed in IGR J16418−4532 compared to other members of the SFXT class is discussed in Chapter 6.

3.5 Conclusions

In this chapter new combined *INTEGRAL* and *XMM-Newton* observations of the intermediate SFXT IGR J16418−4532 have been presented. The *XMM-Newton* data has revealed features that are consistent with the presence of dense stellar wind clumps as predicted by the nominal 'clumpy-wind' model of SFXT emission, along with the first ever detection of an X-ray 'dip' in the light curve of a pulsating SFXT. Through considerations of the cause of this dip and the luminosity levels detected it is concluded that it was most likely generated by the switching of

accretion modes from a Compton cooling dominated to a radiative cooling dominated regime within the framework of a subsonic quasi-spherical accretion flow (Shakura et al., 2012). This scenario requires IGR J16418−4532 to host a highly magnetised, B $\sim 10^{14}G$, neutron star and represents the first observational evidence of such an object being hosted in an SFXT. It is likely that the onset of the radiative cooling dominated accretion regime is in part due to the high level of turbulence in the stellar wind close to the companion star. Such turbulence may also be responsible for generating the enhanced dynamic range observed in IGR J16418−4532 that places it in the SFXT class. The orbital geometry and flare generation mechanisms observed in IGR J16418−4532 represent a departure from the nominal model of SFXT behaviour.

Chapter 4

X-ray pulsations from the region of the Supergiant Fast X-ray Transient IGR J17544−2619

4.1 Introduction

IGR J17544−2619 was first discovered as a hard X-ray transient source on 2003 September 17 (Sunyaev et al., 2003a) with the IBIS/ISGRI instrument aboard *INTEGRAL*. Two short outbursts, 2 and 8 hours long respectively, were observed on the same day, indicating fast and recurrent transient behaviour. A subsequent detection on 2004 March 8 (Grebenev et al., 2004) further illustrated the recurrent nature of the X-ray outbursts in IGR J17544−2619. After the *INTEGRAL* detection, IGR J17544−2619 was associated with the soft X-ray source 1RXS J175428.3-262035 (Wijnands 2003, Voges et al. 2000) and discovered in archival Beppo-*SAX* (in't Zand et al., 2004) and *XMM-Newton* data (González-Riestra et al., 2004). A *Chandra* observation (in't Zand, 2005) precisely located the source with a positional accuracy of 0.6" (RA = 17:54:25.284, DEC = -26:19:52.62, J2000.0), confirming the association of IGR J17544−2619 with 2MASS J17542527-2619526. Pellizza, Chaty, & Negueruela (2006) classified the companion as an O9Ib star with a mass of 25−28 $M_{\odot}$ at a distance of 2−4 kpc. Subsequently Rahoui et al. (2008a) performed SED fitting to the mid-IR spectrum and refined the distance estimate to the system as ∼3.6 kpc.

During the *XMM-Newton* observations IGR J17544−2619 displayed large scale variability between observations with the peak emission being detected at $\sim 1.7\times10^{35}\,\mathrm{erg\,s^{-1}}$ (0.5−10 keV) and an upper limit on the flux during a period of non-detection being placed at $\sim 8\times10^{31}\,\mathrm{erg\,s^{-1}}$, illustrating a dynamic range of at least several 10^3 (González-Riestra et al., 2004). The *Chandra* observations

presented by in't Zand (2005) displayed the evolution of a bright flare from IGR J17544−2619 that began with the source in a quiescent state, at a luminosity of $5.2\times10^{32}\,\mathrm{erg\,s^{-1}}$ (0.5−10 keV), before rising to a peak luminosity of $4.2\times10^{36}\,\mathrm{erg\,s^{-1}}$ over ∼3000 s. This demonstrates an X-ray dynamic range of ∼8000 over this short time period alone and, when compared to the deepest *XMM-Newton* upper limit on the source flux during the non-detection, illustrates a maximal dynamic range of greater than 5×10^4 in this system. As a result of this extreme flaring behaviour, the recurrent hard X-ray outbursts and the spectrally classified 09Ib companion, IGR J17544−2619 is often referred to as the 'prototypical' SFXT. in't Zand (2005) proposed that the origin of the fast flaring observed in this system results from the interaction with the highly structured stellar wind of the supergiant companion, forming the basis of the 'clumpy wind' theory of SFXT emission. Bozzo, Falanga, & Stella (2008a), however, applied the theoretical framework described in Section 1.2.2 to the outburst observed by *Chandra* to propose that the large swings in X-ray luminosity could instead be generated by the action of magnetic or centrifugal barriers to the accretion flow, reducing the requirement for such large variations in the stellar wind density. It was also inferred that, in the case of the compact object being a slowly rotating neutron star, it should possess a magnetar strength magnetic field to generate the observed variations.

Using long baseline IBIS/ISGRI light curves, Clark et al. (2009) identified the orbital period of IGR J17544−2619 as 4.926 ± 0.001 d, one of the shortest orbital periods observed in an SFXT. This orbital period was utilised to place constraints on the binary orbit, with the radius of the companion star required to be $<23\,R_\odot$ for the case of zero eccentricity, and an upper limit of 0.4 placed on the eccentricity if the companion possesses its minimum possible radius of $12.7\,R_\odot$ (Pellizza, Chaty, & Negueruela 2006, Rahoui et al. 2008a).

The spectral properties of IGR J17544−2619 have been studied at all levels of emission. The outburst spectra are often well described by absorbed, hard powerlaw models that display variations in column density, $1.1-3.3\times10^{22}\,\mathrm{cm^{-2}}$, and photon index, 0.75−1.3, between and during outbursts (Rampy, Smith, & Negueruela 2009, Sidoli et al. 2009a, Romano et al. 2008a). The spectral variability is observed to be at its most pronounced on short time scales within outbursts, indicating that a rapidly changeable environment is being experienced by the compact object in the system. The variability in the parameters is reduced when spectra are accumulated over longer timelines suggesting that the mixing of different spectral states occurs over these timescales (Rampy, Smith, & Negueruela, 2009). The quiescence spectra are far softer than those of outbursts with photon indices in the range 2.1 and 5.9 (Sidoli et al. 2008, in't Zand 2005). The softness of these spectra has led to the conclusion that the compact object in IGR J17544−2619 is most likely a neutron star (in't Zand 2005, Pellizza, Chaty, & Negueruela 2006) with the soft spectrum observed during quiescence being generated by the hot surface. However, the

combination of the spectral shape and the low $\sim 10^{32}\,\mathrm{erg\,s^{-1}}$ luminosities of the quiescent states allows for the possibility that the emission seen in this state is that of the intrinsic X-ray emission of the supergiant companion (Berghoefer et al., 1997). Under both of these quiescent scenarios it is possible that accretion on to the compact object has ceased whilst the source is in the quiescent state.

In this chapter a new study performed on the IGR J17544−2619 system using *RXTE* is presented. The dataset is described in Sect. 4.2, followed by temporal and spectral results in Sect. 4.3. A discussion of these results is given in Sect. 4.4 followed by conclusions in Sect. 4.5.

4.2 Data Set and Analysis

Using the orbital ephemeris of Clark et al. (2009) three observations of the region around IGR J17544−2619 were performed across one half of the binary orbit using the Proportional Counter Array (PCA) instrument aboard *RXTE* (Jahoda et al. 2006, Swank 1994 respectively). The observations were performed on 2010 May 15, 16 and 17 at 04:47, 16:54 and 03:53 UTC with each observation having an exposure of $\sim 10\,\mathrm{ks}$. In all subsequent analysis the updated orbital period determination and zero phase ephemeris, $4.9278\pm0.0002\,\mathrm{d}$ and MJD 55924.271 respectively, are used as in Section 2.4.3. These improved determinations were achieved through utilising the analysis methods outlined in Section 2.3.2 on an *INTEGRAL*/IBIS dataset of 13.3 Ms, representing an ∼66% increase in exposure compared with the original study of Clark et al. (2009). Under this new orbital determination the orbital phase of the three observations are $\phi = 0.648$, 0.953 and 0.046 respectively.

The data were analysed using the standard tools within HEASOFT v6.9. The analysis was performed on both the science array (standard mode one) and science event (good xenon) data. PCU 2 was the only detector active for the entirety of all three observations, with PCU 4 active for a small percentage of each, hence extraction was performed on PCU 2 data only. The GTIs of the observations were generated with the ftool MAKETIME using the observation filter files and the standard event selection criteria described in the *RXTE* data analysis manual. Light curves of the standard mode one data, which covers the full energy response of the PCA at 0.125 s time resolution, were extracted using the ftool SAEXTRCT. The light curves were background subtracted using the most recent PCA faint background model and barycentered using the FXBARY ftool. Similarly the event mode data were treated in the same manner, whereby the light curves were extracted using SEEXRCT at 0.125 s resolution. Three light curves were extracted covering the full PCA energy response, 3−10 keV and 10−120 keV with all layers of PCU 2 used in each case. Again the light curves were barycentered using FXBARY. The science event data were also used to create energy spectra of the observations.

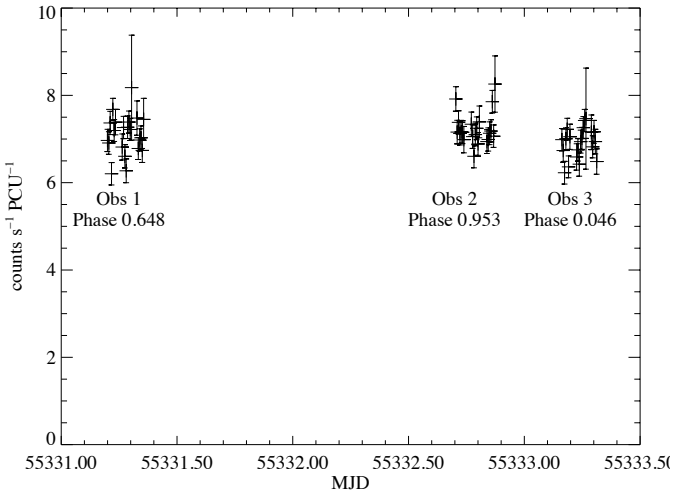

Figure 4.1: Background subtracted, 500 second binned standard mode one light curves of the *RXTE*/PCA observations of IGR J17544−2619. The orbital phase of each observation is shown using the zero phase ephemeris MJD 55924.271 and orbital period 4.9278 d. Periastron occurs at an orbital phase of ∼0.25 under this orbital solution.

The spectra, background and response files were generated for each science event file and for every combination of active detectors using the standard methods. As the majority of the exposure in each observation was achieved whilst PCU 2 was the only active detector, these spectra, and backgrounds, were summed using SUMPHA and the responses combined using ADDRMF.

4.3 Results

Figure 4.1 shows the PCA standard mode one light curves of the observations at 500 s binning. In this mode PCA data has no energy resolution and hence these represent the emission detected across the full 2−120 keV PCA energy range. We see that steady, low level emission at an intensity of ∼7 counts s^{-1} PCU^{-1} is being detected across all three observations. This corresponds to a flux of ∼ 5.0−5.5×10^{-11} erg cm^{-2} s^{-1} in the 3−10 keV energy range using the spectral models outlined in Table 4.2. The orbital phase of the centre point of each observation is also indicated and it is seen by comparing to the left hand panel of Fig. 2.16 that the first observation (Obs 1) occurs approximately half way between periastron and apastron whilst the second and third observations (Obs 2 and 3) were performed as the compact object is approaching periastron.

The shape and intensity of the emission in the three observations was first characterised by assessing the statistical properties of the finely binned (0.125 s) standard mode one light curves. The mean fluxes are seen to vary by a maximum of ∼5% between the observations. The level of variation within each observation was

Table 4.1: Statistical properties of the 0.125 s resolution 2 −120 keV standard mode one light curves of IGR J17544−2619. The $\hat{\chi}^2$ value is that of a fit to the mean count rate in each observation.

Obs	Average Flux counts s^{-1} PCU^{-1}	$\hat{\chi}^2$	Exposure s
1	7.02 ± 0.06	12.1	9102
2	7.19 ± 0.06	10.9	9722
3	6.87 ± 0.06	12.2	8872

also investigated by means of the goodness of fit to a constant flux at the average count rate. All three observations showed a poor fit, indicating variations in excess of statistical noise within the light curves. These statistics are outlined in Table 4.1. The properties of the observed emission suggest that there are no sources undergoing bright, fast outbursts within the PCA FOV during these observations.

4.3.1 Periodicity Analysis

To search for pulsations in the range 1−1000 s in the data, the background subtracted, 0.125 s resolution standard data mode one light curves of each observation were subjected to a Lomb-Scargle analysis. The analysis of Obs 2 and 3 showed no significant signals within their periodograms. However, a peak with a power of 22.039 was observed at a period of 71.49 s in the periodogram of Obs 1, as shown in Fig. 4.2. This period does not correspond to a beat frequency between any characteristic time scales within the data and a peak is present when the analysis is performed on light curves with a wide range of different time binnings. The 99.99% and 99.999% confidence levels were calculated at Lomb-Scargle powers of 20.133 and 22.227 respectively using the randomisation techniques described in Section 2.3.1. By linearly interpolating between these confidence levels the significance of the 71.49 s period is estimated as 4.37σ. The 'blurring' randomisation test described in Section 2.3.2 was used to calculate the error on this period as ±0.02 s. Figure 4.3 shows the phase-folded light curve of Obs 1 using the 71.49 s period. The shape is dominated by a large peak on top of an underlying flux at ∼6.4 counts s^{-1} PCU^{-1}, representing a pulse fraction of ∼13%, where the pulse fraction is defined as $(C_{max} - C_{min})/(C_{max} + C_{min})$. A possible second peak is also observed at lower significance and is offset from the larger peak by a phase of ∼0.3−0.4. A discussion of this shape and the non-detections in Obs 2 and 3 is given in Sect. 4.4

For consistency the event mode data were also investigated for periodicities using the extracted 0.125 s resolution background subtracted light curves. Using the full energy response light curve (2−120 keV) the only significant feature in the periodogram is detected at 71.52 s with a power of 20.37, in agreement with the result from the standard mode one data. The event mode data light curves in the 3−10 and 10−120 keV energy bands were also searched for pulsations (Note: When

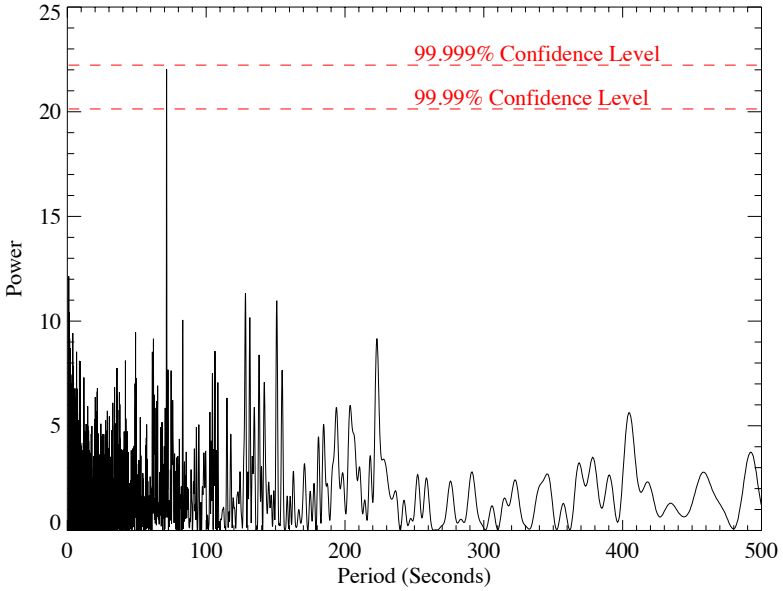

Figure 4.2: Lomb-Scargle periodogram of the background subtracted Obs 1 0.125 s resolution standard mode one lightcurve of IGR J17544−2619, showing a peak at a period of 71.49 s. This period is estimated to have a significance of 4.37σ.

using restricted energy ranges, 3 keV is used as the low energy cut-off point due to the degrading of the PCA energy calibration below this value). In both cases a peak at ∼71.5 s is observed in the periodogram but it is not at a significant level. The sum of these periodograms does, however, produce a single significant peak at the correct periodicity. This is taken to illustrate that, due to the faintness of the emission, a significant detection can only be obtained when the full energy range is included in the dataset and hence the periodicity is present (to some extent) over a broad range of energies.

Variations in the hardness ratio as a function of pulse phase have been investigated. Figure 4.3 shows the 2−120 keV phase-folded light curve (top) above the phase-folded 10−120 keV to 3−10 keV hardness ratio (bottom). It can be seen that the emission hardens during the two pulse phase regions that are coincident with increased flux in the phase-folded light curve. This suggests a physical origin for both the high and lower significance peaks seen in the phase-folded light curve shown in the top panel of Fig. 4.3.

4.3.2 Spectral Analysis

The energy spectra derived from the total data in each observation were investigated to characterise the spectral shape of the emission and aid in the identification of its source. The spectra were fit with models in the 3−20 keV energy range using XSPEC v12.4. All reported errors from the spectral fits are

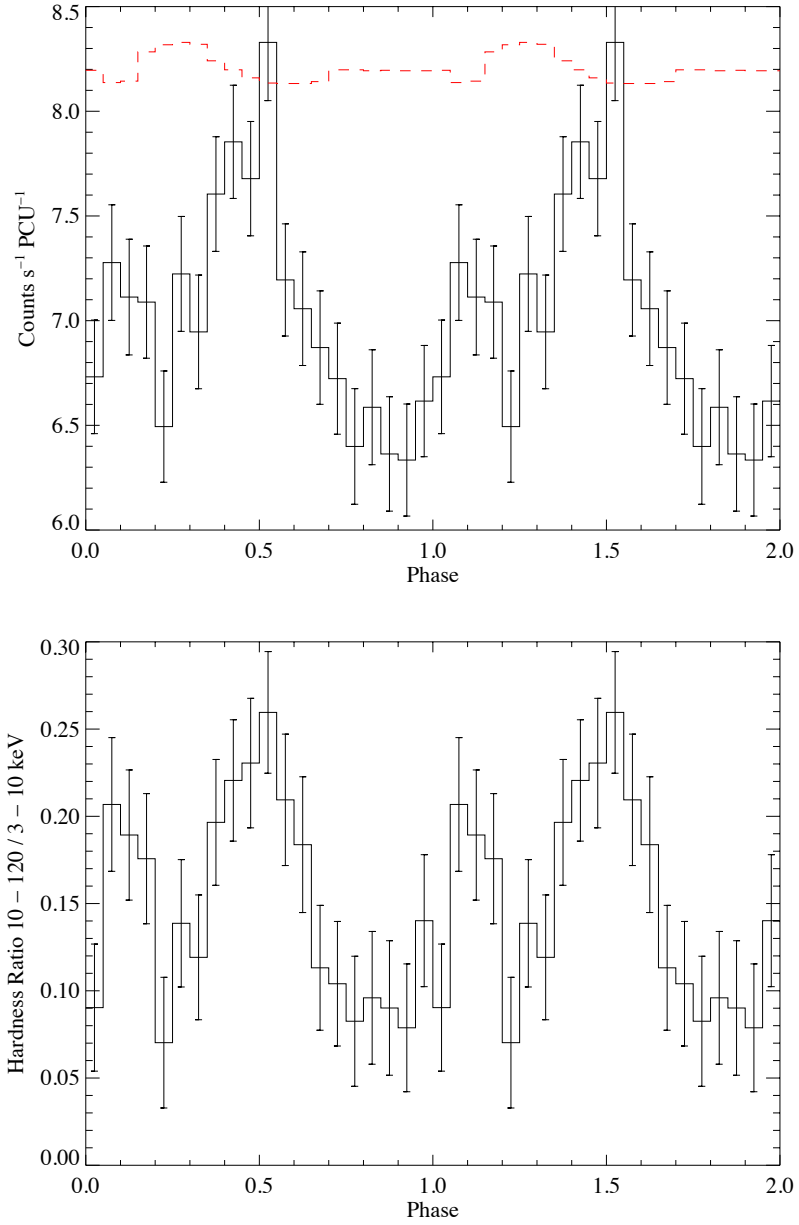

Figure 4.3: Top: Obs 1 light curve of IGR J17544−2619 phase-folded on the 71.50 s period. The profile shows a pulse fraction of ∼13%. The dashed line shows the relative exposure of each phase bin (a relative exposure of 1 equates to a count rate of 8.3 and 0 to 0 within this scaling). Bottom: Hardness ratio between the 3−10 and 10−120 keV energy bands showing a hardening of the observed emission during the peaks in the above phase-folded light curve. Both curves posses the same phase binning and arbitrary zero pulse phase ephemeris.

quoted at the 90% confidence level. The spectra were initially fit with simple absorbed models (e.g. phabs(bremss)), however, the large $\hat{\chi}^2$ values (6.8−12.8 for 37 degrees of freedom) showed a need for an additional Gaussian component, which was interpreted as an iron emission line. It was found that absorbed power-law models, with an additional Gaussian component, gave the best fits across all three observations. Power-laws with high energy cut-offs and thermal bremsstrahlung models were also found to produce statistically similar fits for some individual observations, but neither could produce as good a fit across all three observations.

The results of the power-law fits are outlined in Table 4.2. It is seen that the spectra are quite highly absorbed and do not show a significant variation in column density across the observations. They possess photon indices that vary from $2.37^{+0.09}_{-0.09}$ to $2.69^{+0.13}_{-0.13}$ between Obs 1 and 3. The inferred 3−10 keV fluxes also show some variation across the three observations, declining significantly from $(5.43^{+0.08}_{-0.10})\times10^{-11}$ in Obs 1 to $(5.13^{+0.10}_{-0.12})\times10^{-11}$ erg cm^{-2} s^{-1} in Obs 3. The flux in Obs 2 lies between these two values, suggesting a decline throughout the observations. The spectra of the individual observations were also summed and the total spectrum fitted. The best fit parameters are shown in Table 4.2 and a similar shape is again observed. The spectrum of Obs 3 fitted with the absorbed powerlaw plus Gaussian model is also shown in the top panel of Fig. 4.4.

The large equivalent width of the iron line component in each spectrum, varying from 0.78 to 0.88 keV, is of interest. These values are consistent with those quoted as resulting from Galactic Ridge emission (Koyama et al., 1986), suggesting that Galactic Ridge emission could account for part or all of the emission detected in these observations. To investigate this we fit the spectra with the model of the central ridge region presented in Table 3 of Valinia & Marshall (1998). The Raymond-Smith plasma temperature and power-law photon index were fixed to kT=2.9 keV and Γ =1.8 respectively, whilst the absorption and normalisations were left as free parameters. As Table 4.3 and the lower panel of Fig. 4.4 show, Obs 2 and 3 are well described by this model. However, Obs 1 is not well fit by this model, indicating that Galactic Ridge emission does not fully describe the spectral shape of this observation. A decreasing unabsorbed flux trend is also observed between Obs 1 and 3. Combining the poor fit given by the Galactic Ridge model in Obs 1 and the decreasing flux trend seen across the three observations with the fact that a pulsation is only seen during Obs 1, suggests that in the first observation there is an additional source of X-ray emission that generates the observed pulsed signal in addition to the Galactic Ridge emission.

To further investigate the possible nature of the additional X-ray source we used pulse phase resolved spectroscopy to extract spectra during the pulse on, phase 0.4−0.7 in the top panel of Fig. 4.3, and pulse off, phase 0.7−1.0, regions. The spectrum collected from the pulse off region was then subtracted from the pulse on

Table 4.2: Spectral fits to the total and three individual observations of IGR J17544−2619 using the model: phabs(powerlaw + Gaussian). Error are quoted at the 90% confidence level

Obs	$\hat{\chi}^2$/d.o.f.	Γ	N_H 10^{22} cm^{-2}	Line Energy keV	Line Sigma keV	Line Equivalent Width keV	Flux (3−10 keV) erg cm^{-2} s^{-1}
1	0.95/34	$2.37^{+0.09}_{-0.09}$	$4.4^{+1.3}_{-1.2}$	$6.54^{+0.05}_{-0.05}$	$0.03^{+0.19}_{-0.03}$	0.82	$5.43^{+0.08}_{-0.10}\times10^{-11}$
2	0.39/34	$2.40^{+0.13}_{-0.13}$	$5.1^{+1.7}_{-1.7}$	$6.56^{+0.07}_{-0.07}$	$0.15^{+0.18}_{-0.15}$	0.78	$5.28^{+0.10}_{-0.11}\times10^{-11}$
3	0.78/34	$2.69^{+0.13}_{-0.13}$	$5.9^{+1.6}_{-1.6}$	$6.67^{+0.07}_{-0.06}$	$0.14^{+0.17}_{-0.14}$	0.88	$5.13^{+0.10}_{-0.12}\times10^{-11}$
Total	1.01/34	$2.48^{+0.06}_{-0.06}$	$5.2^{+0.8}_{-0.8}$	$6.58^{+0.03}_{-0.03}$	$0.11^{+0.11}_{-0.10}$	0.80	$5.32^{+0.06}_{-0.06}\times10^{-11}$

Table 4.3: Spectral fits to the three individual observations of IGR J17544−2619 using the model Phabs(Raymond + Powerlaw) of Valinia & Marshall (1998)

Obs	$\hat{\chi}^2$/d.o.f.	Flux (3−10 keV) erg cm^{-2} s^{-1}
1	1.735/35	$5.41^{+0.09}_{-0.08}\times10^{-11}$
2	0.700/35	$5.26^{+0.10}_{-0.08}\times10^{-11}$
3	0.869/35	$5.13^{+0.07}_{-0.09}\times10^{-11}$

region, calculated in 'count rate' space to compensate for the different exposure times accumulated for each phase region. However, whilst there were residual counts in the subtracted spectrum, the signal-to-noise was not sufficient to allow the fitting of spectral models to characterise the pulsed emission and provide a direct estimate of the residual flux. Figure 4.4 (bottom) does show a hardening of the emission during the pulse on phase region, however, suggesting the presence of an additional active, pulsing X-ray source within the FOV as the Galactic Ridge emission does not vary on these timescales.

A refined estimate of the pulsed flux in Obs 1 can be made by using the phase-folded light curve shown in the top panel of Fig. 4.3. Under the assumption that the minimum count rate in the phase-folded light curve corresponds to zero emission from the pulsed source, which is supported by the consistency of the count rate between phases 0.70 and 1.0 in Fig. 4.3, the percentage excess above the minimum count rate is calculated for each phase bin. Taking the average of the excesses observed in each phase bin produces an estimate of the pulsed flux fraction as 8.9%. Using the Obs 1 flux value obtained from the spectral fits outlined in Table 4.2, this corresponds to a flux of 4.8×10^{-12} erg cm^{-2} s^{-1} (3−10 keV) originating from the pulsed signal with the remaining flux being generated by the Galactic Ridge emission. As the Galactic Ridge emission cannot generate a pulsed signal or spectral variations on a timescale of tens of seconds, this pulsed flux component is therefore attributed to another active X-ray source within the FOV during Obs 1.

4.4 Discussion

Following the spectral analysis presented in Sect. 4.3.2 it is concluded that the emission observed in Obs 2 and 3 is most likely originating from the diffuse Galactic Ridge emission. However, in Obs 1 there appears to be evidence for an additional flux component that is generating a periodic signal. This emission is attributed to a further active X-ray source within the FOV during this observation. As no significant periodic signals were observed during Obs 2 and 3, and no structure was seen when these light curves were folded on the known 71.49 s period, it is

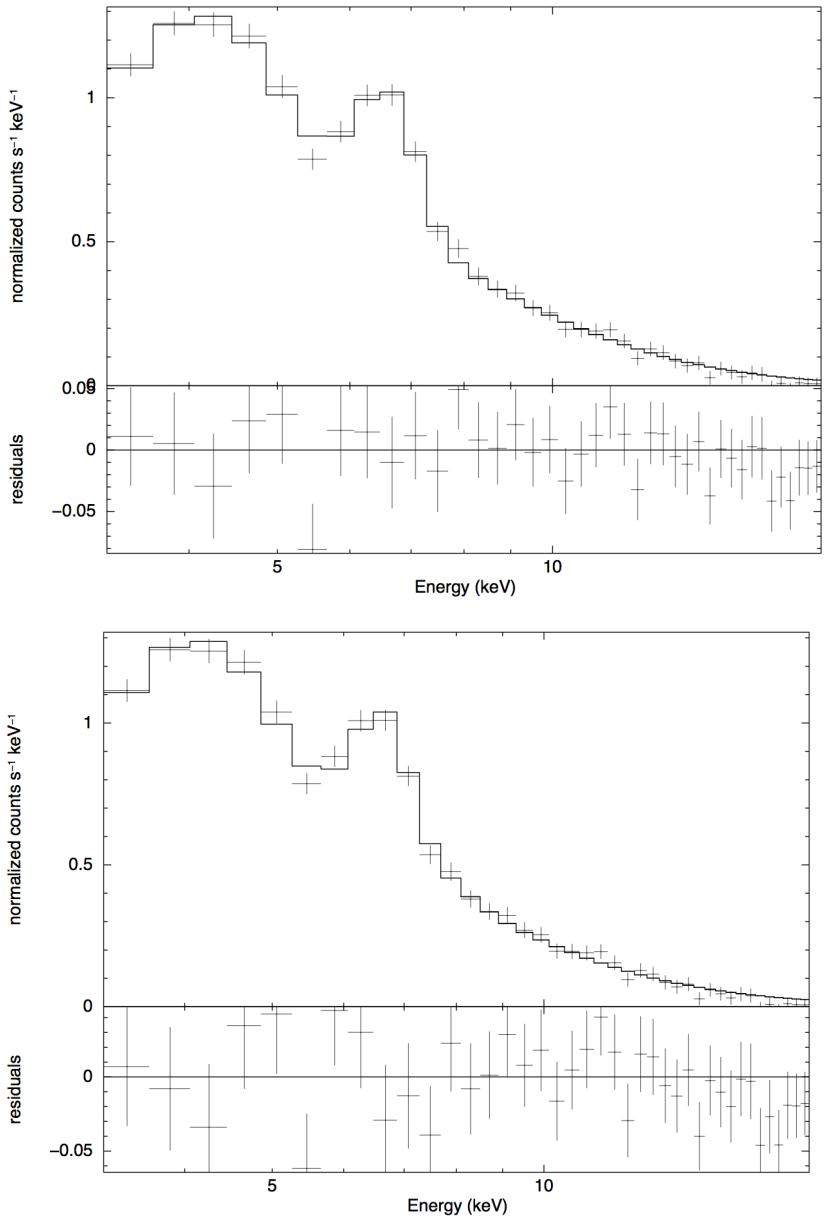

Figure 4.4: Spectral fits to the PCA spectrum of Obs 3 of IGR J17544−2619 in the 3−20 keV band. Top: data, best fit and residuals using the model phabs(powerlaw + Gaussian); Bottom: data, best fit and residuals using the model phabs(Raymond + powerlaw) with the constrained Galactic Ridge emission spectral parameters of Valinia & Marshall (1998). These spectra correspond to the Obs 3 spectral fits in Tables 4.2 and 4.3.

concluded that the additional X-ray source was not active during these observations. This interpretation is supported by the significant decrease in $3-10$ keV flux observed between Obs 1 and 3, see Sect. 4.3.2. It is noted, however, that this interpretation represents the simplest situation, whereby only the two flux components that can be definitively identified, namely the pulsed flux in Obs 1 and a contribution from the Galactic Ridge emission in all three observations, are used. In fact it may be that there are additional faint, non-pulsating sources within the PCA FOV during all three observations that contribute towards the detected flux in each. Changes in the flux emitted by, or the number of, any such sources could cause the variations in the average $2-120$ keV flux detected in each observation as outlined in Table 4.1. Due to the non-imaging nature of the PCA, however, it is not possible to perform identification of any non-pulsating source other than the Galactic Ridge emission, identified by the large equivalent width of the iron line component in the spectral fits, and hence the most simplistic interpretation is used for the remainder of this chapter. A second consequence of the non-imaging nature of the PCA is that further consideration as to the source of the excess, pulsed emission seen in Obs 1 is required.

Figure 4.5 shows the fourth *INTEGRAL*/IBIS survey significance map of the region in the $18-60$ keV energy band (Bird et al., 2010). Overlaid are the PCA half and zero collimator response contours, at 0.5^o and 1^o respectively, for the pointing used, along with the sources in the *INTEGRAL* general reference catalog (squares) (v.31, Ebisawa et al. 2003) and further X-ray detections (circle). Similarly the *ROSAT* all-sky survey photon map of the region in the $0.1-2.4$ keV energy range is shown in Fig. 4.6 (Voges et al., 1999). It can be seen that the only two sources significantly detected in the fourth *INTEGRAL* catalog located within the zero response contour are IGR J17544−2619 and IGR J17507−2647. The latter of these sources, which is at the edge of the FOV, was characterised using *Chandra* observations by Tomsick et al. (2009) as a weak, persistent source with a flux of 4.5×10^{-12} erg cm^{-2} s^{-1} ($0.2-10$ keV) that is most likely a distant HMXB at $\sim$8.5 kpc. The *Chandra* spectrum of the source reported a high level of absorption with $N_H = 1.34\times10^{23}$ cm^{-2} and the source was not detected in the *ROSAT* map. As IGR J17507−2647 is located at the edge of the PCA FOV it is in a region of low collimator response ($< 5\%$) and would therefore require a flux of at least a factor of 20 greater than that reported by Tomsick et al. 2009 to generate the observed pulsed flux. As this is a persistent source with no reported outbursts, it is concluded that the emission observed by *RXTE* is unlikely to be contaminated by IGR J17507−2647.

The soft X-ray source 1RXS J175454.2-264941 (Voges et al., 1999) is reported in the *ROSAT* bright source catalog and is located near the half response contour; it is the only bright soft X-ray source detected within the PCA FOV by *ROSAT*. The hardness ratio reported suggests the source is moderately hard (0.82 for the

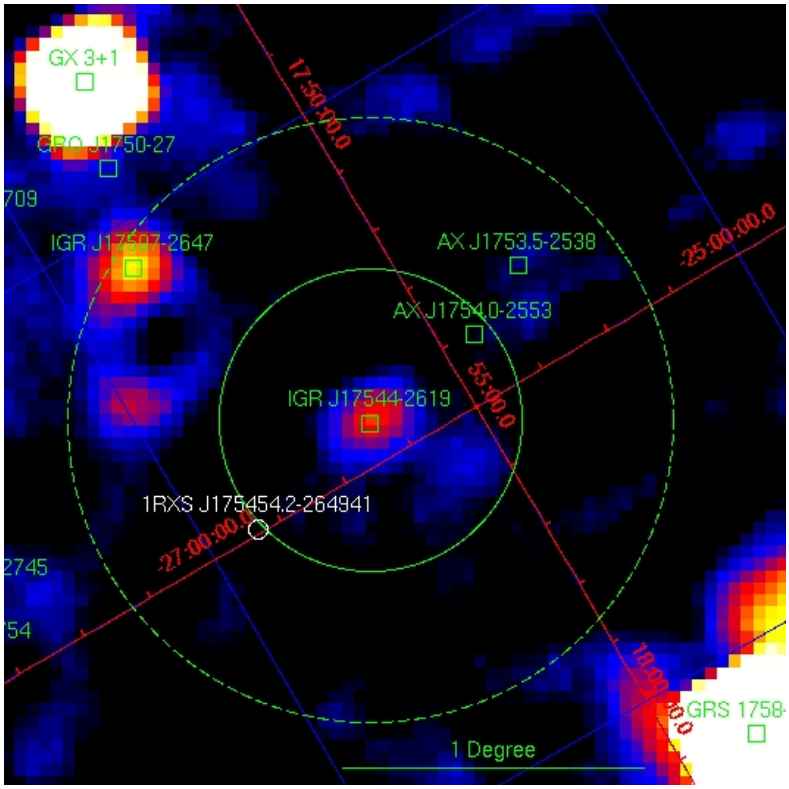

Figure 4.5: The IBIS survey 18−60 keV significance map of the IGR J17544−2619 region, exposure ∼8 Ms, with the PCA FOV half and zero response contours overlaid (Bird et al., 2010). The sources in this region that are contained in the *INTEGRAL* general reference catalog are shown as square points, whilst further X-ray sources are shown as circles.

0.5−2/0.1−0.4 keV energy bands) and could be detected by the PCA. There are also four sources from the *ROSAT* faint source catalog (Voges et al., 2000) within the FOV, however, due to the low flux of these sources a detection with the PCA would not be expected. Finally the ASCA sources shown in Fig. 4.5 are reported as X-ray point sources by Sugizaki et al. (2001). AX J1753.5−2538 was detected at 3σ in the 0.7−2 keV band but was not found in the 2−10 keV band, indicating that it is a soft source, hence a detection with PCA would not be expected. However, the non-detection in the *ROSAT* survey map shown in Fig. 4.6 does suggest a transient nature for this source. AX J1754.0−2553 is not detected in the 0.7−2 keV band but does have a 3.8σ detection in the 2−10 keV energy range. This suggests the source is harder and, as for 1RXS J175454.2−264941, could be detected in the PCA data.

Of all the sources discussed above, IGR J17544−2619 is the most active, showing a large number of outbursts that have been detected by a number of instruments (Clark et al., 2009). Taking into account the nature of the other known sources within the PCA FOV leads to the conclusion that IGR J17544−2619 is the most likely known source of the emission detected by the PCA instrument. This conclusion is drawn from the enhanced level of activity of IGR J17544−2619, especially in the hard X-ray band, compared to the other sources in the FOV, the

compatible flux of the pulsed signal compared to the historical behaviour of IGR J17544−2619 as outlined in the following paragraphs and the position of IGR J17544−2619 in the region of full response of the PCA. For the remainder of this chapter it is assumed to be the case that IGR J17544−2619 is the source of the pulsed signal, but the possibility that the emission is generated by one of the other known sources, 1RXS J175454.2−264941 and AX J1754.0−2553 in particular, or a new unknown source within the PCA FOV cannot be totally ruled out.

If the 71.50 s signal is consider as a pulsation originating in the IGR J17544−2619 system, then this confirms that the compact object in the system is a neutron star as has been suggested from the soft quiescence spectra (in't Zand 2005, Pellizza, Chaty, & Negueruela 2006). Assuming a source distance of ∼3.6 kpc (Rahoui et al., 2008a) makes the estimated source flux equivalent to an unabsorbed luminosity of $\sim 1\times10^{34}$ erg s^{-1} (3−10 keV), indicating that IGR J17544−2619 was observed in an intermediate X-ray luminosity state as opposed to during a large outburst (such as the 10^{36} erg s^{-1} event reported in Grebenev et al. 2004). This flux is consistent with the results of Romano et al. (2011) who found, using two years of *Swift*/XRT monitoring data, that IGR J17544−2619 was most likely to be observed at a luminosity of 2×10^{34} erg s^{-1} (2−10 keV). X-ray pulsations have also been detected in other SFXT systems observed during similar intermediate luminosity states, $\sim 1\times10^{34}$ erg s^{-1} (0.5−10 keV) in IGR J18483−0311 (Giunta et al., 2009) and 2.3×10^{34} erg s^{-1} (2−10 keV) in AX J1841.0-0536 (Bamba et al., 2001) for example. Additionally the hardness ratio has also been seen to vary as a function of pulse phase in the SFXT IGR J11215−5952 (Sidoli et al., 2007a), showing a hardening of emission during the pulse-on phase region as is also observed for IGR J17544−2619 in the lower panel of Fig. 4.3.

The identified signal can also be used to consider the origins of the extreme variability observed in IGR J17544−2619. On several occasions IGR J17544−2619 has displayed bright flaring behaviour during which the source has risen from a quiescent state (a few 10^{32} erg s^{-1}) to a bright X-ray state (a few 10^{36} erg s^{-1}) over a time frame of several hundreds to thousands of seconds (e.g. in't Zand 2005, Rampy, Smith, & Negueruela 2009). The orbital motion of the neutron star cannot be responsible for the onset of individual outbursts of IGR J17544−2619 given the short rise times of the flares and that the quiescent states are observed at varied orbital phases, including during periastron passage as observed by *Suzaku*(Rampy, Smith, & Negueruela, 2009). This observation covered an orbital phase range of $\phi \sim 0.01$ to 0.56 using the ephemeris defined in Section 2.4.3, and displayed several periods of quiescent level emission during this time. Therefore more localised fluctuations in the environment of the neutron star are instead required to generate the individual outbursts observed from IGR J17544−2619. However, it does appear that the likely eccentric orbital motion preferentially allows the conditions under which an outburst can be generated to be met when the neutron star is closer to

periastron in IGR J17544−2619, given the peaked outburst orbital phase distribution shown in the right hand panel of Fig. 2.16.

Using the extreme ends of the luminosity distribution observed from IGR J17544−2619 allows the structure of the stellar wind in the system to be probed. Using the relationship $L_x = GM_{NS}\dot{M}_{capt}/R_{NS}$ allows the mass capture rates required to power the observed quiescent and peak X-ray luminosities (8×10^{31} and $4.2\times10^{36}\,\mathrm{erg\,s^{-1}}$ respectively assuming a source distance of 3.6 kpc) to be calculated as 4.2×10^{8} and $2.2\times10^{13}\,\mathrm{kg\,s^{-1}}$ respectively if the system remains in the 'Direct (Bondi) accretion' regime at all X-ray intensities. These mass capture rates can be converted to representative stellar mass loss rates, assuming the supergiant mass loss is isotropic, with the expression $\dot{M}_{capt}/\dot{M}_w = R_{acc}^2/(4a^2)$ where R_{acc} is the accretion radius (Eq. 1.1) and a is the orbital separation (Frank, King, & Raine, 2002). Performing this calculation requires an assumption as to the dynamical make up of the system in order to derive the orbital separation of the components and the relative velocity between the neutron star and stellar wind. The mass of the supergiant is taken at the upper limit of the range proposed by Pellizza, Chaty, & Negueruela (2006), $28\,\mathrm{M_\odot}$, and combined with a nominal $1.4\,\mathrm{M_\odot}$ neutron star to produce an orbit with a semi-major axis of $37.6\,\mathrm{R_\odot}$. For the sake of simplicity the orbit is assumed to be circular in the remainder of these calculations such that the orbital separation is $37.6\,\mathrm{R_\odot}$ at all orbital phases. This is at odds with the phase-folded light curve and orbital phase outburst distribution shown in Fig. 2.16, which both suggest a significant eccentricity in the orbit of IGRJ17544−2619. However, as stated previously, the variation in stellar wind conditions over large sections of orbital phase cannot be responsible for the fast flares observed in the individual outbursts, with more local variations likely to be responsible. Hence a circular orbit is utilised to describe the typical stellar wind conditions at a characteristic separation from the supergiant but it should be noted that additional variations would be induced by the likely eccentricity in the binary orbit. The supergiant radius is taken as $20.3\,\mathrm{R_\odot}$ by utilising the $R_{sg}/D_{sg} = 1.27\times10^{-10}$ SED parameter of Rahoui et al. (2008a) and assuming their preferred distance of 3.6 kpc (as has also been the case for the luminosity calculations throughout). In this case the stellar radius restricts the orbital eccentricity to being < 0.2 to prevent the initiation of RLO (Clark et al., 2009). Under these assumptions on the stellar and orbital properties of IGR J17544−2619, the neutron star orbital velocity is $\sim370\,\mathrm{km\,s^{-1}}$ and the stellar wind radial velocity is calculated as $460\,\mathrm{km\,s^{-1}}$ using Eq. 3.2, assuming, in the absence of any formal constraints, $\mathrm{v}_\infty = 1000\,\mathrm{km\,s^{-1}}$ and $\beta = 1.0$. Hence the relative velocity at the typical orbital separation is $\sim600\,\mathrm{km\,s^{-1}}$ and the accretion radius is calculated as $R_{acc} = 1.0\times10^{11}$ cm using Eq. 1.1. The representative total mass loss rates of the supergiant companion for the quiescent and peak luminosity states are therefore 1.7×10^{-11} and $9.2\times10^{-7}\,\mathrm{M_\odot\,yr^{-1}}$ respectively.

As shown in the above paragraph, extreme stellar wind density variations, equating to 4−5 orders of magnitude in representative total mass loss rates, over small spatial scales are required to generate the X-ray variability observed in some outbursts of IGR J17544−2619 if the emission is generated through Bondi style accretion. This would imply a high degree of structure in the stellar wind of the supergiant with the majority of the mass lost in clumps embedded in a very rarified intra-clump medium to allow the quiescent states to be inhabited for a high proportion of the time in a system with a short 4.9278 day orbit. The density variations required may be reduced, however, when the likely non-linear nature of the stellar wind velocity profile is taken in to account. As shown by Oskinova, Feldmeier, & Kretschmar (2012), and discussed in Section 1.2.2, the size of the accretion radius, and hence the mass capture rate is very sensitive to the relative velocity between the neutron star and the stellar wind such that $L_x \propto v_{rel}^{-4}$. Under the assumed system parameters discussed in the previous paragraph, the orbital separation in the system is $\sim$1.9 R_{sg} which is in the region of high velocity variability, and associated density variability through continuity considerations, as defined by Oskinova, Feldmeier, & Kretschmar (2012). Variations in the stellar wind velocity by a factor of $\sim$10−20 could therefore have a significant role to play in generating the observed X-ray behaviour of IGR J17544−2619.

An alternative origin of the observed behaviour is that of the action of barriers to the accretion flow acting to increase the X-ray dynamic range of the system for lower intrinsic stellar wind variations. The applicability of these barriers can now be tested assuming the 71.49 s pulsation is that of IGR J17544−2619. The accretion regimes and theoretical framework outlined in Section 1.2.2 (Bozzo, Falanga, & Stella, 2008a) are used along with the assumed orbital parameters discussed previously in the following considerations. Using Eq. 1.3 the co-rotation radius of the neutron star in IGR J17544−2619 is calculated as 2.9×10^9 cm. Hence, under the assumed stellar wind parameters $R_{acc} >> R_{co}$ which rules out the magnetically gated accretion scenarios (see panels A and B of Fig. 1.14), from operating in IGR J17544−2619, as these require R_{acc} to be smaller than both R_{co} and R_M such that the stellar wind material impacts directly on the magnetosphere without any prior gravitational focusing. Instead it may be the case that a centrifugal barrier (i.e the propellor effect as shown in panel C of Fig. 1.14) is acting to inhibit accretion during the periods of quiescence observed in IGR J17544−2619. The propellor effect is initiated when R_M becomes larger than R_{co} and material halted at the magnetosphere cannot overcome the centrifugal force of the rotation and be accreted on to the neutron star. The representative total mass loss rate at which the centrifugal barrier is initiated can be calculated such that the condition $R_M = R_{co}$ is satisfied. Using Eq. 1.3 for the co-rotation radius and Eq. 19 of Bozzo, Falanga, & Stella (2008a) for the magnetic radius, namely:

$$R_M = 2 \times 10^{10} a_{10d}^{4/7} \dot{M}_{-6}^{-2/7} v_8^{8/7} \mu_{33}^{4/7} \text{ cm} \tag{4.1}$$

the limiting mass loss rate can be calculated with the expression:

$$\dot{M}_{-6} = \left(\frac{2 a_{10d}^{4/7} v_8^{8/7} \mu_{33}^{4/7}}{1.7 P_{s3}^{2/3}} \right)^{7/2} \; 10^{-6} \, \mathrm{M_\odot \, yr^{-1}} \tag{4.2}$$

Assuming a nominal neutron star magnetic field strength of 10^{12} G produces a cutoff representative mass loss rate of $7.3{\times}10^{-10} \, \mathrm{M_\odot \, yr^{-1}}$ below which the source will enter the propellor regime and accretion will cease. This value represents an increase of a factor of ∼40 in the minimum wind density required to generate the quiescent states compared to the pure Bondi accretion case. The minimum X-ray luminosity at which accretion is able to proceed in this scenario can be estimated by using the $\dot{M}_{capt}/\dot{M}_w = R_{acc}^2/(4a^2)$ relationship to derive a mass capture rate of $1.8{\times}10^{10} \, \mathrm{kg \, s^{-1}}$, corresponding to an X-ray luminosity of $3.3{\times}10^{33} \, \mathrm{erg \, s^{-1}}$. This derived minimum luminosity corresponds well with the observed distribution of luminosities detected in two years of *Swift*/XRT monitoring of IGR J17544−2619 presented by Romano et al. (2011) which is centred at a luminosity of $\sim 2{\times}10^{34} \, \mathrm{erg \, s^{-1}}$ and extends down to a few $10^{33} \, \mathrm{erg \, s^{-1}}$, with the source being below the sensitivity of the XRT in 55% of the monitoring observations.

The calculations performed above have considered possible alternative origins of the deep quiescences and extreme X-ray flares of IGR J17544−2619. It is shown that the evolution of individual flares cannot be explained by the orbital motion of a neutron star in an eccentric orbit alone due to the orbital distribution of both outburst and quiescence detections. It is also shown that the local stellar wind density being experienced by the neutron star would have to vary by ∼5 orders of magnitude over small spatial scales, with a large proportion of the stellar mass loss rate being contained in dense clumps, in order to generate the observed luminosity variations under Bondi style accretion within a stellar wind of stable velocity. Possible methods of generating the same X-ray dynamic range without invoking such strong local density variations are through a non-monotomically accelerating stellar wind (Oskinova, Feldmeier, & Kretschmar, 2012) and the action of a centrifugal barrier to the accretion flow (Bozzo, Falanga, & Stella, 2008a). Whilst the calculations were performed under a number of assumptions about the orbital and stellar parameters of the binary, as described previously, it was shown that local variations of the stellar wind velocity on the order of 10−20 and/or the action of the centrifugal barrier that is realised below mass capture rates equivalent to an X-ray luminosity of $\sim 3{\times}10^{33} \, \mathrm{erg \, s^{-1}}$ could explain the observed X-ray dynamic

range with a lower intrinsic variability in the local stellar wind density. Presently it is not possible to draw final conclusions as to the exact nature of the processes driving the extreme X-ray behaviour of IGR J17544−2619 due to the uncertainty in the stellar and orbital parameters of the system other than to illustrate the applicability of these processes under the given assumptions. It is of note, however, that the action of a centrifugal barrier to impede accretion onto the neutron star is consistent with the very soft spectral states detected in quiescence (e.g. $\Gamma = 5.9$; in't Zand 2005) which indicate accretion is not taking place at this time. Instead the detected emission may be resulting from the hot surface of the neutron star or the intrinsic emission of the supergiant companion itself. In either case this may explain the lack of the detection of the pulsed signal during observations of the source in quiescence, as such a signal would not be expected to be generated when plasma was not entering the magnetosphere and being funnelled toward the magnetic poles of the neutron star.

The detection reported here, combined with past observations by other observatories, indicates that the pulsation produced by IGR J17544−2619 is not always observable. IGR J17544−2619 has had snapshot observations taken by *XMM-Newton* (González-Riestra et al., 2004) and *Chandra* (in't Zand 2005) along with a monitoring campaign by *Swift*/XRT (Romano et al., 2011), none of which show detections of the 71.49 s signal. However the observational properties of SFXTs make the detection of pulse periods difficult. The biggest obstacle is the X-ray flaring timescale observed at soft X-ray energies which is similar to likely pulsation periods (i.e. tens to hundreds of seconds). Flares dominate many of the soft X-ray datasets and mask pulsation signals due to the larger flux variations they induce. Many of the remaining datasets that are not dominated by flares are short *Swift*/XRT exposures that have too short baselines or insufficient statistics for accurate timing analysis to be performed (e.g. Romano et al. 2011). Given the nature of the previous soft X-ray observations of this source it is plausible that the pulsation of IGR J17544−2619 has not been detected prior to these observations, which show a steady flux at the 10^{34} erg s^{-1} level. These fluxes are consistent with those during which previous SFXT pulsations have been detected (e.g. Giunta et al. 2009).

Furthermore, the observation was performed as the neutron star was approaching apastron in the system which could also help explain why the pulsations were detected here. Clark et al. (2009) showed that at this orbital phase there is still a non-zero probability of stellar wind clump interaction in this system (Clark et al. 2009, Fig. 7). Additionally under the model of Ducci et al. (2009) the stellar wind clumps expand as they move out from the companion supergiant star, likely becoming more homogeneous in density as they travel. As a result it may be expected that the X-ray emission generated during the interaction of the neutron star and the expanded stellar wind clump would also be smoother and less prone to

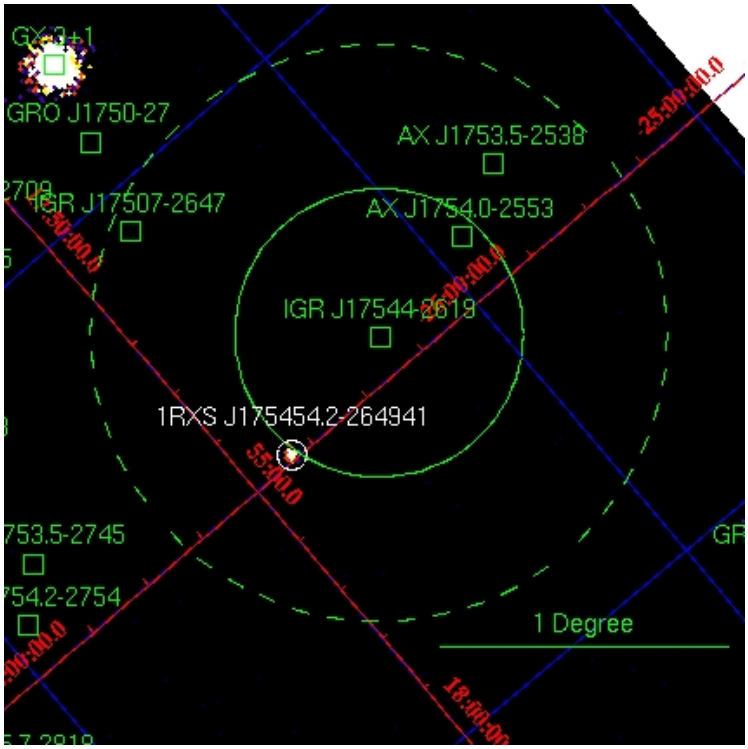

Figure 4.6: The *ROSAT* all sky survey photon map of the IGR J17544−2619 region in the 0.1−2.4 keV energy range (Voges et al., 1999). The annotations are the same as those in Fig. 4.5.

undergo the fast flares that dominate other soft X-ray observations of this source. Until a larger number of detections have been achieved, however, formal conclusions on any link between the detection of the pulsations and the orbital phase of the observations cannot be drawn.

Combining this detected pulsation with the 4.926 d orbital period of Clark et al. (2009) allows the placement of IGR J17544−2619 on the Corbet diagram (Corbet, 1986), Fig. 4.7. IGR J17544−2619 is seen to be located within the region of the parameter space occupied by the classical, wind-fed SgXRBs. Under the 'clumpy wind' model of SFXTs (in't Zand, 2005) the difference in behaviour seen in SFXTs when compared to the classical SgXRB systems is explained by an enhanced eccentricity which results in the compact object spending only a fraction of its orbit within a dense stellar wind environment, during which time bright X-ray behaviour is observed. For a large proportion of its orbit, however, the neutron star inhabits a sparsely populated region of the stellar wind which allows the source to reach a deep X-ray quiescence (Walter & Zurita Heras 2007, Chaty et al. 2008a). Under this SgXRB unification model SFXTs can be considered as an extension of the classical SgXRBs that result from varied orbital parameters. The nature of IGR J17544−2619 appears to both support and somewhat contradict this interpretation of SFXTs. Whist the orbital phase-folded light curve and outburst distribution both suggest that there is a significant eccentricity in the orbit of IGR J17544−2619

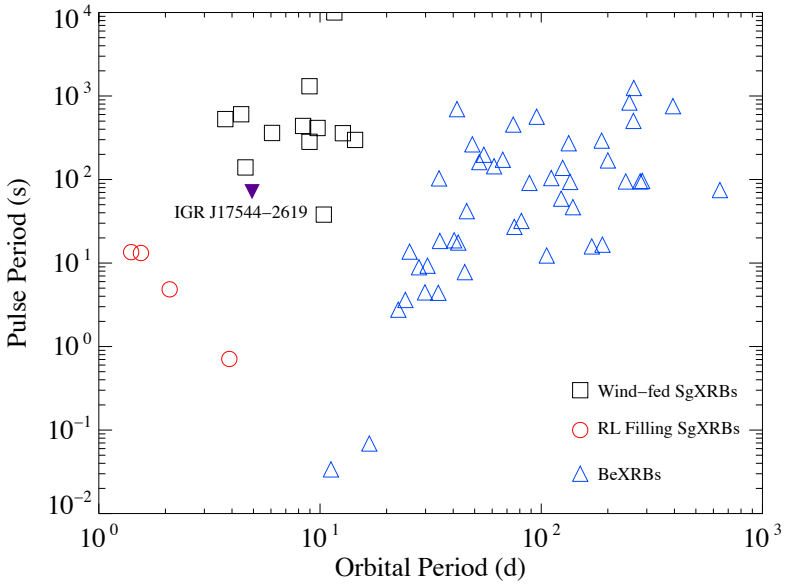

Figure 4.7: The Corbet Diagram (Corbet, 1986) illustrating the location of IGR J17544−2619 (solid purple triangle) within this parameter space assuming the 71.49 s pulsation originates from this source. IGR J17544−2619 lies in the region of parameter space populated by the classical SgXRBs.

and luminous X-ray events are preferentially generated during the periastron passage, the detection of quiescent level emission within the same orbital phase range illustrates it is not simply the location in the orbit that generates the observed range of X-ray luminosities in this system. Instead an additional mechanism is required to produce the large swings in X-ray luminosity. This mechanism may simply be an extreme concentration of the mass lost from the supergiant being contained in clumps, resulting in an extremely rarified intra-clump medium such that the X-ray emission directly traces the stellar wind density, consistent with the clumpy wind model only. In the case of IGR J17544−2619, however, it is also possible that higher order effects such as the action of a centrifugal barrier to impede the accretion flow may be acting to increase the X-ray dynamic range beyond that which would be generated by the variations in the stellar wind density and interaction with dense clumps alone. IGR J17544−2619 may therefore be illustrating physical processes beyond those of the nominal 'clumpy wind' model of SFXT emission.

The implications of the observations presented in this chapter are placed within the context of wider recent results on SFXTs in Chapter 6, where a discussion on the global nature of SFXTs is undertaken.

4.5 Conclusions

Using observations of the region of the SFXT IGR J17544−2619 by *RXTE*/PCA, a transient 71.49±0.02 s pulsed signal has been detected. Through the consideration of the population of X-ray sources within the PCA FOV it is concluded that the signal is most likely generated by the spinning neutron star in IGR J17544−2619. The pulse phase-folded light curve shows a double peaked structure in which the emission is observed to harden during the peaks in the profile. IGR J17544−2619 was observed in a steady state of emission with a luminosity of $\sim 1 \times 10^{34}$ erg s^{-1} (3−10 keV). The emission history of IGR J17544−2619 is considered in the context of the newly discovered pulsation and it is concluded that physical processes beyond the nominal 'clumpy wind' theory of SFXT emission may be occurring in this system. The detected 71.49 s pulse period places IGR J17544−2619 in the same region of the Corbet diagram as the classical wind-fed SgXRBs.

Chapter 5

INTEGRAL studies of Supergiant Fast X-ray Transients

5.1 Discovery of the 51.47 day orbital period in the SFXT XTE J1739−302

XTE J1739−302 was discovered as a new X-ray transient with the PCA instrument aboard *RXTE* during observations of the Galactic centre region (Smith et al., 1998). The source was first detected at 16:58 UT on 1997 August 12; it had not been detected in the previous scan of the region on 03 August and was not detected during the next scan on 14 August. Assuming a thermal bremsstrahlung spectral model, Smith et al. (1998) estimated an unabsorbed peak flux (2 to 25 keV) of 3.0×10^{-9} erg cm^{-2} s^{-1}. The authors proposed that the source was a binary comprised of a Be star and a neutron star based upon its spectral shape, but noted that its brief, yet luminous, outburst was uncharacteristic for such objects.

Sunyaev et al. (2003b) reported the detection of a new transient source, IGR J17391−3021, with the IBIS/ISGRI detector on board *INTEGRAL* that peaked at 00:44 UT on 2003 August 26 and noted that the source position was compatible with the known location of XTE J1739−302. A *Chandra* observation of XTE J1739−302 reported by Smith & Heindl (2004) localised the source to high accuracy at the position RA= 17^h 39^m $11^s.58$, DEC = -30^o 20' 37".6 and identified USNO-B1.0 0596-0585865 as the only optical counterpart within the *Chandra* error circle. Negueruela et al. (2006b) performed optical and IR spectroscopy to identify the optical counterpart as an O8 Iab(f) supergiant and confirm XTE J1739−302 as a member of the SFXT class. The same authors also used optical photometry and extinction measurements to estimate a source distance of ∼2.3 kpc for XTE

J1739−302.

The detection of further outbursts of XTE J1739−302 in the hard X-ray band with *INTEGRAL* and *RXTE* identified flares lasting between 30 minutes and 14 hours that were characterised by a steep X-ray spectrum above 20 keV that is typical of a HMXB with a NS companion (Sguera et al., 2006a). The spectral and timing properties of XTE J1739−302 have also been extensively studied in the soft X-ray band. During bright outbursts the spectra of XTE J1739−302 can be described by hard, absorbed powerlaw models with Γ in the range $\sim$0.8−1.5 and a typical N_H of a few $10^{22}\,\mathrm{cm}^{-2}$ that is observed to vary between outbursts (Sakano et al. 2002,Romano et al. 2008b). Sidoli et al. (2008) also performed broadband spectral fitting to *Swift*/XRT and BAT data accumulated from an outburst in April 2008 and identified a high energy cutoff at $\sim$13 keV, corresponding to a neutron star magnetic field of less than 2×10^{12} G. Monitoring observations with *Swift*/XRT showed that XTE J1739−302 remains active outside of the large $10^{36}\,\mathrm{erg\,s}^{-1}$ outburst events, often occupying intermediate luminosity states in the range of a few $10^{33}-10^{34}\,\mathrm{erg\,s}^{-1}$ (Romano et al., 2009b). XTE J1739−302 was observed to occupy such an intermediate state for $\sim$60% of the monitoring observations, again displaying a range of absorptions and powerlaw photon indices at these luminosities. Bozzo et al. (2010) characterised the quiescent emission of XTE J1739−302 using *XMM-Newton*. The source displays a persistent emission at $4.1\times10^{32}\,\mathrm{erg\,s}^{-1}$ that is interspersed with flares of a duration on the order of 1000 s that demonstrate a rise in flux of a factor of $\sim$10−30. The spectral parameters observed within this state are again consistent with those detected during epochs of higher flux, but with some evidence of an additional soft component which may be resulting from shocks in the wind of the supergiant companion. The consistency in spectral shape and flare behaviour observed across the entire X-ray luminosity range of XTE J1739−302 implies that accretion is actively occurring at all luminosities in this source and that the compact object in XTE J1739−302 is most likely a neutron star. Despite the nature of the spectral shapes, however, X-ray pulsations have not been detected from XTE J1739−302 to definitively identify the compact object as a neutron star.

XTE J1739−302 is located approximately 2 degrees from the Galactic Centre and as a result has a large amount of coverage from the *INTEGRAL* Galactic Centre Bulge Monitoring Campaign (Kuulkers et al., 2007) and Galactic Centre Deep Exposure (Winkler et al., 1999). In this section an analysis of a large *INTEGRAL*/IBIS dataset is presented. Section 5.1.1 reports the data selection used and sections 5.1.2 and 5.1.3 the periodicity and outburst identification analysis performed. A discussion of the results, their physical interpretation and conclusions on the nature of XTE J1739−302 are given in Section 5.1.4.

5.1.1 Data Selection

The analysis presented here used data from the *INTEGRAL* archive covering MJD 52671.7 through MJD 54763.6, an initial dataset of ∼14.4 Ms. Following the methods outlined in Section 2.2, an 18−60 keV light curve was extracted and optimally filtered. This process resulted in a light curve of XTE J1739−302 spanning MJD 52698.2 through MJD 54763.6 with a total effective exposure of ∼12.4 Ms.

XTE J1739−302 also has coverage in the *RXTE* All Sky Monitor (ASM)[1] and *Swift* Burst Alert Telescope (BAT)[2] public databases. As the BAT is also a coded aperture telescope, light curves extracted from its images suffer from similar effects as those discussed for IBIS in Section 2.2. Hence the BAT light curve was also filtered for data points with poor data quality flags, short exposures and low coded aperture fractions. The resulting filtered *Swift*/BAT light curve covers MJD 53413 through to MJD 55208 with an effective exposure time of ∼13.2 Ms. The *RXTE*/ASM lightcurve spans MJD 50088.1 through MJD 55209.9 with a total exposure time of ∼3.45 Ms.

5.1.2 Periodicity Analysis

The optimally filtered IBIS/ISGRI light curve was tested for periodic signals by means of a Lomb-Scargle analysis. The resulting periodogram contained several peaks of relatively high power as can be seen in Fig. 5.1. To determine the significance of the observed peaks the Monte-Carlo based randomisation test outlined in Section 2.3 was performed and the confidence levels extracted. The resulting periodogram, overlaid with the calculated confidence levels, is shown in Fig. 5.1.

As Fig. 5.1 shows, there are several peaks that appear to be above the 99.999% significance level. However, as a binary system containing this number of physical periodicities is unlikely, efforts are made to explain the presence of each signal. The first effect considered was that of the window function resulting from the large scale, non-uniform sampling of data within the IBIS/ISGRI light curve. Additionally power may be generated in the periodogram at periods different to that of the fundamental as a result of the periodic signal not being of a sinusoidal form, as is observed in the phase-folded light curve shown in Fig. 5.2. To evaluate both of these effects, simulated light curves were generated for each peak above 99.999% significance in Fig. 5.1 by repeating the form of the phase-folded profile, generated by folding the IBIS dataset on the period of each peak, across the length of the light curve. Identical data gaps to those of the real light curve are then superimposed on

[1] http://heasarc.gsfc.nasa.gov/docs/xte/ASM/sources.html
[2] http://heasarc.gsfc.nasa.gov/docs/swift/results/transients/

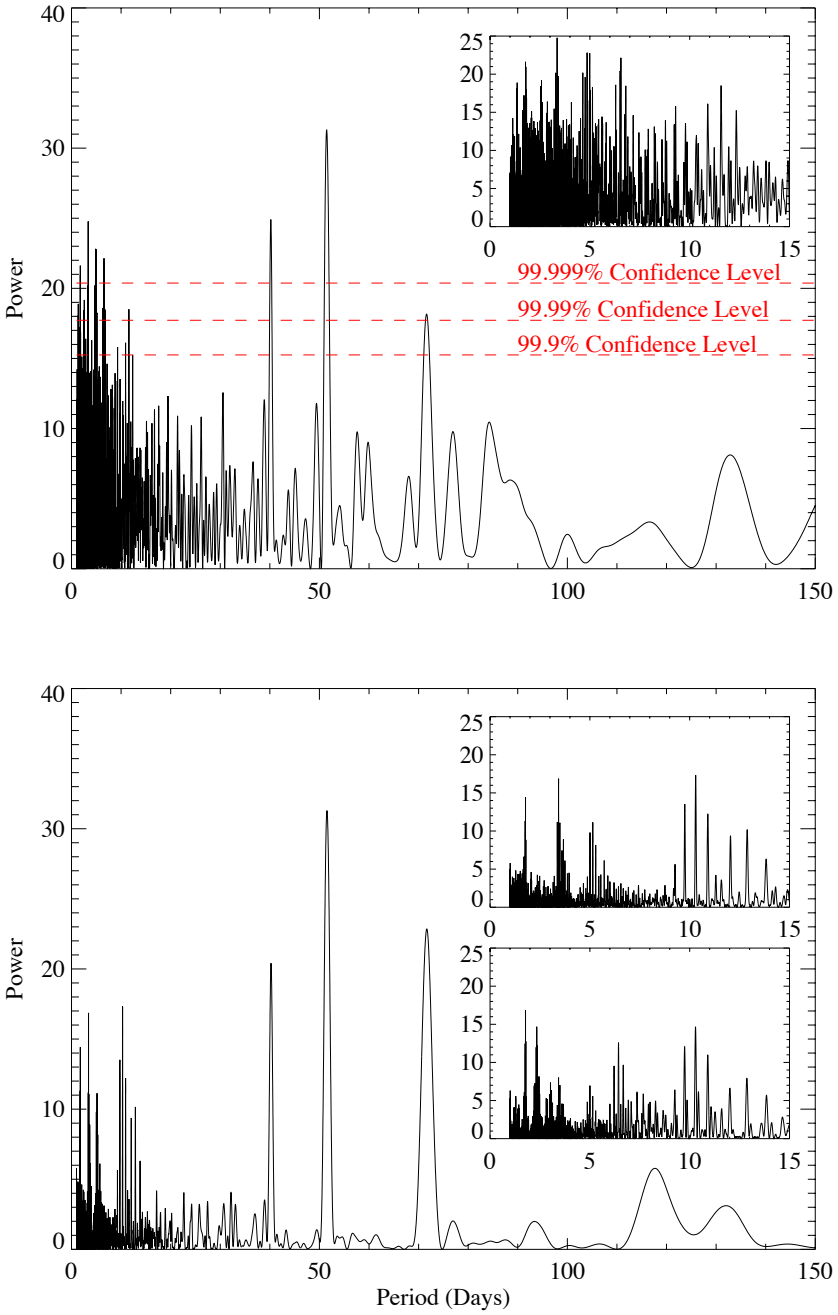

Figure 5.1: Top: Lomb-Scargle periodogram of the optimally filtered IBIS/ISGRI 18 - 60 keV lightcurve of XTE J1739−302 with the 99.9%, 99.99% and 99.999% confidence levels shown. Bottom: Lomb-Scargle periodogram of a function based on the shape of the phase-folded light curve at a period of 51.47 days and modulated with the data gaps present in the IBIS/ISGRI data (see text). From top to bottom the inset panels are zoomed in views of the short period region of the periodogram in the true IBIS light curves, simulated functions and a subset of the simulated function.

the simulated light curve. Synthetic noise was also included in the simulated light curve by randomly blurring the count rate of each point within the uncertainty on the corresponding count rate in the phase-folded profile in the same manner as described in Section 2.3. The simulated light curve generated for each peak is subjected to Lomb-Scargle analysis and a periodogram produced. On inspection it was observed that the simulated light curve of the signal at a period of 51.47 days was able to reproduce the pattern seen in the periodogram of the true light curve; this being also the period with the maximum power in the data. The periodogram produced by the simulated light curve generated from the 51.47 day signal is shown in the lower panel of Fig. 5.1 and is seen to reproduce the large features at ∼40 and 70 days as well as generating a cluster of features at shorter periods (<15 days). These short period features are consistent with many of the signals detected above the 99.999% confidence level in the real data. As such these signals can be interpreted as higher frequency components introduced by the non-sinusoidal profile of the phase-folded light curve of the 51.47 day period as seen in Fig. 5.2.

It is observed that the short period peaks generated by the simulated light curve do not entirely match those seen in the real periodogram. However, it should be noted that this analysis was only performed for the time-averaged phase-folded light curve. As such the effects of local variations in the shape of the detected profile within the real light curve on the periodogram are suppressed. To estimate the influence of this effect on the shape of the generated periodogram the analysis was repeated for three subsets of the data, and the peaks at short periods were found to vary between subsets (e.g. the lowest inset in Fig. 5.1), most likely due to changes in observing pattern and frequency during the mission. Hence a large proportion of the peaks observed at short periods appear to be generated as a consequence of the sampling of the raw XTE J1739−302 light curve and the shape of the phase-folded profile of the 51.47 day signal. Furthermore there are other possible physical sources of periodicity within the short period range that, whilst not related to a celestial source, may generate power at such periods. The *INTEGRAL* orbital period is ∼3 days and during the core program (Winkler et al., 1999) *INTEGRAL* was performing scans of the Galactic Plane and Galactic Centre exposures in a very regimented manner. As a result of these considerations the shorter period significant signals are taken as being either directly related to the 51.47 day signal, from other sources of artificial (non-celestial) periodicity and/or beating interactions between these. Therefore 51.47 days is considered to be a real, physical periodicity in the XTE J1739−302 system. On the contrary, no indication of the ∼8 day period predicted by Blay et al. (2008) is found in the analysis.

The 'blurring' randomisation test described in Section 2.3 was utilised to derive an error on the 51.47 day period of ± 0.02 days. Hence the orbital period of XTE J1739−302 is defined as 51.47±0.02 days. Figure 5.2 shows the orbital phase-folded light curve of the XTE J1739−302 system. The zero-phase ephemeris of

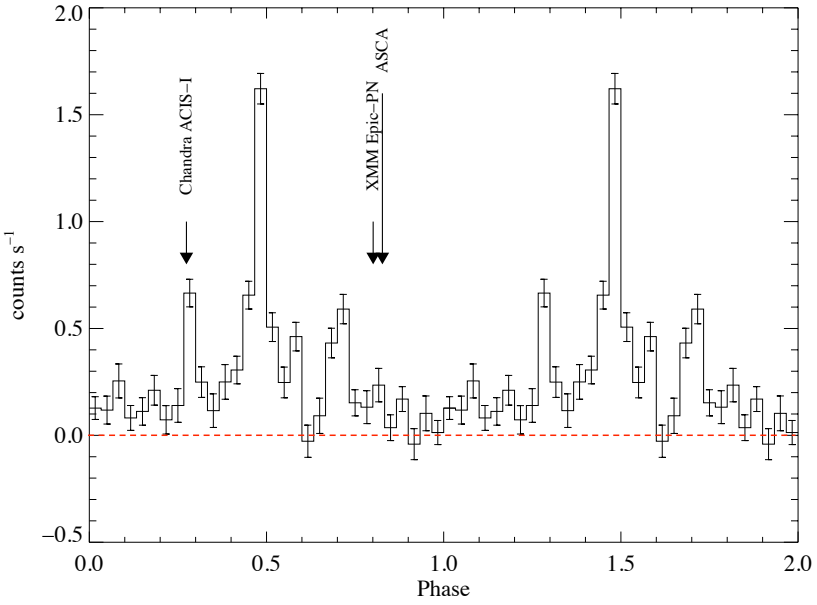

Figure 5.2: 18−60 keV phase-folded light curve of the optimally filtered IBIS/ISGRI XTE J1739−302 dataset using the zero phase ephemeris MJD 52698.2 and an orbital period of 51.47 days. The orbital phase locations of the intermediate and quiescence luminosity level detections discussed in Section 5.1.4 are indicated.

MJD 52698.2 is used, defining the initial phase zero as the first observation of XTE J1739−302 with *INTEGRAL*/IBIS. The phase-folded light curve shows a shape that is dominated by enhancement of emission at what appears to be three points in the orbit. The largest peak occurs between orbital phases of 0.4 and 0.6 and is assumed to be the periastron passage of the neutron star. Two nearly symmetric side-peaks are also observed at orbital phases of 0.25 to 0.35 and 0.65 to 0.75. A more detailed discussion of this profile is given in Section 5.1.4.

The public access *RXTE*/ASM and *Swift*/BAT light curves were also searched for periodic signals using the Lomb-Scargle method, however, in these cases no significant signals were detected at any period. While this is unusual, it is not the first time that the orbital period of an SFXT has been detected with one monitoring instrument and not others (e.g. IGR J17544−2619, Clark et al. 2009). The varied pointing strategies, energy bands and instantaneous sensitivities of the different X-ray monitors (i.e. IBIS, BAT and ASM) are believed to be responsible in determining if a periodicity is detected in a particular instrument.

5.1.3 Outburst Identification

In conjunction with the periodicity analysis, the IBIS/ISGRI light curve was also searched for outbursts using the techniques described in Section 2.4. The minimum significance cutoff for physical outbursts was found to be 4.41σ and all events below

this significance were removed from the outburst history. As a result thirty five outburst events have been identified within the XTE J1739−302 IBIS/ISGRI 18−60 keV light curve. Higher time resolution light curves with a binning of 100 s were generated for each of the remaining events and inspected manually to ensure outburst behaviour could be observed. It was seen that the majority of the remaining events showed distinct flaring features, while the remainder showed lower level activity, possibly due to small flares with emission mostly below the sensitivity of IBIS/ISGRI but where the peak of the emission is detected. The subset of outbursts with a significance greater than 8σ is given in Table 5.1 and examples of finely binned outburst light curves at high and low levels of activity are shown in Fig 5.3.

Combining the outburst history with the new orbital ephemeris allows the phase of each outburst event to be defined. Figure 5.4 shows the phase distribution of the identified outbursts. The histogram shows the number of outbursts observed as a function of orbital phase (right hand axis) and it is seen that the distribution is not strongly structured. However, using the finely binned light curves of each event, a measurement of the fluence of each outburst was made. The outburst fluence distribution as a function of orbital phase is shown by the points in Fig. 5.4. Crosses indicate measurements where a full outburst profile was deemed to be present, whereas diamonds represent lower limits determined from profiles that showed incomplete coverage of the event. It can be seen that the 'periastron' region contains more larger outbursts. Hence while it appears possible to observe outbursts at any point around the orbit of XTE J1739−302, the larger outbursts occur predominantly at periastron. A cluster of higher fluence outbursts are also seen within the phase of the leftmost side-peak of Fig. 5.2. Targeted pulsation searches were performed on the most significant of the identified outburst ScWs, however, no significant pulsations were detected.

The IBIS/ISGRI light curve was also analysed after the outbursts were removed to evaluate if any underlying flux modulation could be observed. The folded light curve with the outbursts removed (Fig. 5.5) shows no sign of an underlying periodicity, suggesting that the 51.47 day signal observed in the periodogram is driven by outburst emission. To safeguard against the possibility that a small number of events separated by multiples of the proposed orbital period falsely create this signal, identified outbursts were iteratively and randomly removed from the light curve and the periodicity analysis performed. There were no indications in either case that the removal of a small number of events could destroy the signal, illustrating that a small number of events do not falsely generate the observed peak. Whilst there is no discernible structure in the phase-folded profile of the light curve with the outbursts removed (Fig. 5.5), there is residual flux with an average value of $4.6\times10^{-12}\,\mathrm{erg\,cm^{-2}\,s^{-1}}$ (18−60 keV).

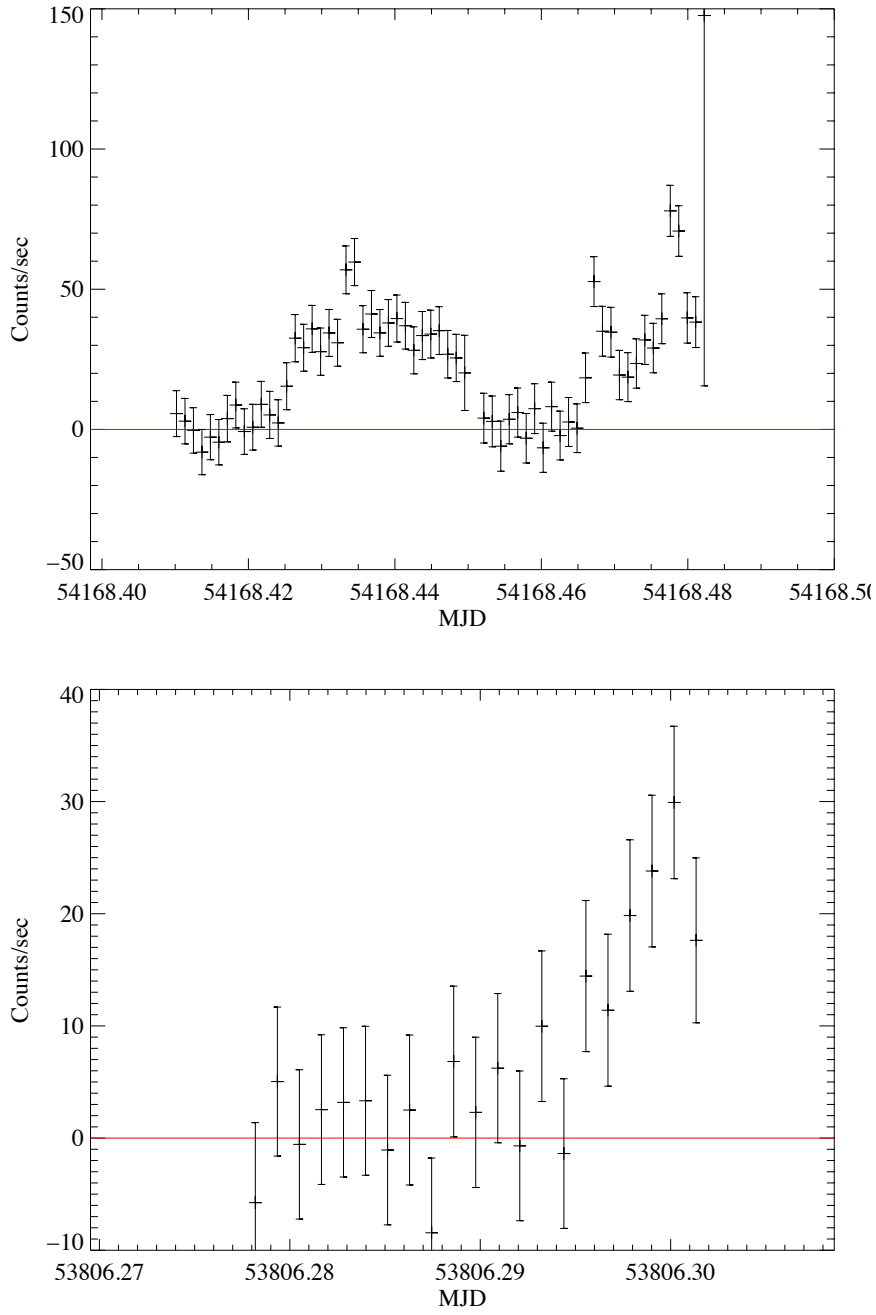

Figure 5.3: 100s binned light curves of example outbursts of XTE J1739−302 showing the temporal behaviour at different levels of activity. Top: the 35.29σ outburst recorded in Table 5.1 (Note: the final data point is likely spurious, resulting from low exposure in that bin). Bottom: a 5.42σ outburst recorded at MJD 53806.29. The larger outburst displays multiple flares within regions of consistent emission, whereas the smaller outburst consists of a single lower level flare.

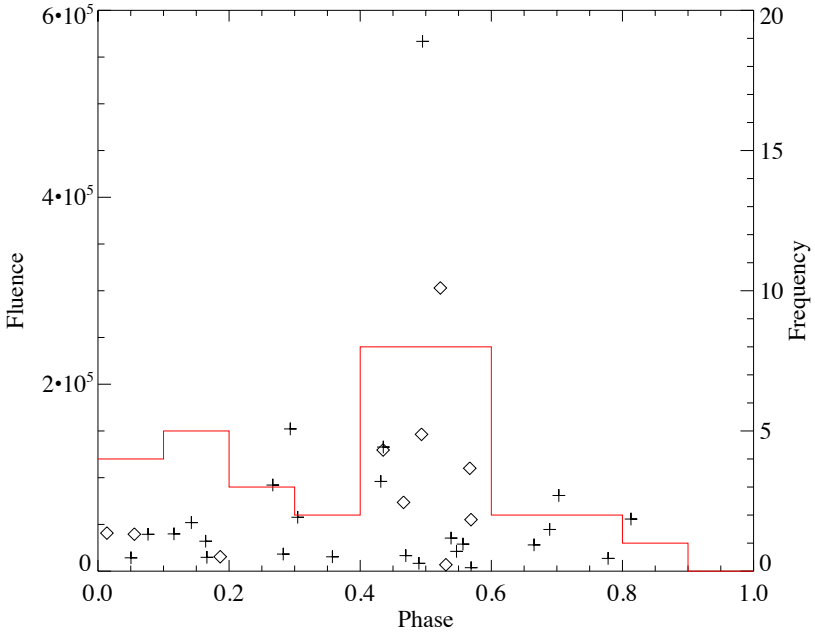

Figure 5.4: XTE J1739−302 outburst distribution in orbital phase space. The histogram shows the number distribution of outbursts in orbital phase (right hand scale) whereas the individual points show fluence estimations, in counts, of each outburst (left hand scale, crosses are full estimates and diamonds lower limits). While the number distribution appears somewhat flat, it is seen that the fluence measurements are peaked around periastron. Hence, while outbursts can occur at any point around the orbit, the larger outbursts are observed at periastron.

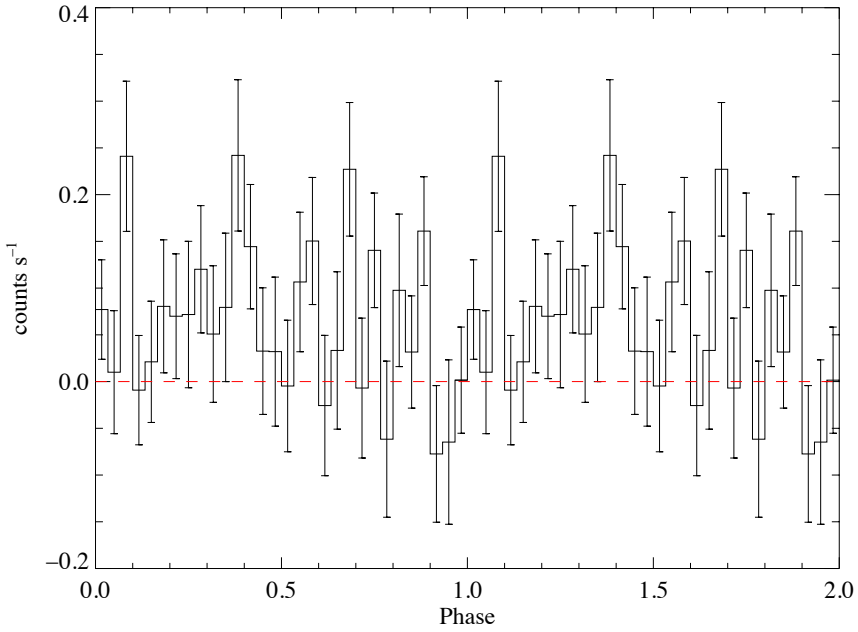

Figure 5.5: Phase-folded 18-60 keV light curve of XTE J1739−302 with the outbursts removed, folded on the 51.47 day period. There appears to be some consistently non-zero, low level emission around the orbit, however, it is not periodic in nature, the maximum power generated in the Lomb-Scargle analysis was 13 and not significant. Hence it is believed that for this system the periodic signal is generated purely from outburst emission.

The *Swift*/BAT orbital light curve was also inspected for outbursts and it was seen to contain twelve outburst events. Coincident detections with IBIS/ISGRI are indicated in Table 1. There were also six events that are not temporally coverred by the IBIS/ISGRI data, these are outlined in Table 2. Of the whole sample, five outbursts occurred in the periastron region, four within the 'side peaks' and three at other phase locations, showing a phase distribution similar to that seen in the IBIS/ISGRI light curve. As the detection of the periodic signal in XTE J1739−302 is believed to be predominantly generated through outburst emission, the lower number of events detected in the *Swift*/BAT light curve, likely due to its lower instantaneous sensitivity compared to IBIS, helps explain why the signal is not seen in the periodicity analysis in this case.

5.1.4 Discussion

An orbital period of 51.47 days identifies XTE J1739−302 as one of the longer period SFXTs, approximately one third the length of IGR J11215−5952 which, with its orbital period of 165 days (Sidoli et al., 2007a), has the longest orbit of the class. The large size of this orbit gives rise to many possible orbital configurations, making it difficult to place tight constraints on the orbital parameters of the system. Using Kepler's third law, assuming a neutron star mass of 1.4 $M_\odot$ and a

Table 5.1: IBIS/ISGRI identified outbursts of XTE J1739−302 with a significance of greater than 8σ

Date MJD[a]	Significance[b]	Orbital Phase	Peak Flux[b]	Luminosity[b,c]	Duration	Also Reported
-	σ	-	10^{-10} erg cm^{-2} s^{-1}	10^{35} erg;s^{-1}	(h)	In
52720.52	36.17	0.44	19.03	12.04	1.55	Sguera et al. 2005
52724.63	8.17	0.55	11.34	7.18	41.20	**
52877.8	49.22	0.5	22.90	14.50	14.59	Sunyaev et al. 2003b
52892.62	8.31	0.78	5.55	3.51	0.38	**
53073.51[d]	35.91	0.29	16.20	10.26	2.31	Sguera et al. 2005
53074.09[d]	16.64	0.3	10.03	6.35	1.26	Sguera et al. 2005
53093.86	12.72	0.69	5.43	3.44	1.75	**
53238.24	39.42	0.49	26.46	16.75	1.82	Sguera et al. 2006a
53248.97	26.48	0.7	13.04	8.26	1.71	**
53479.78	13.29	0.19	11.41	7.22	0.33	Smith et al. 2006
53802.97[e]	27.5	0.47	17.20	10.88	0.63	**
53831.15	14.33	0.01	8.69	5.50	0.64	**
53987.7[e]	13.76	0.06	8.25	5.22	0.62	**
53990.81	14.77	0.12	7.70	4.87	1.25	**
54011.69[e]	28.4	0.52	15.22	9.63	11.60	**
54161.08[d,e]	10.26	0.43	4.69	2.97	9.00	**
54161.57[d,e]	26.7	0.43	24.67	15.62	1.44	Turler et al. 2007
54168.43[e]	35.29	0.57	16.27	10.30	1.37	**
54564.68[e]	23.8	0.27	14.634	9.26	0.38	Romano et al. 2008b

Note: The peak flux represents the highest count rate achieved in a ScW during each outburst. These are converted to the given flux with the conversion factor 1.3×10^{-11} erg cm^{-2} s^{-1} = 1.4×10^{-4} ph cm^{-2} s^{-1}. [a] MJD is that of the mid-point of the first ScW identified in an outburst event. [b] Energy range 18 - 60 keV. [c] Assuming a distance of 2.3 kpc. [d] Part of the same outburst event. [e] Detection in the *Swift*/BAT orbital light curve.

Table 5.2: Outbursts of XTE J1739−302 detected by *Swift*/BAT that are not temporally covered by *INTEGRAL*/IBIS.

Date MJD	Phase	Significance	Duration (h)
53424.69	0.10	8.91	2.4
53765.79	0.73	12.64	18.3
54269.14	0.52	7.53	3.2
54347.45	0.05	7.75	6.2
54411.19	0.28	8.29	3.1
54692.00	0.74	17.47	11.2

stellar mass range of 25 - 28 $M_\odot$ for the supergiant (Cox, 2000), the semi-major axis of the system is estimated to be 173.4 - 179.8 $R_\odot$. The lower and upper limits of the stellar radius are estimated as 14.4 - 23.2 $R_\odot$ from the SED fitting outlined in Rahoui et al. (2008a). In order to place the tightest possible constraints on the orbital dynamics of XTE J1739−302, a stellar mass of 25 $M_\odot$, stellar radius of 23.2 $R_\odot$ and an orbital semi-major axis of 173.4 $R_\odot$ are assumed throughout the remainder of this discussion.

By inspecting the phase-folded light curve, Fig. 5.2, it can be seen that with this ephemeris the maximum flux occurs in the orbital phase bin centred on 0.483. Further inspection of this region of the orbit, from Table 1, shows variations in the properties of outbursts. The fact that an outburst is not observed with each periastron passage, and that the duration of observed outbursts in this region vary from 0.63 to 41.2 hours, indicates that the XTE J1739−302 system does not undergo accretion in the Roche-Lobe overflow regime, whereby persistent periastron emission on a more consistent timescale would be expected. Figure 5.6 shows a plot of the L1 Lagrangian point separation from the supergiant companion as a function of orbital phase for a range of orbital eccentricities (Eq. 3.1, Eggleton 1983). As this figure shows, eccentricities of up to ∼0.8 are dynamically feasible before the L1 point moves within the upper limit of the stellar radius during periastron passage and induces Roche-Lobe overflow. Therefore from this consideration alone it is only possible to place an upper limit of ∼0.8 on the eccentricity of the binary orbit of XTE J1739−302.

The low luminosity state of 8.2×10^{33} erg s^{-1} (2 - 10 keV), assuming a distance of 2.3 kpc, observed with *Chandra* (Smith et al., 2006) and the quiescence detections of a 3σ upper limit at $<7.0 \times 10^{32}$ erg s^{-1} (2 - 10 keV), 6.0×10^{32} erg s^{-1} (2 - 10 keV) and 4.1×10^{32} erg s^{-1} (0.5 - 10 keV) by *ASCA* (Sakano et al., 2002), *Swift*/XRT (Romano et al., 2009b) and *XMM*/Epic-PN (Bozzo et al., 2010) respectively are not consistent with Bondi-Hoyle accretion (Bondi & Hoyle, 1944) from a smooth, spherically symmetric stellar wind. The variation in the density of a smooth wind encountered by the neutron star travelling on an eccentric orbit in XTE J1739−302 can be calculated using the continuity equation:

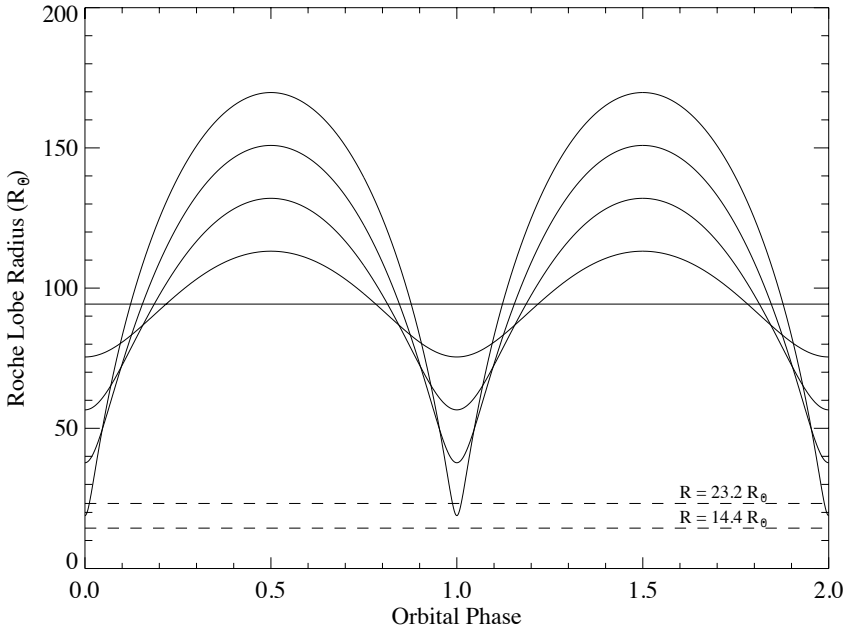

Figure 5.6: The L1 Lagrangian point separation from the supergiant as a function of orbital phase in XTE J1739−302 for orbital eccentricities of 0.0, 0.2, 0.4, 0.6 and 0.8. Eccentricities of up to $e \sim 0.8$ are possible before a Roche-Lobe overflow regime would start to take effect at the upper limit of the supergiant radius.

$$\rho_w(r_{ap}) = \rho_w(r_{peri}) \frac{r_{peri}^2 v_w(r_{peri})}{r_{ap}^2 v_w(r_{ap})} \tag{5.1}$$

where $\rho_w(r)$, $v_w(r)$ and r are the stellar wind density, velocity and orbital separation at periastron (*peri*) and apastron (*ap*) respectively. Assuming the upper limit on the eccentricity ($e = 0.8$) the smooth wind density at apastron $\rho_w(r_{ap})$ is $4{\times}10^{-3}\rho_w(r_{peri})$. The periastron and apastron orbital separations are calculated using Kepler's Third law and the stellar wind velocity at each separation is calculated using the velocity law defined in Eq. 3.2 assuming the stellar parameters defined previously and the nominal stellar wind parameters $v_\infty = 1000\,\mathrm{km\,s^{-1}}$ and $\beta = 1$. Even at the upper limit of the dynamically valid eccentricity range, the change in orbital separation across orbital phase is therefore unable to generate the 10^{4-5} dynamic range observed in this system if the neutron star were accreting from a smooth wind. The action of a centrifugal or magnetic barrier to the accretion flow may enhance the possible dynamic range in this case if the variation experienced during the orbit initiated a switch in the accretion regime, as was discussed for the case of IGR J17544−2619 in Section 4.4. However, the lack of an identified pulsation or well constrained magnetic field prevents the further investigation of these effects in the case of this source. Additionally the spread in the orbital phase location of the quiescence detections (see Fig. 5.2) combined with

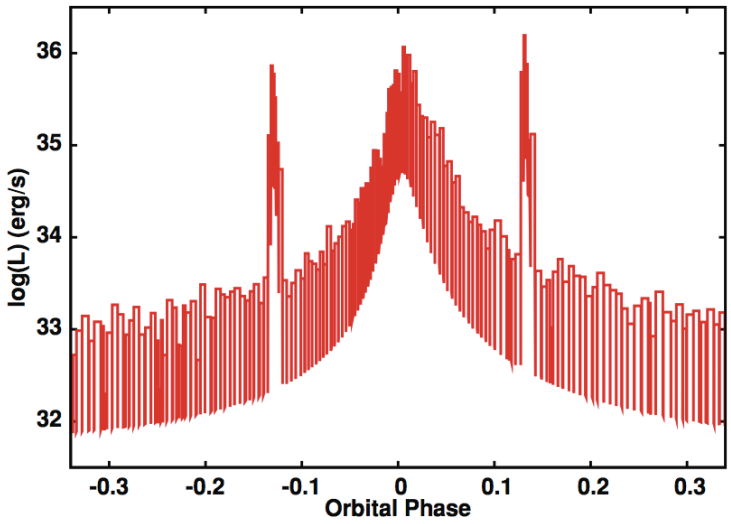

Figure 5.7: Simulated SFXT phase-folded light curve for a system with an orbital period of 80 days, eccentricity of 0.75 and an 'enhanced equatorial density' region within the stellar wind of the supergiant companion that generates the prominent side peaks about the periastron passage (Ducci et al., 2009).

the lack of an underlying flux modulation in Fig. 5.5 and the inconsistency in the flux of different outbursts at approximately the same orbital phase further illustrates that an eccentric orbit within a smooth stellar wind cannot explain the outbursts observed. Instead these properties illustrate that the neutron star is in fact travelling through an inhomogeneous, non-symmetrical stellar wind in the XTE J1739−302 system, in accordance with the "clumpy wind models" of SFXTs (Walter & Zurita Heras 2007, Negueruela et al. 2008).

Looking at Fig. 5.2 it can be seen that the *Chandra* observation occurred at the edge of one of the emission side peaks. Hence the higher level of emission seen in those data compared to the 'quiescent data' could be resulting from observation during an orbital phase that shows a systematic increase in luminosity over the full IBIS/ISGRI light curve. XTE J1739−302 illustrated the extent of its transient nature from the *ASCA* observation, where a deep quiescence was observed followed by rapid flares with dynamic ranges of over 10^3 and rise times of ∼250 s. This behaviour suggests a very high degree of 'clumping' within the wind in order to allow quiescence states, in very close proximity to distinct outbursts, to be observed across a wide range of orbital phase.

The presence of the two side-peaks seen in Fig. 5.2, both detected at ∼4 to 5σ significance, is intriguing and could help in defining the orbital characteristics of the system. Ducci et al. (2009), based on the conclusions of Sidoli et al. (2007a), invoked an anisotropic stellar wind with an 'enhanced equatorial density' region, inclined at some angle to the plane of the neutron star orbit, within the clumpy wind model to explain the profile of the regular outbursts of IGR J11215−5952

described in Section 1.3. Within this model the enhanced equatorial density region is considered as the plane of preferential outflow for the structured, radial wind as opposed to the dense viscous decretion discs present in BeXRBs. Ducci et al. (2009) also modelled a more general wind-fed SgXRB system with an enhanced equatorial region and showed that symmetric outbursts corresponding to the crossing of the enhanced density region by the neutron star, either side of the periastron passage, could produce up to 3 outbursts per orbit (Figure 15 of Ducci et al. 2009). Figure 5.7 also shows the simulated light curve of this general system and it is seen to show a marked similarity to the orbital phase-folded profile of XTE J1739−302 (Fig. 5.2). The presence of such an equatorially enhanced structure within the radiatively driven stellar winds of hot stars has been predicted as a consequence of magnetic confinement of the stellar wind material in the equatorial plane of rapidly rotating OB type stars with aligned dipolar magnetic fields by the MHD simulations of Ud-Doula, Owocki, & Townsend (2008). In these simulations a disc is formed that extends to $\sim 3{-}4\,\mathrm{R}_{OB}$ which is stable on ks timescales. On longer timescales magnetic reconnection within the equatorial plane of the supergiant results in mass ejection events from the disc, with material below the co-rotation radius of the supergiant falling back to the stellar surface and material above this radius being expelled from the system. An example MHD simulation of this process is shown in Fig. 5.8 where the colour scale indicates the logarithmic stellar wind density and the solid lines the magnetic field lines of the supergiant. The radially outflowing stellar wind component is observed along with the enhanced density of the equatorial region resulting from magnetic confinement. As time progresses in the simulation, magnetic reconnection begins to occur within the disc, leading to the formation of density structures and the eventual centrifugal expulsion of the disc material.

Using a simplified geometric version of the equatorial disc-crossing model, with both the inclination angle between the equatorial density region and neutron star orbital planes and the angle between the plane of the equatorial density region and the direction of the orbital semi-major axis being 90^o, the eccentricity of the orbit can be estimated as $e \sim 0.16$ to ensure the intersections of the neutron star orbit and stellar wind disc occur at the orbital phase required by the side peaks in the phase-folded light curve. Since 90^o is the most extreme case of the inclination of the enhanced density region to the orbital plane and there is no requirement for the direction of periastron and the plane of the enhanced density region to be perpendicular, however, the value of $e \sim 0.16$ can act as a lower limit on the eccentricity if the enhanced equatorial density region explanation proves to be correct. If the side-peaks are a real feature then this also has wide implications for the interpretation of some SFXT systems. The presence of an equatorial disc-like structure within the stellar wind of the supergiant goes beyond the application of wider, more eccentric orbits, compared to more classical Sg-XRBs, within a homogeneous clumped stellar wind to explain the observed SFXT behaviour.

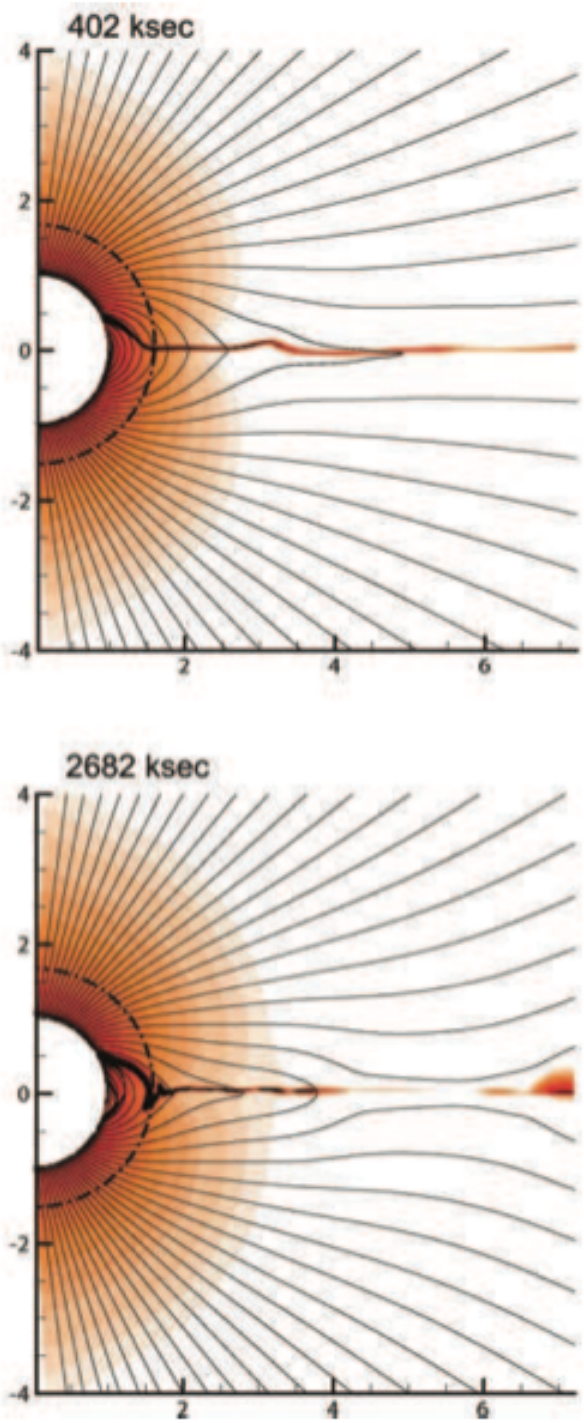

Figure 5.8: MHD simulations showing the presence and evolution of an enhanced equatorial density region within the line-driven wind of a massive OB type star (Ud-Doula, Owocki, & Townsend, 2008). The logarithmic colour scale illustrates the stellar wind density and the solid lines the magnetic field lines of the massive star.

Instead it implies that, in some cases, an interaction with quasi-stable structures in the supergiant stellar wind is driving some of the fast X-ray flaring behaviour observed from the systems.

5.1.5 Summary

Observations of XTE J1739−302 across the lifetime of the *INTEGRAL* mission using IBIS/ISGRI have uncovered a period of 51.47 ± 0.02 days which is interpreted as the orbital period of the binary system. The relatively long period, in SFXT terms, results in an orbital semi-major axis in the range 173.4 - 179.8 $R_\odot$ and allows for orbital eccentricities up to ∼0.8 before Roche-Lobe overflow emission would be expected. No further firm constraints can be placed on the eccentricity at the current time. The outburst history and reported luminosities lead to the conclusion that the neutron star orbits in an inhomogeneous 'clumped' stellar wind, with some evidence that this system may contain an enhanced equatorial density region. The fact that emission at quiescent levels can be seen very near periastron suggests a high degree of 'clumping' within the stellar wind. Further observations and modelling are encouraged to identify with greater certainty if features in the phase-folded light curve are in fact due to an enhanced equatorial density region, as well as directed optical follow-up in an attempt to identify the presence or lack of any features that are akin to the BeXRBs that contain prominent equatorial discs. The identification of an orbital period in XTE J1739-302 makes it the sixth firmly identified periodic SFXT. It also identifies a further characteristic behaviour in a system that is widely considered the archetype of the SFXT class.

5.2 IGR J17354−3255 as an intermediate SFXT possibly associated with the transient MeV source AGL J1734−3310

IGR J17354−3255 is an unidentified Galactic X-ray transient discovered in April 2006 (Kuulkers et al., 2006) during a short outburst with a duration of only 2 ScWs and a flux of 18 mCrab (20−60 keV). Conversely the source is reported in the fourth *INTEGRAL*/IBIS catalog (Bird et al., 2010) as a weak persistent source with a flux of 1.7 mCrab (2.2×10^{-11} erg cm^{-2} s^{-1}). IGR J17354−3255 is also listed in the *Swift*/BAT 54 month survey at a similar flux level (Cusumano et al., 2010) and an 8.448 day periodicity was reported in the long term BAT light curve (D'Aì et al., 2011). The position of IGR J17354−3255 was accurately located as *RA,Dec* 17^h 35^m 27.59^s, -32^o 55' 54.4" with an uncertainty of 0".64 by *Chandra* (Tomsick et al., 2009). No optical counterparts were discovered within the *Chandra* error circle, however, a single IR source was detected and proposed as the counterpart of IGR

J17354−3255, namely 2MASS J17352760−3255544. The location of IGR J17354−3255 in the direction of the Galactic Center (GC), the high inferred optical extinction and the relatively high X-ray absorption suggests that the source is likely a distant HMXB located in or beyond the GC at ≥ 8.5 kpc. IGR J17354−3255 is also spatially coincident with the unidentified transient MeV source AGL J1734−3310 (Bulgarelli et al., 2009) but, as a consequence of the large positional uncertainty of the *AGILE* source, further consideration on the physical association of the two sources is required.

Sguera et al. (2011) performed an archival study of IGR J17354−3255 using *INTEGRAL*/IBIS data and results from *Swift*. The IBIS dataset was searched for outbursts with 16 flaring events being identified (15 of which were previously unreported) having typical durations of a few hours but with some examples of longer activity of up to a couple of days. The peak 18−60 keV fluxes detected in the flares were of the order 20−40 mCrab with one example of a more luminous event with a peak flux of 108±20 mCrab ($1.41 \pm 0.26 \times 10^{-9}$ erg cm^{-2} $^{-1}$). By comparing the outburst fluxes to the flux of the summed out-of-outburst state a maximal dynamic range of ~ 200 is defined in the hard X-ray band. The extreme ends of the flux distribution detected in the soft X-ray band using *Swift*/XRT and *Chandra* also demonstrate a dynamic range of > 311. In both cases the observed dynamic range is in excess of that expected from a classical SgXRB ($\sim$ 20, Walter & Zurita Heras 2007) but less than the large dynamic ranges of $10^4 - 10^5$ observed in the prototypical SFXTs. Hence it was concluded that IGR J17354−3255 is a candidate, intermediate SFXT displaying a similar X-ray dynamic range to other members of the 'intermediate' sub-class such as IGR J16465−4507 (Clark et al., 2010). Subsequently the maximal X-ray dynamic range in the soft X-ray band has been enhanced to >1250 through the 3σ flux upper limit derived from a non-detection of IGR J17354−3255 with *XMM-Newton* (Bozzo et al., 2012). Additionally the IR counterpart has been confirmed as a supergiant (Chaty et al. in prep., private communication) which firmly identifies IGR J17354−3255 as a member of the intermediate SFXTs. Assuming a source distance of 8.5 kpc, the typical outburst luminosities of IGR J17354−3255 are in the range $10^{36} - 10^{37}$ erg s^{-1} and the upper limit on the lowest luminosity state is $\sim 6 \times 10^{32}$ erg s^{-1}. Such values are very consistent with those observed from other SFXTs. X-ray pulsations have not yet been detected from IGR J17354−3255 in any of the soft or hard X-ray datasets.

5.2.1 Temporal Analysis and discussion

Applying the periodicity analysis techniques described in Section 2.3 leads to the detection, at high significance, of a well defined 8.447±0.002 day orbital period in the ∼12.8 Ms optimally filtered IBIS dataset of IGR J17354−3255. The LS periodogram and 99.999% confidence level are shown in Fig. 5.9 with the detection

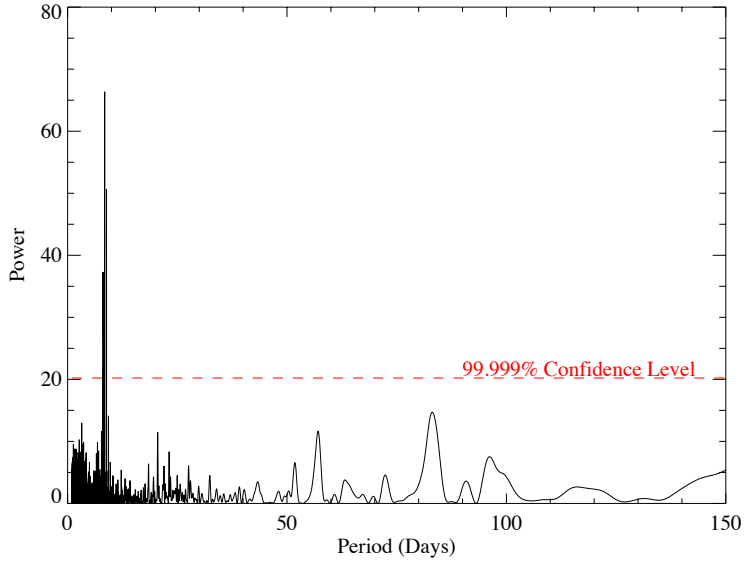

Figure 5.9: Lomb-Scargle periodogram of the optimally filtered IGR J17354−3255 IBIS light curve showing a strong peak at 8.447±0.002 days. The 99.999% confidence level is also drawn at a power of 20.21 as derived by the method outlined in Section. 2.3.1.

providing a strong confirmation of the BAT detection reported by D'Aì et al. (2011). The phase-folded light curve of IGR J17354−3255, computed using the determined orbital period and a zero phase ephemeris of MJD 52698.205, is shown in Fig. 5.10 and displays a smooth flux modulation that peaks at at an orbital phase of $\phi \sim 0.1$ whilst becoming consistent with zero at $\phi \sim 0.6$. The shape of this profile is likely generated by the orbital motion of a NS in an eccentric orbit with orbital phases of 0.1 and 0.6 relating to the passage of periastron and apastron respectively. The orbital phase locations of the IBIS outbursts of IGR J17354−3255 identified by Sguera et al. (2011) are indicated by the green points in Fig. 5.10 and are also seen to be detected at times consistent with the periastron passage of the compact object in the system. Loose constraints can be placed on the dynamically allowed orbital configurations through the L1 point separation as was performed for XTE J1739−302 (Section 5.1.4). In the case of IGR J17354−3255, however, there are no independent constraints on the stellar parameters of the supergiant companion. Hence assuming, as for XTE J1739−302, a supergiant mass of $25\,M_{\odot}$ results in IGR J17354−3255 possessing an orbit with a semi-major axis of $52\,R_{\odot}$ and requiring $e < 0.4$ to allow for a supergiant radius of $\geq 17\,R_{\odot}$.

Given the smooth orbital emission profile and the well defined orbital period of IGR J17354−3255, a 'Recurrence Analysis', first described by Bird et al. (2009), can be performed. This process utilises the orbital parameters of a system to identify all of the periastron passages observed in the IGR J17354−3255 dataset and calculates the significance of the light curve over a certain duration to assess the regularity of emission production at this orbital phase. The same process is also performed on all

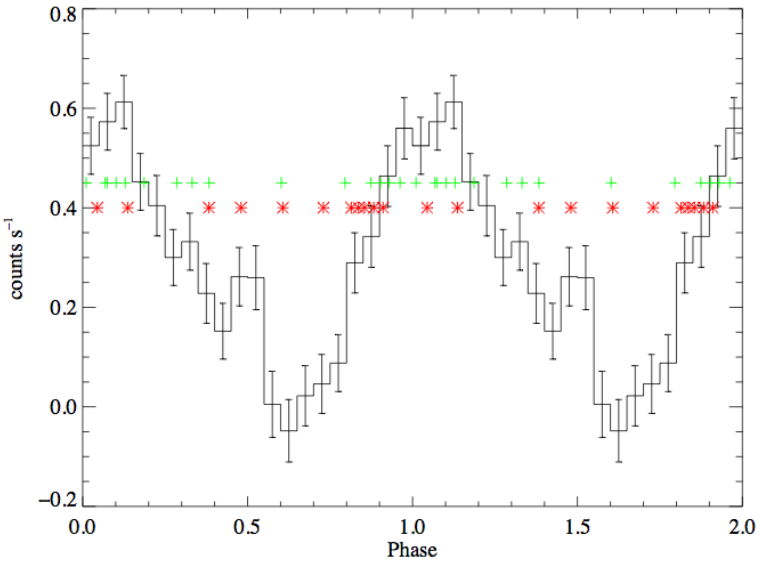

Figure 5.10: The orbital phase-folded light curve of IGR J17354−3255 using the best determined orbital period of 8.447 days and a zero phase ephemeris of MJD 52698.205. The green points illustrate the orbital phase location of the outbursts of the source detected by IBIS (as defined by Sguera et al. 2011) and the red points the phase location of the flares of the spatially co-incident transient MeV source AGL J1734−3310 (Bulgarelli et al. in prep., private communication).

of the identified apastron passages to estimate the significance distribution generated by random noise in the data and the percentage of active periastron passages quantified. The periastron (red) and apastron (black) distributions derived from the IGR J17354−3255 dataset using a window of 3 days (periastron ± 1.5 days) are shown in Fig. 5.11. The apastron distribution is seen to peak at, and be approximately symmetric about, zero, with no detections above 3σ recorded during these times. The periastron distribution, however, displays an excess of detections above 3 sigma, rising to $\sim 9\sigma$ at its most significant, which corresponds to activity being detected on 26% of periastron passages. This is the second highest recurrence rate measured after that of SAX J1818.6−1703, which produces detectable emission on ∼50% of periastron passages (Bird et al., 2009).

Taking into consideration the shape of the orbital phase-folded light curve, the clustering of hard X-ray outbursts around the periastron passage and the recurrence analysis, it is suggested that IGR J17354−3255 is an intermediate SFXT system similar to SAX J1818.6−1703, but with a shorter orbit and a lower eccentricity of ∼0.1−0.2 to account for the reduced recurrence rate. Compared to some other SFXTs the shape of IGR J17354−3255's orbital emission profile is quite smooth. Given that the IBIS dataset used covered ∼ 400 orbital cycles of IGR J17354−3255 (at random sampling) and the recurrence analysis suggests emission detectable with IBIS is produced on approximately a quarter of orbital cycles, it is unfeasible that the 16 bright outbursts, which have luminosities in excess of 10^{36} erg s^{-1} and represent the most luminous events, are responsible for the smooth

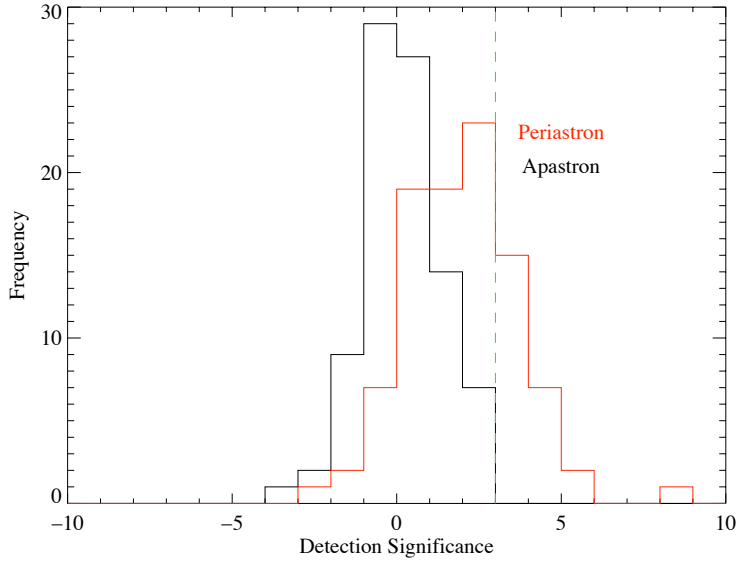

Figure 5.11: The distribution of significances for IGR J17354−3255 generated at times of presumed periastron (red) and apastron (black) when summing a window of 3 days about the central periastron date. It is seen that the distribution of apastron passages is centred on zero and displays no detections above the 3σ whereas the distribution of periastron passages shows an excess above 3σ that relates to activity on 26% of orbits.

orbital profile observed. Instead the shape is attributed to a lower level of X-ray emission that is below the sensitivity of IBIS in an individual ScW but which sums to a significant level when the whole dataset is folded. This emission could either be smoothly varying, following a similar profile during each orbit that is slowly accumulated to a detectable level, or the superposition of many low-intensity flares at X-ray luminosities of $\sim 10^{33} - 10^{34}\,\mathrm{erg\,s^{-1}}$, where the probability of a flare being generated is a function of the orbital phase which, again, cumulatively generates the observed orbital profile. Unfortunately, due to the sensitivity limits of *INTEGRAL*/IBIS on short timescales, it is not currently possible to determine which of these processes is generating the smooth orbital flux variations observed in IGR J17354−3255. In addition to the outbursts and lower level variations, the orbital phase of the quiescent flux upper limit detected with *XMM-Newton* (Bozzo et al., 2012) is calculated as $\phi \sim 0.66$ which is consistent with the apastron region of IGR J17354−3255's orbit. However, the variation in the density of a smooth stellar wind as a function of orbital phase is again insufficient to generate the observed X-ray dynamic range in IGR J17354−3255. Assuming an orbital eccentricity of 0.4 (i.e. at the upper limit of the likely values) and using the same continuity considerations as for XTE J1739−302 results in a maximum variation in smooth stellar wind density of only a factor of 10 between periastron and apastron in IGR J17354−3255. This variation is again incompatible with Bondi accretion of a smooth medium in this system, implying the influence of a highly structured wind to generate the $\sim 10^3$ dynamic range observed in the X-ray band. Due to the lack of

dynamical constraints on the IGR J17354−3255 system, a deeper investigation into the cause of the X-ray variability observed and the possible action of accretion barriers is not possible. It is of note, however, that the presence of structure within the supergiant stellar wind has been shown to be required in systems that span over a decade of the orbital period parameter space of SFXTs.

5.2.2 An association with AGL J1734−3310?

After the initial discovery of AGL J1734−3310 as a transient MeV source, extensive searches for additional MeV flares were undertaken by the *AGILE* team. Several new flares were discovered which have similar durations of ∼1 day and fluxes of a few 10^{-6} photons $\mathrm{cm}^{-2}\,\mathrm{s}^{-1}$ (Bulgarelli et al., in prep., private communication). Through the summation of all of the discovered flares, the determination of the source position was refined, having an uncertainty of $0^o.46$ (95% confidence), allowing IGR J17354−3255 to be confirmed as the only hard X-ray source located within the *AGILE* error circle. In addition to the improved spatial co-incidence of IGR J17354−3255 and AGL J1734−3310, the identification of fast flaring behaviour on daily timescales in IGR J17354−3255 displays a further common characteristic between the low and high energy sources. The locations of the MeV flares of AGL J1734−3310 within IGR J17354−3255's orbital phase are shown by the red points in Fig. 5.10. Whilst the distribution of the MeV flares is not centred on the periastron passage of IGR J17354−3255, as is the case for the hard X-ray flares, a Kolmogorov-Smirnov test of the orbital phase distribution of the two samples provided a D-statistic of 0.33 and does not rule out that the two sets of outbursts originate from the same source. The probability of a chance coincidence of these sources within the Galactic Plane, here defined as a Galactic Latitude of 0 ± 5^o, can be estimated by using the number of SgXRBs within this region (Bird et al., 2010) and the size of the AGILE positional uncertainty. The likelihood of a chance coincidence is found as ∼1% which alone is not sufficiently small a chance to independently confirm an association. However, given all of the above common flaring properties and spatial co-incidence of the X-ray source IGR J17354−3255 and the MeV source AGL J1734−3310, a tentative association of these sources is drawn.

As discussed in Section 1.4.2 other HMXB systems have also been detected as persistent and variable sources at MeV, GeV and TeV energies (e.g. LS 5039, LSI $+61^o$ 303 and PSR B1259−63) illustrating that particles can be accelerated to very high energies in these systems. IGR J17354−3255 shares several of the components believed to be required to produce HE emission, such as a compact object travelling in a likely eccentric orbit and a dense UV photon field produced by the supergiant to act as seed particles for Inverse Compton emission. However, being a supergiant system, IGR J17354−3255 fundamentally differs from the previous examples where

the HE is believed to originate from the interaction of a pulsar wind nebula with the dense Be star decretion disc. Additionally IGR J17354−3255 has not, to date, been detected at radio wavelengths, which is in contradiction with Cygnus X−1 and Cygnus X−3, the high mass microquasars, where the HE emission originates from relativistic jet outflows. Further monitoring of the IGR J17354−3255 region in the radio, hard X-ray and HE bands may allow the association of these sources to be confirmed or dismissed with a greater degree of confidence by the detection, or otherwise, of periodic modulation of the HE flux and/or correlated flares across each waveband. The confirmation of the production of HE emission in some SFXT sources would illustrate yet another extreme characteristic of these intriguing, complex systems, possibly unveil a new class of Galactic HE transient source and stimulate the development of an increased theoretical understanding of particle acceleration in binary systems. A fuller description of the observations, interpretation and conclusions on the nature of the IGR J17354−3255 system that have been summarised in this Chapter can be found in Sguera et al. (2011).

5.3 Conclusions

The *INTEGRAL* studies of the SFXTs IGR J17354−3255 and XTE J1739−302 presented in this Chapter have highlighted the wealth of information that can be extracted from the long term hard X-ray monitoring of these systems. Combining the orbital period determinations achieved with *INTEGRAL* with the hard X-ray outburst histories and observations in other wavebands allows the identification of unique features of individual systems, such as the possible enhanced equatorial density region of XTE J1739−302 and HE association of IGR J17354−3255, in addition to providing insights into the emission mechanisms active within SFXTs as a whole. The following chapter now collates the results presented in this work with a wider body of recent results to consider the current understanding of the emission mechanism occurring in SFXTs, the nature of the SFXT class as a whole and the future direction of this dynamic field of research.

Chapter 6

Conclusions

6.1 Discussions on the global nature of SFXTs and their place within the HMXB hierarchy

Over the lifetime of the *INTEGRAL* mission, SFXTs have been unveiled as one of the most dynamic and variable classes of objects in the high energy sky. In less than a decade the knowledge of these sources and their behaviour has been transformed from bright flashes in a few IBIS ScWs (e.g. Fig. 1.20, Sguera et al. 2005) to the orbital motion of NSs through the extreme, hostile environment of a supergiant star's stellar wind. With increased understanding and characterisation, however, it has started to become apparent that the question of whether or not the SFXTs are in fact comprised of a single population should be addressed.

As has been discussed and illustrated in the pervious chapters, the data obtained by the X-ray monitoring instruments (predominantly *INTEGRAL*/IBIS, *Swift*/BAT and *RXTE*/ASM) have, to date, revealed the orbital periods of 11 SFXTs which are distributed over a large range of between ∼3 and 165 days. Follow-up observations in the soft X-ray band have also identified NS pulse periods in 6 systems that range between 21 and 1212 s. The specific periodicities, along with the citations of the initial discoveries, are given for all sources in which these values are known in Table 6.1. These periodicities can also be used to place the SFXT population on the Corbet diagram (Corbet, 1986) and compare its distribution to that of the original classes of HMXB. Figure 6.1 shows this Corbet diagram distribution using the periodicity information in Table 6.1 for the SFXTs and of Liu, van Paradijs, & van den Heuvel 2006 and Bodaghee et al. 2007 for the original HMXB classes. The SFXTs with both their orbital and spin periods identified are shown by the filled purple triangles and those with only one known period by the dashed lines.

The distribution of the SFXT population within the Corbet parameter space shown in Fig. 6.1 is clearly not restricted to the region of the diagram populated by the

Table 6.1: All orbital and pulse periods identified in the SFXT population along with the works of the initial discoveries.

Source	P_{orb} (days)	P_{spin} (s)	Discovery
IGR J11215−5952	164.6	195	Sidoli et al. 2007 / Smith et al. 2006
IGR J16328−4726	10.068	–	Corbet et al. 2010 / –
IGR J16418−4532	3.73886	1212	Corbet et al. 2006 / Walter et al. 2006
IGR J16465−4507	30.332	228.5	Clark et al. 2010 / Lutovinov et al 2005
IGR J16479−4514	3.3199	–	Jain, Paul, & Dutta 2009 / –
IGR J17354−3255	8.447	–	D'Ai et al. 2011/ –
XTE J1739−302	51.47	–	Drave et al. 2010 / –
IGR J17544−2619	4.9279	71.49(?)	Clark et al. 2009 / Drave et al. 2012
SAX J1818.6−1703	29.9724	–	Bird et al. 2009 / –
IGR J18450−0435	5.7195	–	Goossens et al. in submission / –
IGR J18483−0311	18.5632	21.0526	Sguera et al. 2007 / Sguera et al. 2007
IGR J18462−0223	–	997	– / Bodaghee et al. 2012

classical wind-fed SgXRBs. Approximately half of the SFXT population is consistent with the SgXRB region of the diagram, with IGR J16418−4532 and IGR J17544−2619 being firmly located with these sources. Four additional sources, IGR J16479−4514, IGR J18450−0435, IGR J17354−3255 and IGR J16328−4726, have orbital periods that may be consistent with the location of the SgXRBs depending upon the value of the currently unknown NS spin periods. Alternatively these systems may be consistent with the RLO powered systems if they have anomalously fast spin periods, sub 1 s driven by the efficient transfer of angular momentum. If the systems instead possess spin periods in the range of 1 to a few tens of seconds, however, they may be displaying evidence of a past accretion history in their binary evolution (see the next paragraph for a further discussion). Whilst the possibility of accretion through RLO should not be ruled out in these 4 systems until proven otherwise, and pulsation searches down to sub second timescales should be performed to investigate this possibility where viable, the X-ray properties of these systems do not suggest that RLO is occurring due to the lower peak luminosity, 10^{36} as opposed to $10^{38}\,\mathrm{erg\,s^{-1}}$, and low-state/quiescent luminosities observed, in addition to the systems possessing orbits that make the initiation of RLO unfavourable. Hence these four systems are more likely to be slower rotators possessing spin periods consistent with the classical wind-fed SgXRB population, especially IGR J16479−4514, or spin periods that indicate a past accretion history (again see next paragraph). The SFXTs with longer orbital periods, however, are more consistent with the location of the BeXRBs in the Corbet diagram. IGR J18483−0311 and IGR J16465−4507 are consistent with the left most edge of the BeXRB population whilst IGR J11215−5952 is centrally located within this class in spite of all of these systems having a spectrally confirmed supergiant companion. SAX J1818.6−1703 and XTE J1739−302 are also yet to have pulse periods identified but would be expected to be consistent with the BeXRB population

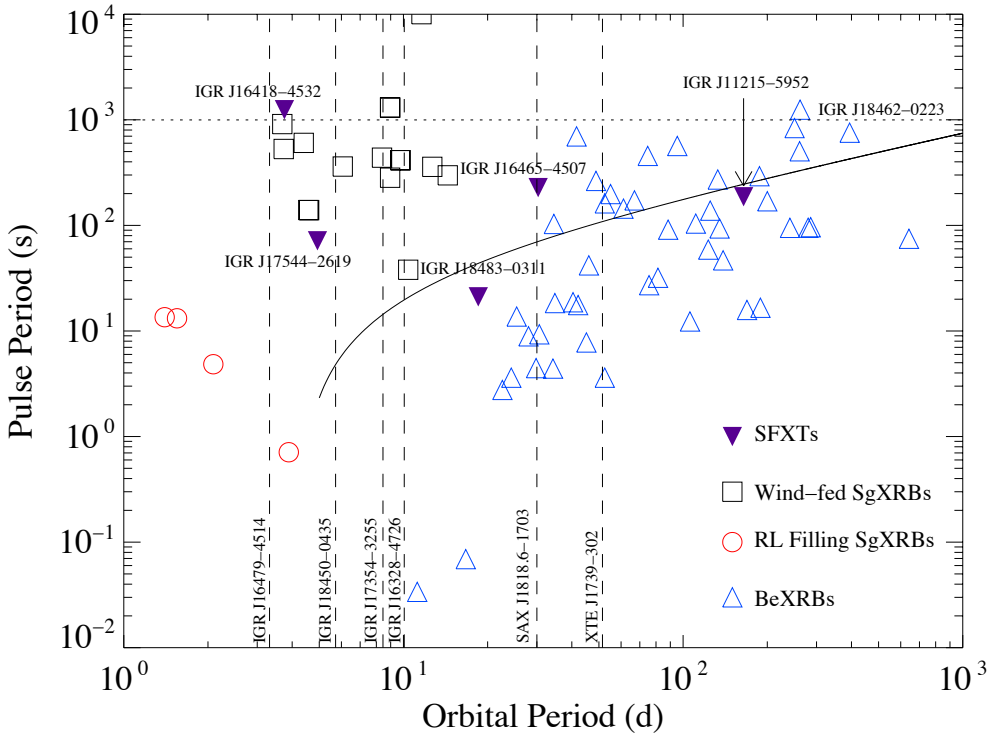

Figure 6.1: The Corbet diagram with the locations of the SFXTs with both P_{orb} and P_{spin} known indicated by the filled purple triangles and the systems with only one identified period shown by the dashed lines, periodicity information from Liu, van Paradijs, & van den Heuvel 2006, Bodaghee et al. 2007 and Table 6.1. The theoretical equilibrium spin period for a NS with a magnetic field of 3×10^{12} G interacting with the wind of a supergiant star is also superimposed (using the formulation of Liu, Chaty, & Yan 2011).

unless the NSs were anomalously rapid or slow rotators. Finally IGR J18462−0223 is the only SFXT without an orbital period to display an unambiguously defined pulse period (Bamba et al. (2001) and Sidoli et al. (2008) also reported a detection of an ∼4.7 s pulsation from IGR J18410−0535 (AX J1841.0−0536), however, this was later disputed by Bozzo et al. (2011)) as displayed by the horizontal line in Fig. 6.1. At a value of 997 s this pulsation allows for IGR J18410−0535 to be consistent with either the SgXRB or BeXRB population.

6.1.1 The evolutionary history of SFXTs

Whilst orbital and spin periods have been detected in a large number of SFXTs there are also a number of sources in which this is not the case. In the case of systems with unidentified orbital periods this is most likely due to the system properties providing challenges to the identification of the binary orbit. In some cases it is simply the lack of diagnostic information provided by the small number of detected outbursts that prevents the determination of the orbital period (e.g.

IGR J20188+3647 and IGR J21117+3427; Sguera et al. 2006b). Such a small number of outbursts may be the result of the systems possessing long, wide orbits such that outbursts are rarely generated or they may be located at large distances so that only the most luminous outbursts are detectable. In other cases systems can display much higher levels of outburst activity without a periodicity being detectable (e.g. IGR J18410−0535 which has a duty cycle of inactivity of only 28%; Romano et al. 2009b). In these cases, where the sources also have confirmed stellar counterparts confirming the binary nature of the X-ray source, the orbits are likely near-circular such that there is no enhancement of emission during a preferential orbital phase to allow the identification of the orbital period. The systems should also be at low inclinations so that X-ray eclipses are not produced to provide a dynamical signal. It may be, however, that with a continued increase in exposure, the orbital periods of the non-periodic SFXTs will be revealed. In the case of spin periods it is the pulsating SFXTs that are the minority with many of the well studied systems yet to have a pulse period identified. The origins of this lack of spin period detections are likely varied but, again, observational limitations provide obstacles to the identification of the periodic signals. With peak luminosities of $\sim 10^{36}\,\mathrm{erg\,s^{-1}}$ SFXTs are detected by hard X-ray monitors with insufficient signal-to-noise to allow the identification of pulsations in this band. At softer energies many observations are short, snap-shot exposures (a few ks) which have an insufficient duration to allow the detection of signals in the range of hundreds to thousands of seconds. Additionally, during longer observations with more sensitive instruments, the pulsed signal can be masked by the large scale flaring that occurs on similar, ks timescales during active states or the generation of the pulsed signal may be inhibited during observations of SFXTs in the quiescent state if magnetic or centrifugal barriers prevent matter from entering the magnetosphere and forming accretion columns. Obscuring material close to the NS may also act to disrupt and dampen the pulsed signal in these (sometimes) highly absorbed systems. Hence the detection of pulsations from the SFXTs is challenging and, along with the fact that the NSs in some systems may be inappropriately aligned to produce observable pulsations, helps to explain why the number of SFXTs with firmly identified NS spin periods is rather small.

The spread of the SFXTs that do have identified orbital or spin periods in the Corbet parameter space (Fig. 6.1), however, is intriguing. Given that the orbital periods of SgXRBs would not be expected to change significantly during the wind-fed X-ray binary stage of their evolution, due to the relatively low mass-loss rate of the supergiant ($< 10^{-6}\,\mathrm{M_\odot\,yr^{-1}}$) compared to the total mass of the binary during the short lived ($<$ Myr) supergiant phase, and the pulse periods would also remain fairly constant due to the inefficient, randomly orientated transfer of angular momentum provided through wind accretion, this implies that SgXRBs occupy their current locations in the Corbet diagram at the onset of the X-ray binary

phase. Hence the SFXTs would also have occupied their current locations at the start of the X-ray binary phase, locations which appear consistent with the nominal SgXRB evolutionary track for the shorter orbital period systems but are distinct in the longer period cases. Therefore certain members of the SFXT class may be illustrating an evolutionary pathway to the SgXRB phase that is not revealed in the classical SgXRB population. Liu, Chaty, & Yan (2011) also considered this implication on the evolutionary pathways of HMXBs using the specific examples of IGR J18483−0311 and IGR J11215−5952. In this work, which is briefly summarised and expanded upon here, the authors considered four scenarios under which the spin periods of these SFXTs could have reached their current values through the considerations of the equilibrium spin periods of the NSs in these binaries. The equilibrium spin period of a NS in a binary (Corbet, 1984) is the spin period at which the outer edge of the magnetosphere rotates with the same velocity as the local Keplerian velocity (i.e. $\mathrm{R}_M = \mathrm{R}_{co}$ in the notation used previously in this work). As the spin period of a NS in a binary evolves after the SN explosion of its birth, it tends towards its equilibrium spin period as at this point the 'spin-down' induced by the expulsion of matter that is centrifugally inhibited from accreting at short rotation periods is balanced by the 'spin-up' induced by accretion of matter on to the NS surface at long rotation periods. In the classical SgXRBs, however, it is believed that NSs possess the equilibrium spin periods corresponding to when their companion stars were still residing on the main sequence (Waters & van Kerkwijk, 1989). This results from the fact that the stellar mass loss rates required to achieve a quantitative agreement between the theoretical and observed NS spin periods in SgXRBs are two orders of magnitude below those expected from supergiant stars.

The SFXTs IGR J18483−0311 and IGR J11215−5952, however, have comparatively short spin periods, for their orbital periods, compared to the equilibrium spin period expected to result from the interaction with the companions stellar wind during the MS phase. Liu, Chaty, & Yan (2011) investigated the possible origins of these comparatively short spin periods. They excluded the possibilities that these SFXTs reached their current locations because:

1. they are in fact spinning at the MS equilibrium periods as this requires the NSs to possess a B-field of only $\sim 10^{11}$ G, for which there is no observational evidence within the HMXB population;

2. they have been spun-up from their equilibrium spin periods to their current location due to accretion in the SgXRB phase as the randomly orientated, inefficient transfer of angular momentum prevents coherent spin-up in non-RLO SgXRBs;

3. that the NSs did not reach their equilibrium spin periods before the companion evolved off the MS due to the incompatibility of NS B-field decay timescales for nominal natal fields compared to the MS lifetime of the

companion star.

Instead these authors argue that IGR J18483−0311 and IGR J11215−5952 are the descendants of OeXRBs in which accretion has been reinitialised after the companion has evolved off the MS into the supergiant phase. As a result the NSs in these systems would have possessed faster equilibrium spin periods generated by the interaction with the slower, dense equatorial wind of the Oe-star. The NSs would have then spun-down to the equilibrium spin period of the supergiant wind to ensure that the centrifugal barrier was overcome and accretion was re-initiated in the supergiant phase. To test this conclusion the theoretical equilibrium spin period, as a function of orbital period, was calculated for a B1 Ia supergiant using the methods of Waters & van Kerkwijk (1989), and both IGR J18483−0311 and IGR J11215−5952 were observed to be in good agreement with this model as shown in Fig. 6.1.

The theoretical equilibrium spin period curve for NSs interacting with the stellar wind of a supergiant companion has been reproduced and superimposed on the Corbet diagram in Fig. 6.1 using the same assumptions as those of Liu, Chaty, & Yan (2011) ($\mathrm{B} = 3\times10^{12}\,\mathrm{G}$, $\mathrm{M}_{Sg} = 20\mathrm{M}_{\odot}$, $\mathrm{R}_{Sg} = 30\,\mathrm{R}_{\odot}$, $\dot{M}_{Sg} = 10^{-6}\,\mathrm{M}_{\odot}\,\mathrm{yr}^{-1}$ and $v_{\infty} = 2.65 v_{esc}$). In addition to the agreement of IGR J18483−0311 and IGR J11215−5952 with this model, it is also of note that IGR J16465−4507 is in approximate agreement with this model under the general system parameters assumed. Furthermore several of the SFXTs without currently identified pulse periods could also be consistent with the OeXRB evolutionary track. Under this interpretation, XTE J1739−302 and SAX J1818.6−1703 would be expected to possess pulse periods in the range of $\sim 80 - 200\,\mathrm{s}$, and the shorter orbital period systems (IGR J16328−4726, IGR J17354−3255 and IGR J18450−0435) in the range $\sim 10 - 20\,\mathrm{s}$. Conversely, due to the turnover observed in the theoretical curve, IGR J16479−4514 cannot be consistent with this model as the intersection with its short, 3.32 day orbital period occurs at a pulse period consistent with the initiation of RLO which, given the earlier arguments against RLO, suggests this source is of a slowly rotating nature. Finally it is of note that the classical SgXRB OAO 1657−415 is also close to this curve, which may suggest that the Oe evolutionary pathway was in fact present in the original class of SgXRBs. The location of OAO 1657−415 should be treated with caution, however, as this system is comprised of a NS and an evolved Ofpe/WN9 star that has undergone significant mass-loss, such that the binary has possibly followed an unusual evolution whilst the primary was in the Luminous Blue Variable state (see Mason et al. 2012 for further discussion).

The agreement in the locations of some SFXTs in the Corbet parameter space to the theoretical equilibrium spin periods generated by the interaction with the stellar wind of a supergiant, as opposed to MS, companion strongly implies that these systems have evolved directly from OeXRBs. The existence of an evolutionary

link between the BeXRB and SgXRB phase has implications for both the individual systems and the nature of HMXBs as a whole, revealing a separate evolutionary branch for the production of SgXRBs and an extension of the duration of the X-ray emitting phase in the lifetime of massive binary progenitor systems that should be taken into account in population synthesis models. Hence it may be considered that SgXRBs can be separated into two distinct sub-groups depending on whether or not the system has an accretion history prior to the SgXRB phase. The question may be asked, however, as to why such an evolutionary link may have been identified in the SFXTs, a small population of sources that have been discovered only recently. This can start to be understood in terms of an observational selection effect. When the systems were OeXRBs they were likely in long, eccentric orbits as is observed in the current BeXRB population. Hence, when the companion star evolved off the MS, the resulting system would be a NS in a long eccentric orbit, that may have contracted by up to 10% (Liu, Chaty, & Yan, 2011), about a supergiant companion. As such the resulting X-ray source would not be expected to be a classical, persistent wind-fed SgXRB as the low ambient wind densities at the large apastron separations and the effect of the structure of the supergiant stellar wind, as discussed in previous chapters and the following paragraphs, would produce a transient X-ray source. Finally, only with the launch of X-ray missions with wide FOVs, high hard X-ray instantaneous sensitivity and a Galactic Plane orientated observing strategy, such as *Beppo-SAX*/WFC (Boella et al. 1997, Jager et al. 1997) and currently *INTEGRAL*/IBIS, would such fast transient sources (i.e. SFXTs) be detectable in sufficient numbers to allow the characterisation of their orbital properties and the identification of such an evolutionary pathway in the population.

Whilst the locations of IGR J16465−4507, IGR J18483−0311 and IGR J11215−5952, along with the possible locations of other members of the SFXT class, within the Corbet diagram provide intriguing insights into the varied evolutionary mechanisms that may form SgXRBs, the detection of further pulse periods is vital in assessing this theory to a higher degree of scrutiny. Independent constraints on the orbital and stellar parameters of individual systems will also allow theoretical evolutionary calculations to be performed within a restricted parameter space that would provide a more thorough testing of this hypothesis on a system by system basis.

6.1.2 The nature of the SFXT class

Considerations of the full SFXT population have aided in the understanding of the possible routes through the evolutionary processes followed by massive binary systems. Beyond the full population, however, the increased characterisation of the individual SFXTs also poses the question of how the fast transient behaviour observed in the individual systems can be reconciled, both between the individual

sources and with the more persistent behaviour of the classical wind-fed SgXRBs. The major factors that affect the X-ray emission observed from any particular SgXRB (persistent or SFXT) are: the orbit of the NS (length and eccentricity); the physical makeup of the supergiant stellar wind (total mass loss rate, degree of structure and morphology); the fundamental properties of the NS (B-field and spin period) and the source distance (due to the limited sensitivity of, in particular hard, X-ray telescopes). In the following paragraphs the differing behaviours of the SFXT and persistent SgXRB populations are discussed in terms of the above factors which have been identified and/or inferred from the sources with current datasets. Section 6.2 then outlines the future direction of SFXT research and highlights the areas in which progress is vital to facilitate the next conceptual step forward in the understanding of the members of the SFXT family.

To begin to consider this question the collective orbital light curves of the SFXTs can be used to evaluate the level of consistency between the SFXTs themselves. Figure 6.2 shows the IBIS 18−60 keV orbital phase-folded light curves of all of the periodic SFXTs listed in Table 6.1 using the most accurately determined orbital periods as shown in each panel. IGR J11215−5952 is not included in this figure, as the small number of its 165 day orbital cycles covered across the baseline of the *INTEGRAL* mission and the relatively low exposure achieved on this source (∼5.5 Ms) prevents the generation of a well defined profile. It is immediately apparent from these phase-folded light curves that the orbital behaviour of the SFXTs are not consistent across the whole population. The most obvious anomalies are the short orbital period systems IGR J16479−4514 and IGR J16418−4532 (top left and right panels of Fig. 6.2 respectively) that display steady emission modulated by deep X-ray eclipses that are consistent with the NS being totally eclipsed by the supergiant. The relatively unstructured out-of-eclipse regions of these profiles suggests that the periodicities in these two systems are driven by the presence of the eclipses in their light curves. Conversely the orbital light curves of the SFXTs with longer orbital periods display pronounced peaks flanked by regions of low flux that, in all cases, become consistent with zero, indicating that in these systems it is the flux enhancement generated by the orbital motion of the NS that drives the observed periodicity. The shape of the flux peaks are observed to vary from system to system, however, with some sources displaying smooth sinusoidal-like variations (e.g. IGR J18450−0435, $P_{orb} = 5.720$ d) and others displaying sharper peaks with wider regions of the orbital phase being consistent with zero (e.g. SAX J1818.6−1703, $P_{orb} = 29.972$ d). Additionally the two SFXTs with the longest orbital periods, XTE J1739−302 and IGR J11215−5952, also show emission profiles that suggest the presence of equatorially enhanced density regions in the stellar wind of their supergiant companions through the side peaks in the phase-folded light curve of XTE J1739−302 and the long duration, orbital phase locked outbursts of IGR J11215−5952. This variety of behaviours displayed in the

phase-folded profiles is indicative of the fact that they may be generated by a variety of mechanisms.

To date there have been two fundamental aspects behind the theory of how the SFXTs produce their extreme flaring behaviour. The first being that the NSs in SFXTs are interacting with a clumped, inhomogeneous spherically symmetric supergiant stellar wind (in't Zand 2005, Walter & Zurita Heras 2007). The second is that the SFXTs possess longer, more eccentric orbits to allow the generation of deep quiescent states at large apastron separations, and flares during the brief times of interaction with a denser region of stellar wind during the NS periastron passage (Chaty, 2008b). The extension to longer, more eccentric orbits forms the basis of the SgXRB unification theory, where the difference in the behaviour between the classical persistent wind-fed SgXRBs and the SFXTs is explained through variations in the orbital geometry. Whilst the orbital configurations and light curves derived in the previous chapters and other works (Table 6.1 and Fig. 6.2) provide strong evidence for a distribution of non-zero orbital eccentricities within the SFXT population, it has also been shown that this cannot be the only factor producing the observed SFXT behaviour. The variations in the shape of the observed profiles of the non-eclipsing systems suggests the presence of such an eccentricity distribution due to the sharpness of the profiles and the proportion of orbital phase where the flux is consistent with zero (with *INTEGRAL*/IBIS) in each case. The examples of SAX J1818.6−1703 ($P_{orb} = 29.972$ d) and IGR J16465−4507 ($P_{orb} = 30.332$ d) in Fig. 6.2 illustrate this, with the emission peak being approximately twice as wide in IGR J16465−4532 despite the sources having approximately the same orbital period, indicating that the NS in SAX J1818.6−1703 follows a significantly more eccentric orbit than that of IGR J16465−4532. However, as discussed in Chapter 5, the variations in a smooth wind between the periastron and apastron separations of even XTE J1739−302, the SFXT with the second longest orbital period, at its maximal dynamically allowed eccentricity ($e \sim 0.8$) would not allow the generation of the observed X-ray dynamic ranges under Bondi-Hoyle style accretion. This discrepancy, between the maximum variation in wind density along an eccentric orbit and the maximum X-ray dynamic range observed, widens for systems at shorter orbital periods. Additionally the wide range of orbital phase locations of quiescence detections from individual systems (i.e. IGR J17544−2619 and XTE J1739−302) also illustrates that the detection of such low flux states is not restricted to the apastron regions of the orbits, hence extra mechanisms must be invoked to allow the habitation of these states at the orbital phases observed. The combination of the orbital locations of the quiescent level detections and the short duration X-ray outbursts of the SFXTs strongly indicate that the NSs in SFXTs are interacting with a highly structured stellar wind. Additional confirmation of this comes from the detection of variability in the amount of soft X-ray absorbing material observed during the flares of the SFXTs IGR J16418−4532 (Section 3.5)

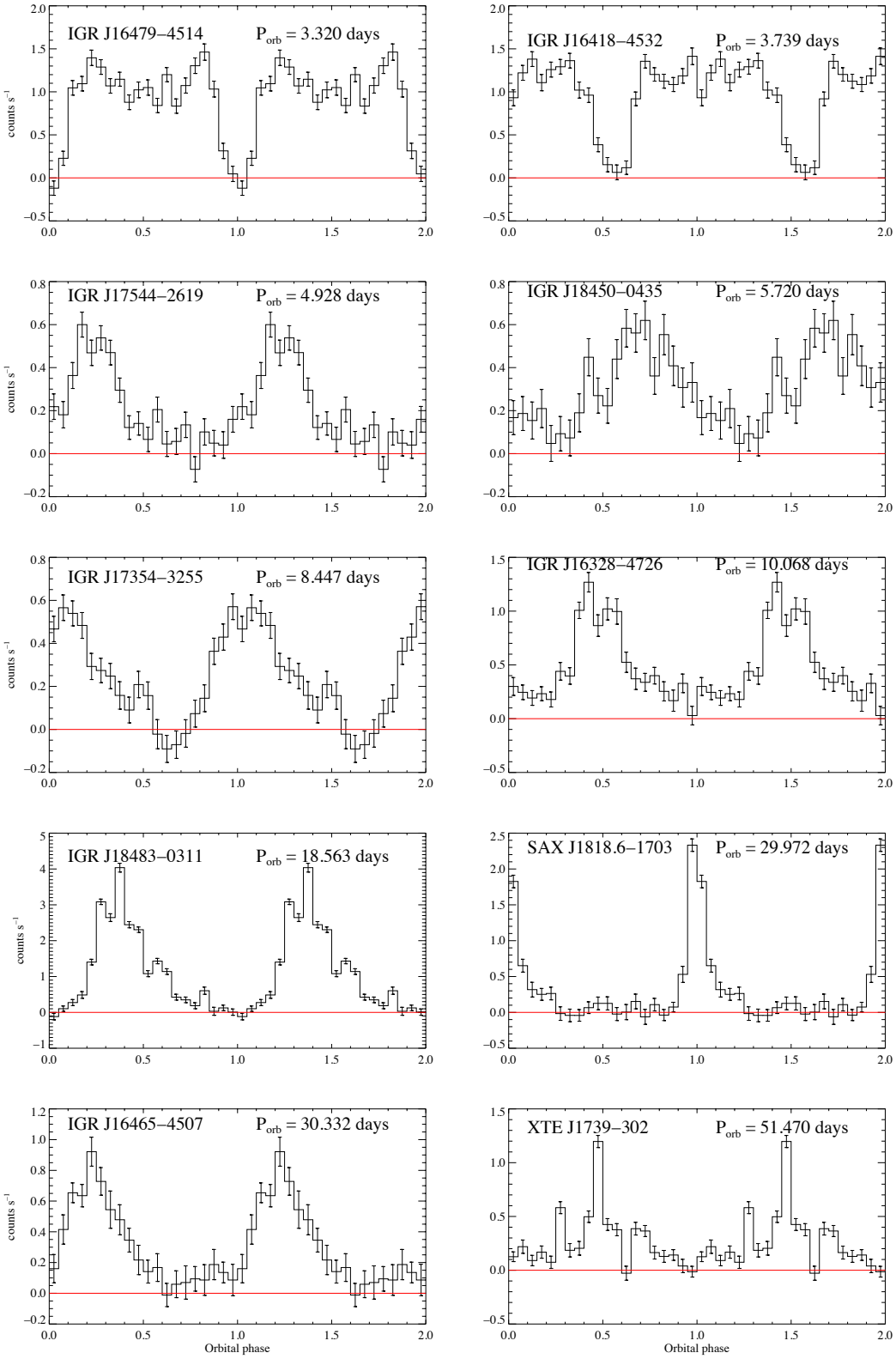

Figure 6.2: The 18−60 keV phase-folded light curves of all of the periodic SFXTs listed in Table 6.1 in order of increasing orbital period. The best determined periods used to perform each of the phase-folds are indicated in each panel.

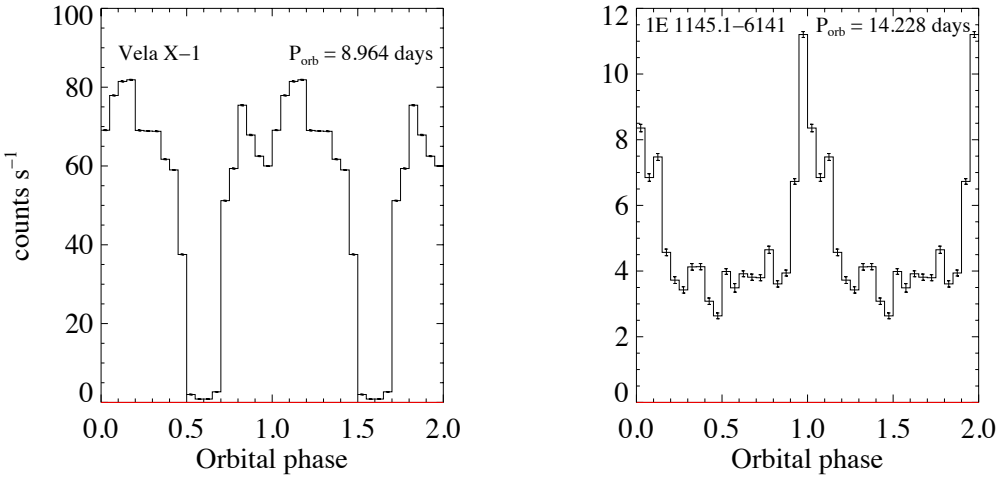

Figure 6.3: The 18−60 keV phase-folded light curves of the persistent wind-fed SgXRBs Vela X−1 and 1E 1145.1−6141. The periods used to perform each of the phase-folds are indicated in each panel (Bildsten et al. 1997 and Ray & Chakrabarty 2002 respectively) where zero phase is arbitrary.

and AX J1841.0−0435 (Bozzo et al., 2011), which occurs over timescales consistent with the passage of typical stellar wind clumps through the line of sight to the NSs.

For comparison the orbital phase-folded profiles of the persistent SgXRB pulsars Vela X−1 ($P_{orb} = 8.964368$ d, Bildsten et al. 1997) and 1E 1145.1−6141 ($P_{orb} = 14.228$ d Ray & Chakrabarty 2002) are shown in Fig. 6.3. In both cases the orbital periods have been derived through the fitting of the dynamically generated Doppler shifts of the pulsar spin frequency, such that the eccentricity of the systems can also be derived. It is seen that the eclipsed profile of Vela X−1 is similar to that of the eclipsing SFXTs IGR J16479−4514 and IGR J16418−4532 which further implies the likely near-circular nature of the orbits in these systems as Vela X−1 has a dynamically determined eccentricity of only $e = 0.09$ (Bildsten et al., 1997). 1E 1145.1−6141, on the other hand, displays a sharp peak covering approximately a quarter of the orbital phase, on top of a consistent non-zero flux of $\sim$4 counts s^{-1} in the IBIS band. Whilst the morphology of the peak is qualitatively consistent with some of the SFXTs, in particular SAX J1818.6−1703, the higher baseline flux is markedly different from the transient sources. The presence of the peak in the light curve is indicative of the influence of the dynamically measured eccentricity of $e = 0.2$ within the NS orbit and also supports the presence of an eccentricity distribution within the SFXT population. The nature of the higher base level compared to SFXT sources is dependent upon both the intrinsic luminosity of, and relative distances to, the sources. In this specific case 1E 1145.1−6141 is located at (8.5 ± 1.5) kpc (Densham & Charles, 1982) which is comparable or greater than the majority of the SFXT population (Table 1.1), indicating that the average, base-level emission in this system is more luminous than the majority of the SFXT

population which display lower peak and inter-peak fluxes despite being located at equal or smaller distances. Further discussions on the physical origin of such a split in the typical luminosity level of persistent SgXRBs and SFXTs are given below. It is of importance, however, that a qualitatively similar range of orbital light curves is observed in both the persistent SgXRBs and the SFXTs (e.g. Figures 6.2 and 6.3), which further adds to the evidence that orbital geometries alone do not generate the different behaviours observed between the persistent SgXRBs and the SFXTs.

Through the observational features discussed in the previous paragraphs it can therefore be concluded that the two fundamental features of the SFXT model, namely the effects of accretion from a clumped stellar wind and the extension to longer more eccentric NS orbits, are driving factors in producing the observed SFXT phenomenology. These features are likely not, however, acting alone or, necessarily, in the way first proposed. As discussed above, there is evidence of some SFXTs possessing longer, more eccentric orbits than many members of the classical SgXRB population. Whilst this helps to explain the morphology of the orbital light curves observed within the SFXT population it cannot, on its own, explain the deep quiescent X-ray states observed as was initially proposed. However, the existence of longer more eccentric orbits does tie in with the concept of some SFXTs having evolved from OeXRB systems. These systems would, by definition, inhabit a 'BeXRB-like' orbit when the Oe star evolves off the MS into a supergiant, creating the longer, eccentric SFXT configuration in the SgXRB phase. Hence it may well be the case that the whole SgXRB population (including the SFXTs) can indeed be separated into two separate populations based on the evolutionary pathways taken to reach their current state, with longer more eccentric systems being evolved from OeXRBs with accretion history, and shorter systems evolving through the nominal MS pathway with no accretion history. But, as shown by the distribution of the SFXTs on the Corbet diagram (Fig. 6.1), these two different evolutionary populations do not correspond to whether or not a SgXRB system is currently observed as an SFXT. Instead the physical properties that determine whether or not a SgXRB behaves as an SFXT or a persistent source must reside within the other key parameters of the systems, namely the properties of the stellar wind, the fundamental properties of the neutron star and the source distances.

Due to the limited sensitivity of *INTEGRAL*/IBIS the exact effect of the eccentricities predicted in the orbits of many of the SFXTs from the shape of the orbital light curves remains unclear. As discussed for the case of IGR J17354−3255 in Section 5.2.1, it is currently not possible, in many cases, to discern if the observed shapes of the phase-folded light curves trace an underlying, smooth wind component or are the result of the superposition of many lower luminosity flares that sum to generate the observed profile. This profile would represent the probability function of the interaction of the NS with a stellar wind clump as a function of orbital phase. Long baseline observations with higher sensitivity,

focusing optics are required to break this degeneracy and aid in fully characterising the stellar winds produced by the supergiant companions in SFXTs. Observing programmes with such aims have started to be performed in some cases, such as the monitoring of almost an entire orbital period of IGR J16479−4514 with *Suzaku* (Sidoli et al., 2013), the restricted orbital phase-constrained monitoring of IGR J16418−4532 using *XMM-Newton* presented in Chapter 3 (also see Sect 6.2) and *Swift*/XRT observations of IGR J18483−0311 across one and half orbital cycles (Romano et al., 2010). In the case of these specific systems differences were observed in the observed orbital light curves. The light curve of IGR J18483−0311 displayed a smooth variation between X-ray luminosities of 10^{33} to $10^{36}\,\mathrm{erg\,s^{-1}}$ across the orbital phase that was argued to be best explained by the superposition of flaring activity resulting from the interaction with stellar wind clumps in the mass range 10^{18} to 10^{21} g. IGR J16479−4514 on the other hand displayed a steady emission at the level of $10^{34}\,\mathrm{erg\,s^{-1}}$ interspersed with small flares, where the flux increases by a factor of 2−3, which are distinct from the bright $10^{36}\,\mathrm{erg\,s^{-1}}$ outbursts also detected in this source. IGR J16418−4532 displayed a steady emission of $2\times10^{36}\,\mathrm{erg\,s^{-1}}$ along with an X-ray intensity dip and flaring activity. From single datasets of these three sources it appears that the mechanisms generating the observed SFXT behaviour vary between systems with different orbital parameters: the longer period system displays a light curve generated by the interaction with discrete stellar wind clumps whilst the shorter orbital period systems interact with a smoother medium. Multi epoch, high sensitivity studies providing full orbital phase coverage of a larger sample of sources are required to allow a more complete characterisation of the emission processes occurring across the SFXT population and aid in determining if the properties of the stellar wind interacting with the NSs vary temporally and between sources.

The discussions in the above paragraphs centre on a traditional Bondi-Hoyle interpretation of the accretion from a clumped supergiant stellar wind. Whilst this interpretation is the natural starting point for developing an understanding of the accretion mechanisms at work in SFXTs it has started to become apparent that higher order accretion scenarios should also be taken into account when considering the physical processes at work in these systems. In IGR J17544−2619, the initiation of the propellor mechanism may aid in producing the X-ray quiescent states observed over a large range of orbital phases in this relatively compact ($\mathrm{P}_{orb} = 4.9279\,\mathrm{d}$) system by reducing the pronounced stellar wind density variations that are required over small spatial extents to explain the largest outbursts by over an order of magnitude (as discussed in Chapter 4). Evidence of different SFXTs inhabiting different active accretion regimes can also be found by comparing the nominal luminosities of the short period, eclipsing systems IGR J16479−4514 and IGR J16418−4532. Chapter 3 discussed recent *XMM-Newton* observations of IGR J16418−4532 in which the source was detected at a nominal luminosity of

$2\times10^{36}\,\mathrm{erg\,s^{-1}}$. By comparing this luminosity to that detected whilst the NS was fully eclipsed by the supergiant, the total stellar mass loss rate was calculated as $(2.3-3.8)\times10^{-7}\,M_{\odot}\,\mathrm{yr^{-1}}$ implying a nominal out-of-eclipse luminosity consistent with that observed in the *XMM-Newton* data. Following the same procedure using a *Suzaku* observation of IGR J16479−4514, however, Sidoli et al. (2013) found that the derived stellar mass loss rate implied a nominal luminosity two orders of magnitude higher than that observed, therefore suggesting the action of a damping mechanism to reduce the nominal X-ray luminosity observed from the system (a few $10^{34}\,\mathrm{erg\,s^{-1}}$). The 'quasi-spherical accretion' model of Shakura et al. (2012), described in Chapter 1, could provide such a damping mechanism such that IGR J16479−4514 occupies the lower luminosity, radiatively-cooled regime for the majority of the time, transitioning into the higher luminosity Compton-cooled regime during the $10^{36}\,\mathrm{erg\,s^{-1}}$ outburst events. Alternatively IGR J16418−4532 would appear to occupy the Compton-cooled regime for the majority of the time and transition into the radiatively-cooled regime during the X-ray 'off-state' observed by *XMM-Newton* (see Chapter 3), the first time such a feature has been observed in an SFXT. As discussed in Chapter 3 IGR J16418−4632 is therefore better characterised as a persistent SgXRB which is only observed as a transient X-ray source due to its large distance which prevents the persistent emission being detected in single observations with X-ray monitoring instruments. Instead the source is detected as transient during bright outbursts resulting from the interaction of the NS with denser regions of the stellar wind and/or the sharp velocity gradients within the radial outflow (e.g. Fig. 1.17, Oskinova, Feldmeier, & Kretschmar 2012). Hence in this particular case it is the distance of the source that is the fundamental factor in defining it as a transient source as opposed to an intrinsic property of the X-ray emission.

Shakura et al. (2013) have suggested that the difference between the persistent SgXRBs and the SFXTs may be that the persistent sources spend the majority of their time in the high luminosity Compton-cooled regime and occasionally enter the radiatively-cooled regime during X-ray dips, as was observed for Vela X-1 and 4U 1907+09. Conversely the SFXTs spend the majority of their time in the low luminosity radiatively-cooled regime and occasionally enter the Compton-cooled regime during the bright outburst events. This picture is consistent with the low luminosity $10^{33}-10^{34}\,\mathrm{erg\,s^{-1}}$ state that many SFXTs have been observed to occupy for the largest proportion of their duty cycles (Romano et al., 2011) and the peak luminosity of outbursts of a few $10^{36}\,\mathrm{erg\,s^{-1}}$. Combining this model with the consistent range of orbital light curves observed in both the persistent SgXRB and SFXT populations and the fact that, in at least one case, IGR J16418−4532, a persistent system masquerades as a transient in monitoring data, leads to the conclusion that a more physically appropriate segregation of the entire SgXRB population should be performed on whether or not a particular system occupies an

impeded or un-impeded accretion regime for the majority of its duty cycle. The impeded and un-impeded regimes are equivalent to the radiatively cooled and Compton cooled regimes of Shakura et al. (2013) respectively. In both cases the interaction with the structured wind of the supergiant generates variability in the sources and may induce temporary accretion regime switches. In the case of the sources that display the deepest quiescent states ($10^{32}\,\mathrm{erg\,s^{-1}}$), additional mechanisms such as centrifugal and magnetic barriers may be responsible for the generation of such low flux levels.

Given the number of unknown physical quantities within all members of the SFXT class it is currently not possible to comment on which single, or combination of, binary properties may lead to some systems inhabiting an impeded accretion regime. The following section outlines the future direction of the field of SFXT research, including accepted and on-going observational programmes, as well as the areas that, as yet, have received little attention but are vital in unraveling the true nature of both the SFXTs and the population of SgXRBs as a whole.

6.2 Future work and direction of the field

As outlined in the previous section the physical parameters that can influence the emission observed from a SgXRB are the binary orbit, the physical nature of the supergiant stellar wind, the fundamental properties of the NS and the distance to the sources. To date the majority of observing programmes undertaken have been in the X-ray band and have focused on the identification and spectral analysis of individual outbursts and lower flux states, the determination of the binary orbital period and the detection of NS spin periods as outlined in earlier chapters. Through these observations other physical parameters have been inferred, such as the typical dimensions of stellar wind clumps and constraints on the B-field strength of the NSs (e.g. $\mathrm{B}\sim10^{14}\,\mathrm{G}$ in IGR J16418−4532, Chapter 3). However, such inferences are typically model dependent and have, to date, often relied upon only loosely constrained stellar and stellar wind parameters, as was previously discussed in detail for the case of IGR J16418−4532. As a result the derived system parameters are somewhat uncertain and prevent firm conclusions being drawn on the physical mechanisms at work.

A key area of understanding that has to be addressed therefore, is the accurate and independent characterisation of the physical properties of the stellar winds produced by the supergiant companions in both SFXTs and persistent SgXRBs. This will allow for an assessment of the degree of variation within the stellar wind parameters between systems and the identification of whether or not the nature of the stellar wind is a driving force behind the different behaviours observed across the whole SgXRB population. The physical properties of the stellar wind can be

investigated both observationally and through the modelling of the observed X-ray emission. Observationally constraints on the total stellar mass loss rate and terminal wind velocity could be obtained through the fitting of the P-Cygni profiles of UV spectral lines (e.g. Lucy & Solomon 1970). Such independent constraints on the total stellar mass loss rates are vital in allowing the effective modelling of the flare luminosity distributions and orbital emission profiles of SFXTs using formulations such as those presented by Ducci et al. (2009). Under this formulation both smooth and clumped components are considered within the stellar wind with these components being tied together through parameters representing the total stellar mass loss rate and the fraction of mass lost in clumps. Hence, without a firm constraint on the total stellar mass loss rates, these parameters can become degenerate and the physical meaning of the clumping fraction and the stellar wind characterisation lost. Additional understanding can be achieved in the optical band by the photometric and spectroscopic monitoring of the Hα emission line to investigate and characterise any variations in the circumstellar environment of the supergiant, particularly in the case of XTE J1739−302 and IGR J11215−5952, which have shown evidence of enhanced equatorial discs within their stellar winds which may generate enhanced Hα variations as is observed in many BeXRBs. Due to the Galactic Plane locations and, in some cases, the intrinsically absorbed companion star emission in SFXTs, the study of these sources in the UV and optical bands can be challenging and will require dedicated, deep monitoring programmes to help unveil the properties of the supergiant stellar winds in SFXTs.

In addition to the uncertainty generated by the unknown make up of the stellar winds in SFXTs, the precise orbital dynamics of these systems are unknown despite the well determined orbital periods of many of these binaries. This is partly due to the unknown mass function of the systems, where the mass of the primary is often only loosely defined by the spectral type and the NS is assumed to have a nominal mass of $1.4\,M_{\odot}$. It is the unknown orbital eccentricity, however, that generates the largest source of uncertainty in the circumstellar environment being experienced by a NS during any particular observation and luminosity state, due to the inability to accurately define the orbital separation of the binary components at this time. Subsequently, the stellar wind velocity and associated NS accretion radius cannot be accurately determined either. The eccentricity of the binary orbit may be determined in some systems by either the characterisation of the radial velocity curve of the supergiant companion or the Doppler modulations of the NS spin period in pulsating sources. Whilst challenging, the application of both of these methods to SFXTs is a possibility. In the case of determining the RV curve it is both the nature of the supergiant stellar atmosphere and the mass ratio of the binary that present observational challenges. Due to the extreme mass ratios present in HMXBs the RV variations induced in the supergiant companions are small, with typical system parameters resulting in velocity semi-amplitudes that

require spectrographs with high resolving powers of $>30{,}000$ to be detectable. Additionally to ensure the true RV curve of the supergiant is derived, photospheric absorption lines must be measured to remove the influence of the variable stellar atmosphere that is traced by the emission lines in the optical spectrum. In the case of SgXRBs, however, the optical spectrum is often heavily absorbed and hence the RV curves must be derived using absorption lines in the NIR band, namely Br10, Br12 and HeI 2.188 μm (Nespoli, Fabregat, & Mennickent, 2008). Hence to measure the RV curve of the supergiant companion requires the use of high resolution, echelle spectrographs that operate in the $1-3$ micron band. Currently only two facilities can perform such studies, CRIRES at the VLT and PHEONIX at KPNO. Two sources in particular, IGR J16479−4514 and IGR J16418−4532, are suited for this study as their short eclipsing orbits constrain the system inclination to be near edge-on, allowing for the derivation of a well defined mass ratio and orbital eccentricity within modest amounts of observing time. The study could then be extended to members of the SFXT class with longer orbital periods and less well constrained inclinations. The alternative method of deriving a dynamical solution for the orbit of an SFXT is through the modelling of the Doppler induced variations in the NS spin period. Monitoring observations with high sensitivity in the soft X-ray band would be required to detect the NS spin periods at multiple epochs and derive the Doppler variations which could be achieved with current facilities, such as *XMM-Newton* or *NuStar*, or a future mission with high X-ray timing capabilities, such as the Large Area Detector (LAD) aboard the proposed *LOFT* mission (Feroci et al., 2012). The best candidate for such a study is IGR J18483−0311, as its relatively short $\sim$21 s spin period allows for an accurate determination of the spin period in short observations which would allow the development of a well sampled spin period history across the orbital phase of the binary through a high sensitivity monitoring campaign. The determination of dynamical solutions of the orbits of members of the SFXT class is vital in allowing the interpretation of the X-ray data to be placed in a truly physical context and provide the most stringent tests for the proposed accretion models in these systems. Of particular interest is the relationship between the physical periastron in the systems and the observed peak in the orbital emission profiles. Any discrepancies in the orbital phase locations of these features would provide diagnostic information as to the mass transfer mechanisms operating in SFXTs and may point to the formation of transient accretion discs or the travel time for material to move through the 'quasi-spherical' atmosphere about the NS and enter the magnetosphere.

In parallel with these new directions to the field of SFXT study, it is imperative to continue observation of these sources in the traditional soft and hard X-ray bands so as to develop the most complete picture possible of their X-ray behaviour. In the hard X-ray band the renewed *INTEGRAL* Galactic Plane Scans (GPS, Fiocchi & Lorenzo Natalucci on behalf of the GPS Team 2013b) and high cadence monitoring

of *Swift*/BAT will allow the development of larger outburst statistics (e.g. a new outburst of IGR J16418−4532 detected on 03 April 2013, Romano et al. 2013) to better constrain the orbital phase distribution of outbursts, the orbital period determinations and orbital phase-folded light curves of the largest possible sample of the SFXT population. Beyond the current generation of X-ray facilities, continued monitoring of these systems in the hard X-ray band may also be provided by the Wide Field Monitor (WFM) aboard *LOFT* and the hard X-ray imagers (CZTI and SMM) under development for *ASTROSAT* (Agrawal & Astrosat Collaboration, 2005). In addition to the increased observational baseline provided for known SFXTs, this continued monitoring of the Galactic Plane provides the only avenue through which currently unknown members of the class may be discovered. Along with the wide field, hard X-ray monitoring of these sources, specific pointed observing programmes should also be pursued. Of particular interest are the new capabilities provided by the focusing hard X-ray optics of the *NuStar* mission. The step change in hard X-ray sensitivity and the unbroken energy coverage between 6 and 80 keV provided by this observatory will allow the study of the X-ray energy spectrum to be performed in greater detail. Such observations may produce the unequivocal detection of both high energy cut-offs and cyclotron absorption lines in the X-ray spectrum and therefore provide independent measurements of the magnetic field strength of the NSs in the SFXT population. The increased sensitivity may also provide the detection of additional NS spin periods. Finally further observing programmes with high soft X-ray sensitivity will continue to provide insights into the circumstellar environment experienced by the NSs in SFXTs, identify unique features and flaring dynamics within these systems and provide additional and/or new spin period detections. In particular, combined *INTEGRAL* and *XMM-Newton* observations that targeted the periastron passages of IGR J16479−4514, IGR J17544−2619 and IGR J17354−3255, using the same observing strategy followed for the observations of IGR J16418−4532 presented in Chapter 3, were accepted and recently performed during *INTEGRAL* AO-9 and AO-10. *XMM-Newton* observations of IGR J17354−3255 and SAX J1818.6−1703 that were not constrained in orbital phase have also recently been performed in AO-11. The analysis of these new datasets is in its early stages but will, when combined with previous work and additional datasets of longer orbital period systems currently being requested, allow a global comparison to be performed of the circumstellar environments being experienced during the periastron passage of the NS in SFXT systems.

To date the field of SFXT research has mainly been performed in the X-ray band. As described in this section, however, the future study of SFXTs must move toward a multi-wavelength approach such that independent constraints on all of the fundamental parameters of these systems may be accessed to allow a full and physically meaningful characterisation of each source and the comparison of the

observed source-to-source behaviour. Only when this has been accomplished will the true nature of the SFXT class and their relationship to the classical, persistent wind-fed SgXRBs be fully defined and understood.

6.3 Summary

This thesis has sought to investigate the Supergiant Fast X-ray Transient class of SgXRBs unveiled by the *INTEGRAL* observatory both on a system-by-system basis and as a population. Through the analysis of several datasets, the physical properties and accretion processes occurring within several individual SFXTs have been investigated and constrained. Some of the main results of this work have been:

- the identification and characterisation of the orbital periods and dynamically viable orbital eccentricities in several systems;
- the identification of possible accretion regime transitions in IGR J16418−4532 which may imply the presence of a highly magnetised neutron star in this system;
- the likely neutron star spin period in IGR J17544−2619, which is consistent with the action of centrifugal accretion barriers to generate the observed X-ray quiescent states and;
- the presence of clumped structures within the stellar winds of the supergiant companions in SFXTs.

By considering the SFXTs as a population, however, two main conclusions can be drawn.

Firstly that the SFXTs as they are currently defined are a phenomenological group defined by the duration and dynamic range of the flares and in fact consist of multiple populations of wind-fed Sg-XRBs whose enhanced level of variability arises from different physical origins. Through the consideration of the full SgXRB population, both persistent SgXRBs and SFXTs, it is concluded that a more physical differentiation between different SgXRB sub-populations is whether or not the systems spend the majority of their time occupying an impeded or un-impeded wind-fed accretion regime, as opposed to the transient nature based phenomenological differentiation currently used, which is heavily influenced by source distance and the limited sensitivity of current observatories.

Secondly, through the distribution of the SFXT class within the Corbet $\mathrm{P}_{orb} - \mathrm{P}_{spin}$ parameter space, it appears that certain members of the SFXT class may have evolved directly from OeXRBs such that they have undergone previous epochs of active accretion which has been reinitialised when the Oe-star evolved off the main sequence and entered the supergiant phase. Hence certain SFXTs may be

demonstrating a previously unidentified evolutionary track toward the SgXRB phase and provide a direct evolutionary link between HMXBs with a MS and post-MS companion for the first time.

It is these identifications of sub-populations within the complete SgXRB population, that do not map directly to the current phenomenologically defined persistent SgXRB and SFXT classes of supergiant HMXB, that form the overarching conclusions of this thesis.

During the decade since their recognition as a class the Supergiant Fast X-ray Transients have revealed many of their key features and components. However, as with all good discoveries, they pose additional questions with every answer they provide and, whilst the understanding of these systems has moved forward, there are still key questions that need to be addressed to provide a fully coherent description of all of the SFXTs and their enigmatic behaviour.

Bibliography

Abdo A. A., et al., 2009, ApJ, 701, L123

Acciari V. A., et al., 2011, ApJ, 738, 3

Agrawal P. C., Astrosat Collaboration, 2005, BASI, 33, 351

Aharonian F., et al., 2005, A&A, 442, 1

Albert J., et al., 2006, Sci, 312, 1771

Alpar M. A., Cheng A. F., Ruderman M. A., Shaham J., 1982, Natur, 300, 728

Arnaud K. A., 1996, ASPC, 101, 17

Arons J., Lea S. M., 1976, ApJ, 207, 914

Avni Y., Bahcall J. N., 1975, ApJ, 197, 675

Bamba A., Yokogawa J., Ueno M., Koyama K., Yamauchi S., 2001, PASJ, 53, 1179

Bazzano A., et al., 2011, ATel, 3361, 1

Belczynski K., Ziolkowski J., 2009, ApJ, 707, 870

Berghoefer T. W., Schmitt J. H. M. M., Danner R., Cassinelli J. P., 1997, A&A, 322, 167

Bhattacharya D., van den Heuvel E. P. J., 1991, PhR, 203, 1

Bildsten L., et al., 1997, ApJS, 113, 367

Bird A. J., Bazzano A., Hill A. B., McBride V. A., Sguera V., Shaw S. E., Watkins H. J., 2009, MNRAS, 393, L11

Bird A. J., et al., 2010, ApJS, 186, 1

Blay P., et al., 2008, A&A, 489, 669

Blondin J. M., Stevens I. R., Kallman T. R., 1991, ApJ, 371, 684

Bodaghee A., et al., 2007, yCat, 346, 70585

Bodaghee A., Tomsick J. A., Rodriguez J., 2012a, ApJ, 753, 3

Bodaghee A., Tomsick J. A., Rodriguez J., James J. B., 2012b, ApJ, 744, 108

Boella G., Butler R. C., Perola G. C., Piro L., Scarsi L., Bleeker J. A. M., 1997, A&AS, 122, 299

Bondi H., Hoyle F., 1944, MNRAS, 104, 273

Bozzo E., Falanga M., Stella L., 2008a, ApJ, 683, 1031

Bozzo E., Stella L., Israel G., Falanga M., Campana S., 2008b, MNRAS, 391, L108

Bozzo E., Campana S., Stella L., Falanga M., Israel G., Rampy R., Smith D., Negueruela I., 2008c, ATel, 1493, 1

Bozzo E., Stella L., Ferrigno C., Giunta A., Falanga M., Campana S., Israel G., Leyder J. C., 2010, A&A, 519, A6

Bozzo E., et al., 2011, A&A, 531, A130

Bozzo E., Pavan L., Ferrigno C., Falanga M., Campana S., Paltani S., Stella L., Walter R., 2012, A&A, 544, A118

Bradshaw C. F., Fomalont E. B., Geldzahler B. J., 1999, ApJ, 512, L121

Bulgarelli A., et al., 2009, ATel, 2017, 1

Burnard D. J., Arons J., Lea S. M., 1983, ApJ, 266, 175

Castor J. I., Abbott D. C., Klein R. I., 1975, ApJ, 195, 157

Castro-Tirado A. J., Brandt S., Lund N., 1992, IAUC, 5590, 2

Chaty S., Rahoui F., Foellmi C., Tomsick J. A., Rodriguez J., Walter R., 2008a, A&A, 484, 783

Chaty S., 2008b, AIPC, 1010, 235

Clark J. S., Tarasov A. E., Okazaki A. T., Roche P., Lyuty V. M., 2001, A&A, 380, 615

Clark D. J., Hill A. B., Bird A. J., McBride V. A., Scaringi S., Dean A. J., 2009, MNRAS, 399, L113

Clark D. J., et al., 2010, MNRAS, 406, L75

Coleiro A., et al., 2013, in prep.

Corbet R. H. D., 1984, A&A, 141, 91

Corbet R. H. D., 1986, MNRAS, 220, 1047

Corbet R., et al., 2006, ATel, 779, 1

Corbet R. H. D., Barthelmy S. D., Baumgartner W. H., Krimm H. A., Markwardt C. B., Skinner G. K., Tueller J., 2010, ATel, 2588, 1

Cox A. N., 2000, asqu.book,

Cusumano G., et al., 2010, A&A, 524, A64

D'Aì A., La Parola V., Cusumano G., Segreto A., Romano P., Vercellone S., Robba N. R., 2011, A&A, 529, A30

Davidson K., Ostriker J. P., 1973, ApJ, 179, 585

Davies R. E., Pringle J. E., 1981, MNRAS, 196, 209

Densham R. H., Charles P. A., 1982, MNRAS, 201, 171

Dickey J. M., Lockman F. J., 1990, ARA&A, 28, 215

Doroshenko V., Santangelo A., Suleimanov V., Kreykenbohm I., Staubert R., Ferrigno C., Klochkov D., 2010, A&A, 515, A10

Doroshenko V., Santangelo A., Suleimanov V., 2011, A&A, 529, A52

Doroshenko V., Santangelo A., Ducci L., Klochkov D., 2012, A&A, 548, A19

Drave S. P., Clark D. J., Bird A. J., McBride V. A., Hill A. B., Sguera V., Scaringi S., Bazzano A., 2010, MNRAS, 409, 1220

Drave S. P., Bird A. J., Townsend L. J., Hill A. B., McBride V. A., Sguera V., Bazzano A., Clark D. J., 2012, A&A, 539, A21

Dray L. M., 2006, MNRAS, 370, 2079

Dubus G., Hameury J.-M., Lasota J.-P., 2001, A&A, 373, 251

Dubus G., Cerutti B., Henri G., 2008, A&A, 477, 691

Ducci L., Sidoli L., Mereghetti S., Paizis A., Romano P., 2009, MNRAS, 398, 2152

Ducci L., Sidoli L., Paizis A., 2010, MNRAS, 408, 1540

Ebisawa K., Bourban G., Bodaghee A., Mowlavi N., Courvoisier T. J.-L., 2003, A&A, 411, L59

Eggleton P. P., 1983, ApJ, 268, 368

Ergma E., van den Heuvel E. P. J., 1998, A&A, 331, L29

Fender R. P., Belloni T. M., Gallo E., 2004, MNRAS, 355, 1105

Fermi LAT Collaboration, et al., 2009, Sci, 326, 1512

Feroci M., et al., 2012, SPIE, 8443,

Fiocchi M., Bazzano A., Bird A. J., Drave S. P., Natalucci L., Persi P., Piro L., Ubertini P., 2013a, ApJ, 762, 19

Fiocchi M., Lorenzo Natalucci on behalf of the GPS Team, 2013b, arXiv, arXiv:1304.1394

Frank J., King A., Raine D. J., 2002, apa..book,

Gabriel C., et al., 2004, ASPC, 314, 759

Galloway D. K., Chakrabarty D., Morgan E. H., Remillard R. A., 2002, ApJ, 576, L137

Gardiner L. T., Noguchi M., 1996, MNRAS, 278, 191

Giacconi R., Gursky H., Paolini F. R., Rossi B. B., 1962, PhRvL, 9, 439

Glasser C. A., Odell C. E., Seufert S. E., 1994, ITNS, 41, 1343

Göğüş E., Kreykenbohm I., Belloni T. M., 2011, A&A, 525, L6

Goldwurm A., et al., 2003, A&A, 411, L223

González-Riestra R., Oosterbroek T., Kuulkers E., Orr A., Parmar A. N., 2004, A&A, 420, 589

Grebenev S. A., Rodriguez J., Westergaard N. J., Sunyaev R. A., Oosterbroek T., 2004, ATel, 252, 1

Greiner J., Cuby J. G., McCaughrean M. J., 2001a, Natur, 414, 522

Greiner J., Cuby J. G., McCaughrean M. J., Castro-Tirado A. J., Mennickent R. E., 2001b, A&A, 373, L37

Grimm H.-J., Gilfanov M., Sunyaev R., 2002, A&A, 391, 923

Giunta A., et al., 2009, MNRAS, 399, 744

Hadasch D., et al., 2012, ApJ, 749, 54

Harrison F. A., et al., 2010, SPIE, 7732,

Hasinger G., van der Klis M., 1989, A&A, 225, 79

Hatchett S., McCray R., 1977, ApJ, 211, 552

Heinke C. O., Wijnands R., Cohn H. N., Lugger P. M., Grindlay J. E., Pooley D., Lewin W. H. G., 2006, ApJ, 651, 1098

Hill A. B., et al., 2005, A&A, 439, 255

in 't Zand J. J. M., Baykal A., Strohmayer T. E., 1998, ApJ, 496, 38

in't Zand J., Heise J., Ubertini P., Bazzano A., Markwardt C., 2004, ESASP, 552, 427

in't Zand J. J. M., 2005, A&A, 441, L1

Illarionov A. F., Sunyaev R. A., 1975, A&A, 39, 185

Jager R., et al., 1997, A&AS, 125, 557

Jahoda K., Markwardt C. B., Radeva Y., Rots A. H., Stark M. J., Swank J. H., Strohmayer T. E., Zhang W., 2006, ApJS, 163, 401

Jain C., Paul B., Dutta A., 2009, MNRAS, 397, L11

Jansen F., et al., 2001, A&A, 365, L1

Knigge C., Coe M. J., Podsiadlowski P., 2011, Natur, 479, 372

Kong A. K. H., Homer L., Kuulkers E., Charles P. A., Smale A. P., 2000, MNRAS, 311, 405

Koyama K., Makishima K., Tanaka Y., Tsunemi H., 1986, PASJ, 38, 121

Kreykenbohm I., et al., 2008, A&A, 492, 511

Kuulkers E., et al., 2006, ATel, 874, 1

Kuulkers E., et al., 2007, A&A, 466, 595

Lebrun F., et al., 2003, A&A, 411, L141

Lépine S., Moffat A. F. J., 2008, AJ, 136, 548

Levine A. M., Bradt H. V., Chakrabarty D., Corbet R. H. D., Harris R. J., 2011, ApJS, 196, 6

Lewin W. H. G., van Paradijs J., van den Heuvel E. P. J., 1997, xrb..book,

Lewin W. H. G., van der Klis M., 2006, csxs.book,

Lewis W., Rappaport S., Levine A., Nagase F., 1992, ApJ, 389, 665

Liu Q. Z., van Paradijs J., van den Heuvel E. P. J., 2000, A&AS, 147, 25

Liu Q. Z., van Paradijs J., van den Heuvel E. P. J., 2005, A&A, 442, 1135

Liu Q. Z., van Paradijs J., van den Heuvel E. P. J., 2006, A&A, 455, 1165

Liu Q. Z., Chaty S., Yan J. Z., 2011, MNRAS, 415, 3349

Lomb N. R., 1976, Ap&SS, 39, 447

Lucy L. B., Solomon P. M., 1970, ApJ, 159, 879

Lucy L. B., White R. L., 1980, ApJ, 241, 300

Lucy L. B., 1982, ApJ, 255, 278

Lund N., et al., 2003, A&A, 411, L231

Lutovinov A., Revnivtsev M., Gilfanov M., Shtykovskiy P., Molkov S., Sunyaev R., 2005, A&A, 444, 821

Maeder A., Meynet G., 2008, ASPC, 388, 3

Masetti N., et al., 2008, A&A, 482, 113

Mason A. B., Clark J. S., Norton A. J., Crowther P. A., Tauris T. M., Langer N., Negueruela I., Roche P., 2012, MNRAS, 422, 199

Matt G., Guainazzi M., 2003, MNRAS, 341, L13s

McClintock J. E., Garcia M. R., Caldwell N., Falco E. E., Garnavich P. M., Zhao P., 2001, ApJ, 551, L147

Meier D. L., Koide S., Uchida Y., 2001, Sci, 291, 84

Nagase F., 1989, PASJ, 41, 1

Naik S., Paul B., Ali Z., 2011, ApJ, 737, 79

Narayan R., McClintock J. E., Yi I., 1996, ApJ, 457, 821

Nazé Y., Oskinova L. M., Gosset E., 2013, ApJ, 763, 143

Negueruela I., 1998, A&A, 338, 505

Negueruela I., Smith D. M., Chaty S., 2005, ATel, 429, 1

Negueruela I., Smith D. M., Reig P., Chaty S., Torrejón J. M., 2006a, ESASP, 604, 165

Negueruela I., Smith D. M., Harrison T. E., Torrejón J. M., 2006b, ApJ, 638, 982

Negueruela I., et al., 2008, AIPC, 1010, 252N

Nespoli E., Fabregat J., Mennickent R. E., 2008, A&A, 486, 911

Okazaki A. T., Negueruela I., 2001, A&A, 377, 161

Okazaki A. T., Hayasaki K., 2007, ASPC, 361, 395

Okazaki A. T., Hayasaki K., Moritani Y., 2012, arXiv, arXiv:1211.5225

Owocki S. P., Castor J. I., Rybicki G. B., 1988, ApJ, 335, 914

Osaki Y., 1999, LNP, 523, 329

Oskinova L. M., Feldmeier A., Kretschmar P., 2012, MNRAS, 421, 2820

Pellizza L. J., Chaty S., Negueruela I., 2006, A&A, 455, 653

Penninx W., Lewin W. H. G., Zijlstra A. A., Mitsuda K., van Paradijs J., 1988, Natur, 336, 146

Penrod G. D., 1986, PASP, 98, 35

Prinja R. K., Massa D., Fullerton A. W., 2002, A&A, 388, 587

Rahoui F., Chaty S., Lagage P.-O., Pantin E., 2008a, A&A, 484, 801

Rahoui F., Chaty S., 2008b, A&A, 492, 163

Rampy R. A., Smith D. M., Negueruela I., 2009, ApJ, 707, 243

Ray P. S., Chakrabarty D., 2002, ApJ, 581, 1293

Reynolds A. P., Quaintrell H., Still M. D., Roche P., Chakrabarty D., Levine S. E., 1997, MNRAS, 288, 43

Rodriguez J., Tomsick J. A., Bodaghee A., Zurita Heras J.-A., Chaty S., Paizis A., Corbel S., 2009, A&A, 508, 889

Romano P., Sidoli L., Mangano V., Mereghetti S., Cusumano G., 2007, A&A, 469, L5

Romano P., et al., 2008a, ATel, 1697, 1

Romano P., et al., 2008b, ATel, 1466, 1

Romano P., et al., 2009a, MNRAS, 392, 45

Romano P., et al., 2009b, MNRAS, 399, 2021

Romano P., Sidoli L., Cusumano G., Vercellone S., Mangano V., Krimm H. A., 2009c, ApJ, 696, 2068

Romano P., et al., 2010, MNRAS, 401, 1564

Romano P., et al., 2011, MNRAS, 410, 1825

Romano P., et al., 2012, MNRAS, 419, 2695

Romano P., et al., 2013, ATel, 4939, 1

Runacres M. C., Owocki S. P., 2002, A&A, 381, 1015

Sana H., et al., 2012, Sci, 337, 444

Sakano M., Koyama K., Murakami H., Maeda Y., Yamauchi S., 2002, ApJS, 138, 19

Scargle J. D., 1982, ApJ, 263, 835

Sguera V., et al., 2005, A&A, 444, 221

Sguera V., et al., 2006a, ApJ, 646, 452

Sguera V., Bird A. J., Dean A. J., Bazzano A., Ubertini P., Malizia A., Masetti N., 2006b, ATel, 873, 1

Sguera V., et al., 2007, A&A, 467, 249

Sguera V., Ducci L., Sidoli L., Bazzano A., Bassani L., 2010, MNRAS, 402, L49

Sguera V., Drave S. P., Bird A. J., Bazzano A., Landi R., Ubertini P., 2011, MNRAS, 417, 573

Shakura, N., Postnov, K., Kochetkova, A., & Hjalmarsdotter, L. 2012, MNRAS, 420, 216

Shakura, N., Postnov, K., & Hjalmarsdotter, L. 2013, MNRAS, 428, 670

Sidoli L., Romano P., Mereghetti S., Paizis A., Vercellone S., Mangano V., Götz D., 2007a, A&A, 476, 1307

Sidoli L., Mereghetti S., Vercellone S., Mangano V., Cusumano G., Romano P., 2007b, ATel, 997, 1

Sidoli L., et al., 2008, ApJ, 687, 1230

Sidoli L., et al., 2009a, ApJ, 690, 120

Sidoli L., 2009b, AdSpR, 43, 1464

Sidoli L., 2011, arXiv, arXiv:1111.5747

Sidoli L., Mereghetti S., Sguera V., Pizzolato F., 2012, MNRAS, 420, 554

Sidoli L., et al., 2013, MNRAS, 482

Smith D. M., Heindl W. A., 2004, ATel, 218, 1

Smith D. M., Heindl W. A., Markwardt C. B., Swank J. H., Negueruela I., Harrison T. E., Huss L., 2006, ApJ, 638, 974

Smith D. M., Bezayiff N., Negueruela I., 2006, ATel, 773, 1

Smith D. M., Main D., Marshall F., Swank J., Heindl W. A., Leventhal M., in 't Zand J. J. M., Heise J., 1998, ApJ, 501, L181

Soria R., Wu K., Page M. J., Sakelliou I., 2001, A&A, 365, L273

Stella L., White N. E., Rosner R., 1986, ApJ, 308, 669

Strüder L., et al., 2001, A&A, 365, L18

Sturm R., Haberl F., Pietsch W., Coe M. J., Mereghetti S., La Palombara N., Owen R. A., Udalski A., 2012, A&A, 537, A76

Sugizaki M., Mitsuda K., Kaneda H., Matsuzaki K., Yamauchi S., Koyama K., 2001, ApJS, 134, 77

Sunyaev R. A., Grebenev S. A., Lutovinov A. A., Rodriguez J., Mereghetti S., Gotz D., Courvoisier T., 2003a, ATel, 190, 1

Sunyaev R., Lutovinov A., Molkov S., Deluit S., 2003b, ATel, 181, 1

Swank J. H., 1994, AAS, 26, 1420

Swank J. H., 2006, AdSpR, 38, 2959

Swank J. H., Smith D. M., Markwardt C. B., 2007, ATel, 999, 1

Tauris T. M., van den Heuvel E. P. J., 2006, csxs.book, 623

Thorsett S. E., Chakrabarty D., 1999, ApJ, 512, 288

Tomsick J. A., Lingenfelter R., Corbel S., Goldwurm A., Kaaret P., 2004, ATel, 224, 1

Tomsick J. A., Corbel S., Goldwurm A., Kaaret P., 2005, ApJ, 630, 413

Tomsick J. A., Chaty S., Rodriguez J., Walter R., Kaaret P., 2009, ApJ, 701, 811

Townsend L. J., Coe M. J., Corbet R. H. D., Hill A. B., 2011, MNRAS, 416, 1556

Torres D. F., Rea N., Esposito P., Li J., Chen Y., Zhang S., 2012, ApJ, 744, 106

Trowbridge S., Nowak M. A., Wilms J., 2007, ApJ, 670, 624

Turler M., et al., 2007, ATel, 1019, 1

Turner M. J. L., et al., 2001, A&A, 365, L27

Ubertini P., et al., 2003, A&A, 411, L131

Ud-Doula A., Owocki S. P., Townsend R. H. D., 2008, MNRAS, 385, 97

Valinia A., Marshall F. E., 1998, ApJ, 505, 134

van Bever J., Vanbeveren D., 1997, A&A, 322, 116

van den Heuvel E. P. J., 1975, ApJ, 198, L109

Vedrenne G., et al., 2003, A&A, 411, L63

Voges W., et al., 1999, A&A, 349, 389

Voges W., et al., 2000, IAUC, 7432, 3

Wagner R. M., Foltz C. B., Shahbaz T., Casares J., Charles P. A., Starrfield S. G., Hewett P., 2001, ApJ, 556, 42

Waters L. B. F. M., van Kerkwijk M. H., 1989, A&A, 223, 196

Waters L. B. F. M., Pols O. R., Hogeveen S. J., Cote J., van den Heuvel E. P. J., 1989, A&A, 220, L1

Walter R., et al., 2006, A&A, 453, 133

Walter R., Zurita Heras J., 2007, A&A, 476, 335

Wijnands R., van der Klis M., 1998, Natur, 394, 344

Wilms J., Allen A., McCray R., 2000, ApJ, 542, 914

Wilson C. A., Finger M. H., Coe M. J., Laycock S., Fabregat J., 2002, ApJ, 570, 287

Wijnands R., 2003, ATel, 191, 1

Winkler C., Gehrels N., Lund N., Schönfelder V., Ubertini P., 1999, ApL&C, 39, 361

Winkler C., et al., 2003, A&A, 411, L1

Zahn J.-P., 1977, A&A, 57, 383

Zamanov R. K., Martí J., Paredes J. M., Fabregat J., Ribó M., Tarasov A. E., 1999, A&A, 351, 543

Zane S., Turolla R., Stella L., Treves A., 2001, ApJ, 560, 384

Zurita Heras J. A., Walter R., 2009, A&A, 494, 1013